MAGNETIZATION AND HYPERFINE INTERACTIONS IN AMORPHOUS FERROMAGNETIC ALLOYS

DISSERTATION

zur Erlangung des Grades eines
Doktors der Naturwissenschaften
der Abteilung für Physik und Astronomie
an der Ruhr-Universität Bochum

von

SUBRATA DEY

aus Hazaribagh (Indien)

Bochum 1981

Digitized by the Internet Archive
in 2026

https://archive.org/details/IA41544719_0003

MAGNETIZATION AND HYPERFINE INTERACTIONS IN AMORPHOUS FERROMAGNETIC ALLOYS

DISSERTATION

zur Erlangung des Grades eines
Doktors der Naturwissenschaften
der Abteilung für Physik und Astronomie
an der Ruhr-Universität Bochum

von

SUBRATA DEY

aus Hazaribagh (Indien)

Bochum 1981

UNIV.
LEIDEN
BIBL.

C O N T E N T S

	pages
0. Deutsche Zusammenfassung	I-XXI
1. Introduction	1
2. Structure of amorphous alloys	
2.1 General Review	9
2.1.1 Radial distribution function	11
2.1.2 Interference functions	18
2.1.3 Structural consideration from mass density and atomic volume	23
2.1.4 DRPHS model	28
2.1.5 Computer simulation of structural models	29
2.2 Magnetic properties and electronic structure of amorphous alloys	
2.2.1 General Review	31
2.2.2 Magnetic moment	34
2.2.2.1 Rigid-band model	34
2.2.2.2 Friedel's model	36
2.2.2.3 Electron transfer model	37
2.2.3 Electronic structure	38
2.2.4 Temperature dependence of magnetization	42
2.2.5 Curie temperature	46
2.2.6 Hyperfine interaction	52
2.2.6.1 Isomer shift	54
2.2.6.2 Magnetic interaction	54
2.2.6.3 Core-polarization	54
2.2.6.4 Electric quadrupole interactions	55

pages

3. Experimental
3.1.1 Systems investigated 58
3.1.2 Formation and phase diagrams 60
3.1.3 Preparation of the amorphous ferromagnetic alloys 66
3.1.4 Schematic clarification 67
3.1.5 Experimental Arrangement 67
3.2 Analysis of the samples 70
3.3 Magnetic measurements
3.3.1 Principle 72
3.3.2 Schematic clarification 72
3.3.3 Croystat 74
3.3.4 Procedure 75
3.4 Mössbauer spectroscopy
3.4.1 General comments 76
3.4.2 The case of ^{57}Fe 77
3.4.3 Experimental arrangement 79
3.4.3.1 Mössbauer source 81
3.4.3.2 Absorber 81
3.4.3.3 Detector 82
3.4.3.4 Measurements at low temperature ($4.2K \leq T \leq 300K$) 83
3.4.3.5 Measurement in the magnetic field 85
3.4.3.6 Errors during measurement 85
3.4.4 Determination of the Mössbauer parameters from the measured spectrum 84

4. Results and Discussion 91
4.1 Magnetic properties of amorphous $Fe_{1-x}B_x$ ($.15 \leq x \leq .26$) 92
4.2 The influence of the metalloid elements (B,Si,C,Ge) on the magnetic properties of amorphous TM-M alloys 107
4.3 Influence of transition metal atoms, Ni and Co on the magnetic properties of the amorphous ferromagnetic TM-M alloys 118

pages

4.4 Magnetic properties of iron-rich amorphous alloys containing chromium and molybdenum 161

4.5 ^{57}Fe isomer shifts due to low concentration of transition metals (T=Ni,Co,Cr, Mn,V) in amorphous $Fe_{80}T_3B_{17}$ 198

4.6 Crystallization of TM-M glasses 203

5. Determination of the separate contributions of Iron, Nickel and Cobalt to magnetic moments of the amorphous alloy systems $(Fe_xCo_{1-x})_{80}B_{20}$ and $(Fe_{1-x}Co_x)_{80}B_{20}$ 207

6. Conclusion 220

References 225

Acknowledgements 236

1. Einführung

Die Existenz von Ferromagnetismus in amorphen Strukturen wurde von Gubanov /3/ theoretisch vorausgesagt. Das Modell, das Gubanov benutzte, gründet auf der Tatsache, daß sich die elektronische Bandstruktur kristalliner Festkörper beim Übergang in den flüssigen Zustand nicht in grundsätzlicher Weise ändert. Daraus folgt, daß die Bandstruktur stärker von der Nahordnung als von der Fernordnung abhängt, so daß der Ferromagnetismus, der von der Nahordnung abhängt, in den amorphen Legierungen nicht zerstört werden sollte. Auf der Basis dieses Modells läßt sich ein Rückgang der Magnetisierung vorhersagen, wenn eine kristalline ferromagnetische Legierung in den amorphen Zustand übergeht.

Wegen ihrer überragenden magnetischen Weichheit sind metallische Gläser, basierend auf Übergangsmetallen (z.B. Fe,Co,Ni zu ca. 75-80%) und sogenannten 'Glasbildnern' von beträchtlichem technischen Interesse.

Anwendungen dieser amorphen Legierungen in magnetischen Geräten, wo sie gewöhnliche kristalline magnetische Materialien ersetzen, sind kürzlich sehr in den Blickpunkt gerückt /4,5,6/. Das Verständnis der Struktur und der thermischen Stabilität dieser metastabilen Materialien sind sowohl in grundsätzlicher als auch in praktischer Hinsicht von großer Bedeutung.

In dieser Arbeit wurde unter Benutzung des Mössbauer Effekts (lokal) und Durchführung gesamt magnetischer Messungen eine detaillierte Untersuchung der magnetischen Eigenschaften der amorphen Legierungen $(ÜM'_{1-x}ÜM"_x)_{100-y}X_y$ (ÜM'=Fe, ÜM"=Ni,Co,Mo,Cr, X=B,C,Ge,Si,P) vorgenommen. Ziel der Untersuchungen an diesen amorphen Legierungen war es,

1) das Verhalten des mittleren magnetischen Moments pro Übergangsmetallatom als Funktion der Konzentration der übrigen Übergangsmetalle (Ni,Co,Mo,Cr) oder der Metalloide (B,Si,Ge,C) zu ermitteln,

2) eine Beziehung zwischen dem mittleren Hyperfeinfeld $\overline{HF}$(Fe), und dem atomaren magnetischen Moment herzuleiten,

3) die individuellen Beiträge der Fe,Co,Ni,Mo und Cr Atome zum mittleren magnetischen Moment zu bestimmen,

4) feststellen, ob Spin-Wellen existieren
und
5) zu versuchen zu klären, welche Rolle die Nahordnung spielt.

Die gesamt-magnetischen Eigenschaften der untersuchten Co- und Ni-haltigen amorphen Legierungen werden im Rahmen des "Ladungstransfer" Modells gedeutet. In diesem Modell wird die Abnahme der Übergangsmetallmoments durch einen 'Transfer' von Valenzelektronen des Metalloids in die teilweise leeren 3d-Bänder des Übergangsmetalls erklärt.

Das Verhalten des magnetischen Moments von Legierungen in Abhängigkeit vom Cr und Mo Gehalt wurde im Rahmen von Friedel's "Virtual bound state" Modell /17/ diskutiert, in dem ein virtueller, gebundener, fünffach entarteter 3d↑ Zustand aufgrund seines repulsiven Potentials aus dem 3d↑-Band nahe der Verunreinigung gehoben wird. Wenn der virtuelle gebundene 3d-"majority spin" Zustand unterhalb der Fermikante bleibt, beeinflusseen die gelösten Cr und Mo Atome die elektronischen Eigenschaften nur durch ihre von der Umgebung verschiedenen 3d↓ Population. Ist das Potential der gelösten Atome genügend repulsiv, den virtuellen gebundenen "majority spin" Zustand über die Fermikante zu heben, so werden fünf 3d↑

Elektronen in 3d↓-Zustände überführt, und in folgenden wird das magnetische Moment zusätzlich zur Änderung aufgrund des Valenz-Elektronen-Unterschiedes um 10 μ_B reduziert. Die experimentellen Resultate dieser Arbeit stimmen quantitativ mit diesem Modell überein. Ähnliche Beobachtungen wurden von Durand /18/ an amorphen Cr-haltigen Legierungen auf Eisen-Basis gemacht.

Mit Hilfe der Mössbauer-Spektroskopie wurden an ^{57}Fe-Atomen, gelöst in $(FeNi)_{80}B_{20}$, $(FeCo)_{80}B_{20}$, $(FeMo)_{80}B_{20}$ und Fe-Cr-B Legierungen, Hyperfeinfeld-Verteilungen gemessen bei temperaturen zwischen 4.2K und 300K. Es zeigt sich, daß das mittlere Hyperfeinfeld nahezu proportional zum mittleren magnetischen Moment von Fe in metallischen Gläsern ist. Das in diesen Legierungen gemessene mittlere Hyperfeinfeld liefert Informationen sowohl über die atomaren 3d-Momente als auch über die Polarisation der Leitungselektronen. Aus der gefundenen Beziehung zwischen atomarem Moment und Hyperfeinfeld wurden die magnetischen Momente in diesen amorphen Legierungen bestimmt.

Die gemessenen Isomerieverschiebungen in amorphen Legierungen werden interpretiert entweder als Elektronenübertrag von Metalloid zum Eisen d-Band, oder als Änderung der s-Elektronen-Dichte. Die Verbreiterung der Linien wird hauptsächlich verursacht durch eine Verteilung von Hyperfeinfeldern. Quadrupolbeiträge zu der Hyperfeinwechselwirkung in ihrem magnetischen Zustand sind, wie gezeigt werden konnte, sehr klein (und tragen nicht signifikant zur Linienverbreitung bei).

2. Experimental

Die vorliegende Arbeit beschäftigt sich mit einer systematischen Untersuchung der magnetischen Eigenschaften amorpher Legierungen des Typs $(ÜM'_{1-x}ÜM''_x)_{100-y}X_y$, wobei ÜM'=Fe, ÜM==Ni,Co,Mo,Cr ist und X ein Glasbildner B,Si, Ge,P. Die Legierungen sind durch kontinuierliches,

schnelles Abkühlen aus der Schmelze hergestellt. Tabelle 3 zeigt die nominalen Zusammensetzungen der amorphen Legierungen, die in dieser Arbeit untersucht wurden.

Die Temperaturabhängigkeit der Magnetisierung wurde mit einem PAR Modell 155, Parallel-Feld-Vibrationsmagnetometer, gemessen im Temperaturintervall 4.2-300K und angelegten Magnetfeldern von .3 und .6T.

Die Temperatur- und Konzentrationsabhängigkeit der Magnetisierung im Nullfeld wurden ermittelt über das Hyperfeinfeld an den Fe-Plätzen. Dabei wurde ein Standard Konstantbeschleunigungs-MS in Transmissionsgeometrie benutzt. Die Gamma-Strahlung der 25 mCi ^{57}Co/Rh Quelle wurde senkrecht zur Probenebene ausgerichtet. Für die Messungen bei Temperaturen zwischen 4.2 und 300K wurde ein Verdampferkryostat verwendet.

Auf Grund der nicht äquivalenten Umgebung eines jeden einzelnen Fe-Platzes ändert sich die Größe der Hyperfeinwechselwirkung von Kern zu Kern in ungeordneten Systemen. Konsequenterweise ergeben Überlagerungen vieler Spektralliniein ein kompliziertes Spektrum. In solchen Fällen ist es möglich, die Hyperfeinfeldverteilungen unter folgenden Näherungen zu berechnen:

a) die Effekte einer Verteilung sowohl der Quadrupol als auch der Isomerieverschiebung auf die Hyperfeinfeldverteilung seien vernachlässigbar,

b) die Intensitätsverhältnisse und Linienbreiten der Einzelspektren, die zum Gesamtspektrum beitragen, seien bekannt und hängen nicht von der Größe der Wechselwirkung ab.

Im allgemeinen wird die Hyperfeinfeldverteilung P(H) mit Hilfe von folgenden zwei verschiedenen Methoden ermittelt /77/:

i) Unter der Annahme einer bekannten Form für P(H) (.z.B. modifizierte Lorentz- oder Gauß-Verteilung), wobei man die Parameter mit Hilfe eines Least Square Fit-Verfahren erhält,

ii) durch eine Reihenentwicklung von P(H) nach trigonometrischen Funktionen, d.h. man nimmt entweder eine diskrete Hyperfeinfeld-Verteilung an oder als Basis eine kontinuierliche Verteilung.

In der vorliegenden Arbeit wurde die erste Methode benutzt, um die gemessenen Spektren auszuwerten, die im Folgenden diskutiert wird.

Unterhalb T_c können die beobachteten Verteilungen der Hyperfein-Komponenten entweder eine Folge der Elektronen Relaxationseffekte oder der Existenz eines nicht einheitlichen Hyperfeinfeldes sein. Die Spektren werden hier mit Verteilung von Hyperfeinfeldern gefittet. Wegen der Unterschiedlichkeit der Fe-Plätze muß man die Hyperfein-Komponenten auf einer statistischen Basis diskutieren und passende Wahrscheinlichkeitsverteilungen angeben.

Bei tiefen Temperaturen sind die magnetischen Momente der Eisen-Atome über einen Bereich geordnet, der erheblich den der interatomaren Abstände übersteigt. Auf der anderen Seite wird der elektrische Feldgradient primär durch die Nachbaratome innerhalb weniger interatomarer Abstände bestimmt. Die metallische Natur dieser Legierungen schließt die Existenz langreichenweitiger elektrostatischer Effekte aus. Im Mittel ist über den Bereich der magnetischen Ordnung der Winkel zwischen der Vorzugsrichtung des elektrischen Feldgradienten und dem magnetischen Feld statistisch verteilt. Die Energieniveaus des angeregten Zustandes sind gegeben durch /96/ mit $\mu H >> e^2qQ$

$$E = -g\mu_N H_m + (-1)^{|m_I|+\frac{1}{2}} \frac{1}{2} e^2qQ\left[\frac{1}{2}(3\cos^2\theta - 1)\right]$$

$$I = \frac{3}{2}$$

Weil Θ im vorliegenden Falle über den Raumwinkel Ω gleichverteilt ist und damit $\langle \cos^2\Theta \rangle_\Omega = \frac{1}{3}$ ist, werden die durchschnittlichen Linienpositionen durch die magnetische Wechselwirkung bestimmt.

Das MS kann darum in Termen einer Verteilung von Hyperfeinfeldern P(H) gefittet werden, einer mittleren Isomerieverschiebung und der Linienbreite Γ, die variieren kann, um die Effekte eines statistisch verteilten EFG und magnetisches Feldes zu berücksichtigen.

Die Formen der Mössbauerlinien, die man durch Unterdrückung der Linien 2 und 5 besser auflöst, sind überwiegend symmetrisch. Die Symmetrie der Hyperfeinfeldverteilung kann durch Messungen in externen Magnetfeldern bestätigt werden Fig. 3.12. Fig. 3.12 kann man entnehmen, daß wegen der Auswahlregel betreffend den Übergang mit $\Delta m=0$, die Linien 2 und 5 unterdrückt sind. Die gemessene Linienform wurde auf der Basis des Faltungsintegrals einer Gaußverteilung von Lorentzlinien berechnet. Es wurde gefunden, daß die gemessenen Linienprofile denen von Gaußlinien entsprechen. So gibt die symmetrische Gaußverteilung von Feldern die Anpassung an die experimentellen Daten, wenn von den gemessenen Linienbreiten Γ_i (mit $i=1,\ldots,6$) die natürliche und apparative Linienbreite Γ_a abgezogen wird. Die Differenz $\Gamma_i - \Gamma_a$ ist proportional zu den Koeffizienten E_i der Mössbauer-Übergangs-Frequenzen $\Gamma_i = E_i H$ in einem Hyperfeinfeld H. Die Linienverbreiterung ist somit einer Verteilung von Hyperfeinfeldern assoziiert und nicht mit einer Verteilung der elektrischen Feldgradienten.

So kann man die Form der Hyperfeinfeldverteilung P(H) als Gaußverteilung

$$P(H) \approx \exp - \frac{(H-H_o)^2}{2(\Delta H)^2}$$

ΔH = Hyperfeinfeldunschärfe
annehmen.
Es wurde auch von anderen Autoren /73,92,97/ berichtet, daß die Hyperfeinfeldverteilung in amorphen Übergangsmetallegierungen ein einziges wohldefiniertes und symmetrisches Maximum besitzt (Abb. 3.13).

3. Die Ergebnisse und ihre Erörterung

In der vorliegenden Arbeit habe ich eine Mößbauer- und magnetische Studie folgender amorpher Systeme

$Fe_{80}M_{20-x}N_x$ (wobei N=Si,C,Ge und M=B), $Fe_{1-x}B_x$ ($0.15 \leq x \leq 0.26$),

$(Fe_xNi_{1-x})_{80}B_{20}$ ($0.25 \leq x \leq 1$), $(Fe_xNi_{1-x})_{80}B_{19}Si_1$ ($0.125 \leq x \leq 0.2$),
$(Fe_{1-x}Ni_x)_{75}B_{25}$ ($0 \leq x \leq 0.7$), $(Fe_{1-x}Co_x)_{80}B_{20}$ ($0 \leq x \leq 0.75$),
$(Fe_{1-x}Mo_x)_{80}B_{20}$ ($0 \leq x \leq 0.125$), $Fe_{85-y}Cr_yB_{15}$ ($0 \leq y \leq 20$) und
$Fe_{95-x}Cr_5B_{20}$ ($0 \leq x \leq 25$) im Temperaturbereich 4.2-300K vorgenommen. Die Resultate dieser Messungen werden jetzt, in zwei Bereiche unterteilt, zusammengefaßt und erörtert.

i) $Fe_{1-x}B_x$ ($0.15 \leq x \leq 0.25$) und $Fe_{80}M_{20-x}N_x$ ($2 \leq x \leq 10$)

Die Abbildungen 4.1(a,b,c,d,e, und f), 4.5(a,b) und 4.6(a,b) zeigen einige typische Mößbauerspektren dieser Legierungen bei verschiedenen Temperaturen (hauptsächlich 300, 77 und 6K). In allen Fällen sind die Spektren zusammengesetzt aus genau festgelegten, aber verbreiterten Linien mit einer relativen Breite von 20%. Solche Spektren beobachtet man gewöhnlich in amorphen Legierungen, in denen eine große Anzahl von verschiedenen Eisenplätzen eine Verteilung der Hyperfeinfelder bewirkt. Die durchgezogene Kurve in jedem Spektrum stellt die optimale Näherung durch eine Gauß-Verteilung für P(H) dar.

Mittleres Hyperfeinfeld als Funktion der B, C, Si

und Ge-Konzentration. Das mittlere Hyperfeinfeld nimmt linear mit der Bor Konzentration ab (Fig. 4.2). Die Veränderung des mittleren Hyperfeinfeldes mit der Bor Konzentration kann man mit Hilfe des Ladungs-Transfer-Modells erklären. In diesem Modell führt die Wechselwirkung zwischen dem Übergangs-Metall und dem Metalloid zu einem Elektron-Transfer von dem Metalloid zum teilweise besetzten 3d-Band des Übergangsmetalls. Also liegt der Grund für die Abnahme des mittleren Hyperfeinfeldes bei Abnahme in B in der Auffüllung des d-Bandes durch die Elektronen.

Also muß nach dem Elektronen-Transfer-Modell bei Substitution von B durch vierwertige Metalloide μ_{Fe} und damit $\overline{HF}$ mit ansteigender Metalloid-Konzentration abnehmen. Tatsächlich führt im Falle von $Fe_{80}B_{20-x}C_x$ eine Menge von 2% C zu einer Abnahme sowohl von μ_{Fe} als auch $\overline{HF}$, aber für Werte von x in der Größenordnung von 10% nimmt μ_{Fe} mit zunehmendem x ab, während $\overline{HF}$ zunimmt. Im Falle von $Fe_{82}B_{18-x}Ge_x$ nehmen nach anfänglicher Abnahme von μ_{Fe} bei 2% Ge sowohl μ_{Fe} als auch $\overline{HF}$ mit x zu. Den einzigen Fall von Verhalten gemäß den Beobachtungen 1 und 2 gab es bei $Fe_{80}B_{20-x}Si_x$, wo μ_{Fe} und $\overline{HF}$ mit zunehmendem x abnahmen. Diesen Widerspruch kann man auflösen, wenn man sich daran erinnert, daß B und C kleinere Ladungszahlen als Fe haben und deshalb die Zwischengitterplätze einer dichten Zufallspackung von Fe-Atomen einnehmen können, während P,Si,Ge mit größeren Ladungszahlen als Fe übergeordnete Plätze einnehmen. Diese Behauptung stimmt überein mit der Tatsache, daß die Dichte von amorphen Legierungen mit B größer ist als solchen mit P. Also kann das beobachtete Verhalten des mittleren magnetischen Momentes als Funktion der Legierungs-Konzentration dem "Size Effekt" zugeschrieben werden.

Das mittlere magnetische Moment in Abhängigkeit vom mittleren Hyperfeinfeld

Es ist wohlbekannt, daß in kristallinem Eisen und zwischenmetallischen Verbindungen (z.B. Fe_3C, Fe_2B und Fe_3P) das magnetische Moment von Fe(μ_{Fe}) in guter Näherung proportional dem Fe-Hyperfeinfeld (HF(Fe)) ist. Man erwartet, daß diese Proportionalität in amorphem $Fe_{1-x}B_x$ und $Fe_{80}M_{20-x}N_x$ Legierungen weiterbesteht. Weil man in amorphen Ferromagneten die Verteilung der Momente nicht direkt mißt, vergleicht man das mittlere magnetische Moment bei Fe mit dem mittleren Hyperfeinfeld. Benutzt man die mittleren Werte von $\overline{\mu}_{Fe}$, findet man, daß das Verhältnis $\overline{HF}/\mu_{Fe}$ nahezu konstant und gleich $14T/\mu_B$. Ähnliche Werte für dieses Verhältnis findet man in anderen amorphen Fe-Metalloidsystemen. Die Konstanz dieses Verhältnisses legt nahe, daß das Fe-Hyperfeinfeld in guter Näherung proportional seinem Moment ist. Also ist der Beitrag der Leitungs-Elektronen-Polarisation zum Hyperfeinfeld in diesen Fällen vernachlässigbar, wie in den kristallinen Eisen-Metalloid Verbindungen.

Isomerverschiebung und Quadrupolmoment

Wegen der Temperaturabhängigkeit der Isomerieverschiebung muß man Vergleiche zwischen Proben mit verschiedenen B-Konzentrationen bei gleicher Temperatur anstellen. Die Isomerverschiebung von amorphen $Fe_{1-x}B_x$-Legierungen bei 77K ist in Fig. 4.3,4.7 als Funktion der B-Konzentrationen dargestellt. Die Isomerverschiebung nimmt zu mit zunehmender Metalloid-Konzentration. In amorphen Legierungen legt das Ansteigen der Isomerverschiebung mit der Metalloid-Konzentration nahe, daß die Abschirmung der s-Elektronen an Fe-Kernort verstärkt wird wegen des La-

dungstransfers vom Metalloid zum leeren Fe-d-Band. Die Tatsache, daß es keine sichtbare Quadrupolaufspaltung gibt (siehe Tabelle 4.1-4.4) kann man auf gleiche Art erklären wie für amorphe Fe-Si Legierungen, d.h. die Werte für den Winkel θ zwischen den Achsen des Feldgradienten und der Hyperfeinfeld-Achse sind zufällig verteilt.

ii) $(Fe_xNi_{1-x})_{80}B_{20}$ $(0.25 \leq x \leq 1)$, $(Fe_xNi_{1-x})_{80}B_{19}Si_1$ $(0.125 \leq x \leq 0.2)$, $(Fe_{1-x}Ni_x)_{75}B_{25}$ $(0 \leq x \leq 0.7)$ und $(Fe_{1-x}Co_x)_{80}B_{20}$ $(0 \leq x \leq 0.75)$

Das mittlere magnetische Moment als Funktion der Ni- oder Co-Konzentration

In Abb. 4.8,4.9 und 4.10 findet man die Abhängigkeit des mittleren magnetischen Moments bei tiefen Temperaturen von der Zusammensetzung dargestellt.

Aus Fig. 4.9 kann man erkennen, daß die Abnahme von $\bar{\mu}$ mit Fe steiler wird auf der Ni-reichen Seite. Dieses Verhalten stimmt mit dem überein, von dem Durand /18/ für das $\bar{\mu}(x)$ der amorphen $(FeNi)_{79}P_{13}B_6$ Legierungen berichtet. In Übereinstimmung damit sollte das magnetische Moment pro Ni-Atom in amorphem $Ni_{80}B_{20}$ viel kleiner sein als das, daß die Extrapolation von $\mu(x)$ auf der eisenreichen Seite liefert.

Im Falle von $(Fe_{1-x}Co_x)_{80}B_{20}$ fällt $\bar{\mu}$, nachdem es im Konzentrationsbereich $0 \leq x \leq 0.125$ bei 2.0 μ_B nahezu konstant war, nahezu linear mit x im Bereich $0 \leq x \leq 0.125$ ab auf 1.27 μ_B. Dieser lineare Abfall von x ist konform mit der Beobachtung, die vorher von Mizoguchi /63/ gemacht worden ist, daß der ungefähre Verlauf der Slater-Pauling-Kurve wiederzufinden ist in den Meß-

werten von $(TM)_{80}P_{10}B_{10}$ amorphen Legierungen. Zusätzlich sind die beobachteten Maximalwerte der magnetischen Momente, z.B. 2.0 μ_B/TM, beobachtet für $(Fe_{1-x}Co_x)_{80}B_{20}$ amorphe Legerungen ebenfalls sehr nahe an den Maximalwerten, die für die entsprechenden kristallinen Proben beobachtet wurden, liegen.

Ein Vergleich der vorliegenden Resultate mit dem magnetischen Verhalten in kristallinem Fe-Ni und Fe-Co zeigt, daß das mittlere magnetische Moment $\bar{\mu}$ der ferromagnetischen Legierungen $(FeNi)_{80}B_{20}$, $(FeNi)_{80}B_{19}Si_1$, $(FeNi)_{75}B_{25}$ und $(FeCo)_{80}B_{20}$ als Funktion der Fe und Co Konzentration ziemlich genau der in kristallinen metallischen Fe-Ni und Fe-Co Legierungen beobachteten Slater-Pauling-Kurve folgt. Eine Verschiebung der Slater-Pauling-Kurve im Falle von amorphen Legierungen gegenüber den kristallinen Äquivalenten folgt aus dem Elektronentransfer von den Glasbildneratomen zu den teilweise besetzten TM d-Bändern.

Wie in kristallinen Fe-Ni und Fe-Co Legierungen nimmt $\bar{\mu}$ in den vorliegenden Legierungen mit zunehmender Konzentration der äußeren Elektronen mit der Steigung -1 ab, was sich auf einfache Art durch das Bändermodell erklären läßt.

Von obigem Vergleich zwischen dem Verhalten von $\bar{\mu}$ in kristallinen und amorphen Legierungen sind zwei Hauptgesichtspunkte zu erwähnen:

i) Die Nahordnung ist hauptsächlich verantwortlich für die beobachtete Änderung von $\bar{\mu}$ mit x. Der Einfluß der Fernordnung ist vernachlässigbar.

ii) Die Abnahme des mittleren magnetischen Moments $\bar{\mu}$ bei Kobalt und Nickel läßt sich auf gleiche Art wie in kristallinen Fe-Co- und Fe-Ni-Legierungen mit Hilfe von Friedel's Modell erklären.

Das mittlere Hyperfeinfeld als Funktion der Fe- und Co-Konzentration

Die Abhängigkeit von $\overline{HF}$(Fe) und $\overline{HF}$(Ni) von x findet man in Abb. 4.9.

$\overline{HF}$(Fe) ändert sich im Bereich $0.25 \leq x \leq 1$ beinahe linear mit der Steigung von 0.029T/% Ni. Unterhalb von x=0.25, d.h. auf der Ni-reichen Seite, fällt $\overline{HF}$(Fe)viel schneller mit ansteigendem Ni-Gehalt von 26.4T für $Fe_{20}Ni_{60}B_{20}$ bis auf 21.3T für $Fe_{10}Ni_{70}B_{19}Si_1$. Das Hyperfeinfeld fällt auf der Eisenseite bei 300K viel schneller, d.h. ungefähr 42% zwischen x=0 und 0.7. Aber $\overline{HF}$(Fe) bleibt für den gleichen Konzentrationsbereich bei 77K und 6K beinahe konstant. Dies ruht von den hohen Curie Temperaturen der Stoffe her (s. Tabelle 4.8 und Abb. 4.18(a,b)). Die Figuren 4.20-4.21 zeigen das gewöhnliche Hyperfeinfeld und die Isomerverschiebung als Funktion der Co-Konzentration für amorphe $(Fe_{1-x}Co_x)_{80}B_{20}$ Legierungen. Das mittlere Hyperfeinfeld nimmt langsam (ungefähr 3%) mit der Co Substitution auf dem gesamten Bereich ab. Diese Abnahme im Hyperfeinfeld von Eisen ist grundsätzlich vergleichbar mit einer ähnlichen Abnahme im gewöhnlichen magnetischen Moment an der Fe-Seite für ansteigende Co-Konzentration.

Das mittlere Hyperfeinfeld in Abhängigkeit vom mittleren magnetischen Moment

Die Abhängigkeit des Hyperfeinfeldes $\overline{HF}$(Fe)als Funktion von $\bar{\mu}$ bei tiefen Temperaturen ist linear (Abb. 4.22,4.23). Die Analyse der Konzentrations-Abhängigkeit sowohl von $\overline{HF}$(Fe) als auch $\bar{\mu}$ zeigt, daß das mittlere Hyperfeinfeld durch die empirische Gleichung(1) beschrieben wird, mit a=12-13 T/μ_B und b=0.1-0.2 T/μ_B für $(Fe_xNi_{1-x})_{80}B_{20}$, a=13.5 T/μ_B und b=0.2 T/μ_B für $(Fe_{1-x}Ni_x)_{75}B_{25}$, a=13.4 T/μ_B

und b=1.02 T/μ_B für $(Fe_{1-x}Co_x)_{80}B_{20}$, a=14 T/$\mu_B$ und b=1.2 T/μ_B für $(Fe_{1-x}Mo_x)_{80}B_{20}$ und a=14.0 T/μ_B, b=1.5 T/μ_B für $Fe_{85-y}Cr_yB_{15}$. In allen betrachteten Systemen beobachtet man, daß der Wert des Koeffizienten 'b' sehr klein im Vergleich zum 'Core-Polarisations-Koeffizienten' 'a' ist. Dies legt nahe, daß in den amorphen Legierungen die 3d-Elektronen stark lokalisiert sind und daß der Beitrag der Polarisation der Leitungselektronen zum Hyperfeinfeld relativ klein ist.

Magnetisierung bei tiefen Temperaturen und Spin-Wellen-Anregung

Die Resultate der Magnetisierungsmessungen, d.h. die reduzierte Magnetisierung, sind in den Abb. 4.27,4.41 gegen $T^{3/2}$ aufgetragen. Man kann sehen, daß das Blochsche $T^{3/2}$ Gesetz für die Temperaturabhängigkeit von $\overline{HF}$(Fe) und $\overline{HF}$(Ni) stimmt. Es ist aus der Abb. 4.25 klar zu ersehen, daß die Gleichung (3) für den Temperaturbereich bis hinauf zu 0.5-0.6 T_c gültig ist.

Sowohl amorphe als auch kristalline Ferromagnetika folgen den Voraussagen der Gleichung (3), die auf dem Heisenberg-Modell aufbaut, nur die Bloch-Koeffizienten B unterscheiden sich bei den amorphen von denen der kristallinen Ferromagnetika auf folgende Arten:

i) Die Werte für B bei kristallinen Ferromagnetika sind ungefähr drei- bis viermal kleiner als bei den entsprechenden amorphen Stoffen.

ii) Der Temperaturbereich, in dem der $T^{3/2}$ Term dominiert, ist bei diesen amorphen Legierungen sehr viel breiter (ungefähr 0.6 T_c) als für kristallines Eisen und

Nickel ($0 \leq T \leq 0.15\ T_c$). Die höheren Werte für B sind charakteristisch für den bildenden amorphen Zustand.

iii) Ebenfalls kann man in den vorliegenden Systemen die generelle Beobachtung machen, daß D für Ferromagnetika im amorphen Zustand kleinere Werte hat als im kristallinen Zustand (siehe Tabelle 4.6,4.9 und 4.11).

Der Term $BT^{3/2}$ in Gleichung (3) entsteht durch die Tatsache, daß die quadratische Dispersions-Relation für kleine Wellenvektoren gilt. Die beobachtung, daß B für amorphe Ferromagnetika ständig einige Male größer ist als für kristalline Ferromagnetika, läßt im amorphen Fall auf höhere Zustandsdichte bei niedrigen Frequenzen schließen.

In Übereinstimmung mit der obigen Erklärung weisen einige theoretische Modelle darauf hin, daß eine zunehmende strukturelle Unordnung zu höherer Zustandsdichte der Spinwellen für Niederfrequenz-Anregungen führt.

Das Verhältnis D/T_c, daß ein Maß für den Bereich der Wechselwirkung ist, unterliegt Schwankungen zwischen 30 und 40 at % Ni für $(FeNi)_{80}B_{20}$ (Abb. 4.26(a,b)). Dies könnte möglicherweise seinen Grund haben in einigen lokalen atomaren Unordnungen. Solche Anomalitäten kann man im Fall von amorphen $(FeNi)_{75}B_{25}$, $(FeCo)_{80}B_{20}$, $(FeMo)_{80}B_{20}$ Legierungen nicht beobachten. Hier bleibt der Bereich der Wechselwirkung beinahe konstant.

Im Falle von amorphen $Fe_{85-y}Cr_yB_{15}$ Legierungen steigt das Verhältnis D/T_c, welches man als Zeichen ansehen kann für eine Verkleinerung des Bereichs der Wechselwirkung mit ansteigendem Chromgehalt. Zusätzlich zu obiger Beobachtung zeigt Tabelle 4.15, daß die Werte für den Koeffizienten B, die sich aus den magnetischen- und Mößbauermessungen ergeben, übereinstimmen. Solch gute Übereinstimmung der durch beide Methoden B Werte legt nahe, daß die konventionelle Spin-Wellen-Theorie das beobachtete magnetische Tief-Temperatur-Verhalten gut erklärt.

Mittlere Hyperfeinfelder als Funktion der Mo- und Cr-Konzentration

Die Abb. 4.31(a,b), 4.36 und 4.37(a,b,c) zeigen Mößbauerspektren von $(Fe_{1-x}Mo_x)_{80}B_{20}$, $Fe_{95-x}Cr_5B_x$ und $Fe_{85-y}Cr_yB_{15}$ bei den Temperaturen 300, 77 und 6K. Die Linien sind wesentlich breiter als im Falle von amorphen FeB und Fe-Ni-B Legierungen (relative Linienbreiten zwischen 20 und 30%). Zeichnung 4.32 zeigt die Abhängigkeit der Werte für das mittlere Hyperfeinfeld von der stofflichen Zusammensetzung bei 300, 77 und 6K. Ersetzt man bei $Fe_{80}B_{20}$ 10% Eisen durch Mo, so sind die Werte für das mittlere Hyperfeinfeld bei 6K um 40% kleiner als vorher. Man findet, daß das mittlere Hyperfeinfeld im Bereich $0 \leq x \leq 0.125$ linear als Funktion der Mo-Konzentration abnimmt.

Eine gute Näherung für das $\overline{HF}$(Fe) bei 6K erhält man in diesem Konzentrations-Bereich durch die folgende Gleichung:

$$\overline{HF}(Fe) = (29.9-86.7x) \text{ Tesla} \qquad (58)$$

Das lineare Verhalten von $\overline{HF}$(Fe) bei 6K als Funktion der Mo-Konzentration stimmt überein mit der Abhängigkeit des mittleren magnetischen Moments/ Übergangsmetall-Atome von x.

Abb. 4.38 zeigt die Abhängigkeit der mittleren Werte für das Hyperfeinfeld $\overline{HF}$(Fe) von der Zusammensetzung bei 77K und 6K. Man beobachtet mit ansteigender Bor-Konzentration eine geringe Abnahme der Werte für das Hyperfeinfeld, während die Hyperfeinfeld-Werte bei Hinzufügen von ein paar Prozent Chrom schneller abnehmen. Im Bereich $0 \leq y \leq 10$ nimmt das Hyperfeinfeld linear ab, um bei 15% Chrom plötzlich abzufallen. Weiteres Hinzufügen von Chrom ändert kaum noch etwas. (bei 20% unterscheidet sich das $\overline{HF}$-Feld kaum von dem bei 15%, 6K.) Das Verhalten von $\overline{HF}$(Fe) als Funktion von y im linearen Bereich kann man näherungsweise durch die Gleichung (61) ausdrücken:

$$\overline{HF}(Fe) = (29.4-.7y) \text{ Tesla} \qquad (61)$$

Das mittlere magnetische Moment als Funktion der Mo- und Cr-Konzentration

Man kann aus den Ergebnissen (Tabellen 4.13 und 4.15) und Abb. 4.33, 4.39) ersehen, daß die Abnahme des magnetischen Moments ($\bar{\mu}$) für amorphes $(Fe_{1-x}Mo_x)_{80}B_{20}$ $(0 \leq x \leq 0.125)$ und $Fe_{85-y}Cr_yB_{15}$ $(0 \leq y \leq 20)$ mit abnehmender Mo- und Cr-Konzentration wesentlich schneller erfolgt als bei den entsprechenden kristallinen Stoffen.

Die Veränderung von $\bar{\mu}$ als Funktion der Mo- und Cr-Konzentration für diese amorphen Legierungen werden in den Abb. 4.30 und 4.36 durch die durchgezogenen Linien dargestellt, die dazugehörigen Steigungen sind $-8.1\ \mu_B$ $(0 \leq x \leq 0.125)$ und $-9.7\ \mu_B$ $(0 \leq y \leq 20)$. Diese Steigungswerte für hohe Mo- und Cr-Konzentrationen sind größer als die, die man aus dem "Rigid-Band-Modell" erwartet $(-2.0\ \mu_B)$, und so zeigen diese Legierungen, wie ihre kristallinen Gegenstücke, beträchtliche Abweichungen von der Slater-Pauling-Kurve. Die Rigid-Band Näherung ist nur anwendbar auf kleine Konzentrationen von Verunreinigungen, die das periodische Potential des Kristalls nur leicht stören. Diese Rigid-Band Näherung ist also nicht anwendbar für $|Z| \geq 2$, z.B. bei Mo und Cr in Eisen, wie Abb. 4.30 und 4.36 und Tabelle 4.13 und 4.15 zeigen.

Man kann zwei andere Näherungen nehmen, um das magnetische Moment TM-Atom für amorphe $Fe_{85-y}Cr_yB_{15}$ Legierungen zu berechnen. In der ersten berechnet man $\bar{\mu}$ aus dem "Weighted average per formula unit" (μ_a)-Verfahren, und setzt jeweils $2\ \mu_B$, $-4\ \mu_B$ und $0\ \mu_B$ für Fe,Cr und B Atome ein.

In der zweiten Näherung benutzt man die Formel von Friedel (17), um μ_F zu berechnen. Man kann aus Tabelle 4.15 und Abbildung 4.36 ersehen, daß die Werte für $\bar{\mu}_F$ (Magnetisches Moment/TM atom, aus Friedels Formel berechnet) näher an den experimentellen Werten liegen als die μ_a. Das Verhalten von μ bei Mo und Cr kann man also physikalisch auf der Basis von Friedels Modell verstehen.

Isomerverschiebung und Quadrupolaufspaltung

Wie man aus Tabelle 4.1 und 4.7 und Abbildung 4.29(a,b,c) ersehen kann, ändert sich die Isomerieverschiebung nicht so sehr bei der Legierung mit Nickel, drastisch aber, wenn man B durch P ersetzt.

Je höher die Ni- und P-Konzentration ist, desto stärker ist die Änderung der Isomerverschiebung in einer Richtung, die eine Vergrößerung der Abschirmung der s-Elektronen und eine Abnahme ihrer Aufenthaltswahrscheinlichkeiten am Fe-Kern vermuten lassen. Der beobachtete Trend läßt darauf schließen, daß es einen Elektronentransfer von P und B zum d-Band des Übergangsmetalls gibt. Den stärkeren Einfluß von P kann man als Folge seiner höheren Anzahl von p-Elektronen im Vergleich zu B erklären. Man muß erwarten, daß die s-Elektronen ins Leitungsband gelangen, während die p-Elektronen hauptsächlich zum leeren d-Band des Übergangsmetalls wandern.

Die beobachtete Zunahme der Isomerverschiebung als Funktion der Co, Ni, Mo und Cr-Konzentration kann man ebenfalls auf der Basis dieses Modells erklären.

Bei $T<T_c$ erwartet man, daß der elektrische Feldgradient vernachlässigbar ist, weil der winkelabhängige Anteil insgesamt Null ist. Dies wird belegt durch die Tatsache, daß die Position der sechs Linien sehr symmetrisch in Bezug auf den Null-

punkt sind. Wenn $T<T_c$, findet man auch die Quadrupolaufspaltung bei amorphen Legierungen vernachlässigbar klein.

4. Zusammenfassung

Es wurde eine systematische Untersuchung des magnetischen Verhaltens von amorphen ferromagnetischen Legierungen mit verschiedenen Übergangsmetall-Metalloid-Zusammensetzungen durchgeführt.

In der ersten Gruppe von Legierungen wird der Gehalt an Übergangsmetall verändert, während dieser in der zweiten Gruppe konstant gehalten und der Metalloidgehalt geändert wird. An den Fe-Plätzen in amorphen Fe-Ni-B, Fe-Co-B, Fe-Cr-B, Fe-Mo-B und Fe-B-M (M=C,Si,Ge) Legierungen wurden mit der Mössbauerspektroskopie Hyperfeinfeldverteilungen in guter Auflösung gemessen. Diese Ergebnisse liefern eine genaue Information über die durch verschiedene Arten von Übergangsmetall und Metalloid-Nachbarn verursachten Hyperfeinfeldverschiebungen. Für die Untersuchung der gesamt-magnetischen Eigenschaften wurde die Sättigungsmagnetisierung als Funktion von Temperatur und Konzentration gemessen. Die individuellen Beiträgen von Fe,Co und Ni zu dem mittleren magnetischen Moment dieser Legierungen wurden aus den Resultaten dieser zwei Arten von Messungen errechnet.

Die Konzentrationsabhängigkeit von $\bar{\mu}$ als Funktion von Ni und Co in $(Fe_xNi_{1-x})_{80}B_{20}$ $(0.125 \leq x \leq 0.2)$, $(Fe_{1-x}Co_x)_{80}B_{20}$ $(0 \leq x \leq 0.75)$ zeigt, daß $\bar{\mu}_{Fe}$ über den ganzen Konzentrationsbereich ändert sich nicht so stark, während $\bar{\mu}_{Ni}$ und $\bar{\mu}_{Co}$ mit zunehmender Ni- bzw. Co-Konzentration stärker abnehmen. Das mittlere Hyperfeinfeld am Fe-Ort nimmt mit zunehmendem Ni-Gehalt viel schneller ab. Experimentelle Untersuchungen an Legierungen ergeben, daß die 3d-Elektronen als großer "Core" Polarisationsbeitrag stärker lokalisiert sind, wohingegen der Beitrag der Leitungselektronen zum $\overline{HF}$(Fe) sehr klein ist. Ein Vergleich der Resultate zweier Meßmethoden zeigt, daß es eine linear Abhängigkeit des $\overline{HF}$(Fe) vom mittleren magnetischen Moment ($\bar{\mu}$) gibt. Das

Verhalten des mittleren magnetischen Moments als Funktion der Ni- und Co-Konzentration in $(FeNi)_{80}B_{20}$ und $(FeCo)_{80}B_{20}$ kann qualitativ auf der Basis des Ladungstransfer Modells verstanden werden.

Die Substitution mit "Cr,Mo" in der amorphen Fe-B-Legierung hat einen stärkeren Einfluß auf die Abnahme des mittleren Hyperfeinfeldes am Fe-Ort als im kristallinen Fall. Die Abhängigkeit des mittleren magnetischen Moments von "Cr,Mo" haltigen amorphen Legierungen von der Zusammensetzung kann im Rahmen des "virtual bound state" Modells von Friedel /17/ verstanden werden.

Der Bloch-Koeffizient 'B', der aus der Mößbauerspektroskopie und aus Magnetisierungsmessungen erhalten wird, hat zumindest für die betrachteten glasartigen Legierungen bei beiden Meßmethoden denselben Wert. Die Abnahme der Magnetisierung mit steigender Temperatur wird durch die theoretischen Vorhersagen aus dem Heisenberg Modell, vgl. (35) (s. Teil 2), zufriedenstellend beschrieben.

Das Verhalten dieser ferromagnetischen Legierungen bei tiefen Temperaturen kann also im Rahmen der Spin-Wellentheorie erklärt werden.

Die Isomerieverschiebung, die ein Maß für die Elektronendichte am Kernort ist, zeigt für die amorphen ferromagnetischen Legierungen verschiedene Werte. Die systematische Änderung der Isomerieverschiebung mit der Änderung der Zusammensetzung, wie in dieser Arbeit festgestellt, läßt jedoch vermuten, daß ein Ladungstransfer vom Metalloid in das teilweise leere d-Band des Metalls möglich ist und damit die stärkere Abschirmung der Leitungselektronen am Fe-Kern.

Weil die Richtung des magnetischen Hyperfeinfeldes verschieden ist von derjenigen der axialsymmetrischen Hauptachse der EFG's, mittelt sich die effektive Quadrupolwechselwirkung heraus. Man beobachtet daher bei allen amorphen ferromagnetischen Legierungen in ihren magnetisch geordneten Zuständen eine fast verschwindende mittlere Quadrupolwechselwirkung.

1. Introduction

The current interest in amorphous metallic alloys dates from the early 1960's when Duwez /1/ and co-workers produced a wide variety of non-crystalline metallic foils. The existence of an amorphous phase obtained by rapid quenching from the liquid state has been first reported in palladium alloys containing from 16 to 22 at % silicon /2/. Since the ferromagnetic elements iron, cobalt and nickel form complete series of solid solutions with palladium, it was anticipated that the amorphous structure could be retained if these elements were substituted for palladium up to a certain concentration. Thus, the ternary amorphous alloys in which the atomic concentration of silicon was kept constant (20 at %) were successfully produced.

The existence of the ferromagnetism in amorphous structures has been theoretically predicted by Gubanov /3/. The model used by Gubanov was based on the evidence that the electronic band structure of crystalline solids did not change in any fundamental way on transition to the liquid state. This implies that the band structure is more dependent on short range order, rather than long range order so that ferromagnetism, which depends on short-range order, should not be destroyed in the amorphous alloys. On the basis of this model, a reduction in magnetization is predicted when a crystalline ferromagnetic alloy undergoes a crystalline to amorphous transition.

Due to their superior soft magnetic properties, metallic glasses, based on transition metal (e.g. Fe,Co,Ni about 75-80 at %) and the so-called glass former (e.g. B,C,Si,P), are of appreciable technological interest. Applications of these amorphous alloys in magnetic devices substituting ordinary crystalline magnetic materials have come

very much into focus lately /4,5,6/. The understanding of the structure and the thermal stability of these essentially metastable materials is of great importance from both the fundamental and practical viewpoints.

Magnetic investigations in crystalline systems of transition metal alloys have revealed that the magnetic moments of metal atoms depend on their local environments rather than on their average electronic properties /7,8, 9,10/. The short range structure in the glassy state does not differ significantly from that in the corresponding crystalline materials /11/. The variation in the local structure, the fact that the atomic environment for each atom is somewhat different, is in a sense the most fundamental structural characteristic of amorphous solid. Such structural fluctuations in amrohpus systems give rise to the distribution in exchange coupling between the spins of the neighbouring sites. This distribution in exchange coupling results in a distribution in both magnetic moment as well as hyperfine field. Thus the hyperfine interactions will show a distribution of values. The effect of this distribution is not apparent in the magnetic moments or critical behaviour but is necessary to account for the details of the microscopic methods. The local method permits examination of the properties of single atoms, rather than bulk as in magnetization measurements. The macroscopic methods such as the bulk magnetic measurement results are difficult to interpret if a complicated and perhaps unknown spin arrangement exists. The microscopic methods are then especially important for elucidating the atomic arrangements and magnetic structures of the amorphous alloys. Microscopic probes such as X-ray, electron and neutron scattering have been used to obtain radial distribution functions which, in turn, give the local atomic arrangement in amorphous alloys /11,12/. Mössbauer and NMR experiments, also probe the local environments around a given atom

by measuring the hyperfine field distribution at the nucleus.

The first measurements of hyperfine field in amorphous ferromagnetic alloys were performed by Tsuei et al /13/ (and also by Bondor et al /14/) using the Mössbauer spectroscopy of ^{57}Fe in ternary and binary Fe-based alloys. It was found that a continuous set of values of the effective magnetic field (H_o) develops at the ^{57}Fe nuclei and hence a considerable line broadening was observed. Since then the Mössbauer effect of ^{57}Fe has been shown to be a convenient tool for stuying amorphous alloys where a variety of environments must exist for each atomic species.

NMR by spinecho method is known to be the most appropriate technique for stuying broad distributions, since the observed signal is proportional to the nuclear magnetization. Durand et al /15/ have applied for the first time the NMR technique to the study of amorphous metallic alloys. On the basis of the results of an NMR study of ^{59}Co in electrodeposited ferromagnetic Co-P alloys with P content ranging between 6-23.5 at %, they concluded that the average local field is proportional to the saturation magnetization. Hasegawa et al /16/ performed an analysis of the ^{31}P and ^{195}Pt NMR spectra of $(NiPt)_{75}P_{25}$ concluding that the 'dense random packing structure' model fits well the data and that the transfer of charge from the metalloid to the transition metal atom takes place in these alloys. While NMR can be done with a large number of different nuclei, Mössbauer spectroscopy is rather limited to certain nuclei. But wherever the Mössbauer nuclei are available, Mössbauer spectroscopy can provide complementary information regarding distribution of hyperfine fields and hence confirm the results of NMR.

In the present work, a detailed study of the magnetism in the amorphous alloy systems $(TM'_{1-x}-TM''_x)_{100-y}X_y$ (TM'=Fe, TM"=Ni,Co,Mo,Cr; X=B,Si,Ge,C,P) has been carried out using the Mössbauer effect (local) and bulk magnetic measurements. This type of study was undertaken in order to

i) investigate the behaviour of average magnetic moment per transition metal atom as a function of either ii the remaining transition metals (Ni,Co,Mo,Cr) concentration or the metalloid (B,Si,Ge,C) concentration

ii) to establish a relation between the average hyperfine field, $\overline{HF}$(Fe), and the average atomic magnetic moment,

iii) to determine the individual magnetic contributions of Fe,Co,Ni,Mo,Cr atoms to the average magnetic moment,

iv) to investigate the spin wave behaviour at low temperatures

v) to study the role of short-range order.

in these amorphous alloys.

The bulk magnetic properties of the investigated amorphous alloys containing Co and Ni are usually interpreted by the charge transfer model. In this concept, the decrease of the transition-metal moment is explained by the transfer of valence electrons supplied by the metalloid to the partially filled d-bands of the transition metal.

The behaviour of magnetic moments of alloys containing Cr, Mo as a function of concentration has been discussed

in terms of Friedel's bound state model /17/, in which, a five fold degenerate 3d↑ virtual bound state is lifted out of the 3d↑ band near the impurity due to its repulsive potential. If the majority spin, 3d virtual bound state, remains below the Fermi-level, then the Cr, Mo solute affects electronic properties only because of the difference of its 3d↓ population relative to that of the host. If the solute potential is sufficiently repulsive to move the majority spin virtual bound state above the Fermi-level, five 3d-electrons will be transferred to 3d↓-states, reducing the average magnetic moment by 10 μ_B in addition to the change due to the valence electron differences. The experimental results of this work are quantitatively in agreement with this model. Similar observation has been made by Durand /18/ for iron-based amorphous alloy containing 'Cr'.

Hyperfine field distributions at the sites of ^{57}Fe atoms dissolved in $(Fe_xNi_{1-x})_{80}B_{20}$, $(Fe_{1-x}Co_x)_{80}B_{20}$, $(Fe_xMo_{1-x})_{80}B_{20}$, Fe-Cr-B, alloys have been measured by Mössbauer spectroscopy at temperatures between 4.2K-300K. The average hyperfine field is found to be nearly proportional to the average magnetic moment of Fe in metallic glasses. The measured hyperfine field furnishes information about both the 3d atomic moments and the conduction electron polarization in these alloys. From the established relation between the atomic moments and hyperfine fields, the magnetic moments in amorphous alloys have been determined.

The isomer shift results in amorphous alloys have been interpreted either in terms of the electron transfer from the metalloid to iron 'd' band or in terms of the change in the 's' electron density. The broadening of the lines is mainly due to the presence of a distribution of hyperfine fields. Quadrupole contributions to the hyperfine interactions in their magnetic state are shown to be very small and do not contribute significantly to the line broadening.

A comparative study of the separate magnetic contribution of Fe,Co,Ni,Mo,Cr to the average magnetic moment extrapolated at OK of the amorphous alloys have been undertaken. The average magnetic moment of iron, $\bar{\mu}_{Fe}$, has been calculated according to the equation given by

$$\overline{HF}(Fe) = a\bar{\mu}_{Fe} + b\bar{\mu} \qquad (1)$$

where 'a' and 'b' are hyperfine constants and $\bar{\mu}$ is average magnetic moment per transition metal of the amorphous alloy. It is found that the $\overline{HF}(Fe)$ and $\bar{\mu}$ are related by equation (1). A plot of $\overline{HF}(Fe)$ versus $\bar{\mu}$ is a straight line with $a\bar{\mu}_{Fe}$ and b as the intercept and slope, respectively. The finding that $b\bar{\mu}$ is considerably smaller than $a\bar{\mu}_{Fe}$ permits us to neglect the second term in equation (1). The value of 'a' is calculated from the value of intercept, i.e., $a\bar{\mu}_{Fe}$ by taking $\bar{\mu}_{Fe}=\bar{\mu}$ at the highest iron concentration for a particular alloy series. Assuming this value of 'a' to be constant for a series, the values of $\bar{\mu}_{Fe}(x)$ have been computed from the values of $\overline{HF}(Fe)$ at different concentrations. Having obtained the values of $\bar{\mu}_{Fe}$ from the above equation, the values of $\bar{\mu}_{Ni}$, $\bar{\mu}_{Co}$, $\bar{\mu}_{Mo}$ and $\bar{\mu}_{Cr}$ are calculated using equation

$$\bar{\mu} = (1-x)\bar{\mu}_{TM''} + x\bar{\mu}_{Fe} \qquad (2)$$

In case of Co and Ni, $\bar{\mu}_{Fe}$ decreases very slowly whereas $\bar{\mu}_{Ni}$ and $\bar{\mu}_{Co}$ decreases with the increasing Ni, Co concentration. The contribution of Mo to the average magnetic moment is found to be negligibly small. But the substitution of small amount of 'Cr' (about 15 %) has a pronounced effect on the average magnetic moment due to the diminishing iron moment which has chromium neighbours.

The low temperature magnetization behaviour is consistent with the Bloch's $T^{3/2}$ law,

$$M_s(T) = M_s(O)[1-BT^{3/2}-...] \qquad (3)$$

where $M_s(T)$ = magnetization at temperature T,
$M_s(O)$ = magnetization at OK
and B is the Bloch coefficient.

It is found that for these amorphous alloys the observed B's are properly accounted for by the measured spin wave dispersion relations. The Mössbauer and bulk magnetic measurements are in close quantitative agreement. The compositional dependence of the spin-wave stiffness constant for the binary and ternary alloys indicates that the range of the exchange interaction is reduced in the non-crystalline Fe-base alloys.

In order to clarify the role of short range order in such alloys, the study of chemical and topological short range order is essential. In the Fe-B system it was shown /19/ that the Fe environments in the glassy phase are remarkably similar to those of the tetragonal Fe_3B (isostructural Fe_3P) intermetallic compound which is found during crystallization. As the structure of Ni_3B and Co_3B (cementite, orthohombic) is different from Fe_3B, one would expect changes in the short-range order of Fe-B glasses due to the replacement of Fe by Co or Ni. The phases appearing during the crystallization of (Fe,Co)B were investigated by Mössbauer spectroscopy. The structures have been identified as (Fe,TM), $(Fe,TM)_3B$ and $(Fe,TM)_2B$ where TM=Co.

The presentation of the work contained in this thesis is organised as follows:

Chapter 1 deals with a brief description of the work already done on the magnetic properties of amorphous alloys which bears close relevance to the present work. This is followed by the purpose of this work. Theoretical background concerning the magnetic properties, electronic

structure and hyperfine interactions in amorphous alloys is given in Chapter 2. The experimental techniques used in the present work is described in Chapter 3. Chapter 4 is devoted to the results of magnetic and Mössbauer measurements on $(TM'_{1-x}TM''_{x})_{100-y}X_{y}$ alloys and their discussion.

The separate magnetic contributions of Fe, Ni and Co to the average magnetic moment in these alloys have been determined in Chapter 5. The conclusions are drawn on the present work in Chapter 6.

2. Structure of amorphous alloys

2.1 General Review

A clear understanding of the magnetic properties of amorphous magnetic alloys depends on how clearly the atomic structure of these alloys is understood. In the following a brief description of the structure of such alloys is given.

The principle used in the experimental study of the structure of crystalline or amorphous solids are the scattering of radiation on the constituent atoms giving rise to interference effects. The most common methods involve x-rays, electron and neutron scattering. In all cases, the radiation must be as monochromatic as possible.

It is impossible by diffraction methods to detect crystallites of size less than 15-20 A^{O}. Thus an amorphous structure is usually defined as a configuration of atoms in which structural order beyond 15-20 A^{O} is absent. Consequently, it is not possible at once to distinguish between a microcrystalline structure and a homogeneous random (liquid like) distribution of atoms. It is, however, well established that the structural arrangement of atoms in metallic glasses is not based on a microcrystalline model /20/.

Diximier and Sadoc (1978) /21/ state the following points as being characteristic for the structure of most metallic glasses:

1. It is a homogeneous, non microcrystalline, but disordered structure.

2. It is densely packed. Each metallic atom has about 12 neighbours, as in a compact crystalline structure.

3. Interatomic distances are not those found in f.c.c or hcp structures, except the first one. In particular the specific distance $a\sqrt{2}$ of compact systems is missing.

4. Non metallic atoms are spread out in metallic matrix, obeying a unique structural rule, i.e. not to be in hard contact with another non-metallic atom.

5. Non-metallic atoms have 9 metallic neighbours instead of 12.

Diximier and Sadoc propose to call the structure of metallic glasses tetrahedral close packing because it resembles a close packing of tetrahedra. From diffraction experiments it is only possible to deduce a statistical atomic positions. The radial distribution function

$$RDF = 4\pi r^2 \rho(r) \tag{4}$$

for instance, which gives the probability to find an atom per unit volume of radial length at a distance 'r' from a given atom chosen as the origin, is rather insensitive to many local structural changes. Therefore comparisons between diffraction experiments and the increasing number of computer simulation experiments may be helpful for a further understanding of non-crystalline structures. A great advantage of computer models is the detailed knowledge of the atomic positions. It should be noted, however, as emphasized by Finney 1977 /22/, that agreement between model and experimental atomic distribution functions is necessary (and not-sufficient) condition for the reliability of the assumed model. Other properties that are strongly dependent on the detailed short-range order as for instance atomic density and magnetic properties must serve as a test of the model. Thus reliable diffraction data are still of great importance especially to the interpretation of magnetic properties of metallic glasses.

A new x-ray technique, called EXAFS, in the recent years has been developed to probe the local atomic structure in amorphous materials in particular. Extended X-ray Ab-

sorption Fine Structure (EXAFS) is the oscillatory modulation of the absorption coefficient on the high energy side of an x-ray absorption edge of a constituent atom in a system. These oscillations are now theoretically understood to be a final state electron effect arising from the interference between the outgoing photoejected electron and that fraction of itself that is backscattered from the neighbouring atoms /100/. These interference directly reflects of the net phase shift of the backscattered electron in the vicinity of the central excited atom, which is largely proportional to the product of the electron momentum (K) and the distance traversed by the electron. The type of central absorbing atom as well as backscattering neighbouring atoms also play a significant role in the interference event. As a result, EXAFS has now been realized to be a powerful structural tool for probing the atomic environment of matter, particularly since the advent of intense, continuous synchrotron radiation in the x-ray region /101/.

Review articles dealing with the general principles of the theory of EXAFS and some experiments on amorphous materials have been reported /26/.

A large number of reviews on the structure of metallic glasses have been given by Wagner 1969 /23/, Giessen and Wagner 1972 /24/, Cargill 1975a,1976 /20/, Waseda 1977 /25/, Wagner 1978 /23/.

2.1.1 Radial distribution function

The atomic distribution and interference functions which are relevant to problems concerning the scattered intensity form and the structure of isotropic non-crystalline materials will be discussed.

In the following, atomic distribution functions will be given at first for i) one kind of atoms and then this will be extended to ii) 'n' kind of atoms.

i) The average atomic density ρ_o is given by

$$\rho_o = \frac{N}{V} \tag{5}$$

where N is the number of atoms in the scattering volume v.

The radial density function $\rho(r)$ describes averaged variations in atomic density around a given atom chosen as the origin.

The pair correlation function or pair distribution function or pair probability function W(r), PDF(r), or g(r):

$$W(r) = PDF(r) = g(r) = \frac{\rho(r)}{\rho_o} \tag{6}$$

Schematic diagrams of the pair distribution function for four different states of matter are shown in Fig. 2.1. The radial distribution function RDF(r)

$$RDF(r) = 4\pi r^2 \rho(r)$$

RDF(r)dr gives the average number of atoms in a spherical shell of radius 'r' and thickness 'dr' around an atom. Examples of the radial distribution function for some amorphous TM-M alloys are shown in Fig. 2.2.

The reduced radial distribution function G(r) is given by

$$G(r) = 4\pi r(\rho(r)-\rho_o). \tag{7}$$

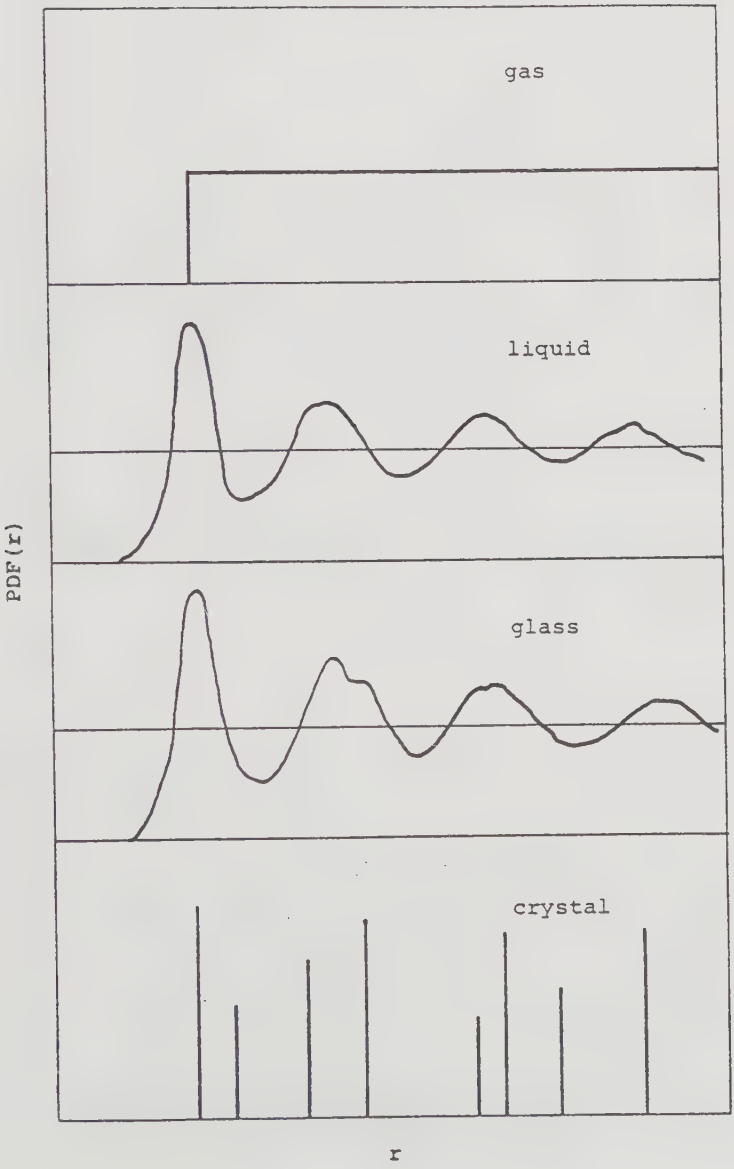

Fig. 2.1: Pair distribution function PDF(r) for four different states of matter: gas, liquid, glass, and crystal.

The reduced radial distribution for some amorphous TM-M alloys are shown in Fig. 2.3.

ii) 'n' kinds of atoms

When the sample consists of 'n' different kinds of atoms with atomic scattering factors $f_1, f_2 \ldots, f_n$ and concentrations $c_1, c_2, \ldots c_n$, where $c_i = N_i/N$, N_i and N being the number of atoms of specimen 'i' and total number of atoms in the scattering volume respectively, partial distribution functions H_{ij} for each of the 'n' kinds of atoms with respect to the remaining n-1 kinds must be defined.

The partial radial density function $\rho_{ij}(r)$ gives the number of j-type atoms per unit volume of a distance 'r' from an i-type atom averaged over all i-type atoms. Thus

$$r = \int_0^\alpha \rho_{ij}(r)\, 4\pi r^2 dr = n_j \qquad (8)$$

independent of i.

The partial pair distribution function $g_{ij}(r)$

$$g_{ij}(r) = \frac{\rho_{ij}(r)}{c_j \rho_o} \qquad (9)$$

The partial reduced radial distribution function $G_{ij}(r)$ is

$$G_{ij}(r) = 4\pi r \rho_o (g_{ij}(r)-1). \qquad (9a)$$

Often the following combination of atomic fraction c_i and atomic scattering factors f_i occurs:

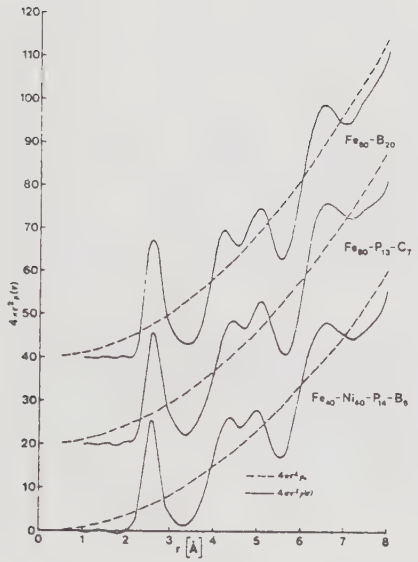

Fig. 2.2: Radial distribution functions $RDF(r)=4\pi r^2\rho(r)$ for $TM_{80}M_{20}$ glasses /23/.

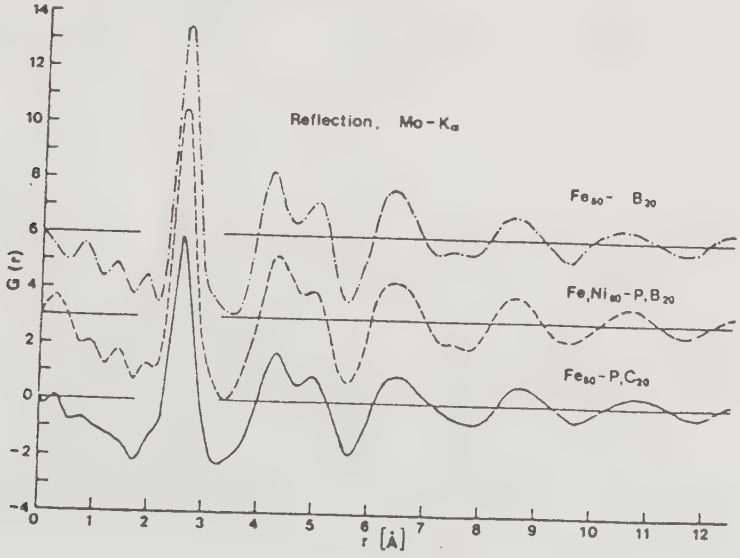

Fig. 2.3: Reduced radial distribution functions G(r) for $TM_{80}M_{20}$ glasses /23/.

$$W_{ij}(K) = \frac{c_{ifi}(K)\, c_{jfj}^{*}(K)}{\left| \sum_{i=1}^{n} c_{ifi}(K) \right|^2} \qquad (10)$$

where $\sum_{i=1}^{n} \sum_{j=1}^{n} W_{ij}(K)=1$, * denotes complex conjugate, and $K = \frac{4\pi\sin\theta}{\lambda}$ is the diffraction vector, 2θ being the angle between the incoming and scattered radiation and λ is the wavelength.

The complex conjugate term suggests that the atomic scattering factors may become complex which they do when absorption is present that is, if the wavelength of the incoming x-ray radiation is close to an absorption edge of one of the constituting elements of the target:

$$f = f_o + \Delta f' + j\Delta f''. \qquad (11)$$

This effect may be utilized to separate the contributions from different components to the total scattered intensity. The correction factors $\Delta f'$ and $\Delta f''$ to the atomic scattering factor 'f' near an absorption edge (anomalous dispersion) is shown in Fig. 2.4.

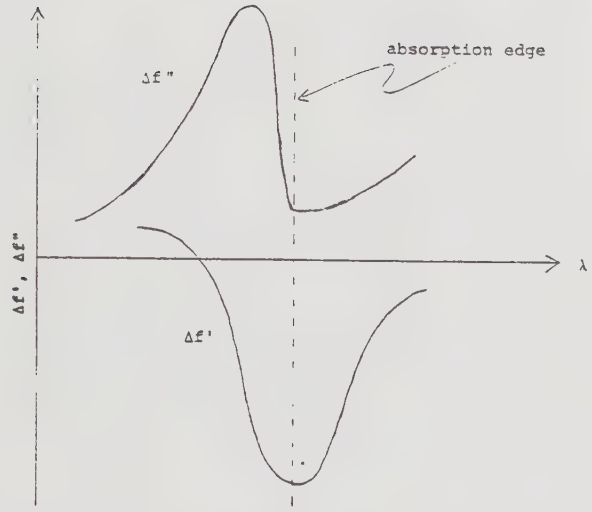

Fig. 2.4: Correction factors Δf' and Δf" to the atomic scattering factor f near an absorption edge (anomalous dispersion)

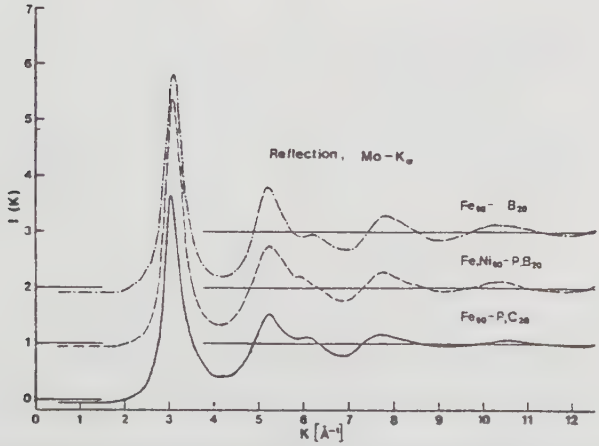

Fig. 2.5: Interference functions I(k) for $TM_{80}M_{20}$ glasses /23/

2.1.2 Interference functions

X-ray, neutron and electron diffraction methods have been frequently used to characterise the structure of non-crystalline materials /12/. A useful and accessible characterisation of atomic arrangements in amorphous solids can be given in terms of a radial distribution function (RDF) $4\pi r^2\rho(r)$, or reduced radial distribution function $G(r) = 4\pi r(\rho(r)-\rho_o)$, where $\rho(r)$ is the average density of atoms at distance r from a reference atom and ρ_o is the overall average density. The distribution function, $\rho(r)$ can not be measured directly from the scattering experiments. This is obtained by Fourier inversion of the coherent scattered radiation.

The coherently scattered intensity from N identical atoms in an irradiated volume v can be expressed in the Fraunhofer approximation as

$$I_N(\underline{K}) = N\,|f(K)|^2 \int q_N(r)\exp(-iK\cdot r)d^3r \qquad (12)$$

Here $K = k-k'$, where k' and k are the incident and scattered wave vectors and $K = \frac{4\pi\sin\theta}{\lambda}$, λ is the wavelength of the x-ray and θ is the scattering angle. f(k) is Fourier transformed atomic form factor for the atomic species being considered and $q_N(r)$ is a generalised Patterson function which describes correlations among the atom positions. $I_N(\underline{K})$ does not include x-ray intensity incoherently scattered in Compton precesses.

Equation (12) also neglects absorption, polarization and multiple scattering effects. Neglecting the generally unobservable volume scattering $N|f(\underline{K})|^2\rho_o\int dr^3\exp(-iK\cdot r)$ and assuming the macroscopic isotropy (i.e. only one kind of atoms), one obtains the epxerimentally measurable coherent intensity at large angles as

$$I_N^{l.a}(K) = N|f(K)|^2[1+4\pi\int_0^\infty r^2 dr(\rho(r)-\rho_o)\frac{\sin Kr}{Kr}] \quad (13)$$

Using the definition of the interference functions, i.e.,

$$I(k) = \frac{I_N^{l.a}(K)}{N|f(K)|^2} \quad (14)$$

equation (13) can be rewritten in the form

$$I(K)-1 = 4\pi\int_0^\infty r^2 dr(\rho(r)-\rho_o)\frac{\sin Kr}{Kr} \quad (15)$$

Fourier-transformation of this equation (15) yields the expression for the reduced RDF as

$$G(r) \equiv 4\pi r(\rho(r)-\rho_o) = \frac{2}{\pi}\int_0^\infty dK K[I(K)-1]\sin(Kr) \quad (16)$$

From this function a number of structural parameters relevant to the amorphous systems can be deduced as shown in the following section.

In Fig. 2.5, the distribution of interference function I(k) for $TM_{80}M_{20}$ glasses are shown following the treatment of Wagner /23/.

n kinds of atoms

The partial interference function $I_{ij}(k)$

$$I_{ij}(K) = 1+\sum_{r=0}^{\infty} 4\pi r^2 \rho_o v(r)\ (g_{ij}(r)-1)\frac{\sin Kr}{Kr}dr \quad (17)$$

The large angle scattering $I_N^{l.a.}(k)$ is given by

$$I_N^{l.a.}(K) = N\sum_{i=1}^{n}\sum_{j=1}^{n} f_1(K)f_j^*(k)c_i c_j I_{ij}(K) \quad (18)$$

The total interference function I(k):

$$I(K) = \frac{I_N^{l.a.}(k)}{N\left(\sum_{i=1}^{n}\sum_{j=1}^{n} c_i f_i^*(k) c_j f_j(k)\right)} = \sum_{i=1}^{n}\sum_{j=1}^{n} W_{ij}(k)\, I_{ij}(k). \qquad (19)$$

Since the magnetic properties of such alloys are dependent on the nearest neighbour distances and co-ordination number of constituting atom, it is worthwhile to give an idea of it. In the following paragraph, a brief discussion of it is given.

Considering the equations (17), for $I_{ij}(k)$, (18), for $I_N^{l.a.}(k)$ and (19) for I(k), the total pair distribution function g(r) in WKM-approximation is given by

$$g(r) = \sum_{i=1}^{n}\sum_{j=1}^{n} W_{ij} g_{ij}(r) \qquad (20)$$

One gets for the total interference function

$$I(K) = 1 + \int_{r=0}^{\infty} 4\pi r^2 \rho_o v(r)(g(r)-1)\frac{\sin Kr}{Kr} dr \qquad (21)$$

The average number of atoms in the range dr at a distance 'r' from an atom is

$$RDF(r)dr = 4\pi r^2 \rho(r) dr$$

and hence the number of atom pairs separated by the distance 'r' is

$$N(r) = \frac{1}{2} N 4\pi r^2 \rho(r) \qquad (22)$$

as all distances are counted twice. Defining the total radial density function $\rho(r)$:

$$\rho(r) = \rho_o g(r) \tag{23}$$

with $g(r)$ given above one gets for $I(k)$:

$$\begin{aligned} I(K) &= 1+\int_{r=0}^{\infty} 4\pi r^2 v(r)(\rho(r)-\rho_o)\frac{\sin Kr}{Kr}dr \\ &= 1 + \frac{2}{N}\int_{r=0}^{\infty} N(r)v(r)\frac{\sin Kr}{Kr}dr \\ &\quad - \int_{r=0}^{\infty} 4\pi r^2 v(r)\rho_o \frac{\sin Kr}{Kr}dr. \end{aligned} \tag{24}$$

The last term will give a diffraction peak at K=0, which may not be detected experimentally. Neglecting this term we get:

$$I'(k) = 1 + \frac{2}{N}\int_{r=0}^{\infty} N(r)v(r)\frac{\sin Kr}{Kr}dr \tag{25}$$

Thus $I'(\underline{K})$ is a "sum" of functions $\frac{\sin Kr}{Kr}$ which according to Fig. 2.6 have their first maximum at $Kr=7.7=\underline{k}_1 r_1$. If $N(r_1)$ is "large" and $N(r_1 \pm \Delta r_1)$ are "small" $I'(K)$ will have a maximum at:

$$K_1 = \frac{4\pi \sin\theta_1}{\lambda} = \frac{7.7}{r_1} \tag{26}$$

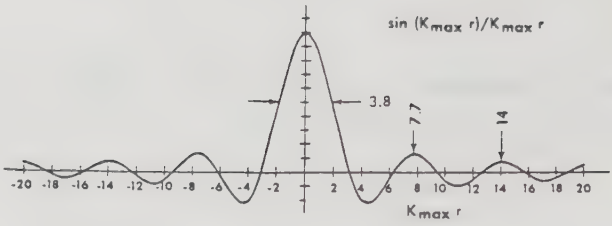

Fig. 2.6: The function sinKr/Kr versus Kr /23/

This is called the Ehrenfest equation and r_1 represents the order of magnitude of the smallest interatomic distance in the material /24/.

r_1 for $TM_{80}M_{20}$ alloy glasses with $Z_{TM} \sim 2Z_M$ (e.g. $Fe_{80}P_{20}$, $Z_{Fe}=26$ and $Z_P=15$) will be determined mainly by the metal-metal nearest neighbour distance (due to the difference in the x-ray atomic scattering factors) and this should to a first approximation be given by the Goldschmidt radius r_G. r_1 values greater then $2r_G$ may be interpreted as a possible loose packing of the metal atoms than the dense random packing of hard spheres (DRPHS) as a consequence of the metalloid atoms being larger than the ideal holes in the DRPHS structure as discussed by Cargill /20/.

The coordination number (CN) may be approximately calculated from the radial distribution function RDF(r), as the area under the first peak. This is, however, non unambignously defined so assuming that the first peak is symmetric around r_p one may define (Fig. 2.3)

$$CN = 2 \int_{r=0}^{r_p} RDF(r)dr \qquad (27)$$

For metallic glasses co-ordination numbers between 11.4 and 13.5 has been observed /24/. The size of the area around an atom in which a certain degree of short range order is present may be estimated by demanding deviations from unity in the pair distribution function g(r) to be less than some small number (e.g. 0.02). By this method areas of radius 14-16 A^{O} are often deduced /24/.

2.1.3 Structural consideration from mass density and atomic volume

Most models of the atomic arrangements in metallic glasses are based on the structures formed by the dense random packing of hard spheres, dense in the sense that they contain no holes large enough to accomodate another sphere. These atoms are randomly distributed in the sense that there are only weak correlations between spheres separated by five or more sphere diameters. On the basis of this model Luborsky /4/ has calculated the packing fraction and densities of various metallic glasses. Cargill /20/ proposed that in connection with packing fractions and densities the atomic radii used should be the 12-co-ordinated Goldschmidt radii, r_G, for the metal atoms and the 4-co-ordinated tetrahedral radii, r_T, for the metalloid atoms. Both Cargill and Luborsky have found that η, the packing fractions of various metallic glasses from measured densities, is fairly independent of composition and constituting elements (see table 2.1). It is evident then that an estimate of the density of metallic glasses is possible by assuming an average packing fraction and then calculate ρ_d from

Table 2.1: MEASURED DENSITIES AND CALCULATED ATOMIC PACKING FOR SOME AMORPHOUS ALLOYS [in part from Cargill (1975a)]

Alloy	Composition x	ρ g/cm^3	ρ_o at./Å^3	η^*	Reference
$Ni_{100-x}P_x$	18.6	8.00 ± 0.04	0.0900	0.678	Cargill (1970)
	21.1	7.93	0.0904	0.676	
	22.8	7.80	0.0897	0.667	
	24.0	7.79	0.0902	0.668	
	26.2	7.73	0.0905	0.665	
$Co_{100-x}P_x$	15.0	7.9	0.0869	0.677	Davis (1976)
	19.0	7.97 ± 0.04	0.0895	0.668	Cargill and Cochrane (1974)
	20.3	7.94	0.0898	0.687	
	22.0	7.89	0.0900	0.685	
	23.6	7.90	0.0909	0.688	
$Fe_{100-x}P_x$	14.5	7.252 ± 0.04	0.0836	0.681	Logan (1975)
	16.0	7.205	0.0837	0.678	
	18.4	7.128	0.0837	0.672	
	21.6	7.025	0.0838	0.665	
$Fe_{75}P_{15}C_{10}$	-	6.95	0.0882	0.658	Tsuei and Lillienthal (1976)
$Fe_{80}P_{16}C_3B_1$ #2615	-	7.7	0.091	0.735	Allied (1975a)
$Fe_{78}Mo_2B_{20}$ #2605A	-	7.39	0.0933	0.698	Allied (1975b)
$Fe_{75}P_{16}B_6Al_3$	-	7.10	0.0885	0.686	Chen (1975)
$Co_{75}P_{16}B_6Al_3$	-	7.29	0.0867	0.641	Sherwood et al (1975)
$Ni_{75}P_{16}B_6Al_3$	-	7.71	0.0921	0.672	Chen (1975)
$Fe_{38}Ni_{39}P_{14}B_6Al_3$	-	7.6	0.0917	0.695	Davis (1976)
$Fe_{29}Ni_{49}P_{14}B_6Si_2$ #2826B	-	7.51	0.0896	0.671	Davis (1976)
$Fe_{32}Ni_{36}Cr_{14}P_{12}B_6$ #2826A	-	7.46	0.0887	0.680	Davis (1976)
$(Fe_xCo_{1-x})_{80}P_{13}C_7$	1.0	6.97 ± 0.05	0.0847	0.654	Lin and Duwez (1969)
	1.0	7.54	0.0917	0.708	Fujimori et al (1976b)
	0.815	7.80	0.0940	0.720	
	0.75	8.00	0.0960	0.734	
	0.63	7.64	0.0911	0.693	
	0.50	8.10	0.0960	0.726	
	0.415	8.33	0.0983	0.741	
	0.27	8.13	0.0954	0.714	
$(Fe_xCo_{1-x})_{75}Si_{15}B_{10}$	0.265	8.13	0.100	0.752	Fujimori et al (1976b)
	0.07	8.00	0.0982	0.728	
	0	8.46	0.1029	0.765	
	0	8.60	0.1045	0.777	Kazama et al (1976)
$(Fe_xCo_{1-x})_{78}Si_{10}B_{12}$	0	8.43			
	0.5	8.06	calculated assuming η = 0.75		
	1.0	7.70			
$Pd_{80}Si_{20}$	-	10.25 ± 0.1	0.0680	0.678	Crewdson (1966)
$(Pd_{.928}Cu_{.072})_{100-x}Si_x$	15.5	10.54 ± 0.04	0.0693	0.694	Chen and Park (1973)
	16.5	10.48	0.0694	0.693	
	17.5	10.40	0.0695	0.691	
	18.5	10.33	0.0696	0.689	
	19.5	10.26	0.0697	0.688	
	20.5	10.19	0.0698	0.686	
$(Pd_{.824}Si_{.176})_{100-x}Cu_x$	0	10.57 ± 0.04	0.0687	0.691	Chen and Park (1973)
	2	10.53	0.0689	0.691	
	4	10.49	0.0691	0.691	
	6	10.48	0.0695	0.693	
	8	10.44	0.0696	0.693	
	10	10.42	0.0700	0.695	
	12	10.39	0.0702	0.695	
	14	10.35	0.0704	0.695	
$(Pt_{1-x}Ni_x)_{75}P_{25}$	0.2	15.71 ± 0.03	0.0708	0.651	Chen et al (1973)
	0.3	15.85	0.0774	0.694	
$(Pd_{.7}Mn_{.3})_{100-x}P_x$	16	9.11 ± 0.05	0.0674	0.670†	Marzwell (1973)
	17	9.07	0.0676	0.669	
	18	9.00	0.0676	0.665	
	19	8.99	0.0681	0.666	
	20	8.91	0.0680	0.662	
	21	8.89	0.0684	0.662	
	22	8.84	0.0685	0.659	
	23	8.80	0.0687	0.658	
	24	8.78	0.0691	0.658	
	25	8.75	0.0694	0.657	
	26	8.71	0.0696	0.656	

Table 2.1 (contd.)

Alloy	Composition x	ρ [g/cm³]	$\rho_{o_{at}}$ [at./Å³]	η*	Reference
$(Pd_{1-x}Mn_x)_{77}P_{23}$	0.15	9.51 ± 0.04	0.0689	0.660†	Marzwell (1973)
	0.17	9.36	0.0685	0.656	
	0.25	9.03	0.0687	0.658	
	0.30	8.80	0.0687	0.658	
	0.35	8.55	0.0685	0.656	
	0.37	8.46	0.0685	0.656	
	0.38	8.41	0.0685	0.658	
$(Pd_{1-x}Ni_x)_{80}P_{20}$	0.20	10.08 ± 0.02	0.0725	0.674	Chen et al (1973)
	0.30	9.97	0.0752	0.681	
	0.40	9.83	0.0778	0.688	
	0.50	9.48	0.0790	0.681	
	0.70	9.05	0.0844	0.689	
	0.80	8.75	0.0867	0.689	
$(Fe_xNi_{1-x})_{80}B_{20}$	0.25	7.94	0.0985	0.697	O'Handley et al (1976a)
	.375	7.83	0.0977	0.697	O'Handley et al (1976a)
	.50	7.14 ± .05	0.0897	0.645	Luborsky,unpublished
	.50	7.72	0.0969	0.697	O'Handley et al (1976a)
	.625	7.65	0.0966	0.701	O'Handley et al (1976a)
	.75	7.53	0.0957	0.700	O'Handley et al (1976a)
	.875	7.46	0.0953	0.703	O'Handley et al (1976a)
	1.0	7.05 ± .05	0.0907	0.674	Luborsky, unpublished
	1.0	7.39	0.0950	0.707	O'Handley et al (1976a)
$(Fe_xNi_{1-x})_{80}P_{14}B_6$	.50	7.52 ± .05	0.0892	0.676	Luborsky et al (1975)
#2826	.50	7.7	0.0913	0.692	Allied (1976a)
	.625	7.21 ± .05	0.0860	0.657	Luborsky, unpublished
	1.0	6.86 ± .05	0.0832	0.650	Luborsky, unpublished
$(Fe_xCo_{1-x})_{80}B_{20}$	0	8.22	0.1004	0.714	O'Handley et al (1976a)
	.125	8.06	0.0991	0.709	
	.25	7.93	0.0981	0.706	
	.375	7.84	0.0976	0.706	
	.50	7.70	0.0965	0.702	
	.625	7.59	0.0957	0.700	
	.75	7.52	0.0954	0.702	
	.875	7.46	0.0953	0.705	
2605**	1.0	7.39	0.0950	0.707	

*Packing fraction $\eta = (4\pi/3)\langle R^3\rangle\rho_o$, with $\langle R^3\rangle$ calculated using Goldschmidt atomic radii (12-fold coordination) for metal atoms (from R.P. Elliot, "Constitution of Binary Alloys," First Suppl., p. 870. McGraw-Hill, New York, 1965, except as noted) and "tetrahedral covalent radii" for metalloid atoms (from L. Pauling, "Nature of the Chemical Bond," 3rd ed., p. 246. Cornell Univ. Press, Ithaca, New York, 1960).
†Twelve-coordinated atomic radius for Mn was taken from W. Hume-Rothery, "The Structure of Metals and Alloys," p. 53. Institute for Metals, London, 1947; this value (1.37Å) is larger than that given by Elliot (1.30Å).
#Allied Chemical Co. METGLAS^R alloy designation.
††Calculated from magnetization values given.

$$\rho_d = \frac{m}{v} = \frac{<A>/N_{AV}}{4\pi/3 \; \frac{<R^3>}{n}} \qquad (28)$$

where

$$<A> = \sum_i c_i A_i$$
$$<R^3> = \sum_i c_i R_i^3$$

A_i, c_i and R_i being the atomic weight, fraction and radius (r_G and r_T) of element i and N_{AV} is Avogadros number.

It is generally observed that metallic glasses are about 2% less dense than the corresponding equilibrium crystalline phase mixtures. $\rho_d(x)$ for $Fe_{80-x}Ni_xB_{20}$ metallic glasses is shown in Fig. 2.7.

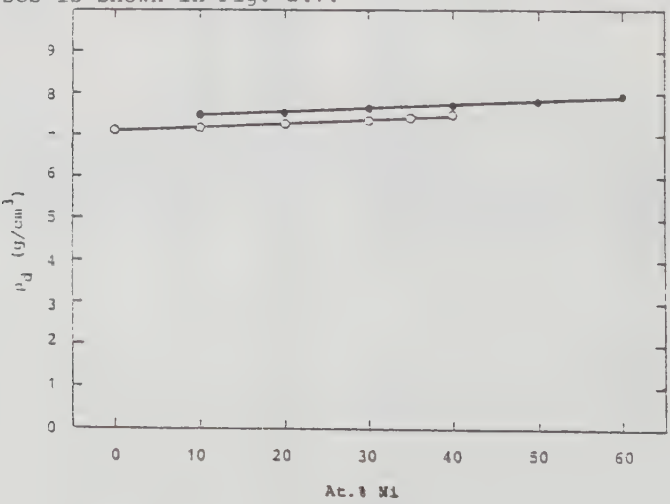

Fig. 2.7: Mass density ρ_d(g/cm^3) versus x(at %) for $Fe_{80-x}Ni_xB_{20}$ metallic glasses as measured by O'Handley et al. /104/ ( ) and as calculated with a packing fraction η=0.676 atoms/A^{O3} by Becker et al. /98/ (O).

During the structural phase transitions in metal, it is found that the atomic volume of a metal in a metal-metalloid glass is equal to that of the metal in a crystalline close packed structure. Based on this assumption Turnbull /28/ calculated the partial atomic volumes of the metalloid elements in a number of metal-metalloid glasses. For alloys with Si or P as a glass former the total average atomic volume $\langle v \rangle$ is equal to the average atomic volume $\langle v_{mt} \rangle$ to within ±2% and the metalloid volume $v_{md} \sim \langle v_{mt} \rangle \pm 10\%$, is a scaling of metalloid volume to "host" metal volume is observed. For B containing glasses, however, the situation is more complicated. The variation of density with B-content for $Fe_{100-x}B_x$ glasses was reported by Ray et al /29/, compared to reported densities of other binary TM-M glasses, and discussed in terms of the structural model of Polk. It seems that the Fe-B glasses with respect to density (and magnetic moment) behave different from glasses containing P as a glass former as also indicated by Turnbull's atomic volume calculation. The density $\rho_d(x)$ curve for electrodeposited $Fe_{100-x}P_x$ glasses and the magnetic moment $\mu(x)$ curve of Takahashi and Koshimura /30/ for liquid quenched $Fe_{100-x}P_x$ glasses both show a linear decrease with increasing x. On the other hand, the corresponding curves for liquid quenched $Fe_{100-x}B_x$ glasses both show a kink around x=20 at % (Hasegawa & Ray /31/, suggesting the existence of two different kinds of short range order in the glasses as also implied by Curie temperature and magnetic moment measurements on $Fe_{100-(x+4)}P_xB_y$ glasses by Durand and Yung /32/. In the latter glasses the two kinds of short range order are thought to resemble those of corresponding crystalline phases, which may be a common feature of the short range order of TM-M glasses.

2.1.4 DRPHS model

A number of models have been discussed to clarify the structural arrangements of atoms in amorphous metals (Pure and alloys). For TM-M metallic glasses a model based on Bernals model of dense random packing of hard spheres for the structure of liquid metals was proposed by Polk /33/. In this model the metalloid atoms are assumed to fill the largest holes in a dense random packing of metal atoms. The idealised holes of the DRPHS structure is shown in Fig. 2.8.

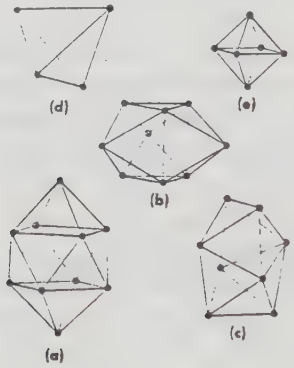

Fig. 2.8: Ideal holes (Bernal holes) in a dense random packing of hard spheres (DRPHS) /20/

Based on the number of holes per atom ratio for the DRPHS structure (given by Polk to be 3.38) and the frequency of occurence of the various holes an alloy of 79 at % metal content and 21 at % metalloid content is formed by filling of the holes of type a, b and c of Fig. 2.8. Turnbull /34/ notes that the corrected analysis indicates that about 13 at % of metalloid could be incorporated into the DRPHS structure in this way without serious deviations of the metal-metalloid spacings from

their values in the intermetallic phases and up to 20 at % metalloid can be included with more severe distortions. The model further ensures that no metalloid atoms are nearest neighbours which is thought to be energetically unfavourable.

The pron and cons of the model have been discussed in detail by Cargill /20/. Lately, several papers have commented on the validity of the model. Nagel /35/ who has found discrepancies between metalloid co-ordination numbers as deduced from the ideal holes of the model and those of exptl. structure studies. Yamamoto /36/ has questioned the number of holes per atom ratio given by Polk. Gonser /37/ interprets a Mössbauer spectrum of $Fe_{80}B_{20}$ in terms of the co-ordination numbers of the idealized holes in the DRPHS structure. Kemeny et al /38/, however get to the opposite conclusion of Gonser et al /37/ from Mössbauer measurements on $Fe_{100-x}B_x$ glasses, Gilman /39/ proposed different cluster configurations which would give another short range structure than that of the DRPHS for liquid TM-M eutectic compositions and possibly the corresponding metallic glasses.

2.1.5 Computer simulation of structural models

It is necessary to have a detail information of local environment of each type of atom (TM and M) i.e. partial co-ordination numbers and interatomic distances of the glasses to explain some of the above mentioned points.

Recently, most papers in this field deal with models constructed by the aid of computer algorithms. Most models begin with a certain configuration of a few atoms e.g. a triangle or tetrahedron, and then add spheres one by one according to some chosen criterion. It seems that

for hard spheres the model densities of the atomic configurations that reproduce positions and relative peak intensities of the experimental distribution functions are too low /22/. Binary systems have been simulated by dense random packing of non-equal sized hard spheres. The large and small spheres are assumed to represent TM and M atoms respectively. Sadoc et al /40/ note that the shoulder on the second peak of the interference function frequently present in amorphous solids is reproduced by the model if the diameter difference is ∿10% and the concentration of small spheres is in the range 10-15%. Computer simulations of the structure of transition metal-metalloid glasses have been critically discussed by Boudreaux and Geregor /41/ and Boudreaux /42/ and measured hyperfine fields at iron sites in Fe-B glasses have been compared to calculations based on computer models by Vincze et al /43/. The 13-atom icosahedral cluster has been discussed as a possible structural unit in amorphous metallic alloys /44/.

Mutual combinations of some of these methods, supplemented with magnetic neutron scattering may also be used to separate the contributions from the different constituting elements.

2.2. Magnetic properties and electronic structure of amorphous ferromagnetic alloys

2.2.1 General Review:

The local environment of a given type of atom changes from site to site in an amorphous structure unlike the ordered crystalline materials. This difference in the nearest surroundings of an atom due to the differences in relative positions and chemical character of the nearest neighbors is assumed to have the largest effect on the basic magnetic properties of a non-crystalline solid. The physical properties of the amorphous alloys are determined by the short range atomic arrangement and not by the structural long-range disorder due to the absence of a periodic lattice /3,4/.

The atomic densities are found to be nearly equal in the two states of TM-M alloys /20/ and transition metal co-ordination numbers are observed to be 11∿13 in metallic glasses /23,24/. Thus, the short range order of the glasses must be very similar to that of the crystalline close packed structures. Magnetic properties such as average magnetic moment, Curie-temperature and temperature dependence of magnetization, which are largely determined by the short-range order are indeed observed not to be substantially different for crystalline alloys and corresponding amorphous TM-M alloys and possible differences are ascribed mainly to the presence of the metalloid atoms in the latter. Generally TM-M alloys that are ferromagnetic in the crystalline state are also ferromagnetic in a non-crystalline state.

Wohlfarth /45/ has pointed out that the itinerant electron model provides a better description of the basic magnetic porperties of amorphous TM-M alloys than the Heisenberg model. It is further believed that the band structures of the TM-M amorphous alloys are similar to those of the corresponding crystalline alloys.

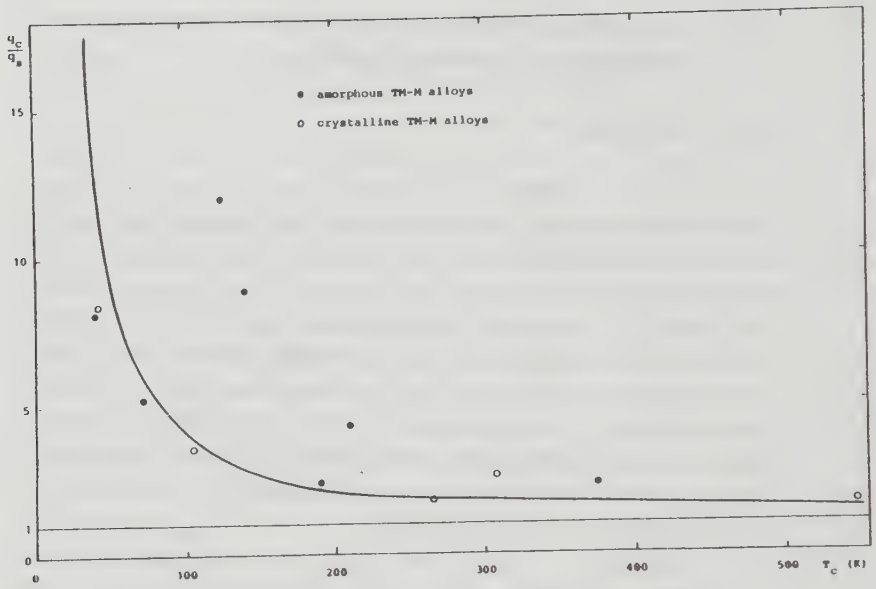

Fig. 2.9: Rhodes-Wohlfarth plot for amorphous and crystalline TM-M alloys /46/.

Fig. 2.9 shows the so-called Rhodes-Wohlfarth plot /46/ which is a plot of the ratio q_c/q_x versus the Curie temperature T_c for some crystalline and amorphous TM-M alloys. q_x is the number of moment carrying electrons per atom as deduced from low temperature measurements of the magnetic moment, where as q_c is deduced from the effective Curie-Weiss constant $c = NP_{eff}^2 \mu_B^2/3k_B$ ($P_{eff}^2 = q_c(q_c+2)$) the susceptibility measurements in the paramagnetic state.

N is the number of atom per unit volume, μ_B is the Bohr magneton, and k_B is Boltzmann's constant. Materials having localized moments should have $q_c/q_s \sim 1$ whereas the ratio for materials obeying an itinerant electron model should behave as $1/T_c$. Although some of the points for the amorphous alloys fall well above the $(T_c)^{-1}$ curve the general trend of this plot seems to point towards the itinerant model.

On the other hand, O'Handley and Boudreaux /47/ have interpreted the magnetic moments and Curie temperatures of $(TM_1,TM_2)_{80}B_{20}$ and $(TM_1,TM_2)_{80}P_{2P}$ metallic glasses, TM_i=Fe,Co or Ni, in terms of a local environment model in which the TM-moments are assumed to be realized and different from site to site and charge transfer from M-atoms to TM-atoms is present. The charge transfer of the B and P-atoms to the Fe-, Co-, and Ni-atoms consistent with the data are given in Table 2.2.

Table 2.2

	to Fe	to Co	to Ni
per B atom	2.2-2.4	1.6	1.4
per P atom	2.6-3.0	2.7	2.4

+ Effective charge transfers from M to TM in $(TM_1,TM_2)_{80}M_{20}$ glasses. Ref. /47/

The magnetic moment data of TM-M glasses have been discussed by Yamauuchi and Mizoguchi /48/ and Becker et al /98/ on the basis of charge transfer model. However, considerable scatter is observed in the different number of electrons assumed to be transferred by a given metalloid to give consistency with the various experimental results. Diffraction data indicates that the metal-metalloid separation in metallic glasses are generally less than the sum of the Goldschmidt raii /20/. This is sometimes taken in favour of the idea of charge transfer from metalloid to transition metal.

2.2.2 Magnetic moment

The saturation magnetization at OK, M(o) of a magnetic material is of utmost importance because M(o) is an experimental parameter which can verify the predictions of the theories based on band structure calculations. The magnetism in Fe, Co and Ni is usually explained in terms of the band or collective approach. In these materials, average magnetic moment per atom is usually non-integral and the contribution of the orbital momentum is small. The non-integral magnetic moment can be easily understood in terms of the rigid-band model.

2.2.2.1 The rigid-band model

In the ridid-band model, the 3d band is assumed to comprise of spin-up and spin-down sub-bands and sub-bands are shifted in energy with respect to each other because of the exchange energy which tends to favour parallel alignment of the spins at the cost of antiparallel ones. Therefore, a net magnetization occurs because the sub-bands are now unequally populated. The observation that the average magnetic moment per atom is non-integral is shown to arise from the energy overlap of the 3d and 4s electron bands, both of which are occupied up to a certain energy level (the Fermi level). Thus, the total integral number of electrons per atom available for both these bands can split up into a non-integral number in each of them. This situation exists in all the transition group metals.

In the rigid band approximation, the average magnetic moment of an alloy with atomic conentration c should be

$$\bar{\mu} = \mu_{matrix} - Zc\mu_B \qquad (29)$$

where Z is the atomic number difference of the solute relative to the matrix.

The famous Slater-Pauling curve for the concentration dependence of average μ_B/TM atom is only applicable to alloys between partners which are not too separated from one another in the periodic table. Otherwise, a too large difference in ionic charge will prevent the mixing of orbitals at E_F. The situation is found to be simple in alloys where transition metal atom are replaced by one another at constant metalloid concentrations. Fig. 2.10 shows an example, the results of Mizoguchi /63/ for amorphous $(T_{1-x}M_x)_{80}B_{10}P_{10}$. The Slater-Pauling curve has the same character as in corresponding crystalline binary solid solutions but is apparently shifted to lower number by about 0.4 electrons transferred from the metalloids.

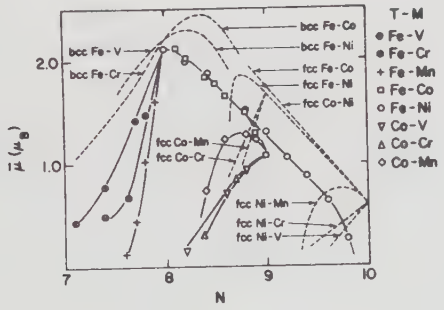

Fig. 2.10: The average magnetic moment $\bar{\mu}$, of 3d atoms in quasibinary $(T_{1-x}M_x)_{80}B_{10}P_{10}$ ferromagnetic alloys as a function of the average outer electron concentration, N, of the metallic atoms, along with that for crystalline alloys (broken lines) /63/.

Alben /64/ stated that the rigid band model is not correct in this context but this model through the Slater-Pauling curve does serve as a useful guide to the interpretation of the variation of magnetic moment of transition metals upon alloying with metalloid.

2.2.2.2 Friedel's model

It has been found that, in amorphous $Fe_{80}B_{20}$ alloy, the magnetic moment per transition metal atoms follows the Slater-Pauling curve when Ni or Co substitutes for Fe, while strong departures are observed for Cr, Mo substituted alloys. The magnetic moments are discussed for dilute (Cr,Mo) impurities in strong ferromagnetic host Fe in terms of Friedel's virtual bound state model /17/. According to this model, these elements (Cr,Mo) have nuclear charges much smaller than the matrix (large negative Z's). They introduce a perturbation which is strongly repulsive as well as highly localized. Now one expects such a perturbation, when strong enough, to subtract a bound state from the full half of the d-band and to move it towards higher energies. When it comes above the Fermi-level E_F, such a state will empty itself into the conduction band, mainly in the other half of the d-band with opposite spin direction, because of its high density, Fig. 2.11. The degeneracy of the 'd' state makes it possible to have room for at most 5 electrons in it. 5 electrons less with spin upwards, turning into 5 more electrons with spin downwards, make a change of 10 μ_B when the bound state crosses the Fermi-level. Thus the equation for the average magnetic moment would be

$$\bar{\mu} = \mu_{matrix} - (Z+10)c\mu_B \qquad (30)$$

where c = concentration of Cr, Mo and $\xi = -(Z+10)$, ξ is the slope of the moment versus solute content curve.

Such a law is approximately followed by the amorphous alloys containing light impurities like Cr,Mo in a strong ferromagnetic host.

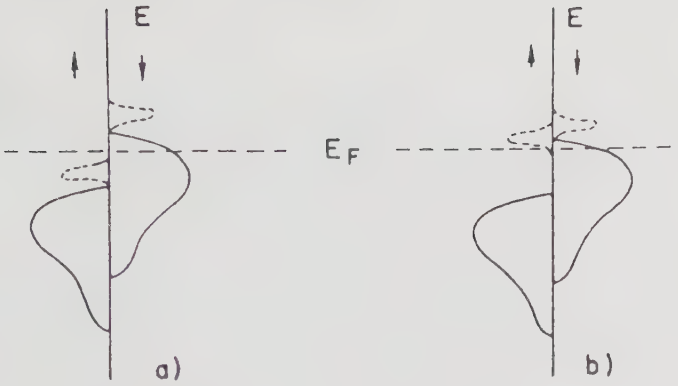

Fig. 2.12: Schematic representation of virtual bound state in cobalt-rich glasses containing (a) small concentrations of Mn (less than 6 at %) and (b) V impurities /103/.

2.2.2.3 Electron transfer model

The magnetic moment per transition metal atom extrapolated at O K of amorphous alloys is in most cases lower than in the pure crystalline elements. This has very little to do with disorder, instead due to 'electron transfer' between the metalloid and the unfilled 3d-band of transition metal. According to Yamauchi and Mizoguchi /48/ every metalloid atom is surrounded by the transition metal atoms as its first neighbors, and the interatomic distances between the former and the latter are much less than the sum of their Goldschmidt radii. As a result, the electronic state must be strongly preturbed, that is, electrons are transferred from metalloid atoms to transition metal atoms which have the unfilled d-band. And the number of holes in the down-spin band of 3d metal atoms would be primarily affected by the nearest neighbor atoms. As for a metalloid, it is assumed to offer its s-electrons to the conduction band and p-electrons to the d-holes of the transition metals. The extent of the electron transfer can be found from the reduction of the magnetic moments of transition

metal atoms. The calculation on the basis of rigid band model shows that the magnetization of the amorphous alloy is simply shifted along the Slater-Pauling curve by a corresponding amount of transferred electrons.

In the following section (sec. 4) the analysis of the experimental results of average magnetic moment per transition metal atom extrapolated to O K have been done on the basis of rigid band model (based more or less on the work of Mott /65/ and Friedel's virtual bound state model. It is assumed that for crystalline TM_1TM_2 alloys there will be a common s-band and that the d-band will stay in the same position relative to the s-band so that transfer of electrons from one band to the other is avoided /65/. Following Alben /64/, it is also assumed that the form of the density of states curves is not substantially changed by the non-crystalline structure.

2.2.3 Electronic structure

The behaviour of average magnetic moment ($\bar{\mu}$) as a function of composition of amorphous alloys of TM-M type can be qualitatively explained on the basis of charge transfer model as seen above. According to this model, there is a transition of electrons from metalloid to the unfilled level of 3d-minority spin band of transition metal and consequently there should be a shift of the Fermi-level (E_F). This shift should be reflected in the maximum of the density of states of d-electrons and can be observed in photoemission experiments. It has been shown from the measurement of photoemission for a series of amorphous transition metal alloys /49,50,51/ and transition metal-metalloid alloys /52/ that the constituent d-electron density of states N(E) changes

considerably upon alloying. As such d-band center shifts have been observed which depend on alloy composition and on the valence difference of the alloy constituents. Moreover, N(E) is expected to be highly sensitive to the changes in local atomic order, to changes in the co-ordination number and atomic distances which exist in amorphous alloys. The large changes in the consituent density of states upon alloying are expected to strongly affect various electronic properties of the alloy. As a result of the d-band shifts and distortion, the screening of the charges of the nuclei changes. Consequently, core-level shifts and changes of the core-level shapes are expected /53/.

Nagel and Tauc /54/ used a free electron type argument and argued that for $\rho=2k_F$, where k_F is the Fermi wave vector and ρ the wave vector of the first peak in the static structure factor S(q), the Fermi-level falls into a minimum in the electronic density of states. Thus the disordered state should have a relatively low electronic energy. However, recent photoemission experiments /55,56/ failed to confirm the predominantly s-like character of

the electronic states near the Fermi-level of $Pd_{80}Si_{20}$ postulated by Nagel and Tauc and low-temperature specific heat measurements on amorphous Pd-Si-Cu and Pd-Si alloys failed to confirm the minimum in the density of states at E_F /57/.

From the low temperature specific heat measurements on $(Fe\text{-}Ni)_{80}B_{20}$ and $(FeNi)_{80}P_{14}B_6$, Krause et al /58,59/ have also shown that the change in the electronic specific heat coefficient (γ) as a function of iron concentration (x), which is related to the change in the density of states $N(E_F)$, is about two times larger in boron containing glasses. Such behaviour of $d\gamma/dx$ can not be explained on the basis of rigid band model and the usefulness of the split band model of L. Berger /60/ has been suggested by the authors.

Kübler et al /51/ calculated the density of states for ordered intermetallic compounds of the same stoichiometry as the transition metal glassy alloys using the self consistent augmented spherical wave method. By comparing these results with the photoemission spectra of related glassy alloys, they concluded that the overall shape of $N(E_F)$ in the glassy transition metal alloys and of $N(E_F)$ calculated for hypothetical close packed ordered compounds of approximately the same stoichiometry is similar.

Furthermore, by decomposition of the total density of states $N(E_F)$ into the local density of states of the alloy constituents, they showed that large shifts of the peaks in $N(E_F)$ of the late transition metal occur. These shifts arise from the change of the Fermi-energy from the hybridization of the d-states of the alloy constituents and from electron charge transfer between the alloy constituents. In addition, the calculated core level shift (which results from the interatomic electron charge transfer) and observed shift is quite satisfactory.

However, in case of metal-metalloid amorphous glasses, the changes of electronic structure and atomic structure may be different from that of the amorphous transition metal alloys. Matsura et al /62/ measured the x-ray photoemission of Fe 3s and Fe 3p levels and Fe 3d valence band of amorphous iron-boron alloys as a function of boron concentration over the range from 12 to 25 at % B. It was found that a characteristic hump appeared at lower energy region in Fe 3d band spectrum of every amorphous Fe-B alloy Fig. 2.12.

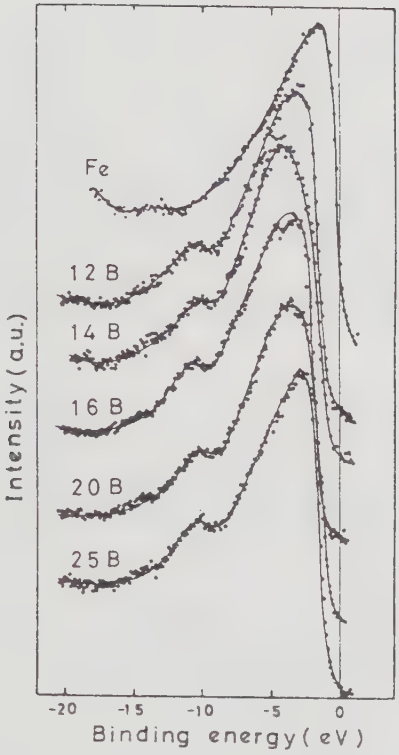

Fig. 2.12: Valence band spectra of amorphous Fe-B alloys and pure Fe /62/.

The intensity and the binding energy of the hump with boron concentration have been observed to be almost invariant. Based on these observations, they concluded that the origin of the hump is due to a bonding state created between B 2p and Fe 3d electrons and the electronic structure of the Fe 3d band in amorphous Fe-B alloys can be regarded to be quite far from a conventional rigid band model.

2.2.4 Temperature dependence of magnetization

The overall temperature dependence of the magnetization of an ordered magnetic system can be treated with a molecular (mean) field approximation (MFA). However, at low temperature we know that a model involving spin-wave excitation is better. Near T_c, that is, in the critical region, the MFA also fails because fluctuations become dominant.

It is a general feature of the plot of normalized spontaneous magnetization $\sigma(T)=M_s(T)/M_s(0)$ versus normalised temperature T/T_c that the curves for amorphous ferromagnets fall well below those of their crystalline counterparts, Fig.2.13. Several theoretical models have been proposed to explain this fact. Most of these models are based on a Heisenberg ($H_{ex} = - \sum_{ij} J_{ij} \bar{S}_i \bar{S}_j$) or Ising ($H_{ex} = - \sum_{ij} J_{ij} S_{zi} S_{zj}$) description of the interacting spins, that is, a localized moment picture. The theoretical treatment can be classified into two categories:

i) an unique constant exchange interaction ($J_{ij}=J$) between magnetic atoms is assumed but the angles between neighboring spins are randomly distributed.

ii) a distribution of exchange integrals is assumed in order to reflect the structural fluctuations in the amorphous alloy.

Both assumptions allow for the observed lowering of the σ-curve for the amorphous ferromagnets. The first model however predicts that amorphous alloys should exhibit a structureless Mössbauer spectrum, in contrast to experimental evidence /13/. On the basis of second assumption Handrich /66/ gave the following equation for the reduced magnetization

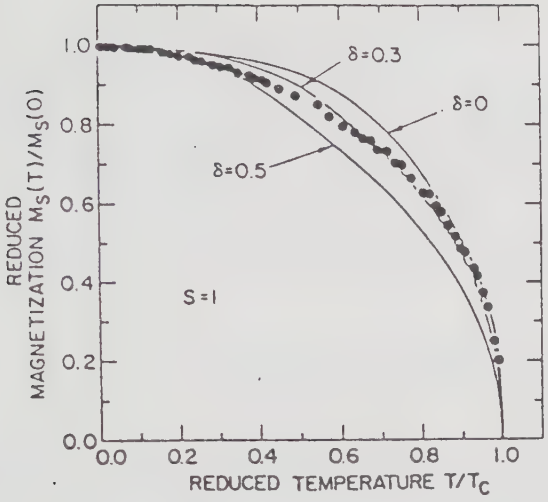

Fig. 2.13: Temperature dependence of the reduced spontaneous magnetization $M_S(T)/M_S(0)$ for $Fe_{75}P_{15}C_{10}$ metallic glass compared to curves calculated from (31) for different values of the disorder parameter δ (with S=1) /13/.

$$\sigma(T) = M_s(T)/M_s(0) = \frac{1}{2}\{B_s(1+\delta)x + B_s(1-\delta)x\} \qquad (31)$$

where B_s = Brillouin function of spin 's' and

$$x = \frac{3s\sigma}{(s+1)} \cdot \frac{T_c}{T}$$

and δ is a measure of the degree of disorder

$$\delta^2 = \frac{\langle \Sigma_j \Delta J_{ij} \Sigma_k \Delta J_{ik} \rangle}{\langle J_{ij} \rangle^2} \qquad (32)$$

$$J_{ij} = \langle J_{ij} \rangle + \Delta J_{ij} \qquad (33)$$

J_{ij} being the exchange integral between spins at the sites $\bar{r}_i$ and $\bar{r}_j$, ΔJ_{ij}, the deviation of J_{ij} from the average value $\langle J_{ij} \rangle$ and $\langle \Delta J_i \rangle$ denotes structural average. Thus, 'δ' is the root mean square of deviation from an average exchange integral between two nearest neighbour spins.

In an amorphous magnetic alloy, the fluctuation in magnetization can occur due to the following causes:

i) compositional disorder
and ii) structural disorder.

While the compositional disorder is common to both crystalline as well as amorphous materials, the structural disorder occurs only in amorphous alloys. It is rather difficult to decide to what extent each kind of disorder contributes to the magnetization distribution. The fact that the Mössbauer spectra in amorphous ferromagnets could not be fitted with a model in which the hyperfine field at a given Fe-site is a function of the number of metalloid neighbours as determined by a binomial distribution, clearly demonstrates that the contribution of the structural disorder is significant.

The magnetization of an impurity atom in a ferromagnetic host has been experimentally found to decrease much faster than that of the host /67/. This approach has been theoretically justified by Callen /68/. It can be shown by similar calculations that localized spin-wave states above the spin band could be formed for a ferromagnet containing weakly coupled magnetic impurities. Of these states, the low lying virtual s-like states which result in a large density of states at low energies, were shown to give rise to an accumulation of spin disorder in the vicinity of the impurity resulting in a local decrease in magnetization /69/. Probably a similar situation exists in amorphous magnetic alloys, where a distribution of the exchange interaction could

lead to spatial fluctuations in magnetization as concluded from the Mössbauer data. The characteristic relatively fast decrease in magnetic alloys is then a manifestation of the temperature dependence of these magnetic spins with exchange interaction strength that deviates sufficiently from the average. Detailed theoretical explanation on the temperature dependence of magnetization may be found in the paper of Montgomery et al /70.

At low temperatures T→0, the temperature dependence of magnetization of crystalline ferromagnets has been described by the well known $T^{3/2}$ law, indicating that long wavelength excitations determine the magnetization behaviour. By generalizing the Landau-Lifshitz /71/ theory of ferromagnetic spin waves to amorphous ferromagnets it may be shown that extended and localized spin-wave states can exist in amorphous ferromagnets and the localised states are due to the randomness of the ferromagnets. It has been found that at long wavelengths such amorphous alloys exhibit well-defined spin-wave excitations with a normal ferromagnetic dispersion relation.

$$h\omega(\vec{q}) = \Delta + Dq^2 + Eq^4 + \ldots \qquad (34)$$

where Δ is an effective anisotropy gap due to the dipole-dipole interactions. Correspondingly, the magnetization at low temperature shows the usual ferromagnetic behaviour

$$M(T) = M(O)[1-BT^{3/2} - CT^{5/2}\ldots] \qquad (35)$$

Simple spin wave theory gives a relation between $T^{3/2}$ coefficient 'B' and spin-wave stiffness coefficient 'D' by the equation

$$B = 2.612[g\mu_B/M(O)]\ (k_B/4\pi D)^{3/2} \qquad (36)$$

where 'g' is gyromagnetic factor taken to be 2.05, μ_B is Bohr magneton and k_B is Boltzman's constant. The major difference between amorphous and crystalline ferromagnets seems to be found in the values of 'B'. The values of B for amorphous ferromagnets is, in general, five to ten times larger than that for a crystalline ferromagnet. The large value of B in amorphous alloys has been interpreted as a softening of the exchange interaction, while the small value of C/B implies that the exchange interactions damp out rapidly beyond the first nearest neighbor /5/. On the basis of the analysis of the experimental results, Birgeneau et al /72/ have suggested that

i) the spin wave density of states is proportional to $\omega_q^{1/2}$ for small magnon frequency ω_q in both crystalline and glassy ferromagnets with higher density of states at low ω_q in the latter case.

and

ii) exchange interactions between atoms carrying magnetic moments are greatly reduced and more localized in non-crystalline solids.

The experimental results related to spin-wave excitation at low temperature carried out in this work using microscopic and macroscopic techniques will be discussed in section 4.

2.2.5 Curie temperature

The Curie temperature (T_c) of a ferromagnetic material is a measure of the exchange energy between the non-compensated spin moments. It is therefore understandable that the average atom moment and Curie temperature of ferromagnetic alloys often change in the same sense.

Inspite of the distribution of exchange interactions apparently present in amorphous ferromagnetic alloys, these do usually show a well defined Curie-temperature, which has been confirmed from magnetization-temperature /11,6/, Mössbauer /73/ and specific- heat measurements /58/.

In the molecular field approximation based on the localized Heisenberg model, Hamiltonian is

$$H = - \sum_{ij} J_{ij} \bar{S}_i \cdot \bar{S}_j + g|\mu_B| H \cdot \sum_i \bar{S}_i \qquad (37)$$

the Curie temperature is given by

$$Tc = \frac{S(S+1)}{3k_B} \sum_{ij} J_{ij} \qquad (38)$$

There is a significant discrepency between the Tc of crystalline bcc alloys and that of the fcc alloys, Fig. 2.14 suggesting the complexity of the effect of crystalline structure on Tc. But in case of amorphous alloys, the Tc is a smooth function of the alloy composition in the entire

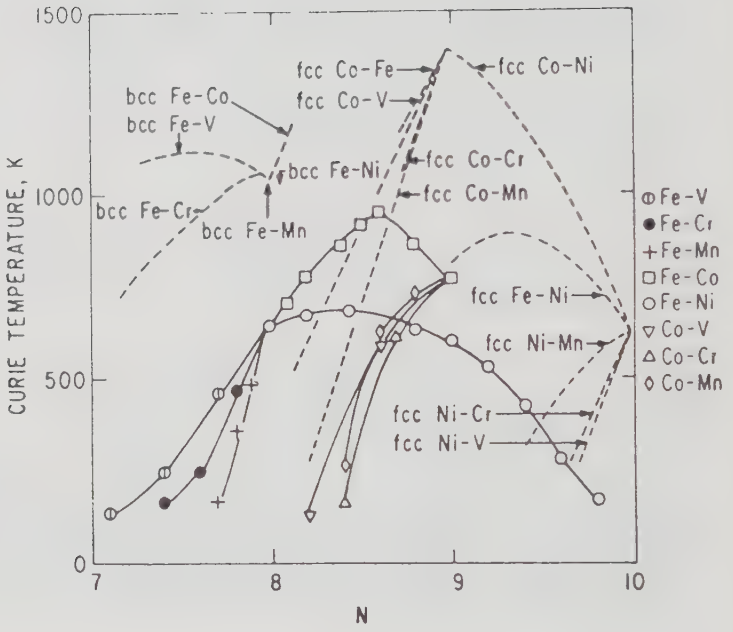

Fig. 2.14: Curie temperatures of quasibinary amorphous alloys of 3d transition metals $(A_{1-x}B_x)_{80}P_{10}B_{10}$ as a function of average outer electron concentration N of the metallic atom. Corresponding crystalline alloys, without P and B, are shown by the dashed curves /5/.

range. Generally, it is found that the Curie temperatures of amorphous alloys are equal to or slightly lower than those of the corresponding crystalline alloys /5/ , which again emphasizes the strong influence of the short range order on the exchange interaction. The difference in Curie-temperature between amorphous and crystalline alloys is much larger for Tc than for the magnetization. The effect of the metalloid concentration on Tc depends not only on the kind of metalloid but also on the d-electron concentration of the transition metal and the interatomic distances. Analysis of the experimental results /5,11,13/ suggests the following points.

1. The Curie-temperature generally varies with the concentration of metalloid atoms such as B, C, Si, P. This is understandable because molecular field and 'Tc' are expected to be proportional to the spins 'S' which vary proportional to the metalloid concentration because of the electron transfer.

2. The variation of Curie-temperate (Tc) in amorphous Fe, Co, Ni alloys with the number of outer 'd' electrons, N, is almost of the same type as in crystalline alloys, but the maximum of Tc is shifted to lower N-values due to electron-transfer.

3. The decrease of 'Tc' with decreasing interatomic distances R, which occurs in the Slater-Pauling curve for Fe-rich amorphous alloys, suggests similar invar properties as well known for fcc crystalline Fe-Ni alloys in the region $8.5<N<8.7$, Fig. 2.14.

The high values of Tc for the Fe-rich alloys show that the Fe-Fe exchange interaction is ferromagnetic and quite significant. With the addition of Ni, a sharp decrease in Tc has been observed /99/ which suggests that the Ni-Ni interaction is weak. The experimentally determined values of Tc as a function of dilutant (namely Ni, Co, Cr, Mo) has

been compared to several theoretical models /5/. It is obvious then that, Kouvel's theory /74/, which is a phenomenological model based on the molecular field theory suitably modified so that the individual atomic moments are allowed to vary in magnitude with their local environment, reproduces the variation of Tc with the dilutant up to a certain cencentration range and fails to describe it for the entire concentration range /5/ . This is a consequence of the fact that this theory does not predict a critical concentration for the appearence of ferromagnetism. On the other hand, experimental variation of Tc with the dilutant, has been well interpretated with the help of the model proposed by Foo and Wu /75/ for disordered ferromagnetic binary alloys. This theory does not assume that the variation of the individual moments with the composition is small. The disordered composition dependent exchange interaction is treated in a coherent potential approximation (CPA). In the weak scattering limit the CPA reduces to the result of the mean field theory, but in the strong scattering limit, CPA predicts such effects as a critical concentration for the appearence of ferromagnetism. According to this theory, at Tc=0 K, the critical concentration is given by

$$x_c = 1-[z - \frac{2}{z}]^{1/2} \qquad (39)$$

where z = number of nearest neighbor.

Detailed derivation of the equation (39) can be found in Luborsky /5/. Fig. 2.15 show a plot of Tc as a function of the dilutant (x), calculations have been done on the basis of CPA theory. It is found that Tc in the CPA is always lower than that of mean field theory. Montgomery et al /70/ have observed also from their theoretical calculation that the ferromagnetic Curie-temperature decreases linearly with disorder. The predominant effect of disorder on the magnetization is the Curie-point depression, which varies linearly with the disordered parameter. Al-

though this theory is not strictly applicable to an amorphous material but rather a disordered alloy, the general conclusions are expected to remain valid. The density of spin wave states, the ferromagnetic Curie-temperature and the magnetization were found to be a function of disorder.

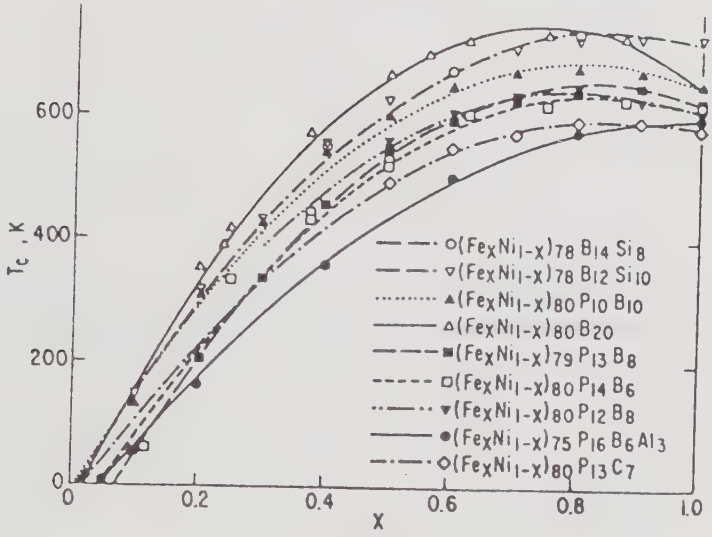

Fig. 2.15: Curie temperatures of Fe-Ni base amcrphous alloys as a function of iron content /102/.

2.2.6 Hyperfine Interaction

The interaction of the nucleus with its surroundings in a solid can be described by the Hamiltonian

$$H = H_{IS} + H_M + H_Q \tag{40}$$

The first term, H_{IS}, is the electric monopole component of the Coulombic interaction

$$W_e = -e^2 \iint \frac{\rho_n(r_n)\cdot\rho_e(r_e)}{|r_e - r_n|} d\tau_e d\tau_n \tag{41}$$

where the substripts 'n' and 'e' referer to the nucleus and the electron. As is shown below, this interaction leads to the isomer shift, which in essence measures differences of charge densities at the nucleus - the most unique feature of the Mössbauer effect, H_M is the magnetic interaction $-\mu . H_{eff}$ and H_Q is the electric quadrupole interaction with the electric field gradient.

2.2.6.1 The isomer shift

If one considers a simple nuclear decay of transition energy E_o from an excited state B to a ground state A, one can evaluate equation (41) for state B and for state A. This would shift the states A and B by a small amount of energies W_A and W_B, respectively, giving a net shift δ_s to E_o:

$$\delta_s = \frac{2\pi}{3} Ze^2 |\Psi_o|_s^2 \left(\langle r_E^2\rangle - \langle r_G^2\rangle\right) \tag{42}$$

Here $|\Psi_o|_s^2$ is the electron density at the nucleus, and $\langle r_E^2\rangle$ and $\langle r_G^2\rangle$ are the excited and ground state mean

square nuclear charge radii. If one considers δ_s to be the shift for the emitting nucleus (source), then one can derive a similar expression for the absorbing nucleus (absorber), δ_a.

The net difference is then

$$\delta_a - \delta_s = (\frac{2\pi}{3}) Ze^2 (|\Psi_o|^2_a - |\Psi_o|^2_s) \; (\langle r_E^2 \rangle - \langle r_G^2 \rangle) \qquad (43)$$

This expression is called the isomer shift (IS) of the absorber with respect to the source.

Equation (43) is more compactly written as

$$IS = (\frac{2\pi}{3}) Ze^2 \Delta|\Psi_o|^2 \; \Delta\langle r^2 \rangle \qquad (44)$$

This expression is subject to relativistic corrections /76/. $\Delta|\Psi_o|$ is the electron density at the nucleus, which depends on the chemical property of the material. As such this will be affected not only by the s-electron population but also screening effects of p-, d-electrons and by the chemical bonding of the atom. Electrons in 1s, 2s, 3s,..., shells all contribute to $|\Psi_s(0)|^2$ but in decreasing amounts as the principal quantum number rises. However, the inner shells are not markedly affected by chemical bonding so that the principal influence on the isomer shift will be by the outer most occupied s-orbital. Shielding by other electrons effectively increases the s-radial functions and decreases the s-density at the nucleus. For example, a $3d^6 4s^1$ outer configuration will have a higher s-density than $3d^7 4s^1$, similarly for $3s^2 3p^6 3d^5$ and $3s^2 3p^6 3d^6$ because of the penetration of the 3d-orbitals into the 3s.

2.2.6.2 Magnetic Interaction

The hyperfine field at the iron nucleus in an amorphous alloy with ferromagnetic transition metals may be described as the sum of a core polarization term and of a conduction-electron polarization term /77/.

$$\bar{H}_{Fe} = H_{CP} + H_{CEP} \qquad (45)$$

where H_{CP} is due to the polarization of inner core 1s, 2s and 3s electrons by the magnetic electrons. The core polarization term is directly related to the magnetic moment on the iron atom and hence to the number of unpaired d-electrons. H_{CEP} is due to the polarization of 4s-like conduction electrons by the moment on the transition metal atoms; the d-like it-inerant electrons of course have zero probability of being at the nucleus and therefore do not contribute to the hyperfine field. The hyperfine field is found to be nearly proportional to the magnetic moment of Fe in metallic glasses. The significant decrease of the conduction electron polarization contribution in metallic glasses would indicate a dominant p character of the s-p hybridized conduction band in these materials.

2.2.6.3 Core-polarization

The dominant contribution to the hyperfine field comes from the core polarization term. Its actual origin may be from intrinsic impairing of the actual s-electrons or indirectly as a result of polarization effects on filled s-shells. These can occur if the atom has unpaired electrons in magnetic shell, namely, the 3d-shell. The exchange interaction between the spin-up polarized d-shell and the spin-up s-electrons will be different to

that between the d-shell and a spin-down s-electrons. As a result the radial parts of the two s-electron wave-functions will be different, one being pushed towards the nucleus, the other pulled outward. Hence the spin densities at the nucleus no longer cancel and a Fermi contact-interaction field (core polarization) is observed.

According to Watson and Freeman /78/ the field per unit spin, which is a convenient measure of the hyperfine interaction, is given by

$$\chi = \frac{4\pi}{2s} \sum_{ns} \{ |\Psi(0)|^2_{ns\uparrow} - |\Psi(0)|^2_{ns\downarrow} \} \frac{H_{cp}}{spin} \qquad (46)$$

where s is the total spin of the ion in question and $\Psi(0)$ is a single s-wave function of the electron.

2.2.6.4 Electric quadrupole Interactions

The existence of an electric quadrupole interaction is one of the most useful features of Mössbauer spectroscopy. Any nucleus with a spin quantum number of greater than $I = \frac{1}{2}$ has a non-spherical charge distribution, which if expanded as a series of multipols contains a quadrupole term. The nuclear electric quadrupole moment Q, interacts with an electric field gradient (EFG), $q(=\frac{\partial^2 V}{\partial z^2})$, via the Hamiltonian /79/,

$$H_Q = \frac{eqQ}{4I(2I-1)} \{3I_z^2 - I(I+1) + \eta(I_x^2 - I_y^2) \qquad (47)$$

where the asymmetry parameter is given by

$$\eta = (\frac{\partial^2 V}{\partial x^2} - \frac{\partial^2 V}{\partial y^2}) / (\frac{\partial^2 V}{\partial z^2}) \qquad (48)$$

and $\frac{\partial^2 V}{\partial x^2}$, $\frac{\partial^2 V}{\partial y^2}$ and $\frac{\partial^2 V}{\partial z^2}$ are electric field gradient in x, y

and z directions.

For amorphous alloys, the model of random packing of hard spheres has been shown to be a reasonable approximation for the description of their disordered structures. The site symmetry of the atoms in such alloys is in general lower than cubic. A quadrupole interaction is then expected, due to non-vanishing electric field gradients, in all amorphous magnetic alloys. The value of the electric field gradient is ultimately connected to the detailed atomic arrangement of the amorphous alloys. The measurements of the quadrupole interaction in amorphous magnetic alloys, however, can be made only if the sample is in its paramagnetic states. Most of the amorphous magnetic alloys investigated in this work have relatively high values of Curie temperature (T_c) and therefore are not suitable for studies of quadrupole interaction. Below T_c, both magnetic and quadrupole interactions are present.

If the electric field gradient is axially symmetric and its principal axis makes an angle θ with the magnetic axis, then a relatively simple solution exists providing that $e^2qQ \ll \mu H$; in this case the quadrupole interaction, can be treated as a first order perturbation to the magnetic interaction and the energy eigenvalues are given by equation (50) of section 3. The effective quadrupole interaction energy can be approximated as $e^2qQ(3\cos^2\theta-1)$, where e^2qQ is the quadrupole interaction energy at the nuclear site and θ is the angle between the magnetic hyperfine field direction and that of the principal EFG $\frac{\partial^2 V}{\partial z^2}$.

The orientation of the principal EFG axes vary from site to site throughout the amorphous sample whereas the magnetic hyperfine field axis, which is determined by the magnetization axis in a ferromagnetic sample, does not.

A collective measurement of all sites in a macroscopic sample, in effect takes the spatial average of $(3\cos^2 -1)$ which gives zero.

The apparent absence of quadrupole interaction in all amorphous alloys in their magnetically ordered state can be thus attributed to a directional range of electric field gradients, with respect to the magnetic hyperfine field, which gives rise to a broadening rather than a line shift. This is consistent with the experimental observation (see section 4).

3. Experimental

The present section is a brief discussion of the method of production of amorphous alloys by various techniques. A detailed explanation of the melt spining' device has been given here as all the amorphous alloys studied in this work are prepared by this method. The details of the measuring methods have also been described in the following.

3.1.1 Systems investigated

The present work deals with a systematic study of the magnetic properties of amorphous alloys of the type $(TM'_{1-x}TM''_{x})_{100-y}X_{y}$, where TM'=Fe, TM"=Ni,Co,Cr,Mo and X a glass former B,Si,Ge,P, which are produced by continuous rapid cooling from the liquid state. Table 3.1 shows the different types of amorphous alloys with their compositions (most of them are nominal) which have been investigated in this work.

Table 3.1

Compounds	Concentration
$Fe_{100-x}B_x$ *	X=14,15,16,18,20,22, 24,26
$(Fe_{0.5}Co_{0.5})_{1-x}B_x$ *	X=0.15,0.19,0.20, 0.24
$(Fe_{1-x}Ni_x)_{80}B_{20}$ *	X=125,0.25,375,.5,.625, .75
$(Fe_{1-x}Ni_x)_{80}B_{19}Si_1$ *	X=0.8,.8375,.875
$(Fe_{1-x}Co_x)_{80}B_{20}$ *	X=0.125,0.25,0.375, 0.625,0.75
$Fe_{95-x}Cr_5B_x$ +	X=15,20,25
$Fe_{85-y}Cr_yB_{15}$	Y= 5,10,15,20
$(Fe_{1-x}Mo_x)_{80}B_{20}$ +	X=.0125,.025,.0375 .05,.0625,.0875,0.125
$(Fe_{1-x}Ni_x)_{75}B_{25}$ ·	X=0.1,0.2,0.3,0.4,0.5, 0.6,0.7
$Fe_{80}T_xB_{20-x}$ Δ T=V,Cr,Mo,W,Mg,Fe,Co,Ni	X=3
$Fe_{80}B_{20-y}M_x$ * M=C,Si	X=2,4,6,8,10 (C) X=2,4,6,8 (Si)
$Fe_{82}B_{18-x}Ge_x$ *	X=2,4,6

* General Electric Company, Schenectady, N.Y., U.S.A.

\+ TU, Copenhagen

· Institut für Werkstoffe der Elektrotechnik, RUB

Δ Central Research Institute for Physics, Budapest

3.1.2 Formation and Phase diagrams

In principle, any liquid can be quenched so rapidly that it has not enough time to crystallize before its atoms or molecules begin to move so sluggishly that the structure within it becomes frozen. This may be understood by considering Fig. 3.1, a time temperature crystallization diagram. Here the C-shaped curves indicate the times at which crystallization will start and finish if a liquid is quickly cooled below its melting point to a particular temperature level.

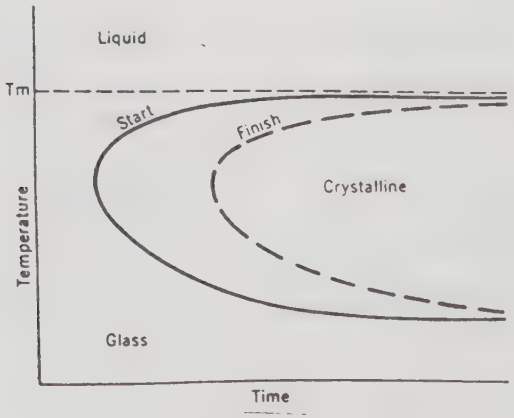

Fig. 3.1: Time temperature crystallization diagram /39/

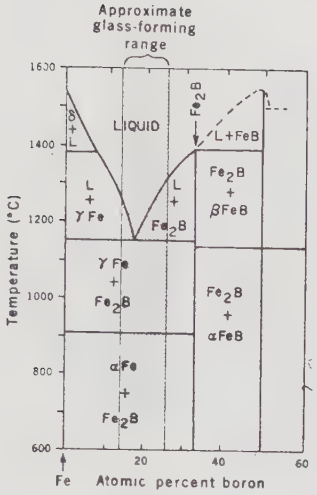

Fig. 3.2a: Portion of the iron-boron phase diagram /39/

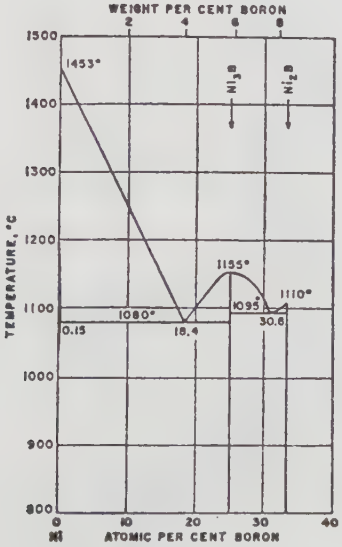

Fig. 3.2b: Phase diagram of B-Ni /93/

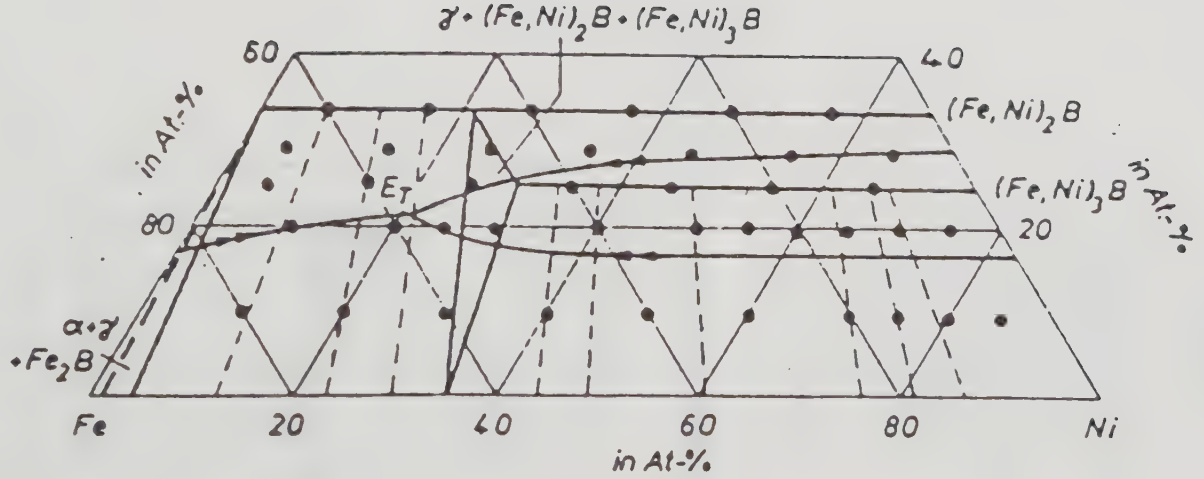

Fig. 3.2c: Ternary phase diagram Fe-Ni-B /95/

The nose of the C-curve indicates the minimum time for crystallization to start. The higher the temperature is above the nose, the smaller the supercooling and so the longer it takes to start crystallization. To avoid crystallization and thereby obtain a glass, the time taken to cool below the C-curve's nose must be less than the time at which the nose is positioned. For pure metals, because of their simple atomic structures, it may take less than a microsecond for crystallization to begin at the nose temperature. However, for the selected alloys that form interesting metallic glasses, the nose lies at a few milliseconds. Thus cooling rates of 10^5 to 10^6K per second are adequate.

The alloys that can most easily be obtained in glassy form are usually eutectic compositons /39/. The phase diagram of Fig. 3.2.a illustrates this for the practically important Fe-B system. At a eutectic composition, the melting temperature is a minimum, but this is not the most important feature of a eutectic liquid for easy glass formation. The most important feature appears to be the large structural change that must occur between the liquid just above and the two solid phases just below the eutectic temperature.

Fig. 3.2b shows the phase diagram of binary system Ni-B. The diagram shows the existence of the compound Ni_3B, Ni_2B and a considerable low liquids . The examination of /93/ Ni_ rich alloys confirmed the eutectic point at 1082^oC, 18.4 at % B and the solubility of B in Ni is found to be 3.7 at % at the eutectic.

The $Ni_{80}B_{20}$ glass is not readily fabricated by the liquid quenching techniques /47/ and as experieneed in the Institute der Werkstoffe für Elektrotechnik, RUB, also. Very recently, however, Takahashi et al /89/ have been able to fabricate an apparently amorphous Ni-B alloy of

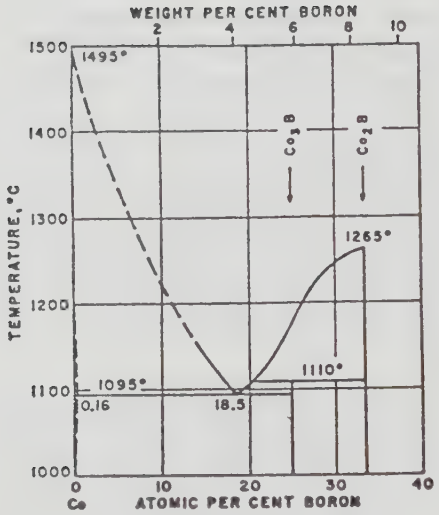

Fig. 3.2d: Phase diagram of B-Co /93/

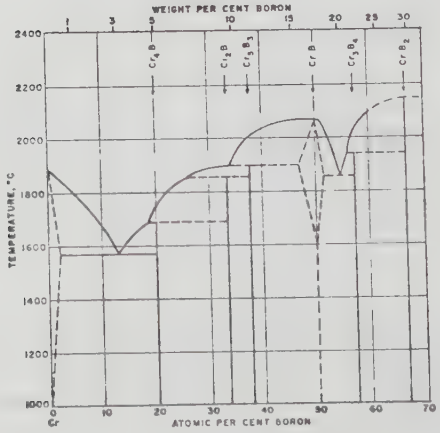

Fig. 3.2e: Phase diagram of Cr-B /93/

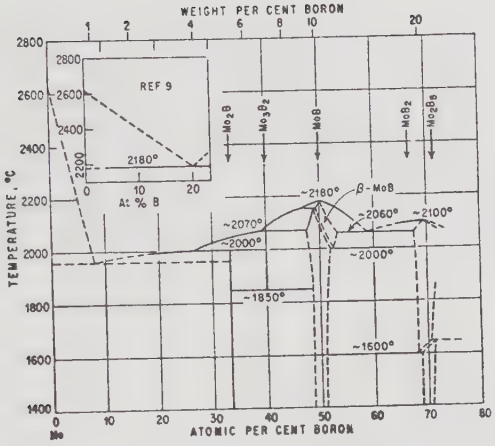

Fig. 3.2f: Phase diagram of Mo-B /93/

18.5 at % B-content by this technique, so perhaps it is producible in the glassy state only in a very narrow composition range near the eutectic. Similarly, the existence of Co_3B and Co_2B is established as shown in Fig. 3.2d. The $Co_{80}B_{20}$ glass can be easily produced by the liquid quenching technique. In Fig.3.2e and Fig. 3.2f, the phase diagrams of Cr-B and Mo-B are given. The possible phases with the increase of B concentration are also shown. According to Chen /11/, the ternary amorphous alloys are more stable against crystallization than binary ones. Fig. 3.2c shows the phase diagram of the ternary system Fe-Ni-B. It shows a section of the isotherm at 800°C. It is seen that the three eutectic runs meet at the ternary eutectic point $T=\gamma+(FeNi)_2B+(Fe,Ni)_3B$. The maximum solubility of iron in in Ni_3B is found to be 45 at % Fe at 25 at % B. It is also concluded /80,95/ that the solubility of iron in Ni_3B increases with the increase of temperature.

Preparation of the amorphous ferromagnetic alloys

All amorphous alloys are in a metastable state. The preparation and stability of these materials depend mainly on various kinetic barriers to growth of crystal nuclei. During quenching, the alloy must pass rapidly through the temperature range where nucleation can occur so as to prevent nucleation and diffusion. A review of the origins of these barriers and their dependence on the parameters of the materials has been given by Cohen and Turnbull /94/. More recently, Davis et al /81/ reviewed in detail the technology of metallic glasses. Various ways in which amorphous alloys can be produced are:

i) Vapour Deposition,
ii) Sputter Deposition,
iii) Electrodeposition and Chemical deposition,
iv) Quenching from the melt.

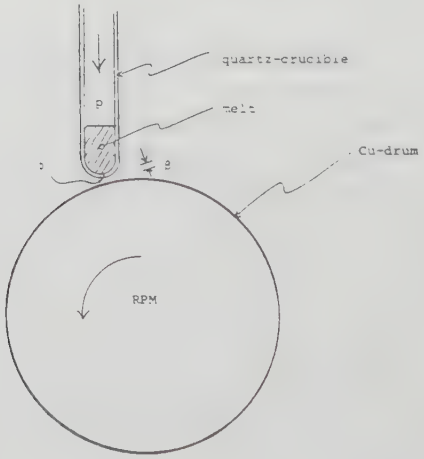

Fig. 3.3: Principle of fabrication and variable parameters: p: Ar,He-pressure, ϕ: orifice diameter, β: crucible to drum distance, and RPM: drum rotation frequency /83/

In the following a short description of the quenching technique will be given:

3.1.4 Schematic clarification:

Amorphous alloy ribbons are prepared by a method in which a jet of liquid alloy impinges on a cold, moving substrate. The jet flattens into a ribbon and heat is largely lost by conduction into the substrate, providing cooling rates of the order of 10^6K/sec. A schematic diagram of the process is shown in Fig. 3.3.

3.1.5 Experimental Arrangement:

The apparatus for producing metallic glass $(Fe_{1-x}Ni_x)_{75}B_{25}$ ($0 \leq x \leq 0.7$) by melt-spinning method has been fabricated in the Institute der Werkstoffe für Elektrotechnik, RUB is shown in Fig. 3.4, in which the liquid alloy jet is directed on the surface of a copperdisk of 12 cm diameter.

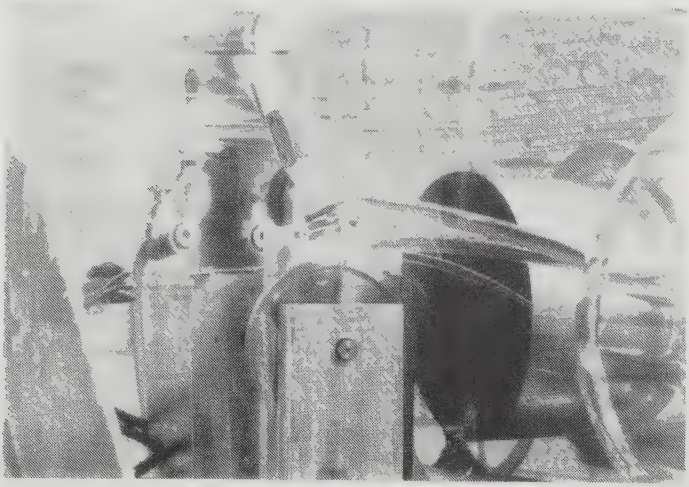

Fig. 3.4: Apparatus for the production of metallic glass ribbons (IWE, RUB).

The alloy charge, weighing a few gram, is contained in a quartztube with an orifice of about 0.5 mm diameter at its bottom end. The alloy is melted by r,f induction heating and the ejected alloy through the orifice by argon or helium gas pressure. The liquid metal jet impinges on the circumference of a copper disk rotating at several thousend revolution/min. The jet then flattens, cools rapidly and solidifies into a ribbon, remains in contact with the surface of the disk through about 10^{o} of arc, and leaves the disk under the action of centrifugal force. The form of the sample thus produced is retangular in shape with a width of about 1.5mm-2mm and a thickness of about 30µm-40µm. The different types of samples produced by this process are shown in Table 3.1. The influence of orifice diameter, ejection gas pressure and disk speed on the dimensions of the resulting ribbon have been systematically studied by Lieberman et al /82/ and more recently by Nielson /83/. Fig. 3.5(a,b,c) show the effect of the variation of the different parameters on the resulting ribbons.

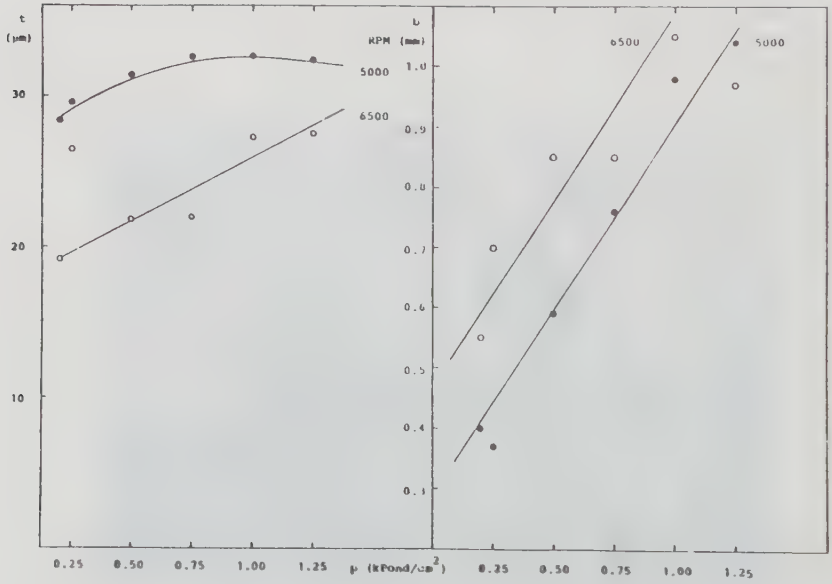

Fig. 3.5a: Thickness t and width b versus Ar-pressure p with drum rotation frequency (RPM) as a parameter for $Fe_{40}Ni_{40}P_{14}B_6$ ribbons /83/.

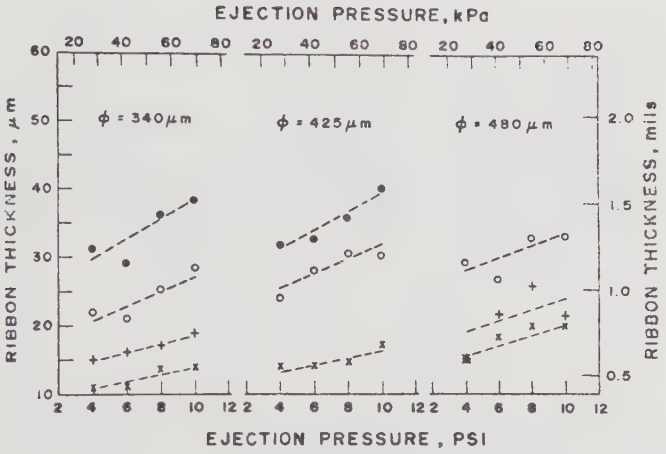

Fig. 3.5b: t versus p with ϕ as a parameter for $Fe_{40}Ni_{40}P_{14}B_6$ /82/

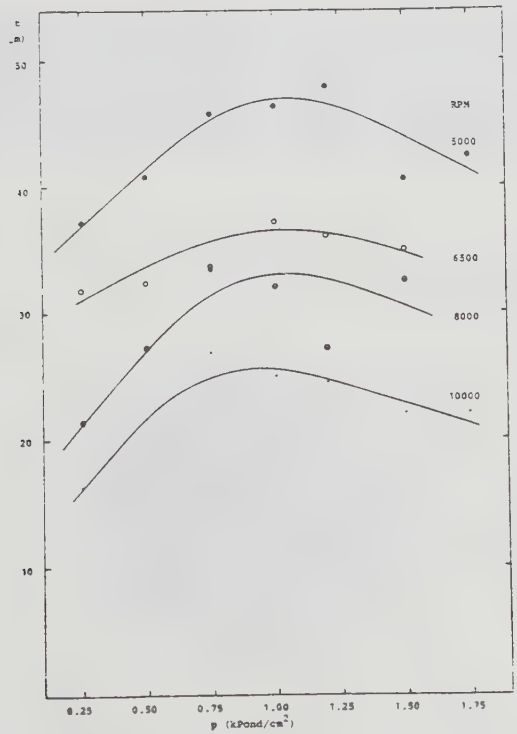

Fig. 3.5c: t versus p with RPM as a parameter for $Fe_{40}Ni_{40}B_{20}$ ribbons /83/

3.2 Analysis of the samples:

The absence of long-range crystalline order in these samples under investigation has been confirmed by the following experimental techniques within limit of resolution:

i) Mössbauer spectroscopy,
ii) x-ray diffraction.

i) The information on structure may be inferred from microscopic measurements such as Mössbauer spectroscopy, which is sensitive to the short range atomic order surrounding the probe atom. Fig. 3.6a shows the spectrum of amorphous $Fe_{80}B_{20}$ which is very different from crystalline alloy. In the crystalline case, the sharp lines originate from α-Fe, Fe_3B and Fe_2B (see section 4). Thus, Mössbauer effect is reasonably sensitive to certify the non-amorphicity of the sample.

ii) X-ray diffraction of amorphous alloys exhibit a diffuse scattering pattern Fig. 3.6b, which is distinctively different from that of a crystalline solid (see section 4). The Fourier form of the scattered intensity, or the radial distribution function, describes correlations among the atomic positions. X-ray diffraction experiments have a resolution of about 20 A^{o} and therefore can only verify a lack of crystalline ordering beyond this range. The electron diffraction pattern of amorphous $Fe_{40}Ni_{40}B_{20}$ show also broad rings typical for amorphous solids Fig. 3.6c.

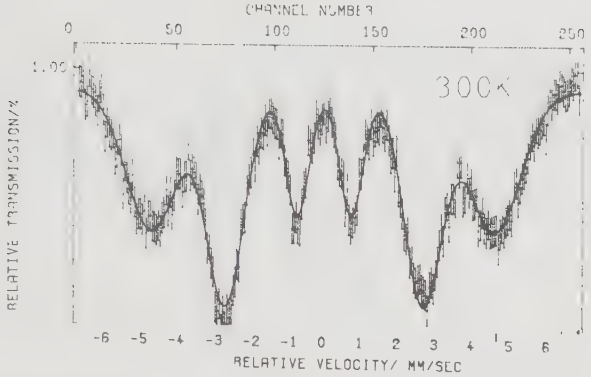

Fig. 3.6a: Mössbauer spectrum of amorphous $Fe_{80}B_{20}$ at 300K

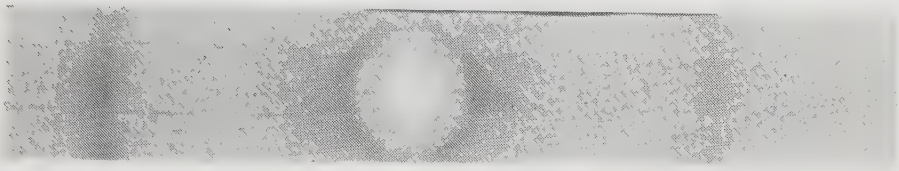

Fig. 3.6b: A Debye-Scherrer fi lm of a $Fe_{40}Ni_{40}B_{20}$ metallic glass with the characteristic diffuse halos

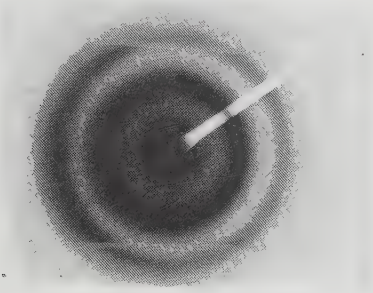

Fig. 3.6c: Electron diffraction pattern of a $Fe_{40}Ni_{40}B_{20}$ metallic glass

3.3 Magnetic measurements:

The temperature dependence of magnetization have been measured with the Princeton Applied Research Model 155 Parallel Field Vibrating Samples Magnetometer with precision over the cryogenic temperature range.

3.3.1 Principle:

The vibrating sample magnetometer is an induction instrument in which the output voltage is sinusoidal. The sample is vibrated in a uniform field in a periodic motion relative to a pick-up coil, and the changing flux through the coil generates a voltage which is proportional to the sample magnetic moment. The vibration sample magnetometer covers a wide range of moments, from 10^{-5} to 10^{4} emu, by variation of sample size and amplifier gain.

3.3.2 Schematic clarification:

Fig.3.7 shows the blockdiagram of the PAR Model 155 magnetometer. The drive mechanism is composed of the permanent ordinary loudspeaker. The driver head vibrates the sample rod vertically at approximately 82 Hz. A set of capacitor plates moves with the vibrating rod. These plates provide a signal to the electronics in the console for nulling out components of signal due to vibration but not related to magnetic moment. The signal picked up by the coils from the vibrating sample is of the frequency of vibration, and is of an amplitude proportional to the magnetic moment and amplitude and frequency of vibration. In order to determine the magnetic moment from this compo-

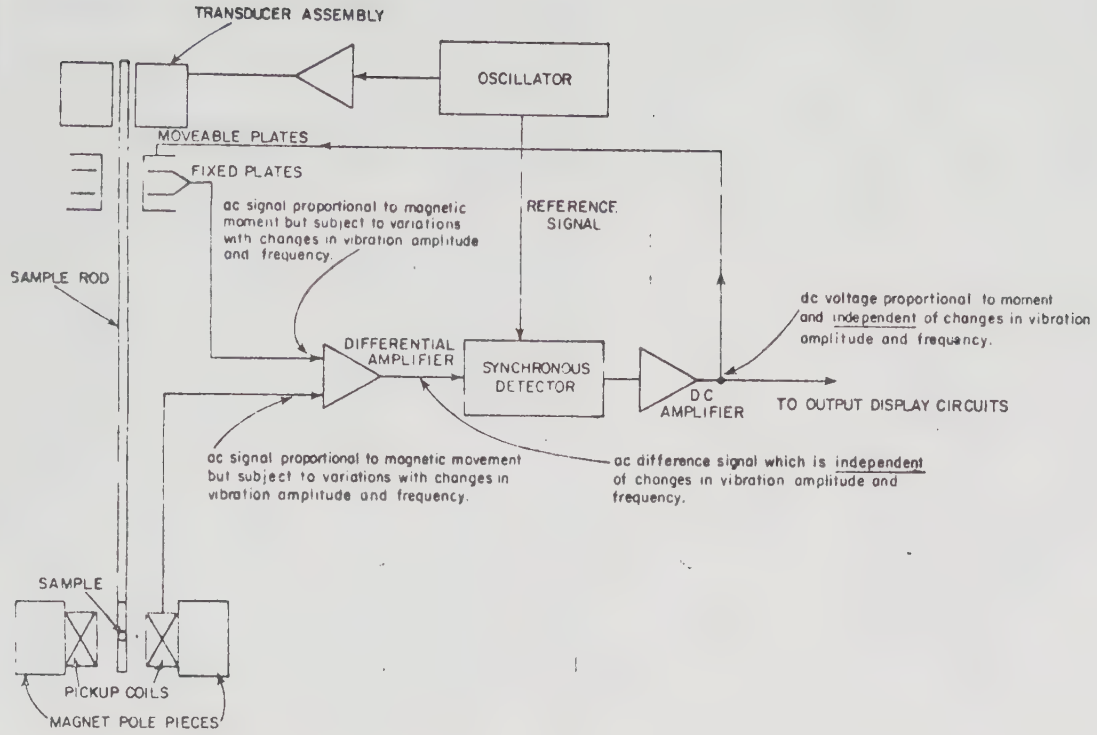

Fig. 3.7: Simplified block diagram of model 155 magnetometer

site signal, the amplitude and frequency components must be eliminated. This is achieved by including the vibrating capacitor in a feedback loop. The units are connected in an operation amplifier type of feedback loop, with the signal from the pickup coils used as the reference, and with feedback via the movable capacitor plates. If a dc voltage is applied to the movable plates, an ac voltage appears on the fixed plates which is proportional to the amplitude and frequency of vibration and to the dc voltage on the movable plates. The operational loop makes the level of dc voltage that which caused the ac voltage on the fixed plates to exactly equal the voltage induced in the pickup coils. Variations in amplitude and frequency of vibration cause the signal and feedback voltage to vary equally. If the magnetic moment changes, however, the change of signal voltage must be matched by a proportional change of dc voltage on the capacitor plates in order for the loop to be satisfied. Therefore, the output voltage, which is the same voltage applied to the capacitor plates, varies proportionally with the magnetic moment. The amplified difference signal from the input amplifier is an ac signal of the frequency of vibration. This ac voltage must be converted to an equivalent dc for application as feedback to the movable capacitor plates. This is achieved with a synchronous detector.

3.3.3 Cryostat:

The vibration sample magnetometer (PAR 155) can be operated over a wide temperature range if provision is made to protect the sense coils. This is relatively simple at low temperatures. The coils may be located inside the cryostat but the cryostat must be mechanically isolated from the

drive mechanism. The Model 153 Variable Temperature cryostat has been used here. This cryostat provides a sample temperature environment which can be varied over a temperature range from 4.2 K to 300 K. An electrical heater is incorporated in such a position that an adjustable amount of heat is added to the vapor stream. A balance between heating and cooling may be maintained at any temperatures between 4.2 K and room temperature. The same sample rod is used with the 153 cryostat as is used in normal room temperature measurement, and the x,y and z adjustments are unaltered.

3.3.4 Procedure:

Magnetization measurements were made with the above mentioned vibration sample magnetometer calibrated with a pure nickel sample in applied fields of 0.1 T and 0.5 T. The measurement of sample temperature was made by using a copper-constantan thermocouple (reference point was dipped in ice) situated adjacent to the sample and was accurate within ±0.1 K around 4.2 K and about ±1 K around 300 K. The magnetization of amorphous alloys as a function of temperature have been studied here over a temperature range from 4.2 K to 300 K. The rectangular shaped samples had dimensions approximentely 3 mm x 2 mm x 40 μm. The field was applied in the sample plane to reduce the demagnetizing field effects. This type of magnetometer have a resolution of about 10^{-4} emu. The magnetization of a magnetic material is generally given in emu/g , so a small error in the denominator will have a pronounced effect in the resulting saturation magnetization of the material. The samples used for magnetic measurement were less than 5 mgm and the accuracy of the weighing balance was ±0.05 mg. Because of their small weight, special care

was taken during weighing of the samples.

3.4 Mössbauer spectroscopy:

In this section, a general description of the Mössbauer effect in regard to the ^{57}Fe is given followed by the experimental aspects.

3.4.1 General comments:

While there are several reviews on the Mössbauer effect /e.g. 84,85,86,79/, only a few relevant aspects will be pointed out here.

Recoilless nuclear resonance absorption, as one may call the Mössbauer effect, comes about when the X-ray, corresponding to a nuclear decay to its ground state, is emitted without energy loss due to nuclear recoil or Doppler broadening due to thermal motion. This condition is met when the emitting nucleus is embedded in a crystalline or amorphous material, thus impairing the recoil momentum to the crystallites as a whole. Similarly, this "coherent" X-ray which has an energy spread $\Gamma = \frac{h}{\tau}$, where τ is the life time of the excited state, can be absorbed by an absorber containing the same nuclei in their ground state. One, therefore, has a nuclear resonance fluorenscence.

In the case of ^{57}Fe, the 14.4 keV transition has a width $\Gamma = 4.7 \times 10^{-9}$ eV. While Mössbauer absorption does not measure the absolute values of the transition energy, it can measure shifts within several orders of magnitude

of the line width. To measure these shifts, one notes that Doppler velocities of the order of mm/s(v) produce shifts $\Delta E = E(\frac{v}{c})$, where E is the γ-ray energy and c is the speed of light. For ^{57}Fe, 1 mm/s corresponds to $\sim 4.8 \cdot 10^{-8}$ eV.

In general, the fraction of recoil free events is given in the Debye model by the f-factor:

$$f = \exp\{-\frac{6E_R}{k\Theta_D}[\frac{1}{4} + (\frac{T}{\Theta_D})^2 \int_0^{\Theta_D/T} \frac{x\,dx}{e^x - 1}]\} \qquad (49)$$

where T is the temperature (K), Θ_D is the Debye temperature of the host crystal, and $E_R = E_\gamma^2/2Mc^2$, M being the mass of the nucleus. For ^{57}Fe of 14.4 keV, f is 0.91.

3.4.2 The case of ^{57}Fe:

In this part the experimental aspects in regard to the ^{57}Fe resonance are presented, especially the problem of observing the 14.4 keV γ-rays.

The decay scheme:
The decay scheme for ^{57}Fe is shown in Fig. 3.8. The excited state at 136.32 keV is populated by electron capture with 99.8% efficiency from ^{57}Co whose half-life of 270 days is conveniently large. 11% of the decays from the 136.32 keV state result in a 136.32 keV γ-ray and 85% a 121.9 keV γ-ray. The first excited state of energy 14.4 keV (present work) is thus efficiently populated by ^{57}Co decay. A Mössbauer resonance from the 136.32 keV level has also been reported, but this is of minor importance in this work. The 14.40 keV transition occurs, without change in parity, between an excited state of nuclear spin quantum number 3/2 and a ground state of spin 1/2 and the quan-

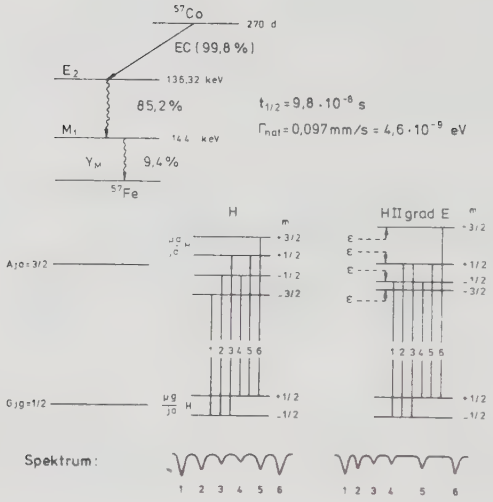

Fig. 3.8: Decay scheme for ^{57}Fe

tum number 3/2 and a ground state of spin 1/2 and the transition is primarily M1 type, the amount of E2 admixture being only 0.0006%, which is negligible. The life time of this level is $9.8 \cdot 10^{-8}$ sec, corresponding the natural line width is of the order of 0.097 mm/s ($= 4.6 \cdot 10^{-9}$ eV) for the Mössbauer resonance which is large enough to prevent major problems in instrumentation.

The relative abundance of ^{57}Fe in natural iron is low (2.19%) but the isotope has a large cross-section for capture of the 14.4 keV y-ray (theoretically $2.57 \cdot 10^{-18}$ cm^2) and isotopic enrichment is only needed when the iron content at the sample is very low.

3.4.3 Experimental arrangement:

In all velocity experiments a sinusoidal electromechanical drive /87/ was used. The entire assembly of drive, source and absorber was rigidly mounted in an evacuated can to avoid vibrational and accoustical disturbances. The schematic of the electronics is shown in Fig. 3.9. The multichannel analyzer used had 1024 channels. This is needed for the high resolution of the spectrum.

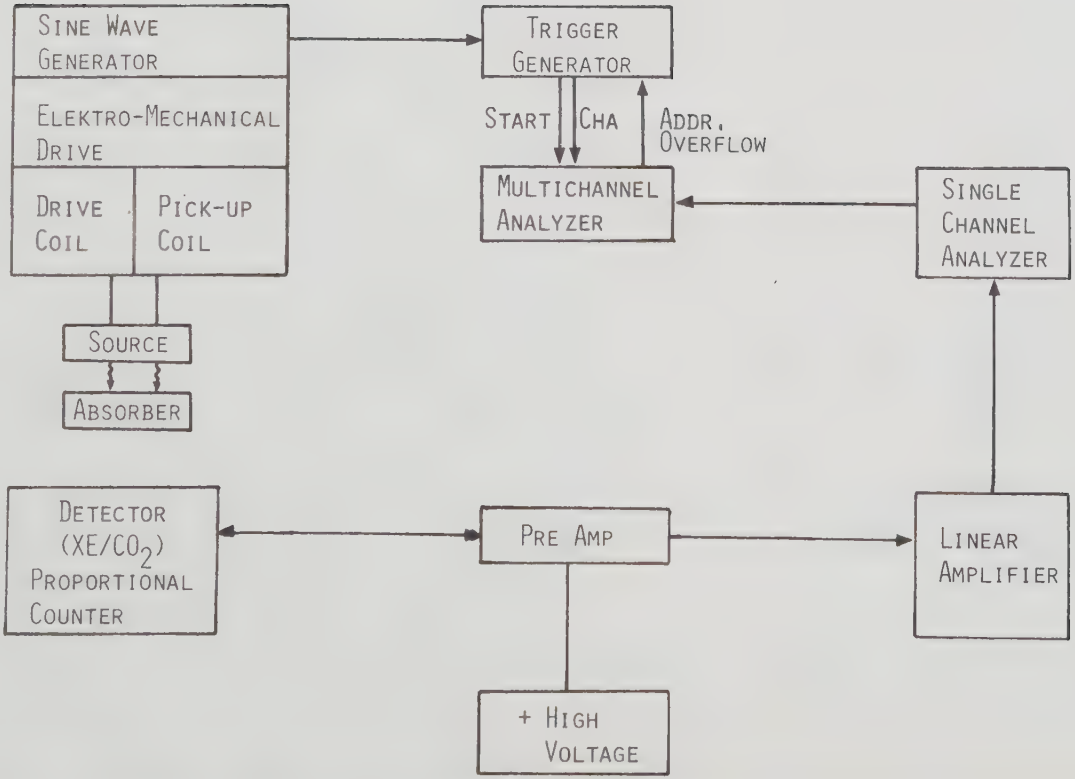

Fig. 3.9: Block diagram of the electronic components

Mössbauer source:

The source used in this work is ^{57}Co in a diamagnetic matrix rhodium (Rh), which is produced by the Radiochemical Centre, Amsterdam. The physical parameters and the properties of the source are as follows:

Matrix

Material	Rhodium
Thickness	12 µm
Size	5 mm diameter
Activity of the source	27.7 mCi
Recoilless fraction	0.78
Linewidth measured	0.21 mm/sec

This matrix is particularly suitable for sources used at 4.2 K, since the magnetic ordering temperature is only 4 K/atomic % of iron in rhodium /88/ and sources of up to 250 mCi/cm^2 in 6 µm foil can be expected to give unsplit lines.

Absorber:

All absorbers were made by holding several amorphous ribbons of dimensions (5 mm x 12 mm), (4 mm x 12 mm) parallel to each other with adhesive tapes and covering an absorber circle of 20 mm diameter. The sample so prepared were then put inside a pure Aluminium sample holder of diameter 22 mm for low temperature measurements. The thickness of the absorbers used in this work was in the range from 20 microns to 40 microns.

Detector:

To detect the 14.4 keV γ-rays a Xenon 97%-3% Co_2 refillable proportional counter was used. Fig.3.10 shows the γ-ray spectrum for the ^{57}Co source detected by the proportional counter. The detecting gas selection should be based on optimizing the efficiency for and spectral resolution of the energies of interest. The inert gases are normally used with a small quantity of quench gas (namely 3% Co_2). This improves the pulse characteristics of the gas and prevents it from going into continuous discharge, thus shortening counter life. Here Co_2 is chosen as quench gas because it provides excellent pulse and life time characteristics. The operating voltage of the proportional counter used is 2000 volts and the resolution is 10.3% at 14.4 keV.

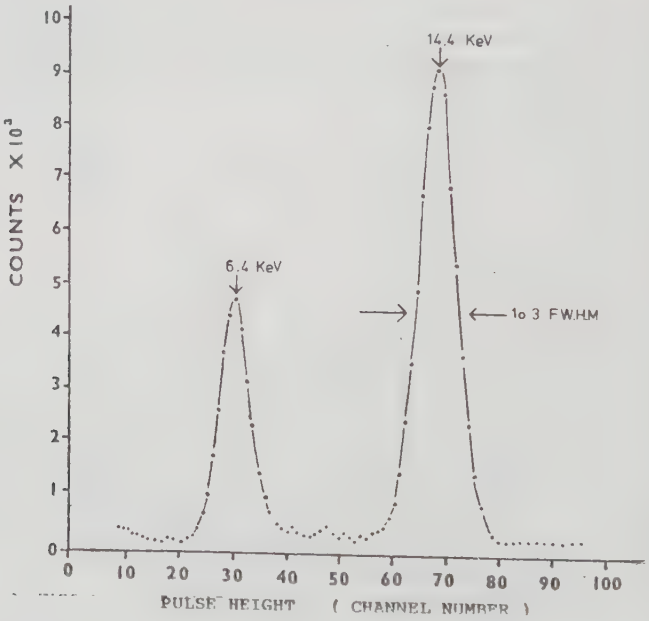

Fig. 3.10: γ-ray spectrum for the ^{57}Co/Rh source detected by the proportional counter (97% Xenon 3% Co_2)

Measurements at low temperature (4.2 k ≤ T ≤ 300 k):

The measurements at low temperatures down to Helium (4.2 k) were made in a standard continuous flow cryostat. The Thor-cryogenies S-3010 temperature controller is used for controlling the temperature of the sample accurately, attaining stability of the set temperature to within 0.01 degrees (K or ^{o}C). A built-in current source is provided for use with resistance sensors. The temperature of the sample is measured using calibrated carbon-resistor (4.2 k - 77 k) and with thermistor (77 k - 300 k). To avoid any temperature gradient between the cold surface of the continuous flow cryostat and the middle of the absorber, Al-sample holders were used.

Measurement in the magnetic field:

For the measurement in high magnetic field, that is, up to 8 T, and at various temperature (4.2 K $\leq$ T $\leq$ 300 K), the continuous flow cryostat is placed inside the Bath cryostat of the superconducting magnet. Here, the magnetic field is parallel to the γ-radiation. Fig. 3.11 shows the typical arrangement for such an experiment.

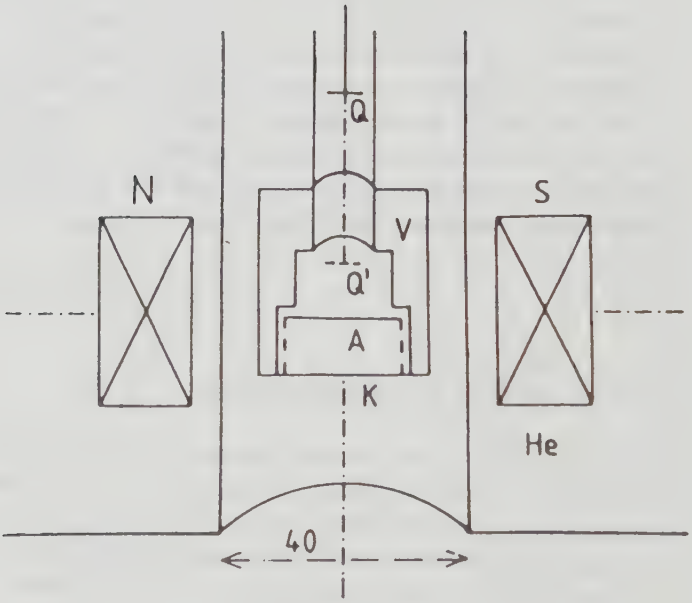

Fig. 3.11: Arrangement of the continuous flow cryostat for the Mössbauer spectroscopic measurement in external field.

A = Absorber
K = Cold surface of the continuous flow
Q = Source outside the field
V = Continuous flow coil
He = Helium bath for magnetic coil
S = Superconducting coil
Q' = Source inside the field

Errors during measurement:

During measurement, many errors can arise, which effect the spectrum and consequently the resultant Mössbauer (or Magnetic) parameters.

It is observed that because of the use of small transducer rod at room temperature measurement, the error is limited to 1%. Whereas, measurements in superconducting magnet in high field, because of the long rod, give an error of about 5% which causes an uncertainty of 1.5 channel in 256 channel. Of course, this is within the limit of error, but care should be taken to minimize it.

There may be a change in the line width of the spectrum due to the vibration of the sample holder. This can be avoided by keeping the whole system in vacuum during measurement. Many more possible error might arise like 'temperature gradient' between the sample holder and the sample. This will definitely have a pronounced effect in the resulting spectrum. Also, the stability of the magnetic field and the measuring temperature, during the experiment should be taken into account to avoid unnecessary complication in the evaluation of the measured spectrum.

3.4.4 Determination of the Mössbauer parameters from the measured spectrum:

Due to the fluctuating environments, the strength of the hyperfine interactions changes from nucleus to nucleus in the disordered systems. Consequently, many spectral lines overlap giving an unresolved spectrum. In such cases, the calculation of the hyperfine field distribution can be done on the basis of following assumption:

a) The effect of both the quadrupole and isomer shift distributions are negligible.

b) The intensity ratios and linewidths of the single spectra contributing to the overlapped one are known and do not depend on the strength of interaction. Generally, the evaluation of the hyperfine field distribution P(H) is carried out /77/ in the following two different ways:

   i) by assuming a known shape for P(H), as modified Lorentzian or split Gaussian distribution for instance where the parameters of these presupposed functions are determined by a least square procedure.

   ii) by series expansion of P(H) using trigonometric functions, i.e., a discrete hyperfine field distribution is assumed (Window /99/) or step functions as a basis, i.e. a continuous hyperfine field distribution is assumed (Hesse and Rubartsch /90/).

There are advantages and disadvantages of all these methods, which have been discussed by Vincze /77/. In the present work, the first method was used to evaluate the measured spectra, which is being discussed in the following.

Below the transition temperature, the observed broadening of the hyperfine components could be due to either the effects of electronic relaxation or the existence of a non unique hyperfine field /91/. The spectra have been fitted here in terms of a non-unique hyperfine field. Due to this non-uniqueness of the sites, one must discuss the hyperfine components on a statistical basis and give appropriate probability distributions. In the present discussion in explaining the Mössbauer spectrum (MS) well below the transition temperature, the complications arising due to a combined electric quadrupole and magnetic interaction can be overlooked. At low temperature, the magnetic moments

of the iron atoms are aligned over a range considerably larger than the interatomic distances. The electric field gradient (efg) on the other hand is primarily determined by neighbouring atoms within a few interatomic distances. The metallic nature of these alloys prevents the existence of long range electrostatic effects. Because of the structural fluctuations, the local principal axis of the electric field gradient can not be obtained over any significant distance. That is, on the average over the region of magnetic ordering, the electric field gradient principal axis and magnetic field are at random angles. Because in the case of amorphous alloys $\eta \neq 1$, one can assume the assymetry parameter to be $\eta \sim 0$. The excited state energy levels are then given by /56/ when $\mu H >> e^2 q_Q$ as

$$E = -g\mu_N H_m + (-1)^{|m_I| + \frac{1}{2}} \frac{1}{2} e^2 q_Q \left[\frac{1}{2}(3\cos^2\theta - 1)\right] \qquad (50)$$

$$I = \frac{3}{2}$$

since θ in the present case has an uniform distribution over the solid angle Ω, and $\langle \cos^2\theta \rangle_\Omega = \frac{1}{3}$, the average line positions due to the magnetic interaction will be maintained.

The Mössbauer spectrum can therefore be fitted in terms of a distribution of hyperfine field P(H), an average isomer shift and linewidth Γ, which is allowed to vary in order to take into account of the effect of a random distribution of efg and magnetic field. The shape of the Mössbauer lines, better resolved by suppression of the line 2 and 5 is predominantly symmetrical. The symmetrical hyperfine field distribution may be confirmed from the measurement in external magnetic field Fig. 3.12. It can be noted in Fig. 3.12 that because of the selection rule, that is the transition with $\Delta m = 0$, the lines 2 and 5 are suppressed.

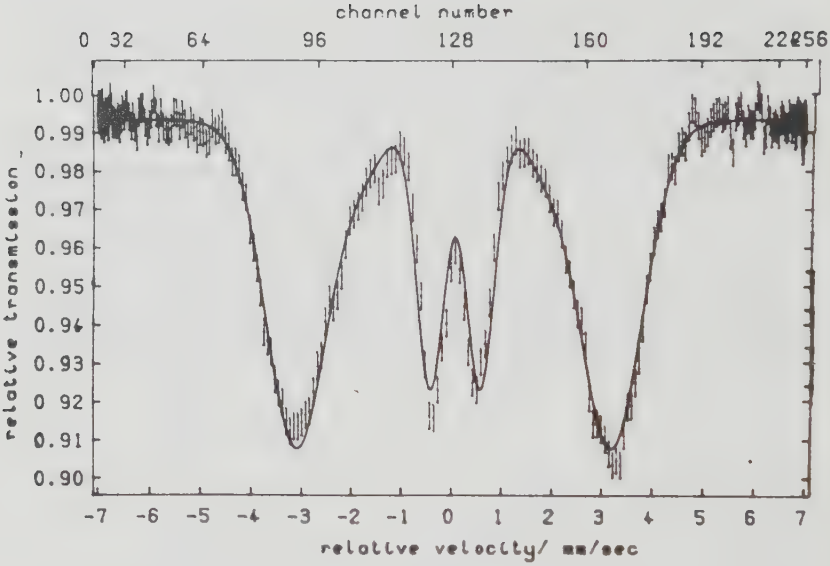

Fig. 3.12: Mössbauer spectra of amorphous $Fe_{40}Ni_{40}B_{20}$ at an external field of 7 T.

The measured line form is calculated on the basis of 'folding integral' of a Gaussian distribution of Lorentz lines. It is found that the measured lineform have the same shape as that of Gauss-lines. Thus symmetrical Gaussian distribution of fields has been found to be the best fit to the experimental data after subtracting from the measured line width Γi (with i=1,2,...6) the natural and apparatus line broadening denoted by Γa. The difference $\Gamma i - \Gamma a$ were found to be proportional to the coefficients Ci of the Mössbauer transition frequencies $\Gamma i = CiH$ in a hyperfine field H, thus giving evidence that the line broadening is associated with a distribution of hyperfine fields rather than to a distribution of electric field gradients. Thus, the form of the hyperfine field distribution P(H) can be taken as Gaussian distribution

$$P(H) = \exp\left[-\frac{(H-H_o)^2}{2(\Delta H)^2}\right] \qquad (51)$$

where ΔH = dispersion parameter.

It has been also reported by many authors' /73,92,97/ that the hyperfine field distribution in TM-M amorphous alloys is single maximum, well defined and symmetrical as shown in Fig. 3.13. The evaluation of hyperfine field distribution in amorphous alloys has been discussed on the basis of different shape of distribution by J. Hesse et al /90/. They concluded that these methods give very similar results. Smooth and broad distribution functions of hyperfine fields can be found correctly with both methods.

Fig. 3.14 shows the influence of hyperfine field distribution /87/ on the Mössbauer spectrum. The outer lines 1 and 6 are seen to be six times wider than the inner lines 3 and 4. This effect can be seen in all the spectrums used in the following section.

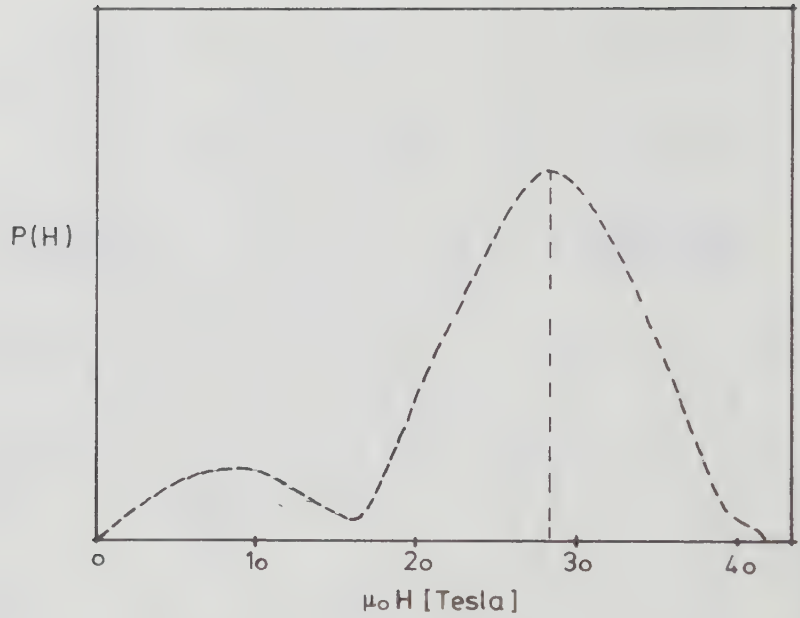

Fig. 3.13: Hyperfine field distribution of amorphous $Fe_{80}B_{20}$ at 4.2 K.

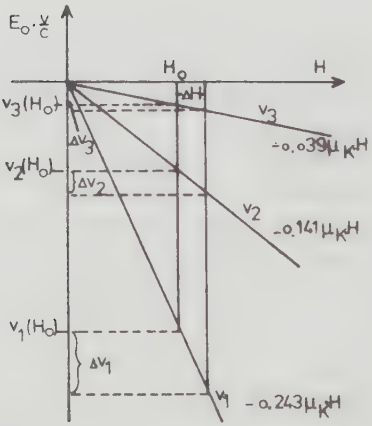

Fig. 3.14: Broadening of the lines of the Mössbauer spectrum due to hyperfine field distribution

4. Results and Discussion

The key to the difference between crystalline and non-crystalline solids is that no two atomic sites are equivalent in amorphous structures, whereas all macroscopic directions may be equivalent in the bulk. The first is a necessary condition for an amorphous solid.

Inequivalency of sites in amorphous systems leads to a distribution in magnitude of atomic moments, even at zero temperatures. In amorphous transition metal-metalloid alloys, not only the distances but also the number and type of nearest neighbours can vary from one site to the next. In addition, the transition metal, can sometimes be present in the magnetic state and sometimes in the non-magnetic state in the same material and consequantly very broad distributions result. Moment distributions are best inferred from the hyperfine field distributions P(H) as measured by Mössbauer spectroscopy or NMR.

If the distribution function $P(HF_a)$ can be approximated by a Gaussian function, then the average value of the hyperfine field at Fe-site is given by

$$\overline{HF_a}(Fe) = \int HF_a P(HF_a) dHF_a \ . \qquad (52)$$

The normalization condition requires

$$\int P(HF_a) dHF_a = 1. \qquad (52a)$$

The distribution of the hyperfine field determined from the Mössbauer effect in amorphous ferromagnets is a manifestation of the distribution in the magnetic moment caused by the random distribution of the exchange interaction resulting from the structural fluctuations in amorphous solids. Assuming that the TM' and TM" atoms

in the pseudo-binary alloy. $(TM'_{1-x}TM''_x)_{100-y}X_y$ have magnetic moments μ_a and μ_b whose magnitudes depend on their local environments, the average magnetic moment of the alloy is given by

$$\langle\mu\rangle = x\int P(\mu_a)\mu_a d\mu_a + (1-x)\int P(\mu_b)\mu_b d\mu_b \qquad (53)$$

where $P(\mu_a)$ and $P(\mu_b)$ denote the partial distribution of the magnetic moments at O K with the normalization condition

$$\int P(\mu_a)d\mu_a = 1 \quad \text{and} \quad \int P(\mu_b)d\mu_b = 1 \; . \qquad (53a)$$

For a Gaussian form of $P(\mu_a)$ and $P(\mu_b)$ the above equation can be written as

$$\langle\mu\rangle = x\bar{\mu}_a + (1-x)\bar{\mu}_b. \qquad (54)$$

In the following sections, the average hyperfine field and the average magnetic moment for the investigated systems are determined by the above mentioned procedure.

4.1 Magnetic properties of amorphous $Fe_{1-x-x}B_x$ $(.15 \leq x \geq .26)$

The magnetic properties of amorphous metal-metalloid systems are governed mainly by the species and concentrations of the metallic elements. The presence of the metalloid atoms is thought mainly to stabilize the amorphous state. However, there is experimental evidence which indicates that the metalloid atoms notably affect the magnetic properties as well. Furthermore, the influence due to various kinds of metalloid elements appears to be quite different /98/. Binary systems, such as Fe-B, represent the simplest amorphous metal-metalloid systems.

In the present work amorphous $Fe_{1-x}B_x$ ($.15 \leq x \leq .26$) have been studied by ^{57}Fe Mössbauer spectroscopy between 300K and 4.2K (in some cases up to 6K). The results of this measurement will be first presented and then discussed.

Results

In table 4.1, the value of the average hyperfine fields, isomer shift, quadrupole splitting and relative width at 300, 77 and 4.2K (or 6K) for amorphous $Fe_{1-x}B_x$ alloys are given. Figs. 4.1a,b,c,d,e,f show some typical Mössbauer spectra of these alloys at different temperatures (namely, 300, 77 and 6K). In each case, the spectrum is composed of well defined but broadened lines with a relative width of about 20%. Such spectra are commonly observed in amorphous alloys in which the large number of inequivalent Fe sites causes a distribution of hyperfine fields. The fact that each of the six spectral lines shows no fine structure suggests that the P(HF) is continuous.

There are a number of ways in which one can obtain qualitative and quantative information about the P(HF) contained in the spectrum /104/. A Gaussian distribution of fields has been found as the best fit to the experimental data. The details of this method as applied to the spectra of amorphous alloys have been described in sect. 3. The solid curve for each spectrum represents the best fit using a Gaussian distribution for P(HF). In each case, a smooth and essentially structureless P(HF) has been found.

The line broadening and anisotropic distribution of intensities commonly observed in amorphous materials are

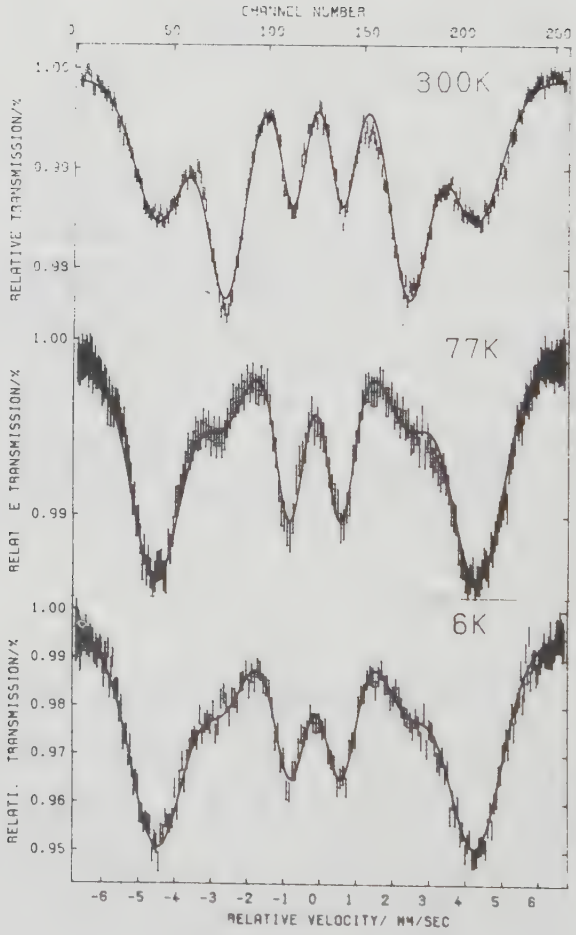

Fig. 4.1a: Magnetic hyperfine spectra of amorphous $Fe_{74}B_{26}$ at 300K, 77K, 6K, respectively

Table 4.1: Parameters obtained from analysis of Mössbauer effect data of $Fe_{100-x}B_x$ at 300, 77 and 6K

Fe	B	T/K	$\mu_o \cdot H^*$/T	I·S $^+$ mm/sec	Q·S(x10) mm/sec	$2\Delta H_o$/H_o %
74	26	300	24.95	0.095(1)	-0.002	20.0
		77	26.40	0.094(1)	-0.001	19.5
		6	26.58	0.095(1)	-0.001	20.0
76	24	300	24.85	0.085(2)	-0.005	20.5
		77	26.80	0.085(1)	-0.003	20.5
		4·2	27.20	0.086(1)	-0.003	20.5
78	22	300	26.42	0.071(2)	-0.001	21.0
		77	27.58	0.070(1)	-0.001	20.5
		6	27.90	0.071(2)	-0.001	19.0
80	20	300	26.25	0.043(1)	-0.003	21.5
		77	28.01	0.055(1)	-0.005	20.0
		6	29.08	0.059(1)	-0.002	21.5
82	18	300	26.85	0.047(1)	-0.002	20.5
		77	28.00	0.049(1)	-0.002	20.0
		4·2	29.50	0.050(2)	-0.001	20.5
84	16	300	25.97	0.043(1)	-0.003	19.5
		77	29.50	0.043(1)	-0.001	20.0
		4·2	30.02	0.045(1)	-0.001	20.5
85	15	300	26.06	0.035(1)	-0.002	20.5
		77	29.20	0.037(1)	-0.001	20.0
		-	-			
86	14	300	26.33	0.029(1)	-0.001	19.5
		77	29.84	0.030(2)	0.001	20.0
		4·2	30.50	0.030(1)	-0.002	20.0

$^+$ I.S. values are calculated with respect to α-Fe at room temperature. Figures in the paranthesis indicate the error in third place.

* Error in hyperfine field calculation ±0.20 T.

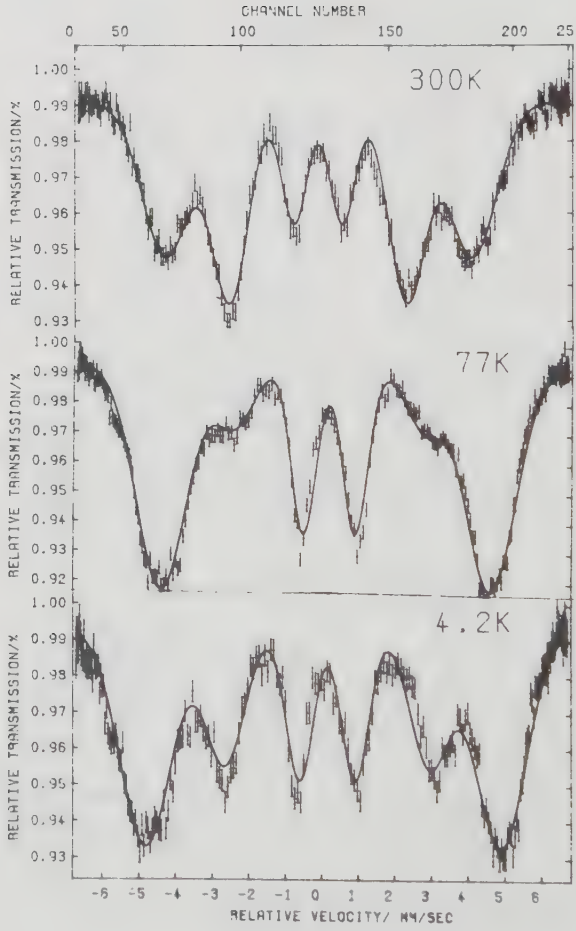

Fig. 4.1b: Magnetic hyperfine spectra of amorphous $Fe_{76}B_{24}$ at 300K, 77K, and 4.2K, respectively

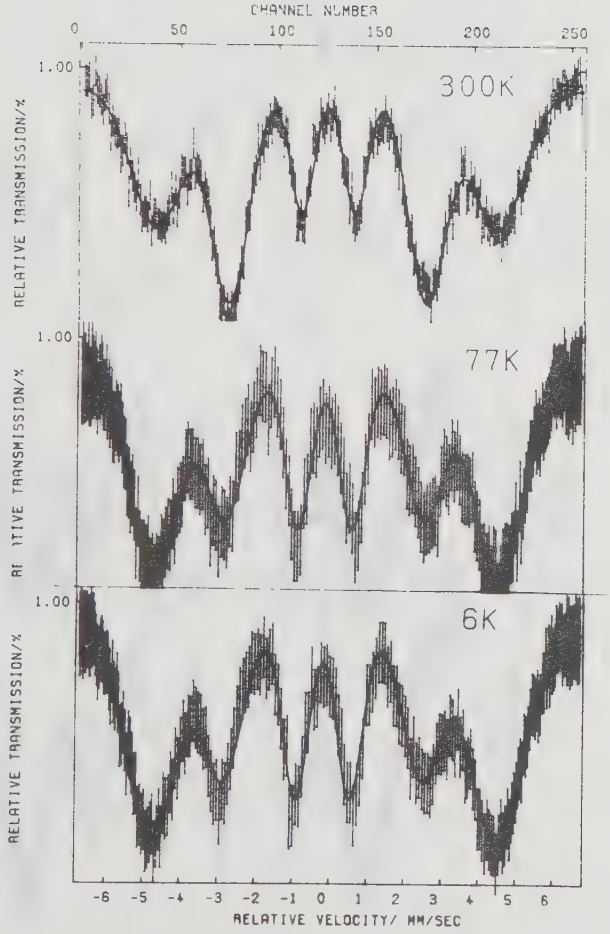

Fig. 4.1c: Magnetic hyperfine spectra of amorphous $Fe_{78}B_{22}$ at 300K, 77K, 6K, respectively

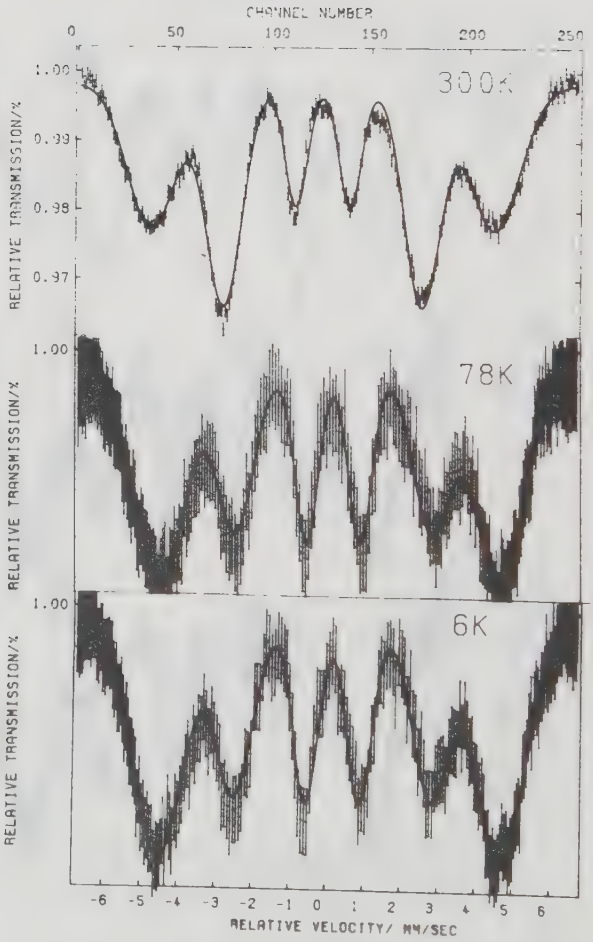

Fig. 4.1d: Magnetic hyperfine spectra of amorphous $Fe_{80}B_{20}$ at 300K, 78K, and 6K, respectively

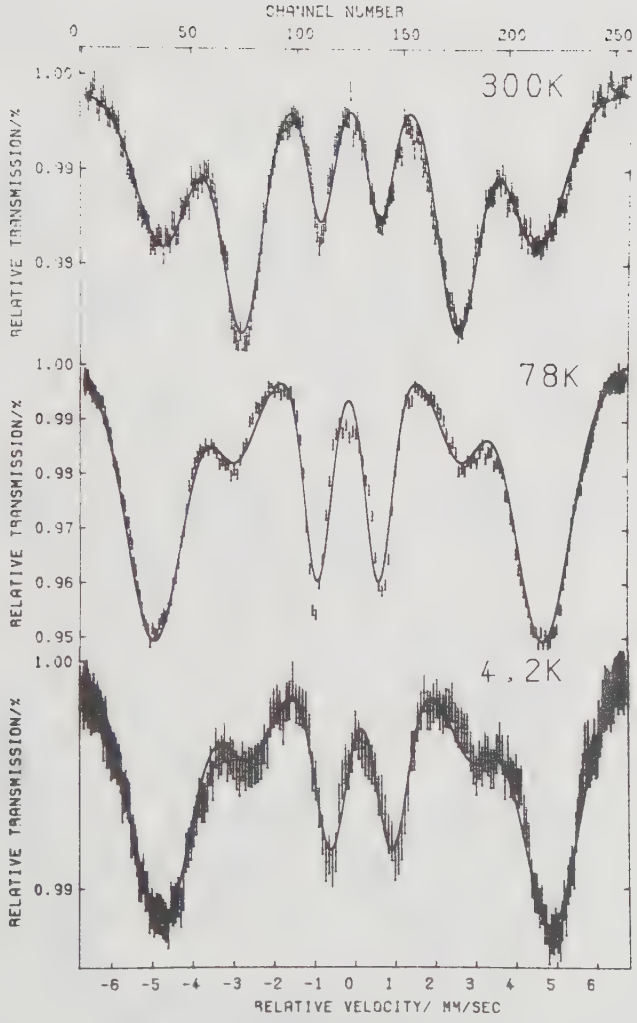

Fig. 4.1e: Magnetic hyperfine spectra of amorphous $Fe_{82}B_{18}$ at 300K, 78K, and 4.2K, respectively

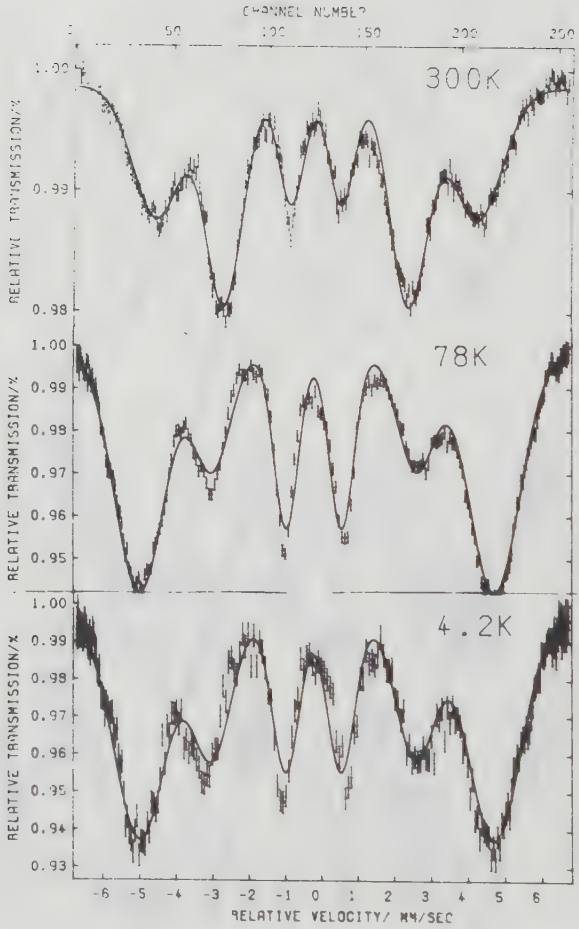

Fig. 4.1f: Magnetic hyperfine spectra of amorphous $Fe_{86}B_{14}$ at 300K, 78K, and 4.2K, respectively

characteristic for the measured spectrum. Contrary to the results reported by /106/, the anisotropy of the Mössbauer spectrum at 77K (4.2K) did not change drastically when the absorber was not under mechanical constraint. Thus, the changes in the anisotropy of the Mössbauer spectrum at lower temperatures observed in /106/ could be attributed to some kind of mechanical constraint acting through the high magnetostriction of these materials. In fact, by glueing the metglass strips to a non-metallic holder it was possible at 77K (or 4.2K) to obtain the dramatic changes in the anisotropy of the Mössbauer spectra as shown in Fig. 4.1. By decreasing the temperature to 77K (or 4.2K) the difference between the thermal expansion coefficients of the amorphous strips and the support could give rise to a compression in the plane of the anisotropy, could create on average a direction of easy magnetization making an angle with the ribbon plane.

Denoting with L_i the intensity of the lines in the sequence of increasing energy (from left to right in the recorded Mössbauer spectra) the intensity ratio I_3/I_1 is found to lie in the vicinity of 1/3, whereas I_2/I_1 changes drastically from about 1 at 300K to .33 at 77K for $Fe_{1-x}B_x$ alloys. From the intensity average ratios, the average angle between magnetization and gamma-ray direction can be known. The calculated values of this angle show that, at room temperature there is a strong tendency of the magnetization to lie in the ribbon plane whereas the intensity distribution at 77K (4.2K) for the glued samples points towards a strong tendency of the magnetization to orient itself perpendicular to the ribbon plane.

Fig. 4.2 shows the average hyperfine field as a function of boron concentration. At 77K average hyperfine field decreases linearly with the metalloid (B) concen-

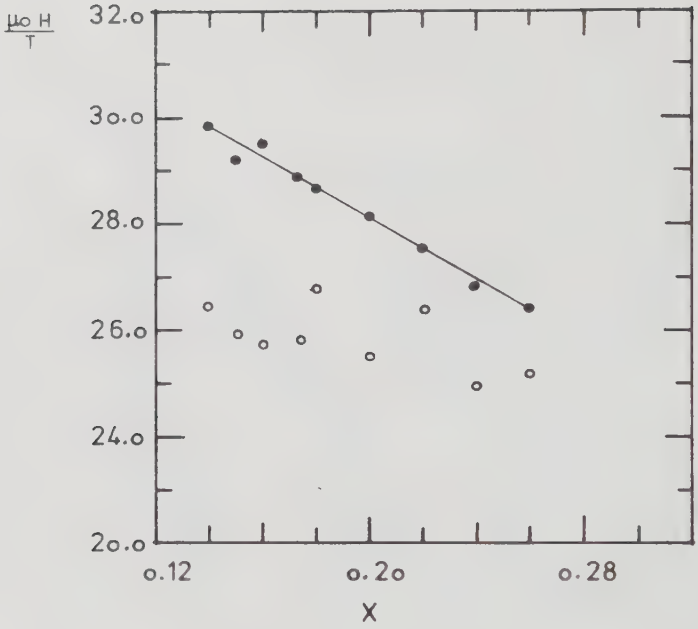

Fig. 4.2: Average hyperfine field versus x for $Fe_{1-x}B_x$ at 300K (O) and 77K (·)

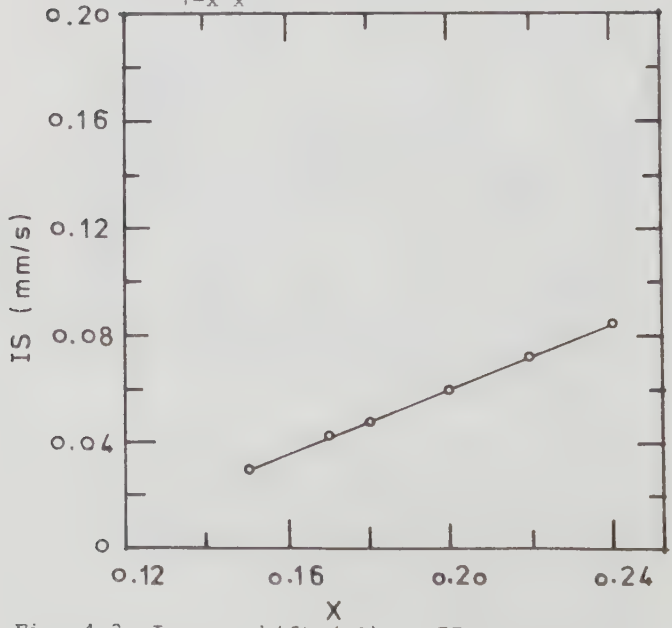

Fig. 4.3: Isomer shift (IS) at 77K versus x for $Fe_{1-x}B_x$

tration. But at room temperature, the average hyperfine field passes through a minimum around 15 at % boron.

The average isomer shift (relative to Fe at room temperature) of amorphous $Fe_{1-x}B_x$ alloys as a function of B concentration is shown in Fig. 4.3. The isomer shift increases smoothly with increasing boron concentration.

In Fig. 4.4 the average hyperfine field is plotted against the average magnetic moment of $Fe_{1-x}B_x$ alloys. The ratio of the hyperfine field and the magnetic moment in the investigated systems is $14T/\mu_B$, which is same as that in the intermetallic compounds /97/.

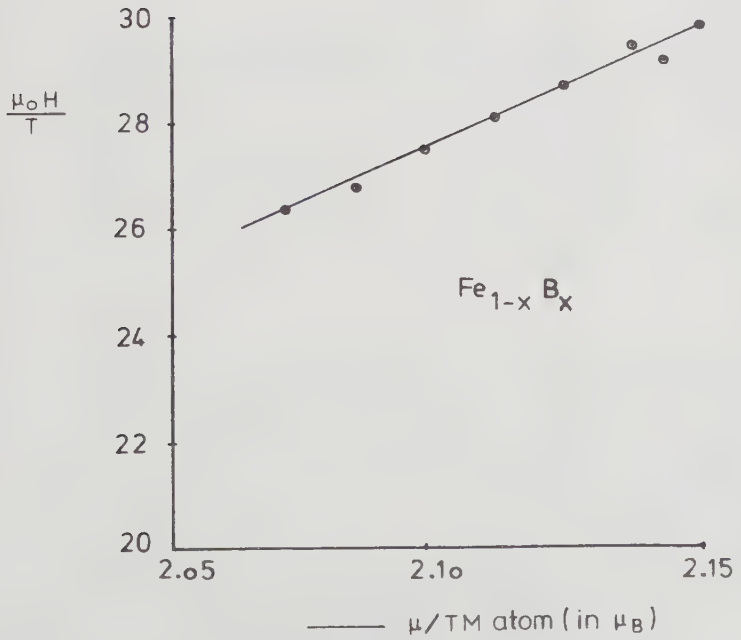

Fig. 4.4: Average hyperfine field as a function of average magnetic moment/TM atom for amorphous $Fe_{1-x}B_x$ alloys.

Table 4.2: Compositional dependence of Curie temperature 'T_C', saturation magnetization M(O) and coefficient B and Stiffness constant D for glassy ferromagnets $Fe_{100-x}B_x$.

Compound	B ($10^{-5}K^{-3/2}$)	D (MeV $A^{\cdot 2}$)	T_C [K]	D/T_C MeV $A^{\cdot 2}K^{-1}$	$\bar{\mu}$ (μ_B/TM)
$Fe_{88}B_{12}$	3.1	70±3	509	0.138	2.14
$Fe_{87}B_{13}$	3.4	66±3	531	0.124	2.13
$Fe_{86}B_{14}$	3.4	65±3	556	0.117	2.12
$Fe_{84}B_{16}$	3.4	66±3	598	0.110	2.12
$Fe_{82}B_{18}$	3.1	71±3	636	0.112	2.07
$Fe_{80}B_{20}$	2.6	83±3	647	0.128	2.00
$Fe_{78}B_{22}$	2.3	92±3	690	0.133	2.00
$Fe_{76}B_{24}$	2.2	96±3	723	0.133	2.00
$Fe_{72}B_{28}$	2.0	106±3	760	0.153	1.94
Fe	3.4[+]	286±11	1752[+]	0.27[+]	2.24*

[+] Ref. /135/

* Ref. /5/

Discussion

Average hyperfine field as a function of boron concentration

Because of the relatively high values of T_c for these amorphous alloys, the difference in the values of the average hyperfine field at 77K and at OK is expected to be not significant. Therefore, the average hyperfine field value at 77K is assumed to be the same as that extrapolated at OK.

The variation of the average hyperfine field with boron concentration can be interpreted in terms of the charge transfer model. In this model, the interaction between the transition metal and metalloid results in an electron transfer from the metalloid to the partially filled transition metal 3d-band. On this basis, the decrease in average hyperfine field with increase in B is due to filling of the d-band by the electrons donated by boron. The concentration dependence of the magnetic moment exhibit also similar trend /4/, (see table 4.2), therefore supporting the above statement.

Average magnetic moment versus average hyperfine field

It is well known that in crystalline Fe and intermetallic compounds (e.g., Fe_3C, Fe-B, Fe_2B and Fe_3P) the magnetic moment of Fe (μ_{Fe}) is, to a good approximation, proportional to the Fe hyperfine field, HF(Fe). For a wide range in the values of the moment, nearly constant ratios of $HF(Fe)/\mu_{Fe}$ from 13 to $14T/\mu_B$ have been found /97/. Such a proportionality is expected to hold in amorphous $Fe_{1-x}B_x$ alloys. However, since in amorphous ferro-

magnets the distribution of moments is usually not directly measured, one compares the average moment per Fe with the average hyperfine field. As shown in Fig. 4.2, $\overline{HF}$(Fe) for $Fe_{1-x}B_x$ decreases monotonically with B concentration. The values of μ_{Fe} for $Fe_{1-x}B_x$ reported by Hasegawa et al /107/ have been used in this work. $\bar{\mu}_{Fe}$ is found to decrease $\overline{HF}$(Fe). Using the average values of $\bar{\mu}_{Fe}$, the ratio $\overline{HF}/\mu_{Fe}$ is found to be nearly constant and equal to $14T/\mu_B$. Similar values of the ratio have been found in other amorphous Fe-metalloid systems /92/. The consistency of the ratio suggests that the Fe hyperfine field is to a good approximation proportional to its moments.

Isomer shift and Quadrupole splitting

Because of the temperature dependence of the isomer shift, meaningful comparison between samples with different B concentrations must be done at the same temperature. The isomer shift of amorphous $Fe_{1-x}B_x$ alloys at 77K is shown in Fig. 4.3 as a function of B concentration. The isomer shift decreases with increasing boron concentration. These isomer shift results can be interpreted in terms of a charge trnasfer model or by direct effects of changes in s-electron density with composition, both mechanism can be involved. In Fe-B amorphous alloys, the increase of isomer shift with increasing boron concentration suggests a tendency to an enhancement of the screening of the s-electrons at the Fe-nuclei owing to electron transfer from boron to the unfilled Fe d-band.

The fact that there is nor apparent quadrupole splitting (see table 4.1) can be explained in the same way as for Fe-Si amorphous alloys /8/, i.e., the values of the angle ϑ between the axis of the electric field gradient and the hyperfield axis are randomly distributed.

4.2 The influence of the metalloid elements (B,Si,C,Ge) on the magnetic properties of amorphous TM-M alloys

In this section, a systematic study of amorphous magnetic alloys, in which the composition of one type of glass former is varied at the cost of other metalloid, is undertaken. The general form of the composition can be written as $Fe_{80}M_{20-x}N_x$ where N=Si,C,Ge and M=B. In this work, the amorphous alloys have been studied by ^{57}Fe Mössbauer spectroscopy and magnetization measurements. Since these samples have only one magnetic constituent, that is, Fe, so the situation is somewhat favourable for understanding the effect of changing the metalloid concentration on the Fe magnetic moment and the Fe-Fe interactions.

Substitutions with tetravalent elements of the IVA column of the periodic table in the Fe-B amorphous alloys give rise to a change in the Mössbauer spectrum. Systematic studies of these effects have been performed on the following alloy systems at 300K and 77K.

i) $Fe_{80}B_{20-x}C_x$ x=2,4,6,8,10
ii) $Fe_{80}B_{20-x}Si_x$ x=2,4,6,8
iii) $Fe_{82}B_{18-x}Ge_x$ x=2,4,6.

In the binary amorphous systems $Fe_{100-x}B_x$ and $Fe_{100-x}P_x$ both the average magnetic moment per Fe-atom ($\overline{\mu}_{Fe}$) and the average value of the hyperfine field ($\overline{HF}$) at the ^{57}Fe nucleus decrease with the increase of the glass former concentration x, the decrease being faster in the case of $Fe_{100-x}P_x$ or when B is substituted with P in the ternary alloys $Fe_{100-x}(B,P)_x$ /32/. This behaviour was considered as evidence for electronic charge transfer from metalloid to iron d-band in connection with a rigid band model for the electronic states of the 3d-metals. The stronger decrease in the case of P substitution

in $Fe_{80}B_{20-x}P_x$ could be due to the transfer of three electrons from P to the Fe d-band instead of one in the case of B. Despite the advantage of its simplicity, the electron transfer model has to be considered as an approximate model only, as can be seen from the rather large variations in the values of the transferred electrons reported for the same element but in different compounds /4/ in Table 4.3. According to the electron transfer model, substitutions with tetravalent elements of the IV A column of the periodic table in the Fe-B amorphous alloys should give rise to a decrease of the Fe moment, intermediate between those given by B and P, since the tetravalent elements could transfer two electrons to the unfilled Fe-d-band. In some cases, e.g., C and Ge, the experimental results contradict the above prediction based on this model. In the following a detailed analysis of the results obtained on the above mentioned samples is given.

The Mössbauer spectra were taken at 300K and 77K and are typical for ferromagnetic amorphous alloys with broadened lines, due to the distribution of the hyperfine field. The spectra could be fitted to quasi-symmetric Gauss profiles after subtracting from the measured line-width, the natural and apparatus line broadening. The relative half intensity line width thus found is about 18-20%. In Fig. 4.5 (a,b) typical Mössbauer spectra of $Fe_{80}B_{20-x}C_x$ and $Fe_{80}B_{20-x}Si_x$ at 77K are shown. Fig. 4.6(a,b) shows the Mössbauer spectra of $Fe_{82}B_{18-x}Ge_x$ at 300K and 77K. It can be clearly seen that as the temperature is changed from 300K to 77K, the intensities of the lines 1,2,5 and 6 change which is associated with the change of direction of easy axis of magnetization. This directional change of the easy axis is due to the thermally produced stresses. Fig.4.7(a,b) shows the plot of average hyperfine field and of the isomer shift (IS) of the three investigated systems as a function of the concentration (x) of the tetravalent elements C, Si and Ge at 300K and 77K. The

Table 4.3: Electrons transferred from the metalloids in amorphous alloys based on rigid band model

Alloy	B	C	Si	P	References
Fe-Ni-P-B	0.3			1.0	Becker et al (1977)
Fe-Ni-B	1.2*			2.1	*Becker et al (1977)
Fe-P-B	1.4			1.6	Durand and Yung (1977)
Fe-Co-B-P	1.6			2.4	O'Handley et al (1976a)
Fe-Ni-B-P					
Co-P				5	Kanabe and Kanematsu (1968)
				2	Cargill and Cochrane (1974)
				<5	Pan and Turnbull (1974)
				<5	Simpson and Brambley (1971)
CoBP,FeBP	1	2	2	3	Yamauchi and Mizoguchi (1975)
FeCP,NiBP					

* Moment of transition metal varies linearly with alloy conc.

Table 4.4: MS parameters for $Fe_{82}B_{18-x}Ge_x$, $Fe_{80-x}B_{20-x}C_x$ and $Fe_{80}B_{20-x}Si_x$

Fe	B	Ge	$\frac{T}{H}$	$\frac{\mu_o.H^*}{T}$	I.S. * (mm/s)	Q.S. (x10) (mm/s)	$\frac{2\Delta H_s}{H}$
80	20	-	300	26.3	0.042(1)	-0.003	18
			77	28.1	0.046(1)	-0.005	18.5
82	16	2	300	25.8	0.089(2)	-0.006	18.2
			77	29.3	0.104(2)	-0.005	18.4
82	14	4	300	28.3	0.091(1)	-0.004	18.5
			77	29.6	0.129(1)	-0.000	18.0
81	12	6	300	28.6	0.113(2)	-0.000	18.6
			77	29.8	0.151(1)	-0.009	18.5
Fe	B	C					
80	20	-	300	26.3	0.042(1)	-0.003	18
			77	28.1	0.046(1)	-0.005	18.5
80	18	2	300	27.5	0.104(1)	-0.006	18.0
			77	27.7	0.073(1)	-0.005	19.0
80	16	4	300	27.7	0.104(2)	-0.006	20.0
			77	28.0	0.089(1)	-0.007	20.0
80	14	6	300	27.5	0.103(2)	-0.006	19.5
			77	28.5	0.111(2)	-0.001	19.5
80	12	8	300	27.7	0.125(1)	-0.009	20.2
			77	28.6	0.128(2)	-0.006	20.5
80	10	10	300	27.7	0.130(1)	-0.001	20.0
			77	28.7	0.146(1)	-0.007	19.0
Fe	B	Si					
80	20	-	300	26.3	0.042(1)	-0.003	18
			77	28.1	0.046(1)	-0.005	18.5
80	19	1	300	25.2	0.060(1)	-0.006	19.5
			77	28.6	0.056(1)	-0.004	19.0
80	18	2	300	25.1	0.067(2)	-0.008	19.5
			77	28.1	0.060(1)	-0.008	20.0
80	16	4	300	25.3	0.084(3)	-0.000	20.5
			77	28.0	0.066(1)	-0.001	20.0
80	15	5	300	24.7	0.082(1)	-0.000	21.2
			77	27.7	0.071(1)	-0.001	20.6
80	14	6	300	24.9	0.088(2)	-0.005	19.2
			77	27.6	0.075(1)	-0.008	19.5
80	12	8	300	25.3	0.113(2)	-0.005	20.0
			77	27.4	0.081(1)	-0.000	20.5

* I.S. values are calculated with respect to α-Fe at room-temperature. Figures in the paranthesis indicate the error in third place. Error in hyperfine field calculation ±0.25T.

Table 4.5*: Magnetic moments (in μ_B) at 77K and OK of $Fe_{80}B_{20-x}C_x$ (x=2,4,6,8,10), $Fe_{80}B_{20-x}Si_x$ (x=1,2,4,6,8) and $Fe_{82}B_{18-x}Ge_x$ (x=2,4,6), respectively.

Fe	B	C	μ(in μ_B)/Fe atom at 77K	$\mu(\mu_B)$/Fe atom at OK
80	20	-	2.11	2.09
80	18	2	2.09	2.09
80	16	4	2.07	2.07
80	14	6	2.06	2.06
80	12	8	2.04	2.04
80	10	10	2.03	2.04
Fe	B	Si		
80	20	-	2.11	2.09
80	19	1	2.11	2.09
80	18	2	2.11	2.10
80	16	4	2.12	-
80	15	5	2.09	-
80	14	6	2.08	-
80	12	8	2.00	-
Fe	B	Ge		
82	18	-	2.13	-
82	16	2	2.05	-
82	14	4	2.08	
82	12	6	2.13	-

* Ref. /4/.

values of μ_{Fe} measured at 77K by Luborsky et al /4/ are also shown. Since all the investigated systems have Curie temperatures lying well above 77K, the values of $\overline{HF}$ and μ_{Fe} at 77K will not differ practically from that at OK. That is the reason why the 77K data are the most relevant for the subsequent discussion.

The analysis of the results can be formulated in the following way:

1. The conduction electron polarization contribution to the hyperfine field appears to be very negligible in these cases, like in the crystalline Fe-metalloid compounds. This leads to a proportionality between the magnetic moment and the hyperfine field. In case of crystalline Fe-metalloid compounds, the ratio H/μ_{Fe} is found to be constant for a large number of compounds. It is likely that such a proportionality also holds for amorphous magnetic Fe-metalloid alloys. In case of symmetric Gaussian hyperfine field distribution $\overline{HF}$ equals the mean value of HF and therefore

$$\overline{HF} = A\ \mu_{Fe}$$

where A can be considered as constant in a given compositional series.

2. According to the electron transfer model the substitution of B with tetravalent metalloids has to decrease μ_{Fe} and therefore $\overline{HF}$ with increasing metalloid concentration (x). As a matter of fact, in the case of $Fe_{80}B_{20-x}C_x$, an amount of 2% C leads to a decrease of both μ_{Fe} and $\overline{HF}$, but for values of x up to 10%, μ_{Fe} decreases whereas $\overline{HF}$ increases with x. In the case of $Fe_{82}B_{18-x}Ge_x$, after an initial decrease of μ_{Fe} at 2% Ge, both μ_{Fe} and $\overline{HF}$ increase with x. The only case of behaviour according to the observations 1 and 2 occurs for $Fe_{80}B_{20-x}Si_x$ where both μ_{Fe} and $\overline{HF}$ decrease with increase of x.

On the other hand, for all the investigated systems, the isomer shift increases with 'x' with slopes of about 0.01, 0.003 and 0.015 mm/sec. for (i), (ii) and (iii), respectively. An increase of I.S. means either an increase in the 3d-electron density or a decrease in the 4s electron density; the former possibility being in qualitative agreement with an electron transfer from the tetravalent elements to the unfilled d-band of iron. Such a transfer implies on the other hand a decrease of μ_{Fe} and so a decrease of $\overline{HF}$ with increasing x. But this trend occurs only in the case of the substitution with Si. For C and Ge substitutions, both $\overline{HF}$ and IS increase with 'x'. This paradox can be resolved when it is recognised that B and C have atomic sizes smaller than Fe and hence can occupy the holes of a dense random packing of Fe atoms, whereas P, Si, Ge with atomic sizes larger than Fe can occupy substitutional sites. The above statement is consistent with the fact that the density of the amorphous alloys with B is larger than those with P /104/. Thus the observed behaviour of average hyperfine field (and the average magnetic moment) as a function of metalloid concentration can be attributed to a "size effect".

If Ge replaces Fe substitutionally, the strongest influence on IS observed in the case of Ge could then be due to the disturbance in the $4s^2$ electrons around the Fe atoms caused by screening the Ge extra charge. In the present case, it appears that μ_{Fe} is not disturbed and the slight increase of $\overline{HF}$ could be due to a change in the hyperfine constant A because of the disturbance of the 4s-electrons. On the other hand, Si, which is only slightly smaller than Ge, seems to disturb more strongly the Fe-moment, through a stronger involvement of the 3d-electrons of 'Fe' in the chemical bonding.

The influence of the metalloid elements on the magnetic proporties have also been studied by C.L. Chien et al /92/. It is observed that a change of the metalloid spe-

cies, transition metal concentration being fixed, has a large effect on the Curie temperature. An increase of about 200K in T_c value has been found when phosphorous in $Fe_{40}Ni_{40}P_{20}$ has been replaced by B. In $Co_{75}Si_{25-x}B_x$ glasses, T_c is found to increase as boron replaces silicon /5/. Similarly, it is found that T_c of $Fe_{80}B_{20}$ is much higher than that of $Fe_{80}P_{20}$ /32/. Thus higher T_c values observed in boron rich samples suggest that the type of metalloid noticeably affects the average exchange interactions between the transition metal elements. The rapid increase of Curie temperature when boron is replaced by germanium may be attributed to the effect of the large size of the Ge on the Fe-Fe co-ordination and interatomic distance. Thus it is concluded that interstitial substitutions decrease magnetic moments whereas substitutional additives improve it, provided their atomic radii are not too much different from their host atoms.

On the basis of charge transfer model /48/ one can estimate the number of electrons of transferred by each metalloid. However, it is found that the number of transferred electrons from C, Si and Ge is not constant but different inspite of the same number of outer electrons (s^2p^2). This fact clearly shows that the magnetic moment of amorphous iron based alloys can be not explained only on the basis of charge transfer model but instead the factors such as the size of the metalloid atoms and the short range order variations must also be taken into account.

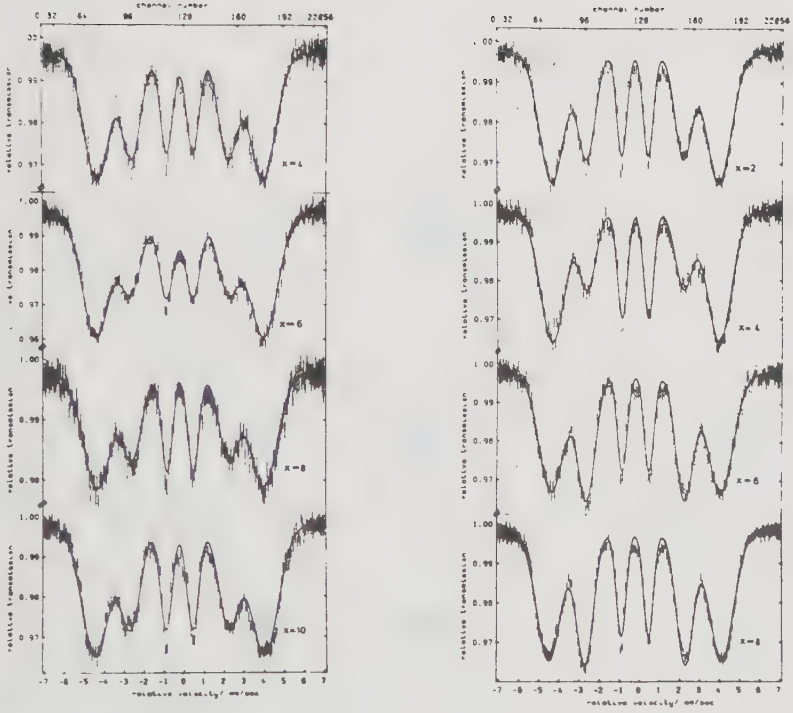

(a) (b)

Fig. 4.5: Mössbauer spectra of $Fe_{80}B_{20-x}C_x$ (a) and $Fe_{80}B_{20-x}Si_x$ (b) at 77K

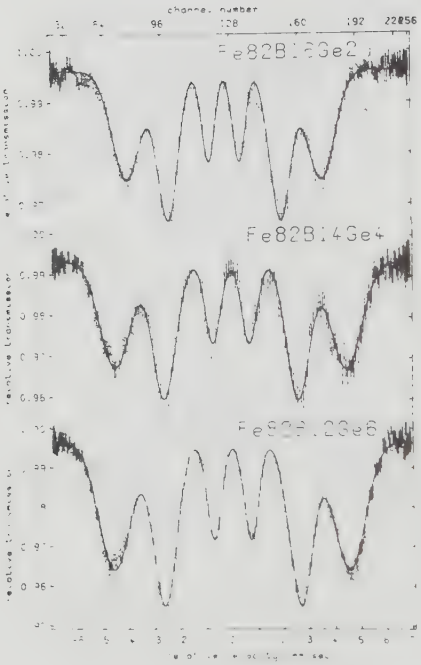

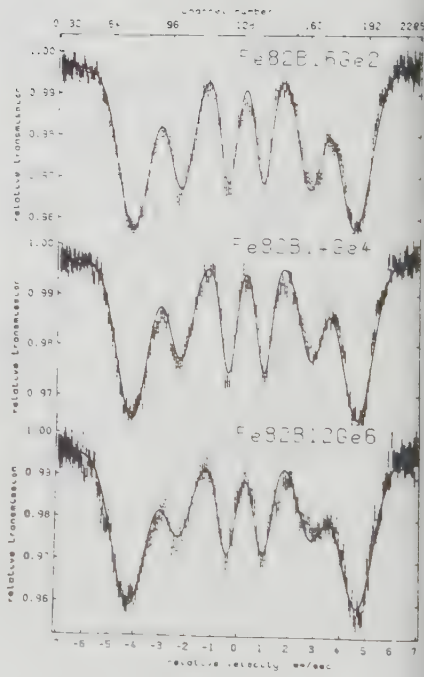

(a) (b)

Fig. 4.6: Mössbauer spectra of $Fe_{82}B_{18-x}Ge_x$ at 300K (a) and 77K (b)

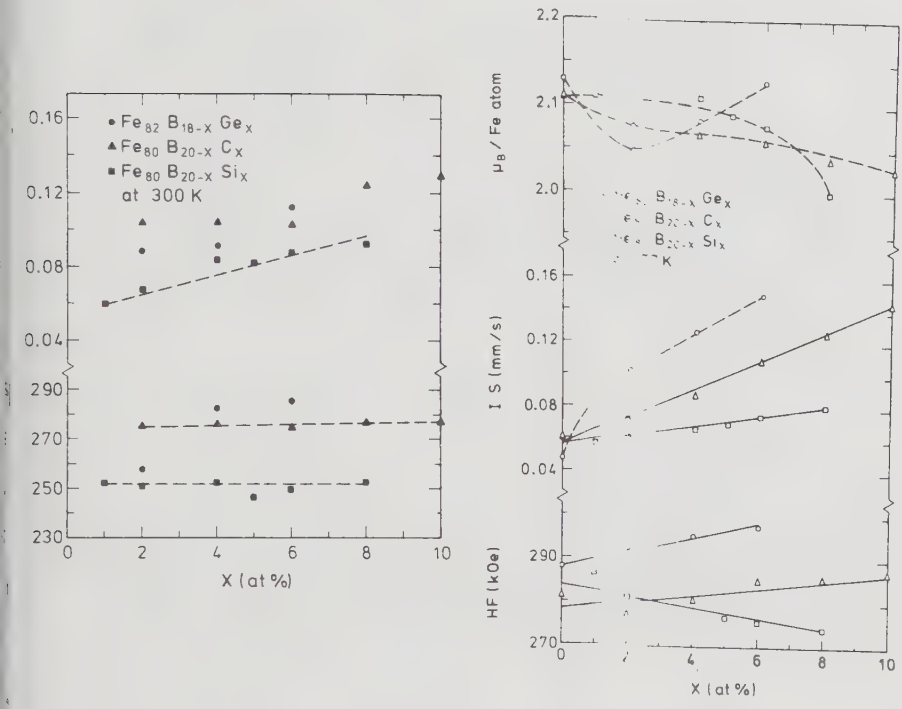

(a) (b)

Fig. 4.7: Plot of hyperfine field and IS versus concentration at 300K (a) and 77K (b) according to table 4.4 . Also the dependence of average magnetic moment on metalloid concentration are shown after ref. /4/.

4.3 Influence of transition metal atoms Ni and Co on the magnetic properties of the amorphous ferromagnetic TM-M alloys

The advantage of studying amorphous alloys of the type $(TM'_{1-x}TM''_x)_{100-x}X_y$, where TM′ and TM″ are 3d-transition metals and X a glass for B,Si,Ge or P, is that for a given value of y one can vary the transiton metal composition continuously ($0 \leq x \leq 1$) to prepare homogeneous alloys without any complications arising from structural phase transitions.

In the following, the results of the systematic studies on the amorphous systems

i) $(Fe_xNi_{1-x})_{80}B_{20}$
ii) $(Fe_xNi_{1-x})_{80}B_{19}Si_1$
iii) $(Fe_{1-x}Ni_x)_{75}B_{25}$ and $(Fe_{1-x}Co_x)_{80}B_{20}$

using both Mössbauer and magnetic measurements will be first presented and then discussed.

Results

A. Average magnetic moment per TM atom as a function of iron concentration

A Mössbauer and magnetic study of the amorphous systems $(Fe_xNi_{1-x})_{80}B_{20}$ $(.25\leq x\leq 1)$, $(Fe_1Ni_{1-x})_{80}B_{19}Si_1$ $(.125\leq x\leq .2)$, $(Fe_{1-x}Ni_x)_{75}B_{25}$ $(0\leq x\leq .7)$ and $(Fe_{1-x}Co_x)_{80}B_{20}$ $(0\leq x\leq .75)$ in the temperature range 4.2-300K has been undertaken. Results of the measurements are summarised as follows.

$(Fe_xNi_{1-x})_{80}B_{20}$ $(.25\leq x\leq 1)$, $(Fe_xNi_{1-x})_{80}B_{19}Si_1$ $(.125\leq x\leq .2)$ and $(Fe_{1-x}Ni_x)_{75}B_{25}$ $(0\leq x\leq .7)$.

In table 4.6, 4.7, 4.8 and 4.9 are given the values of the Curie temperature (T_c), magnetic moment per transition metal atom at OK in μ_B, density (ρ), the saturation magnetization M(O) at OK, the spin wave parameters, B and D and the range of exchange interaction (D/T_c) for the amorphous $(Fe_xNi_{1-x})_{80}B_{20}$, $(Fe\ Ni)_{80}B_{19}Si_1$ and $(Fe\ Ni)_{75}B_{25}$ alloys.

The dependence on composition of the low temperature average magnetic moment ($\bar{\mu}$) per transition metal atom is given in Fig. 4.8,4.9. Values of the average magnetic moment ($\bar{\mu}$) for $(Fe\ Ni)_{80}B_{20}$ and $(Fe\ Ni)_{80}B_{19}Si_1$ amorphous alloys reported by Kaul /108/ (and also /104/) have also been included in table 4.6 for comparison. It can be seen from Fig. 4.9 that the decrease of $\bar{\mu}$ with Fe becomes steeper on the Ni-rich side, this behaviour being similar to that reported by Durand /18/ for $\bar{\mu}(x)$ of the amorphous $(Fe\ Ni)_{79}P_{13}B_8$ alloys. Accordingly, the magnetic moment per Ni-atom in amorphous $Ni_{80}B_{20}$ should be much smaller than that given by the extrapolation of $\bar{\mu}(x)$ from the iron rich side.

Table 4.6:Magnetization and spin-wave parameters, density (ρ) and Curie temperature (T_C) for amorphous $(Fe_xNi_{1-x})_{80}B_{20}$ and crystalline Fe and Ni

Compound	$M_s(o)$ (emu/g)	B $10^{-5}K^{-3/2}$	D ^{*1} meV·A·^{2}	T_C [K]	D/T_C meV·A·$^2K^{-1}$	ρ (g/cm^3)	$\bar{\mu}$ (μ_B/TM)
$Fe_{80}B_{20}$	199.7$^+$	1.92[a]	99.7[a]	647[3]	0.151	7.39[b][1]	2.095[a]
	201.0 [2]	1.90[a]	100.0[7]	651[2]			2.109[a]
		2.2[5]MS	80.83[9]	685[5]			1.990[1]
		2.6[6]	83.00[6]				2.090[7]
		2.0[a]	97.97[f]				1.980[2]
$Fe_{70}Ni_{10}B_{20}$	182.0[a]	1.11[a]	152[a]	733[2]	0.209	7.46[b][1]	1.90[1]
		1.12[a]	153[f]				1.86[2]
							1.92[a]
$Fe_{60}Ni_{20}B_{20}$	159.5[a]	0.99[a]	177[a]	738[2]	0.240	7.53[b][1]	1.750[1]
		1.02[a]					1.690[2]
							1.694[a]
$Fe_{50}Ni_{30}B_{20}$	141.6[a]	1.05[a]	183[a]	725[2]	0.252	7.65[b][1]	1.55[1]
		1.08[a]					1.52[2]
							1.513[a]

Table 4.6: contd.

Compound	$M_s(o)$ (emu/g)	B $10^{-5}K^{-3/2}$	D *1 meV·A·2	T_c [K]	D/T_c meV·A·$^2K^{-1}$	ρ (g/cm^3)	$\bar{\mu}$ (μ_B/TM)
$Fe_{40}Ni_{40}B_{20}$	121.5[a]	2.27[a]	121[a]	662[1]	0.182	7.72[b][1]	1.305[a]
	129.0**	2.32[a]	160[9]	669[2]	0.210		1.290[1]
	121.4[a]	1.75**	140**		0.241		1.310[2]
			121.3[f]				
$Fe_{30}Ni_{50}B_{20}$	101.5[a]	2.76[a]	118.0[a]	575[a]	0.209	7.83[b][1]	1.095[a]
	101.2	2.72[a]	120.0[f]	573[10]			1.060[1]
		2.80[a]					
$Fe_{20}Ni_{60}B_{20}$	73.45[a]	5.09[a]	97[a]	415[a]	0.234	7.94[b][1]	0.80[a]
	72.66[a]	5.13[a]	97.2	419 }[4]			0.79[a]
		5.30[a]	80	404			0.78[1]
		3.26[a] M·S					
$Fe_{16}Ni_{64}B_{19}Si_1$	61.5[a]	7.5[a]	84[a]	349[4]	0.242	7.96[c][4]	0.67[a]
	61.2[a]	7.6[a]	85.6[+]	358[4]		7.98[d]	
		6.8[a] M·S					
$Fe_{13}Ni_{67}B_{19}Si_1$	54.1[a]	12.15[a]	66[a]	288[4]	0.235	7.98[c][4]	0.59[a]
	53.9[a]	12.30[a]	67.8[f]			8.01[d]	
		5.78[a] M·S					

Table 4.6: contd.

Compound	$M_s(o)$ (emu/g)	B $10^{-5}K^{-3/2}$	D *1 meV·A·2	T_C [K]	D/T_C meV·A·2 K^{-1}	ρ (g/cm^3)	$\bar{\mu}$ (μ_B/TM)
$Fe_{10}Ni_{70}B_{29}Si_1$	41.5[a]	21.4[a]	54[a]	212[a]	0.258	8.03[c][4]	0.45[a]
	41.3[a]	22.0[a]	54.8[f]	213[4]		8.04	
		20.4[a] M·S					
Fe	-	3.4[e]	286[11]	1043[e]	0.27[e]	-	2.24
Ni	-	7.5[e]	397[7]	631[e]	0.64[e]	-	0.60

a) present work (H=3 T) [1,3] Ref. /104/
b) experiment [2] Ref. /5/
c) calculated [4] Ref. /98/
d) calculated by extrapolation from values (1) [5] Ref. /106/
e) after Argyle, Charap, Pugh, Phys. Rev. 132(5)2051(1963) [6,7,8,10] Ref. /14/
f) D values with different 'g' factor [9] Ref. /111/
\+ samples from Nielson [7,11] Ref. /108/
*2 Allied chemicals
** samples IWE, RUB
*1 calculated considering g=2.05

Table 4.7: Mössbauer parameters for $(FeNi)_{80}B_{20}$, $(FeNi)_{80}B_{19}Si_1$ and $(FeNi)_{80}P_{14}B_6$ at 300, 77, 20 and 4.2K.

Compound					$\frac{T}{K}$	$\frac{\mu_o \cdot H^*}{T}$	$\frac{I \cdot S}{mm/sec}$	$\frac{Q \cdot S (x10)}{mm/sec}$	$\frac{2\Delta H_{\frac{1}{2}}}{H}$
Fe	Ni	P	B	Si					
80	-	-	20	-	300	26.25	0.045(1)	-0.002	20
					77	28.01	0.052(1)	-0.003	20
					20	28.50	0.054(1)	-0.001	20
					4.2	29.00	0.055(1)	-0.005	20
70	10	-	20	-	300	25.70	0.044(1)	-0.001	19.5
					77	27.74	0.043(1)	-0.001	19.0
					20	28.35	0.045(1)	-0.001	20.0
					4.2	28.54	0.046(2)	-0.001	19.5
60	20	-	20	-	300	25.10	0.059(1)	-0.002	19.5
					77	27.20	0.058(1)	-0.005	19.5
					20	27.63	0.059(1)	-0.003	20.0
					4.2	27.95	0.061(2)	-0.001	20.5
50	30	-	20	-	300	24.70	0.075(1)	-0.003	20.1
					77	26.50	0.079(1)	-0.001	20.5
					20	27.34	0.079(1)	-0.001	20.0
					4.2	27.60	0.078(1)	-0.001	20.0
40	40	-	20	-	300	23.30	0.070(2)	-0.007	19.0
					77	26.98	0.071(1)	-0.006	18.5
					20	27.21	0.072(1)	-0.001	20.0
					4.2	27.38	0.071(1)	-0.001	21.0
30	50	-	20	-	300	21.50	0.088(1)	-0.001	20.0
					77	25.30	0.088(2)	-0.001	20.0
					20	26.82	0.085(1)	-0.001	19.5
					4.2	27.20	0.088(2)	-0.001	20.0
20	60	-	20	-	300	19.57	0.090(1)	-0.005	20.5
					77	25.25	0.091(1)	-0.003	19.5
					20	26.27	0.092(2)	-0.004	20.5
					6	26.48	0.090(1)	-0.001	20.0
16	64	-	19	1	300	16.50	0.140(1)	-0.005	19.0
					77	23.80	0.138(2)	-0.002	19.5
					6	25.10	0.141(2)	-0.001	19.5
13	67	-	19	1	300	-	0.144(2)	-0.053	20.0
					77	21.45	0.135(1)	-0.002	20.5
					20	22.05	0.140(1)	-0.002	20.0
					6	22.65	0.143(2)	-0.004	20.0

Table 4.7: contd.

Compound Fe	Ni	P	B	Si		$\mu_o \cdot H^*$ / T	I·S [+] / mm/sec	Q·S(x10) / mm/sec	$2\Delta H_{\%}$ / H
10	70	-	19	1	300	-	.150(1)	0.054	19.5
					77	18.25	0.149(1)	-0.001	19.0
					20	21.20	0.150(1)	-0.002	18.5
					6	21.30	0.153(2)	-0.001	19.0
80	-	14	6	-	300	26.12	0.160(1)	-0.004	19.5
					77	27.72	0.158(1)	-0.002	19.0
					20	28.00	0.161(2)	-0.001	19.5
					4.2[a]	29.50	0.160(1)	-0.001	19.5
70	10	14	6	-	300	24.70	0.137(1)	-0.002	20.0
					77	27.81	0.139(1)	-0.004	20.5
					4.2[a]	29.00	0.141(2)	-0.001	20.0
60	20	14	6	-	300	23.84	0.171(2)	-0.003	20.0
					77	26.34	0.169(1)	-0.001	20.0
					20	27.13	0.171(2)	-0.001	20.0
					4.2[a]	28.30	0.172(1)	-0.002	20.1
40	40	14	6	-	300	20.79	0.152(1)	-0.001	20.5
					77	26.61	0.150(1)	-0.002	19.5
					20	26.93	0.145(2)	-0.001	20.0
					4.2[a]	27.6	0.149(1)	-0.001	20.5
30	50	14	6	-	300	18.46	0.140(2)	-0.004	20.0
					77	25.49	0.142(1)	-0.001	20.0
					20	26.70	0.140(1)	-0.002	20.5
					4.2[a]	27.00	0.144(2)	-0.001	20.0
20	60	14	6	-	300	-	0.157(1)	-	-
					77	21.74	0.158(2)	-0.002	19.5
					4.2[a]	25.5	0.157(1)	-0.001	20.0
10	70	14	6	-	300	-	0.194(1)	-0.054	-
					77	-	0.193(1)	0.054	19.5
					4.2[a]	24.33	0.194(2)	-0.001	20.0

[+] I.S. values are calculated with respect to α-Fe at room temperature. Figures

[*] Errors in hyperfine field calculation ±0.25 T.

[a] Ref. /73/

Table 4.8: Fitting parameters of the Mössbauer spectra of $(Fe_{1-x}Ni_x)_{75}B_{25}$ at 300, 77 and 6 K respectively

Compound			T	$\mu_o \cdot H^*$	I·S +	Q·S(x10)	$2\Delta H_{\frac{1}{2}}$
Fe	Ni	B	K	T	mm/s	mm/sec	H
75	-	25	300	24.38	0.107(1)	-0.001	19.4
			77	27.17	0.109(1)	-0.006	20.9
			6	27.28	0.124(1)	-0.001	19.8
67.5	7.5	25	300	24.29	0.119(1)	-0.002	18.5
			77	26.64	0.143(2)	-0.002	19.0
			6	26.74	0.139(1)	-0.006	19.2
60	15	25	300	23.62	0.153(1)	-0.003	20.0
			77	25.85	0.153(1)	-0.008	20.0
			6	25.91	0.152(1)	-0.005	20.0
52.5	22.5	25	300	23.18	0.157(2)	-0.001	20.7
			77	25.69	0.167(1)	-0.001	20.5
			6	25.68	0.169(1)	-0.001	20.0
45	30	25	300	22.03	0.178(2)	-0.002	20.7
			77	25.04	0.180(2)	-0.001	20.5
			6	25.10	0.182(1)	-0.001	20.0
37.5	37.5	25	300	21.15	0.189(1)	-0.002	22.1
			77	24.65	0.193(1)	-0.003	22.0
			6	24.75	0.195(1)	-0.001	22.0
30	45	25	300	18.62	0.206(1)	-0.001	21.3
			77	23.76	0.207(1)	-0.001	20.0
			6	23.85	0.208(1)	-0.001	20.0
22.5	52.5	25	300	13.98	0.215(1)	-0.001	20.9
			77	22.98	0.219(1)	-0.003	20.5
			6	23.05	0.221(1)	-0.002	20.8

+ I.S. values are calculated with respect to α-Fe at atom temperature. Figures in the paranthesis indicate the error in third place.

* Error in hyperfine field calculation ±0.25 T.

Table4.9:Magnetization and spin-wave parameters, density (ρ), g-factor, Curie temperature (T_c) and range of exchange interaction (D/T_c) for amorphous $(Fe_{1-x}Ni_x)_{75}B_{25}$.

Compound	$Bx10^{-5}$ $K^{-3/2}$	$M(o)\frac{emu}{g}$	$\rho(g/cm^3)$	$\sim g$	D meV $A^{\cdot 2}$	$\bar{\mu}/TM_{atom}$ (μ_B)	T_c* [K]	D/T_c (meV $A^{\cdot 2}K^{-1}$)
$Fe_{75}B_{25}$	1.28±0.06	182.3±5.8	7.19+	2.08	142(143)	1.99±0.06	723	0.195
$Fe_{67.5}Ni_{7.5}B_{25}$	1.1 ±0.1	174.3±0.1	7.28	2.08	160(162)	1.87±0.03	715.4	0.223
$Fe_{60}Ni_{15}B_{25}$	1.1 ±0.1	162.9±0.1	7.34	2.085	166.5(168)	1.75±0.04	707.7	0.234
$Fe_{52.5}Ni_{22.5}B_{25}$	1.35±0.1	144.1±0.03	7.45	2.085	156(158)	1.56±0.03	692	0.225
$Fe_{45}Ni_{30}B_{25}$	1.7 ±0.1	128.3±0.1	7.53	2.09	144(146)	1.39±0.03	669	0.215
$Fe_{37.5}Ni_{37.5}B_{25}$	2.1 ±0.1	110.5±0.1	7.61	2.105	137(139)	1.21±0.03	615.4	0.223
$Fe_{30}Ni_{45}B_{25}$	3.45±0.1	91.8±0.2	7.70	2.115	110(112)	1.01±0.03	538.5	0.204
$Fe_{22.5}Ni_{52.5}B_{25}$	5.8 ±0.3	70.5±0.1	7.78	2.12	92(94)	0.78±0.02	415.4	0.222

( ) values are calculated considering the value of g

* I. Vincze et al, KFKI 1980-90, Budapest

In case of $(Fe\ Ni)_{75}B_{25}$, Fig. 4.10 shows that $\bar{\mu}$ decreases linearly with increasing Ni concentration. The decrease in the entire range is about 60%.

$(Fe_{1-x}Co_x)_{80}B_{20}$ $(0 \leq x \leq .75)$

Fig. 4.8 and table 4.10 show $\bar{\mu}$, the average moment per TM atom for $(Fe_{1-x}Co_x)_{80}B_{20}$ series as a function of transition metal content. Values of the average magnetic moment for these amorphous alloys reported by O'Handley /106/ previously have also been included both in Fig. 4.8 and table 4.10 for comparison. Both the room temperature and the saturation magnetization at OK are in good agreement with the results of reference /104/.

Table 4.10: Average magnetic moment/TM atom, magnetization at 300K and densities of amorphous $(Fe_{1-x}Co_x)_{80}B_{20}$ alloys

x	$\bar{\mu}$ (μ_B/TM atom)		M(300K) (emu/qm)	ρ* (qm/cm^3)
0	1.99		170	7.39
0.125	2.00	2.10*	176	7.46
0.25	1.98	2.00*	174	7.52
0.375	1.95	1.93*	165	7.59
0.500*	1.79		155	7.70
0.625	1.65	1.66*	145*	7.84
0.750	1.52	1.55*	131	7.93
0.875*	1.41*		122*	8.06
1.000*	1.27*		111*	8.22

*R.C. O'Handley et al, Appl. Physics Letters, Vol. 29, No.6, 1976, page 330-332 /A/.

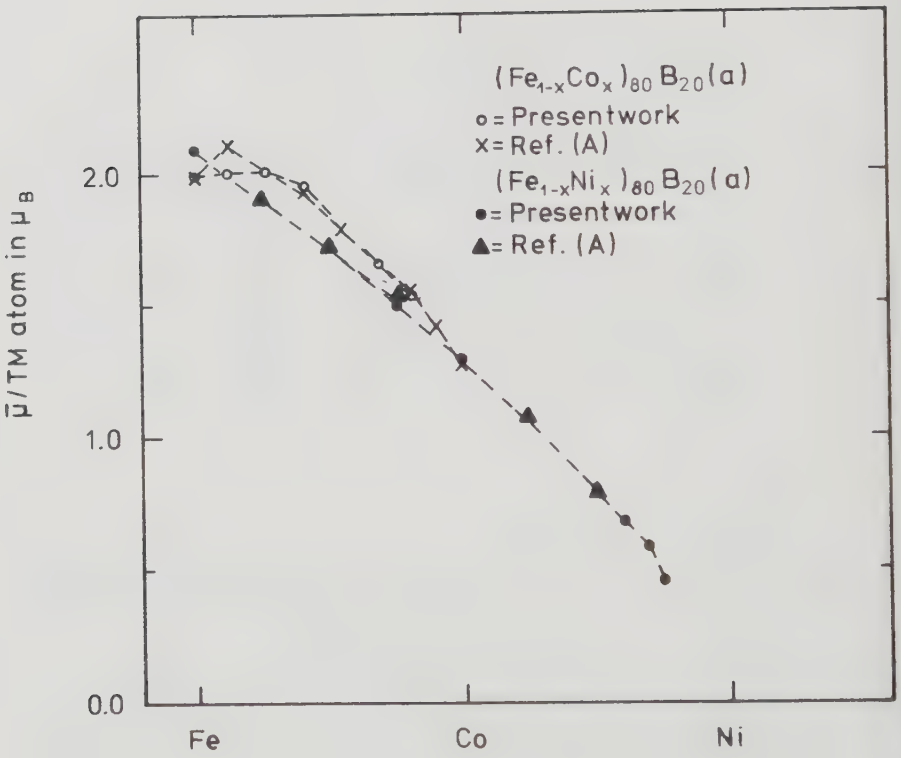

Fig. 4.8: Variation of average magnetic moment with Co and Ni concentrations for
a) $(Fe_{1-x}Co_x)_{80}B_{20}$ and
b) $(Fe_{1-x}Ni_x)_{80}B_{20}$ amorphous alloys

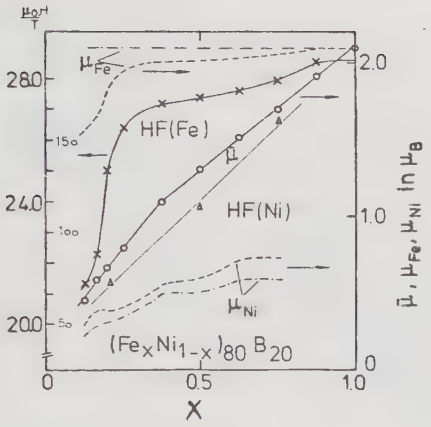

Fig. 4.9: Average hyperfine fields and average magnetic moments versus composition

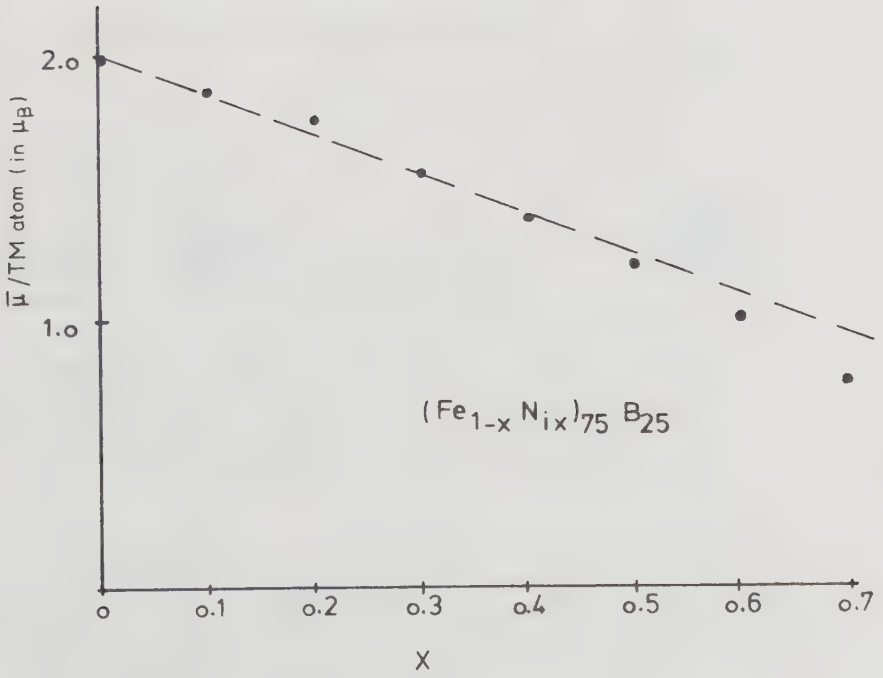

Fig. 4.10: Average magnetic moment/TM atom as a function of Ni-concentration for amorphous $Fe_{1-x}Ni_x)_{75}B_{25}$ alloys

After being roughly constant at 2.0 μ_B in the concentration range $0 \leq x \leq .125$, $\bar{\mu}$ decreases almost linearly with x down to 1.27 μ_B for x=1, i.e., $Co_{80}B_{20}$. This linear decrease with x is in conformity with the observation made previously by Mizoguchi /63/ that the approximate shape of the Slater-Pauling curve is reproduced by the data taken on $(TM)_{80}P_{10}B_{10}$ amorphous alloys. In addition, the observed maximum value of the magnetic moment, i.e., 2.0 μ_B/TM atom, observed for $(Fe_{1-x}Co_x)_{80}B_{20}$ amorphous alloys to the right of iron is also reasonably close to the maximum value observed in crystalline counterparts.

Hyperfine field as a function of iron concentration

$(Fe\ Ni)_{80}B_{20}$, $(Fe\ Ni)_{80}B_{19}Si_1$, $(Fe\ Ni)_{75}B_{25}$

For all the investigated samples, Mössbauer spectra were taken at 4.2K (6K for some cases), 77K and 300K. Mössbauer spectra were taken at ten different temperatures in the range 4.2-180K for $Fe_{20}Ni_{60}B_{20}$ and the compositional series $(Fe\ Ni)_{80}B_{19}Si_1$. Below the Curie temperature the ^{57}Fe Mössbauer spectra are typical for ferromagnetic amorphous alloys, with broadened lines due to hyperfine field distributions. The hyperfine field distributions could be fitted to quasi-symmetrical Gauss profiles according to the method discussed in section 3.

Some typical ^{57}Fe Mössbauer spectra taken at 300K, 77K and 6K are shown in Fig. 4.11-4.13. The temperature variation of the Mössbauer spectra for the composition $Fe_{16}Ni_{64}B_{19}Si_1$ is shown in Fig. 4.14. The relative width of the $\overline{HF}(Fe)$ distribution varies between 18-20%. Besides the average hyperfine fields at the iron sites,

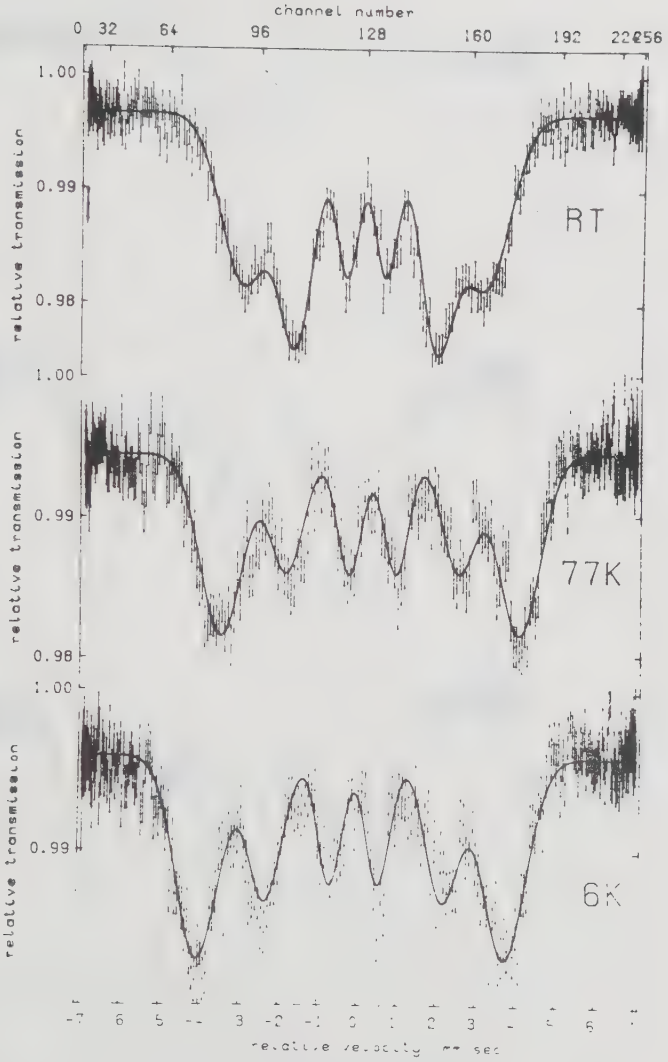

Fig. 4.11: Mössbauer spectra of amorphous $Fe_{20}Ni_{60}B_{20}$ sample at 300K, 77K and 6K, respectively

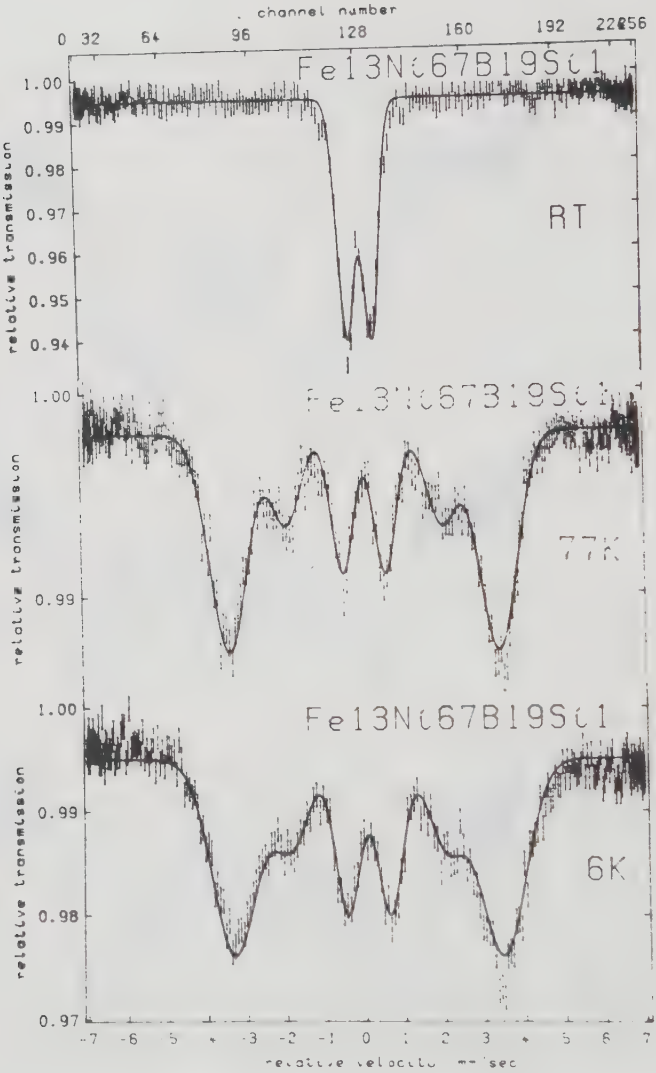

Fig. 4.12: Mössbauer spectra of amorphous $Fe_{13}Ni_{67}B_{19}Si_1$ alloy at 300K, 77K and 6K, respectively

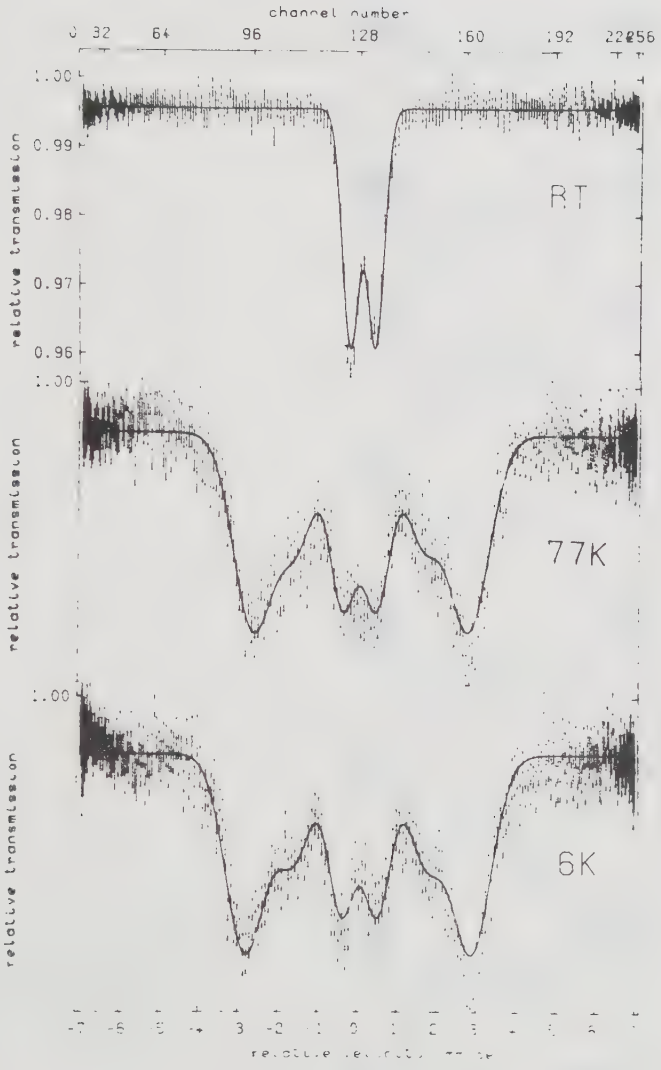

Fig. 4.10. Mössbauer spectra of amorphous $Fe_{10}Ni_{70}B_{10}Si_{1}$ alloy at 300K, 77K and 6K, respectively

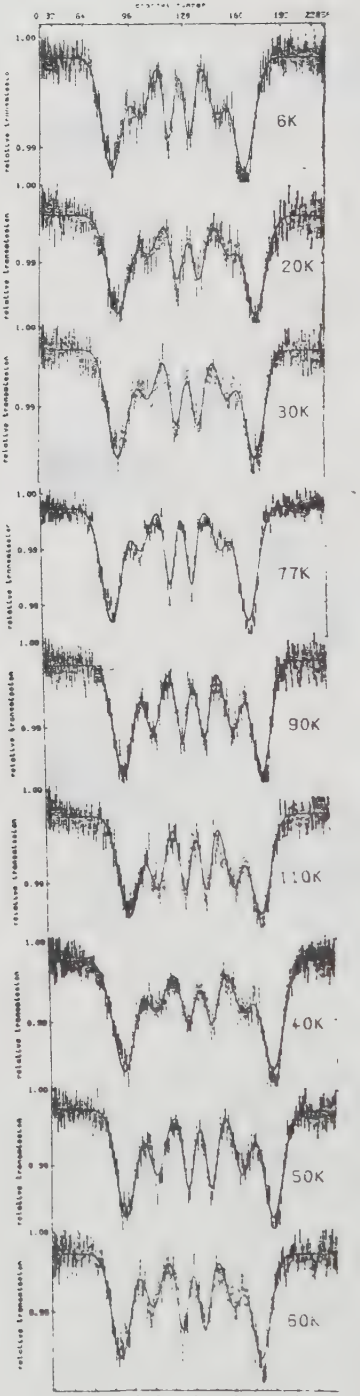

Fig. 4.14:
Mössbauer spectra of amorphous $Fe_{16}Ni_{64}B_{19}Si_1$ alloy at various temperatures

The dependence of $\overline{HF}$(Fe) and $\overline{HF}$(Ni) on x is given in Fig. 4.9. $\overline{HF}$(Fe) varies almost linearly in the range $.25 \leq x \leq 1$ with a slope of 0.029T/at%Ni. Below x=.25, i.e., on the Ni rich side, $\overline{HF}$(Fe) decreases much faster with increasing Ni content, decreasing from 26.4T for $Fe_{20}Ni_{60}B_{20}$ down to 21.3T for $Fe_{10}Ni_{70}B_{19}Si_1$.

The ^{57}Fe hyperfine field at 20K decreases with increasing Ni content, Fig. 4.16-4.17, in good agreement with the measurements on $(Fe_xNi_{1-x})_{80}P_{14}B_6$ at 4.2K reported earlier /73/. The values of $\overline{HF}$(Fe) increase with Fe-concentration in both compositional series (table 4.7) and for a given value of x, the average hyperfine field is lower when B is partially substituted by P. The lower value of the average hyperfine field at the Fe-site as compared to that in the crystalline iron is obviously due to a reduction of the Fe-moment via electron transfer from the metalloid to the transition metal d-band.

In table 4.8, the values of the average hyperfine field, isomer shift, quadrupole splitting and relative line width for $(Fe\ Ni)_{75}B_{25}$ amorphous alloys taken at 300,77 and 6K are given.

The hyperfine field at Fe-site at 300K decreases much faster, i.e., about 42% between x=0 and .7. But $\overline{HF}$(Fe) remains almost constant for the same concentration range at 77K and 6K. This may be attributed to their high Curie temperatures (see table 4.8 and Fig. 4.18 (a,b)).

in three cases, namely $Fe_{60}Ni_{20}B_{20}$, $Fe_{40}Ni_{40}B_{20}$ and $Fe_{20}Ni_{60}B_{20}$, the ^{61}Ni average hyperfine field have also been determined /109/. In the case of Ni rich sample, i.e., $Fe_{20}Ni_{60}B_{20}$, ^{61}Ni spectra were taken at different temperatures in the range between 4K and 180K /109/. The fitting procedure of the ^{61}Ni spectra for amorphous alloys is given in /110/.

Such spectra show the characteristic magnetic line broadening and the relative width of the $\overline{HF}$(Ni) distribution ranging from 44 to 60%. The ^{61}Ni spectrum of $Fe_{60}Ni_{20}B_{20}$ at 4.2K is shown in Fig. 4.15, the corresponding ^{57}Fe spectrum for the same alloy at 4.2K is given for comparison.

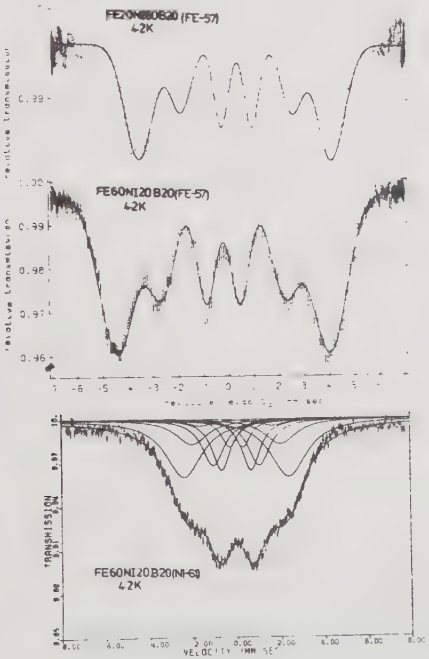

Fig. 4.15: Typical ^{57}Fe and ^{61}Ni Mössbauer spectra at 4.2K

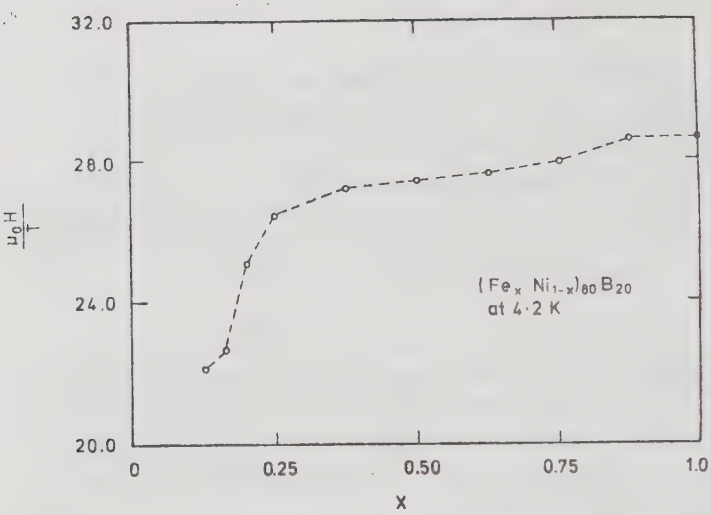

Fig. 4.16: Average hyperfine field versus x in amorphous $(Fe_xNi_{1-x})_{80}B_{20}$ alloys at 4.2K

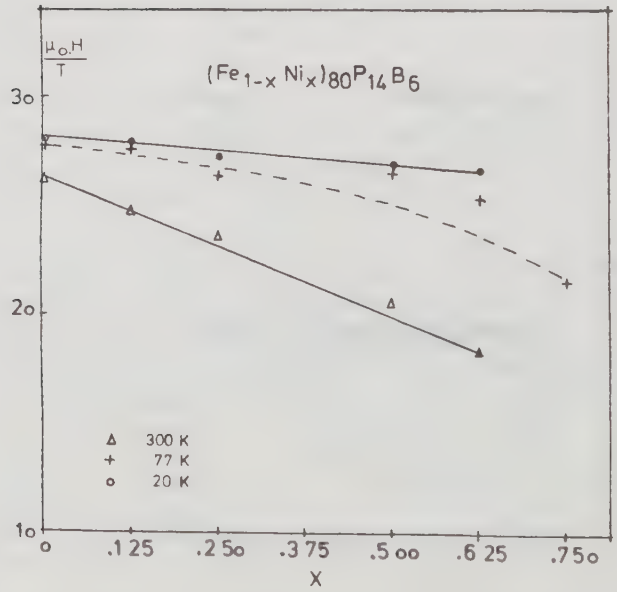

Fig. 4.17: Average hyperfine field versus Ni concentration in amorphous $(Fe_{1-x}Ni_x)_{80}P_{14}B_6$ alloys

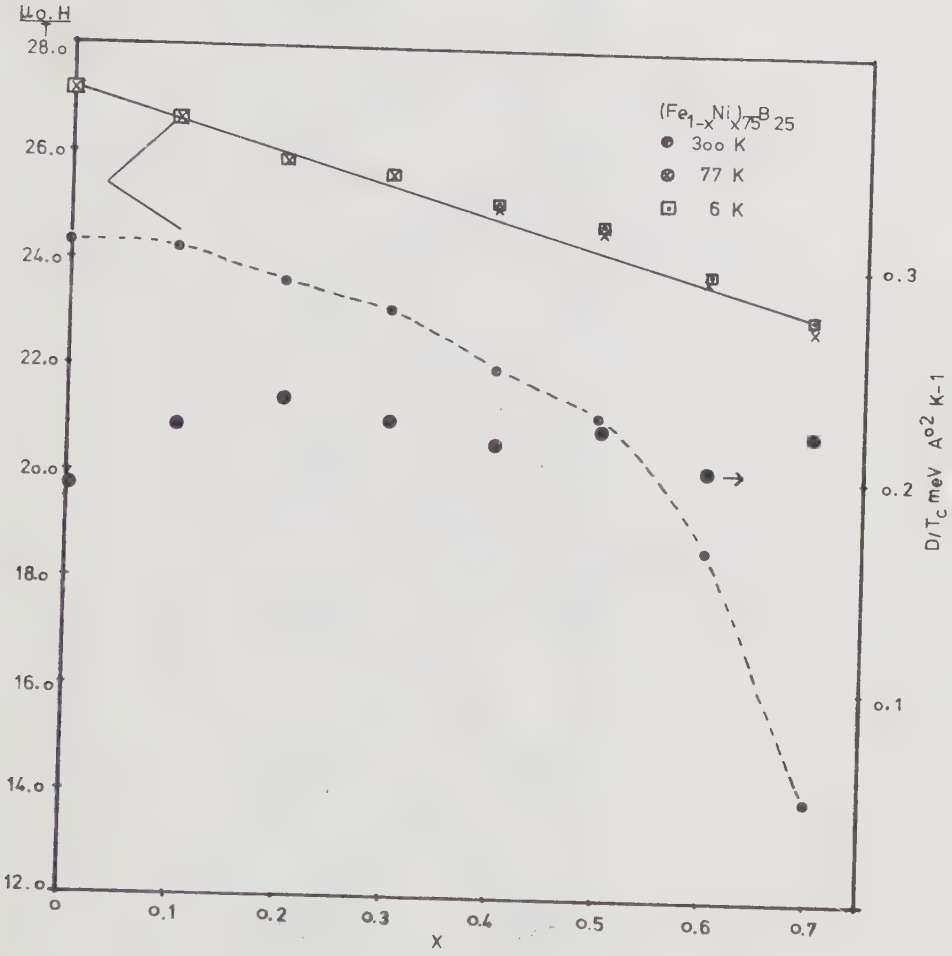

Fig. 4.18(a): Average hyperfine field as a function of x for amorphous $(Fe_{1-x}Ni_x)_{75}B_{25}$ ($0 \leq x \leq 0.7$) alloys at 300K, 77K and 6K, respectively. Also, the ratio D/T_c is plotted as a function of x

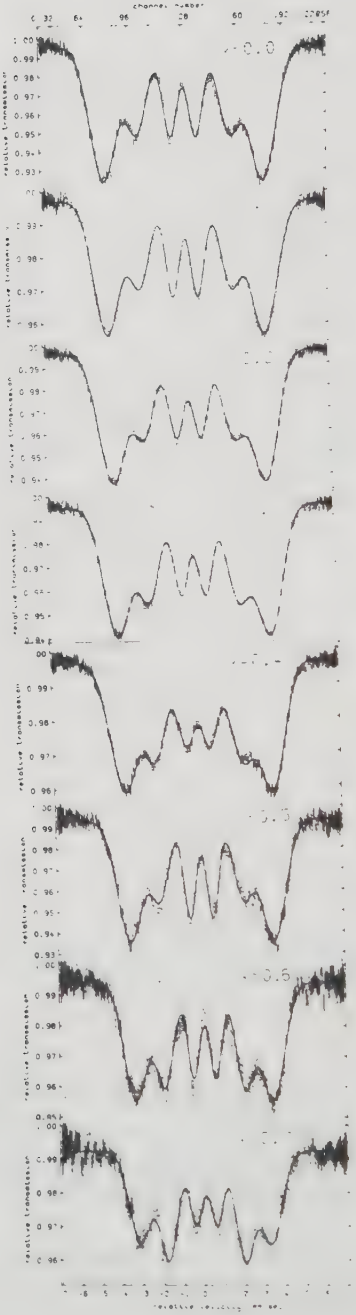

Fig. 4.18(b): Mössbauer spectra of amorphous $(Fe_{1-x}Ni_x)_{75}B_{25}$ $(0 \leq x \leq .7)$ alloys at 6K

$(Fe_{1-x}Co_x)_{80}B_{20}$ $(0 \leq x \leq .75)$

Typical Mössbauer spectra for all the samples taken at 300, 77 and 6K are shown in Fig. 4.19(a,b,c). In two cases, x=.625 and .75, the low temperature dependance of the Mössbauer spectra was systematically investigated in the temperature range 6-300K. The relative width increases from about 16% for $Fe_{20}Co_{60}B_{20}$ upto about 18% for $Fe_{50}Co_{30}B_{20}$.

Fig. 4.20-4.21 show the average hyperfine field and isomer shift as a function of Co concentration. In table 4.11 the values of average hyperfine field, isomer shift, quadrupole splitting at 300, 77 and 6K are listed. The average hyperfine field decreases slowly (about 3%) with Co substitution in the entire range. This decrease in iron hyperfine field basically corresponds to a similar decrease in the average magnetic moment at the Fe-site for increasing Co concentration as will be shown in the next chapter.

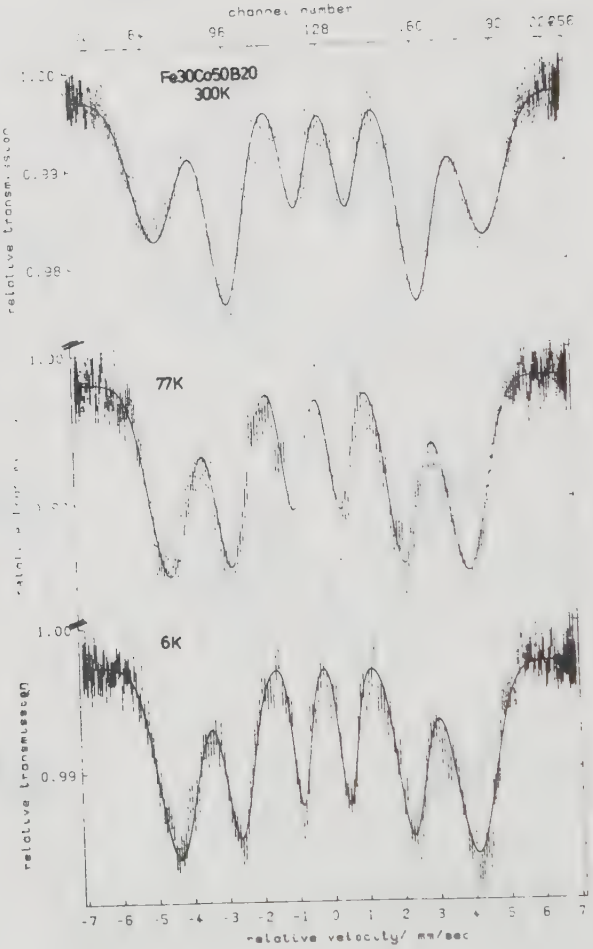

Fig. 4.19(b): Mössbauer spectra of $Fe_{30}Co_{50}B_{20}$ at 300K, 77K and 6K, respectively

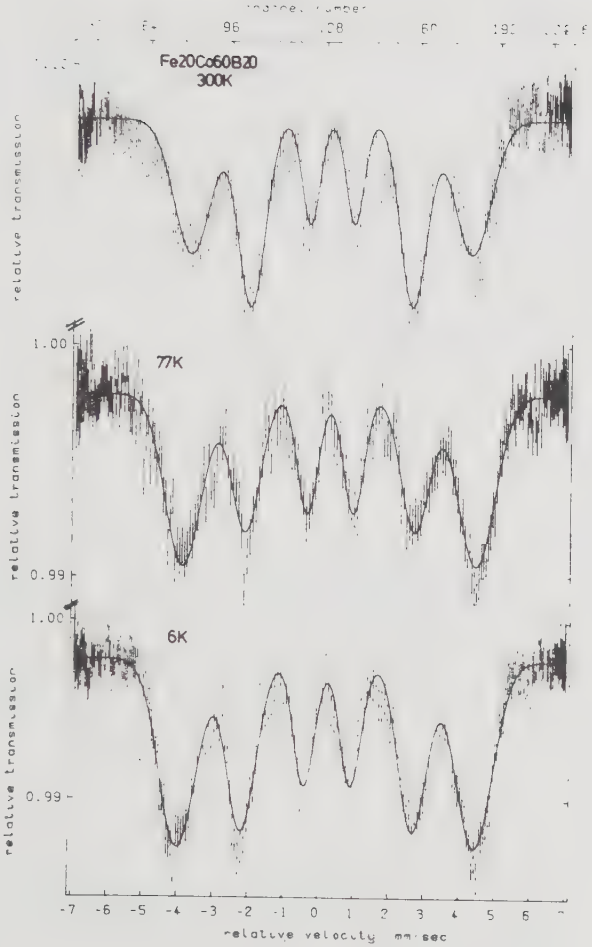

Fig. 4.19(c): Mössbauer spectra of $Fe_{20}Co_{60}B_{20}$ at 300K, 77K, 6K, respectively

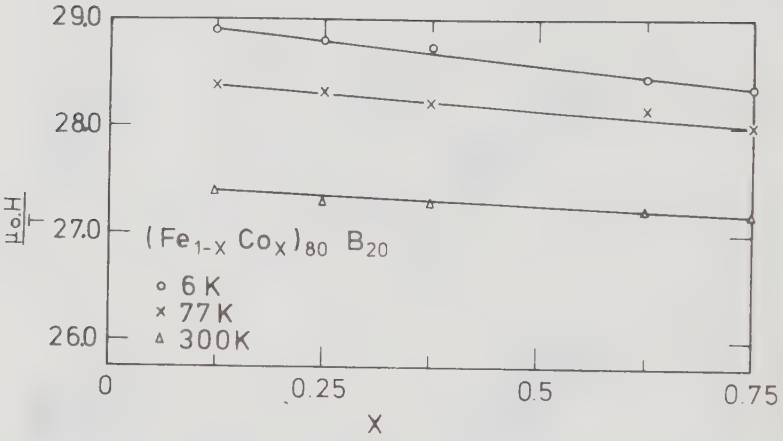

Fig. 4.20: Average hyperfine field as a function of Co-concentration at 300K, 77K and 6K, respectively

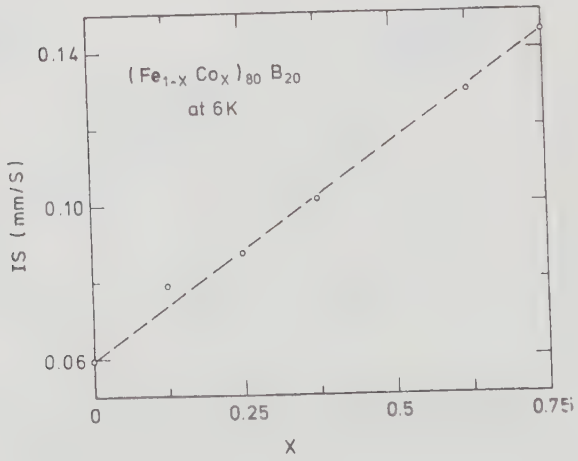

Fig. 4.21: Isomer shift (IS) at 6K versus x for amorphous $(Fe_{1-x}Co_x)_{80}B_{20}$ alloys

Average hyperfine field versus average magnetic moment

$(Fe\ Ni)_{80}B_{20}$, $(Fe\ Ni)_{80}B_{19}Si_1$ and $(Fe\ Ni)_{75}B_{25}$

The analysis of the concentration dependances of both $\overline{HF}$(Fe) and $\bar{\mu}$, shows that the hyperfine field can be described by the empirical equation (1), with a=12-13 T/μ_B and b=.1-.2 T/μ_B for $(Fe_xNi_{1-x})_{80}B_{20}$ and a=13.5 T/μ_B and b=.2 T/μ_B for $(Fe_{1-x}Ni_x)_{75}B_{25}$. Figs. 4.22-4.23 show plots of the $\overline{HF}$(Fe) as a function of $\bar{\mu}$ for $(Fe_xNi_{1-x})_{80}B_{20}$ and $(Fe_{1-x}Ni_x)_{75}B_{25}$, respectively.

The hyperfine field at the Ni-sites, $\overline{HF}$(Ni) is roughly linear in x in the range $.25 \leq x \leq .75$ as can be seen from Fig. 4.16. Since $\overline{HF}$(Ni) has been measured only for three compositions, a fit to the dependance of the type

$$\overline{HF}(Ni) = a'\mu_{Ni} + b'\bar{\mu} \qquad (55)$$

is not expected to be too accurate. In spite of that such an analysis, using the calculated μ_{Ni} values, show that b' is larger than a'. The same type of observation has been made in the case of crystalline Fe-Ni alloys, where a=.2 T/μ_B while b=10 T/μ_B /111/.

$(Fe_{1-x}Co_x)_{80}B_{20}$ $(0 \leq x \leq .75)$

The plot of the low temperature value of hyperfine field, $\overline{HF}$(Fe), as a function of $\bar{\mu}$ is linear, Fig. 4.24, and can be described by the relationship

$$\overline{HF}(Fe) = (26.8\ \bar{\mu}_{Fe} + 1.02\ \bar{\mu})T \qquad (55a)$$

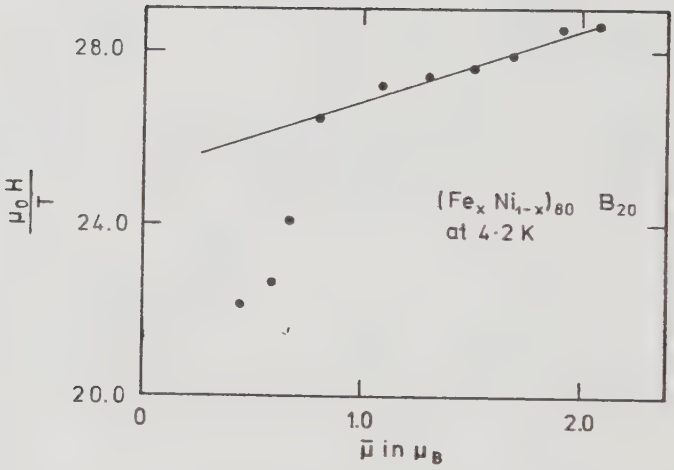

Fig. 4.22: Average hyperfine field as a function of average magnetic moment ($\bar{\mu}$)

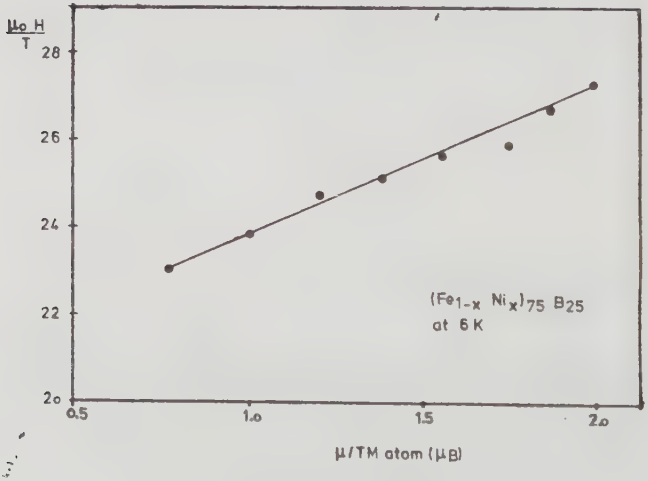

Fig. 4.23: Average hyperfine field at 6K versus average magnetic moment ($\bar{\mu}$/TM atom) for amorphous $(Fe_{1-x}Ni_x)_{75}B_{25}$ alloys

Equation (55a) can be compared to the frequently used phenomenological expression (1) for the above mentioned alloys. The first term in equation (55a) is, therefore, the Fe-core polarization contribution to $\overline{HF}$(Fe), and the second one is the conduction electron polarization. Taking for $\bar{\mu}_{Fe}$ the value of 1.99 μ_B (for $Fe_{80}B_{20}$) equation (55) transforms to

$$\overline{HF}(Fe) = (13.4 + 1.02\ \bar{\mu})T \qquad (56)$$

with a=13.4 T/μ_B and b=1.02 T/μ_B.

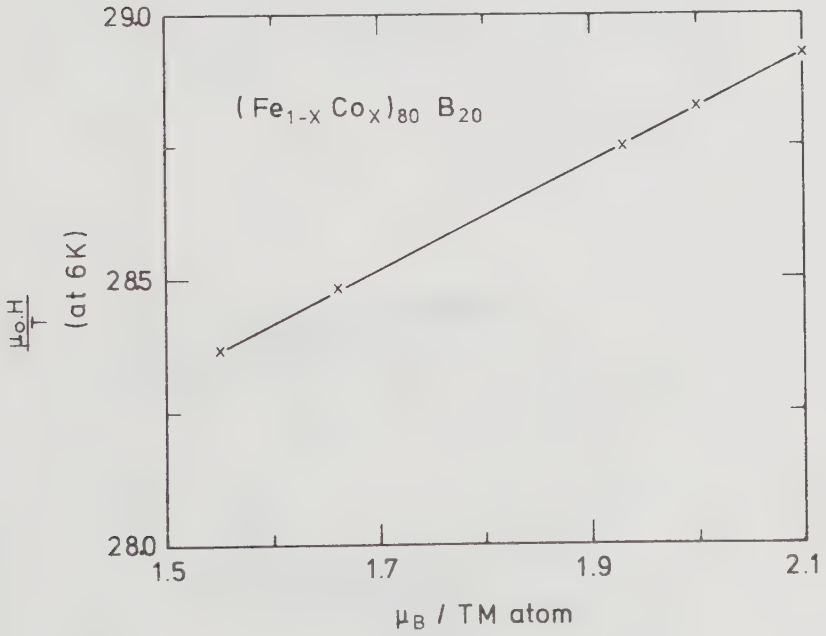

Fig. 4.24: Average hyperfine field as a function of average magnetic moment

Low temperature magnetization and spin-wave excitations: $(Fe\ Ni)_{80}B_{20}$, $(Fe\ Ni)_{80}B_{19}Si_1$ and $(Fe\ Ni)_{75}B_{25}$

The results of the magnetization measurements, i.e., the reduced magnetization, performed on these amorphous alloys are plotted against $T^{3/2}$, Fig. 4.25. One can see that the Bloch's $T^{3/2}$ law holds for the temperature dependance of both $\overline{HF}$(Fe) and $\overline{HF}$(Ni). It is clear from Fig. 4.25 that the equation (3) is valid for temperature upto 200K (.5-.6 T_c). This observation is in conformity with the previous magnetic and Mössbauer studies on other glassy alloys /107,112/. A good agreement is obtained between the B_{Mag} and $B_{Möss}$ values for the samples with x=.2 and .125, whereas a rather large discrepency was observed for x=.25 and .165, for which $B_{Möss}$ is only 50-60% of B_{Mag}.

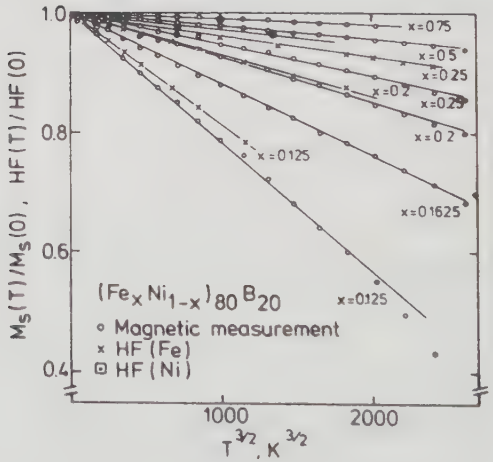

Fig. 4.25: Reduced magnetization M(T)/M(O) and hyperfine field HF(T)/HF(O) versus $T^{3/2}$

The values of B calculated from the magnetization are plotted as a function of composition in Fig. 4.26 (a,b) The present values of B and D for these amorphous alloys determined from magnetic and Mössbauer studies are listed in table 4.6, where the corresponding values for crystalline Fe and Ni have also been included for comparison. The values of $B=(2.8\pm.7)\cdot10^{-5}$ $K^{-3/2}$ determined for a $Fe_{20}Ni_{60}B_{20}$ sample from $\overline{HF}$(Ni) is comparable with the value $(3.2\pm.3)\cdot10^{-5}$ $K^{-3/3}$ found for the same alloy from $\overline{HF}$(Fe). The spin wave stiffness constant D incerases from about 98 meV $\AA^2$ for $Fe_{80}B_{20}$ to about 183 MeV $\AA^2$ for $Fe_{50}Ni_{30}B_{20}$, drops rather suddenly to about 122 meV $\AA^2$ for $Fe_{40}Ni_{40}B_{20}$ and increases further with increasing Ni-content, reaching 55 meV $\AA^2$ for $Fe_{10}Ni_{70}B_{19}Si_1$. This drop in the spin-wave stiffness constant value leads to a similar discontinuity in the concentration dependence of the range of exchange interaction D/T_c, Fig. 4.26 (a,b), where T_c is the Curie temperature.

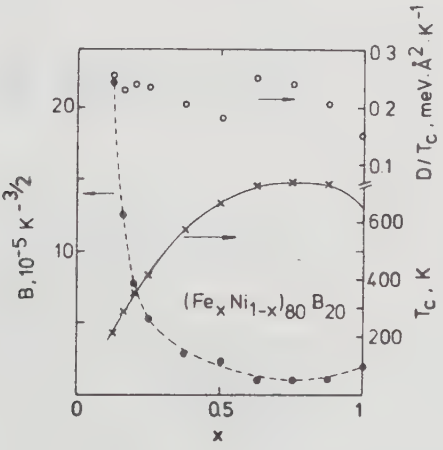

Fig. 4.26(a): Dependence of B coefficient, Curie temperature and D/T_c ratio on composition

In table 4.9, the values of spin-wave parameters for amorphous $(Fe\ Ni)_{75}B_{25}$ alloys are listed. The value of B increases almost linearly from $(1.28\pm.06)\cdot10^{-5}\ K^{-3/2}$ (for x=0) to $(5.8\pm.3)\cdot10^{-5}\ K^{-3/2}$ (for x=.7). Fig. 4.18a shows the dependence of range of exchange interaction (D/T_c) on the composition x. After a slight increase from .195 meV A^{o2} (for x=0) to .230 (for x=.1) this ratio remains almost constant in the entire range.

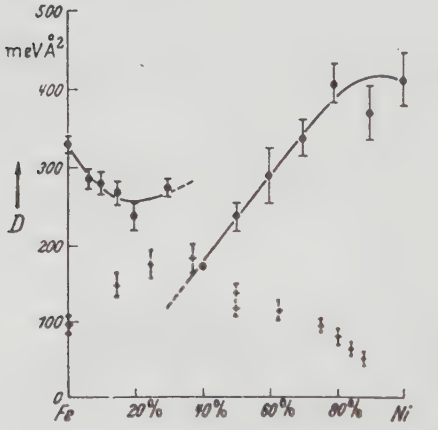

Fig. 4.26(b): Comparison between the concentration dependence of the spin-wave stiffness constant D in amorphous $(FeNi)_{80}B_{20}$ alloys and in crystalline FeNi alloys.
+ - amorphous, from magnetic measurements, present work; · - crystalline, from neutron scattering, after M. Hatherley et al, Proc. Phys. Soc. 84,55(1964)

$(Fe_{1-x}Co_x)_{80}B_{20}$ $(0 \leq x \leq .75)$

Fig. 4.27 shows the plott of the reduced magnetization as a function of $T^{3/2}$ for amorphous $(Fe\ Co)_{80}B_{20}$ alloys. Bloch's $T^{3/2}$ law is seen to hold for temperature up to 300K (.6-.7 T_c) in agreement with the previous studies /5,72/. A plot of the relative hyperfine field (normalised to the value at OK) against $T^{3/2}$, for the compositions $Fe_{20}Co_{60}B_{20}$ and $Fe_{50}Co_{30}B_{20}$ is shown in Fig. 4.28. The values of the corresponding Bloch's coefficient B, are $.62 \cdot 10^{-5}$ $K^{-3/2}$ and $1.0 \cdot 10^{-5}$ $K^{-3/2}$ in good agreement with the values of B obtained from magnetic measurements. The present values of B and D for these amorphous alloys determined from magnetic and Mössbauer studies are listed in table 4.12, where the corresponding values for crystalline Fe and Co have also been included for comparison.

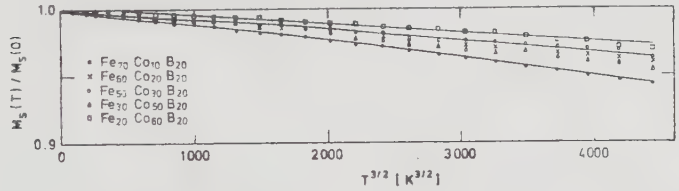

Fig. 4.27: Reduced magnetization Vs.$T^{3/2}$ in a field of 6K Tesla for $(Fe_{1-x}Co_x)_{80}B_{20}$

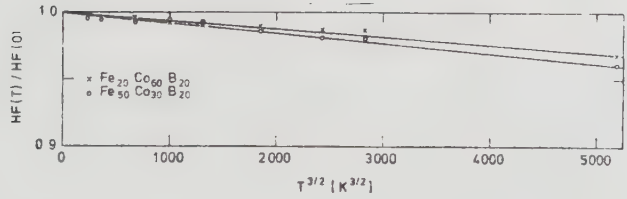

Fig. 4.28: Reduced hyperfine field Vs.$T^{3/2}$ for $Fe_{20}Co_{60}B_{20}$ (x) and $Fe_{50}Co_{30}B_{20}$ (o) amorphous alloys

Table 4.12:Spin-wave parameters, i.e. coefficients B and D for glassy $(Fe_{1-x}Co_x)_{80}B_{20}$ and crystalline Fe and Co from magnetic and ME measurements

Sample	g	B($10^{-5}K^{-3/2}$) Magn.	B($10^{-5}K^{-3/2}$) Möss.	D(meV $A^{o\ 2}$) Calc.	D(meV $A^{o\ 2}$) Obs.
$Fe_{20}Co_{60}B_{20}$	2.05[1] (0.02)	0.667 (0.02)	0.613	239.0 (5)	-
$Fe_{30}Co_{50}B_{20}$	2.05 (0.02)	0.945 (0.03)		179.3 (5)	-
$Fe_{50}Co_{30}B_{20}$	2.05 (0.02)	0.852 (0.04)	1.000	179.8 (6)	-
$Fe_{60}Co_{20}B_{20}$	2.05 (0.02)	0.874 (0.04)		174.9 (3)	-
$Fe_{70}Co_{10}B_{20}$	2.05 (0.02)	1.254 (0.05)		136.5 (5)	-
Fe	2.09[2]	0.34[2] (0.2)		286[2a] (11)	266[2b] (20)
Co	2.22[3]	0.33[3] (0.12)		350[3] (10)	-

( ) denote estimated uncertainty limits

1 Reference /106/

2 Reference /108/

2a Reference /108/

2b Reference /108/

3 Reference /107/

Isomer shift and quadrupole splitting

The isomer shift as a function of x for these amorphous alloys are shown in Fig. 4.21, 4.29(a,b,c) and tables 4.7, 4.8 and 4.11. As can be seen from Figs. 4.21, 4.29 (a,b,c), the isomer shift increases linearly with the increasing Ni and Co concentration. Up to 50 at % Ni, the isomer shift varies slowly but for higher Ni-concentrations it increases steeply. In case of $(Fe\ Co)_{80}B_{20}$, the isomer shift increases linearly from .06±.001 (for x=0) to .145±.001 (for x=.75). The increasing tendency of isomer shift has also been observed for $(Fe\ Ni)_{75}B_{25}$ (Fig. 4.29(a)).

The value of quadrupole interaction in these alloys are negligibly small as can be seen from the tables 4.7, 4.8 and 4.11.

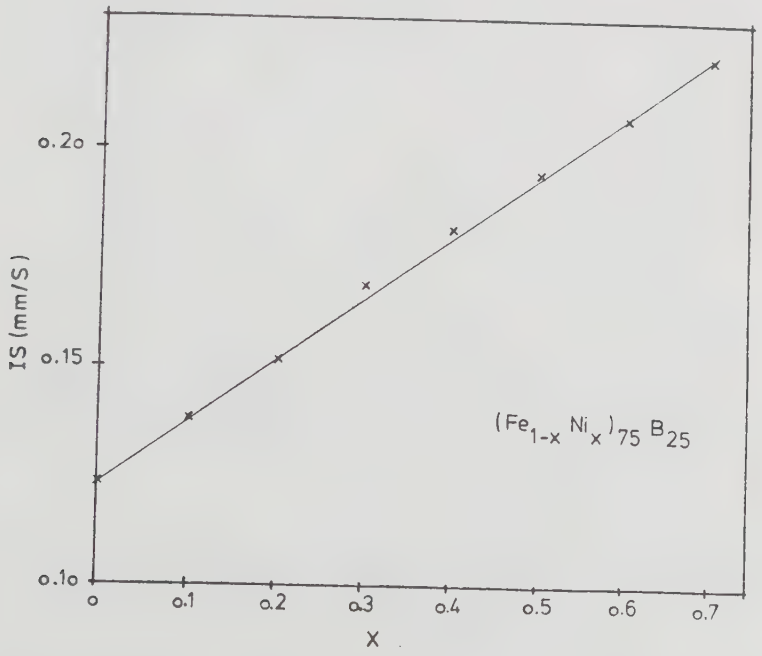

Fig. 4.29(a): Isomer shift at 6K versus x for amorphous $(Fe_{1-x}Ni_x)_{75}B_{25}$ alloys

Discussion

Average magnetic moment ($\bar{\mu}$) as a function of Fe and Co concentration

A comparison of the present results with the magnetic behaviour in crystalline Fe-Ni and Fe-Co shows that the average magnetic moment $\bar{\mu}$ of 3d-TM atoms in quasibinary amorphous $(Fe\ Ni)_{80}B_{20}$, $(Fe\ Ni)_{80}B_{19}Si_1$, $(Fe\ Ni)_{75}B_{25}$ and $(Fe\ Co)_{80}B_{20}$ ferromagnetic alloys as a function of Fe and Co concentration (or outer electron content) follows closely crystalline alloys. However, a shift of the Slater-Pauling curve in the case of amorphous alloys with respect to crystalline counterparts results from the electron transfer from the glass former atoms to the partially filled TM d-bands. As in crystalline Fe-Ni and Fe-Co alloys $\bar{\mu}$ in the present alloy series also decreases with increasing average outer electron concentration with the slope of -1, which finds a simple interpretation in terms of the rigid band model. The rigid band model in its simple form concerns only with the energy spectrum of electrons and cannot give information about the spatial distribution of the magnetic moment. However, when Friedel's modification, which takes into account the screening effect, is incorporated in this model, this model furnishes useful information about the spatial distribution of the magnetic moment.

Becker et al /98/ have measured magnetic moments for amorphous $(Fe_xNi_{1-x})_{80}P_{14}B_6$, $(Fe_xNi_{1-x})_{80}B_{20}$ and $Fe_{40}Ni_{40}(P_{1-y}B_y)_{20}$ alloy in the concentration range $0.375 \leq x \leq 1$, $0.5 \leq x \leq 1$, and $0 \leq y \leq 1$, respectively, and made the following observation:

> The average moment data can be fitted equally well by considering two different possibilities: one by assigning 2.1 and 0.6 μ_B per Fe and Ni atom, respectively, while lowering the moment by 0.3 per B atom and 1.0 per P

atom, and other by varying the moment on Fe and Ni atoms with TM composition as shown by neutron diffraction in crystalline alloys combined with a lowering of 1.2 and 2.1 per B and P atom, respectively.

However, Kaul /108/ has obtained a close fit to the moment data on the same alloy system (including the compositions on the Ni-rich side) by allowing not only the moments on Ni and Fe atoms to vary with Fe concentration, as revealed by neutron diffraction in crystalline alloys, but also the number of electrons per atom n_p and n_b that P and B atoms, respectively, donate to the transition metal d-band. A theoretical justification for the variation of n_p and n_b with x is provided as follows:

Coherent-potential approximation calculation /113/ performed on the crystalline $Ni_{1-x}Fe_x$ alloys show that the density of states at the Fermi-level ($N(E_F)$) decreases sharply with increasing x up to x=0.5 because the density of the state function of the spin down d-band deforms to a considerable extent, even for small values of x. However, when x increases beyond 0.5, the Fermi level progressively dips into the spin up d-band, and consequently $N(E_F)$ increases till attains a value of 0.74 beyond which $N(E_F)$ remains roughly constant. Since the present alloys are in the amorphous state with practically no complications due to structural changes, it seems reasonable to assume that the spin up d-band continues to lie below the Fermi level, while the density of the state function of the spin down d-band goes on deforming with increasing iron concentration till it approaches unity. Under such conditions, the probability of the electrons donated by the metalloid to get transferred to the spin down d-band decreases continuously as iron concentration increases.

From the above comparison between the behaviour of $\bar{\mu}$ in crystalline and amorphous alloys under considera-

tion, two main features become apparent:

i) short-range order is basically responsible for the observed variation of $\bar{\mu}$ with x and that long-range structural disorder has negligible effect and

ii) the decrease of average magnetic moment $\bar{\mu}$ with Cobalt and Nickel finds the same interpretation as in crystalline Fe-Co and Fe-Ni alloys in terms of Friedel's model /17/.

Though the results of the magnetic measurements can be qualitatively understood on the basis of rigid band model, the low temperature specific heat data /110/ on similar amorphous alloys find a more satisfactory explanation in terms of the split-band model than that in terms of band-model. Such a contradiction can be resolved when one realizes that the unfilled states in the split band model and the rigid band model spin up bands are the same so that from $\bar{\mu}$ values alone one cannot distinguish between the two models.

Average hyperfine field versus average magnetic moment

The linear dependence of $\overline{HF}$(Fe) on $\bar{\mu}$ has been previously observed in the case of binary crystalline alloys /115/ and more recently in $(Fe_{1-x}Ni_x)_{80}P_{14}B_6$ amorphous alloys /73,116/. Equations (55) through (55a) show that such a linear dependence is also maintained in amorphous $(Fe\ Co)_{80}B_{20}$, $(Fe\ Ni)_{80}B_{20}$ and $(Fe\ Ni)_{75}B_{25}$ alloys. The dependence of $\overline{HF}$(Fe) as a function of $\bar{\mu}$ can be described by the relationship of the type (1). It is observed in each system studied that the value of the coefficient 'b' is very small compared to the core polarization

coefficient 'a'. This suggests that in the amorphous alloys the 3d-electrons are highly localised and that the contribution from the conduction electron polarization to the hyperfine field is rather small. However, the dependence of $\overline{HF}$(Ni) as a function of $\bar{\mu}$ shows that the core polarization coefficient 'a" is smaller than the coefficient 'b". This implies that the conduction electron polarization gives the main contribution to $\overline{HF}$(Ni).

Low temperature magnetization and spin-wave excitations

Although both crystalline and amorphous ferromagnets follow the predictions of equation (3) based on Heisenberg model, the results of the glassy alloys under consideration differ from those for crystalline ferromagnets in the values of Bloch's coefficient, B, in at least the following ways:

i) the values of B or crystalline ferromagnets are roughly three to four times smaller in magnitude than that observed for the present alloy

ii) the temperature range in which the $T^{3/2}$ terms dominates is much wider (up to about .6 T_c) in these amorphous alloys than that for crystalline Fe and Ni ($0 \leq T \leq .15\ T_c$). Moreover, there exists sufficient evidence to prove that the higher values for B are characteristic of only the glassy state /112/

iii) the general observation that D has a smaller value for ferromagnets in the amorphous state for those in the crystalline state is found to be maintained in the present system too (see table 4.6,4.9 and 4.11).

For a crystalline ferromagnet, the conventional spin-wave theory /71/ shows that q^2 and q^4 terms inthe spin-wave dispersion relation eq. (34) give rise to $T^{3/2}$ and $T^{5/2}$ terms, respectively in eq. (3). Despite the fact that transplational invariance is totally absent in amorphous ferromagnets and hence crystal momentum is no longer a good quantum number, neutron-diffraction measurements /117,118,72/ clearly show that the amorphous ferromagnets do indeed exhibit well defined spin-wave excitations at long wavelength and the spin-wave dispersion data display the same q dependence as expected for crystalline ferromagnets (i.e., eq. (34)). At first thought the above mentioned observation may sound puzzling but reconciliation with such a situation is brought by field theoretical calculation of Herring and Kittel /119/ which reveals that for spin-waves with long wavelength (wavelength exceeding many times the average atomic distance) the details of atomic arrangement, periodic or otherwise, are not important.

The term $BT^{3/2}$ in eq. (3) arises from the fact that the quadratic dispersion relation holds at small wave vectors. The observation that B for amorphous ferromagnets are consistently several times larger than those for crystalline ferromagnets, therefore, implies higher low-frequency density of states for the amorphous case. In conformity with the above argument, a number of theoretical models indicate that the increased structural disorder results in higher spin-wave density of states for low-frequency excitations /120,121/.

The ratio D/T_c, which is a measure for the range of the exchange interaction, has a rather pronounced discontinuity between 30 and 40 at % Ni for $(Fe\ Ni)_{80}B_{20}$, Fig. 4.26(a,b). This could possibly be due to some changes in the local atomic arrangement. Such anomaly, in case

of $(Fe\ Ni)_{75}B_{25}$, has not been observed. Here, the range of exchange interaction remains almost constant.

The examination of table 4.12 shows that the Bloch constant 'B' has small values as expected from the relatively high T_c values for $(Fe\ Co)_{80}B_{20}$ amorphous alloys. The good agreement between the B values obtained from both Mössbauer and magnetic measurements for $Fe_{20}Co_{60}B_{20}$ and $Fe_{50}Co_{30}B_{20}$ samples, provide evidence for the localized nature of the Fe and Co moments. The range of exchange interaction, i.e., the ratio (D/T_c) for amorphous $(Fe\ Co)_{80}B_{20}$ alloy could not be calculated because the T_c values are very high. In some cases these (T_c) values are near crystallization temperature, so it is not possible to determine T_c values accurately. Therefore, a comparison for crystalline and amorphous Fe-Co alloys is not possible.

A close agreement between the D values as determined from magnetization and Mössbauer spectroscopy suggests that the conventional spin-wave theory completely accounts for the observed low temperature magnetic behaviour in the present systems.

Isomer shift and quadrupole splitting

It can be seen from table 4.7, 4.8 and Fig. 4.29 (a,b,c) the isomer shift does not change so much by alloying with Ni but it changes drastically when B is substituted by P. The higher the Ni and P concentrations, the stronger the variation of the isomer shift in a direction which suggests an enhancement of the screening of the s-electrons and a decrease in their probability density at the Fe-nucleus. The observed trend, therefore, gives evi-

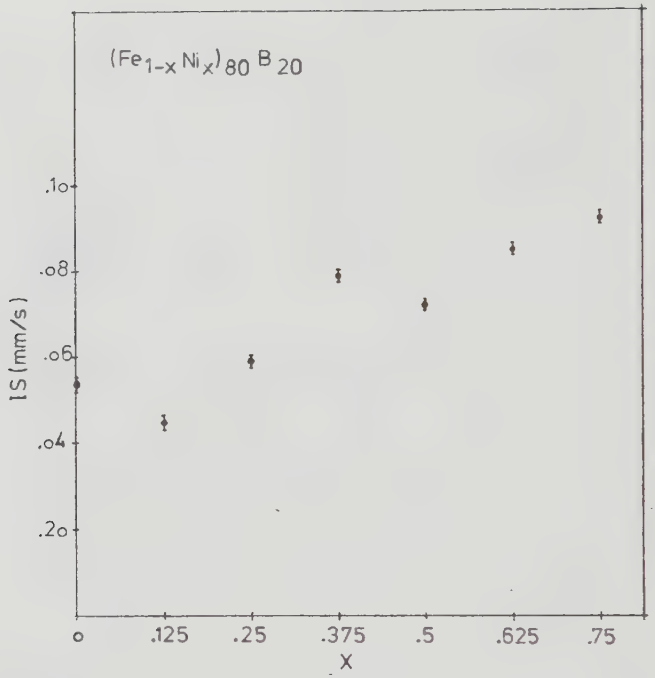

Fig. 4.29(b): Variation of isomer shift (IS) as a function of Ni-concentration

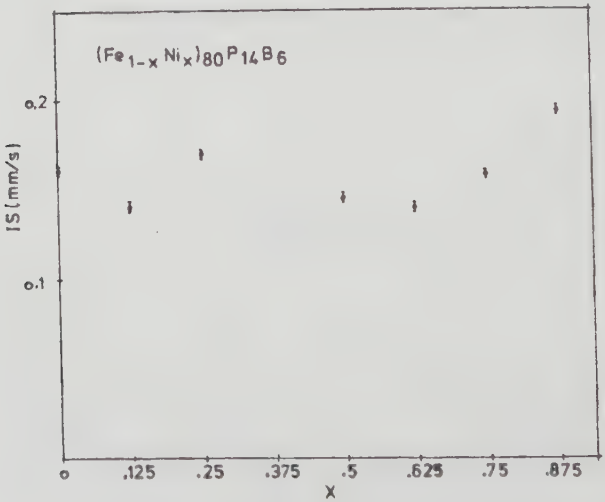

Fig. 4.29(c): Isomer shift as a function of Ni-concentration

dence of electron transfer from P and B to the d-band of the transition metal atoms. The stronger influence of P can be explained as a result of the higher number of its p-electrons (3) in comparison with that of B (1). It is to be expected that the s-electrons find their way into the conduction band while the p-electrons are mainly transferred to the unfilled d-band of the transition metals.

The observed increase of isomer shift as a function of Co and Ni concentration can also be explained on the basis of the above model.

At $T<T_c$, because the angular factor is spatially averaged to be nearly zero, the effective EFG is expected to be negligible. This is manifested by the fact that the positions of six spectral lines are very symmetric about the centroid of the spectrum. The quadrupole splitting (table 4.8, 4.8 and 4.11) observed in these amorphous alloys are found to be negligibly small at $T<T_c$.

4.4 Magnetic properties of iron-rich amorphous alloys containing Chromium and Molybdenum

The results of saturation magnetization measurements of ferromagnetic transition metal-metalloid alloys are used to calculate the average magnetic moments which, in turn, provide an experimental test to the predictions of various theoretical models. This approach has been found useful in amorphous alloys in which Fe is replaced fully or partially by nickel and cobalt. When the magnetic moments of these alloys are plotted as a function of electron concentration /74/, the results of the different alloy systems superimpose to give the right hand position of the Slater-Pauling curve. This supports the applicability of a rigid-band model to these alloys.

In the case of crystalline alloys containing Cr, Mo a strong departure from the Slater-Pauling curve has been observed /122/. A systematic study of the magnetic properties of Fe-based amorphous alloys with Cr and Mo has been undertaken in this work to acertain whether such deviations are observed when these alloys are in the amorphous state. Mössbauer data have been used to evaluate the compositional variation of the average iron moment in these alloys. The results of the bulk magnetic measurements and Mössbauer spectroscopy (local measurement) for amorphous alloys $Fe_{85-y}Cr_yB_{15}$ ($0 \leq y \leq 20$), $Fe_{95-x}Cr_5B_x$ ($15 \leq x \leq 25$) and $(Fe_{1-x}Mo_x)_{80}B_{20}$ ($0 \leq x \leq .125$) have been presented and later discussed in the following sections.

Results

$(Fe_{1-x}Mo_x)_{80}B_{20}$ $(0 \leq x \leq .125)$

Table 4.13 lists for all the alloys, the saturation magnetization at OK, M(O) spin-wave parameters B and D, Curie temperature (T_c), the ratio (D/T_c), calculated density (ρ), the average magnetic moment of iron ($\bar{\mu}_{Fe}$) calculated per Fe-atom and the average magnetic moment/TM at OK. In Table 4.14, the values of the average hyperfine field, isomer shift, quadrupole splitting and relative dispersion at temperatures 300K, 77K and 6K are given.

The average magnetic moment ($\bar{\mu}$) is plotted as a function of Mo concentration (x) in Fig. 4.30, where the corresponding moment variation with x observed in crystalline $Fe_{1-x}Mo_x$ alloy is also included for comparison. The average magnetic moment decreases rather linearly with increasing Mo concentration. The solid curve in Fig. 4.30, which gives an excellent fit to the observed data, can be described by the following equation:

$$\bar{\mu}(x) = (2.09-8.1x)\mu_B \qquad (57)$$

Table 4.13: Compositional dependence of magnetic moments, Curie Temperature T_c, saturation magnetization M(O) (emu/g), coefficients B and D, the range of exchange interaction D/T_c and densities for $(Fe\text{-}Mo)_{80}B_{20}$ alloys.

Compound	M(O) (emu/g)	B $10^{-5}K^{-3/2}$	D meV·A·2	T_c K	D/T_c meV·A·$^2K^{-1}$	ρ (g/cm^3)	$\bar{\mu}$ (μ_B/TM)	$\bar{\mu}_{Fe}$ calc. (μ_B/Fe at)
$Fe_{80}B_{20}$	199.7 210*	1.92 2.6 2.2±0.2+	98.84	602 647 634 655*	0.164 0.128 0.153	7.50	2.09	2.09
$Fe_{79}Mo_1B_{20}$	189.7	2.24	91.97	555	0.166	7.54	2.01	2.04
$Fe_{78}Mo_2B_{20}$	181.4	2.95 2.8±0.2+	78.58	517	0.152	7.58	1.94	1.99
$Fe_{77}Mo_3B_{20}$	165.4	3.22	78.62	477	0.165	7.61	1.78	1.85
$Fe_{76}Mo_4B_{20}$	155.9	4.54	64.82	440	0.147	7.65	1.69	1.78
$Fe_{75}Mo_5B_{20}$	142.8	5.48	60.41	410	0.147	7.69	1.56	1.66
$Fe_{73}Mo_7B_{20}$	122.6	8.00	51.65	340	0.152	7.76	1.36	1.49
$Fe_{70}Mo_{10}B_{20}$	97.9	12.24	44.81	253	0.177	7.86	1.120	1.27

* Ref. /5/

\+ Ref. /106/

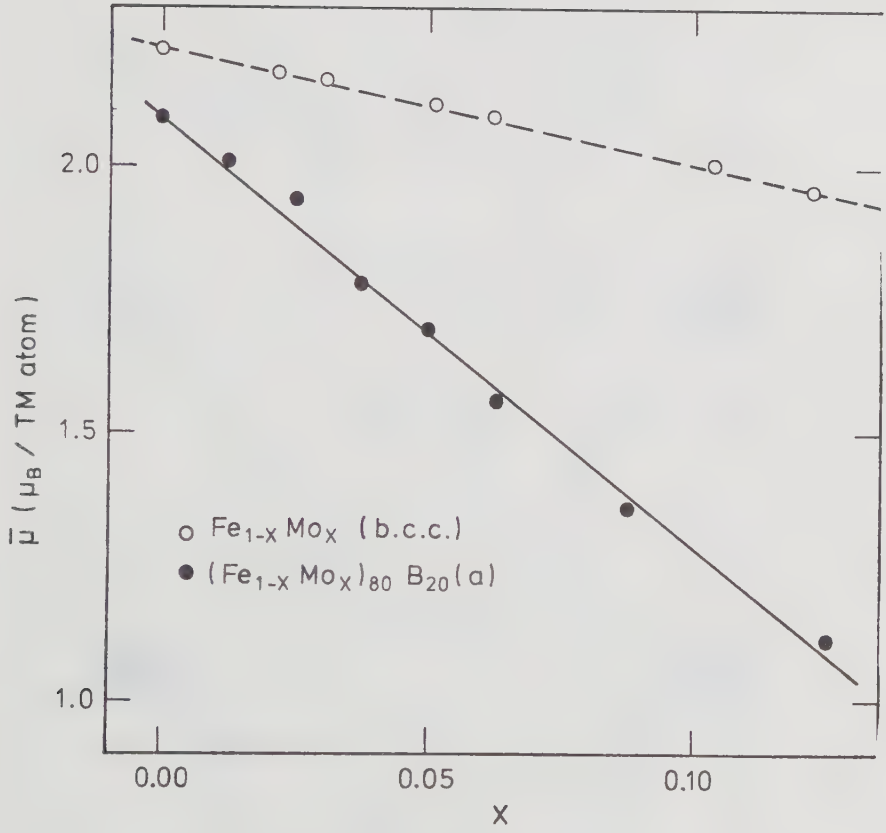

Fig. 4.30: Average magnetic moment per transition metal atom at OK of crystalline and amorphous Fe-Mo alloys (present work) as a function of Mo concentration

Mössbauer spectra of $(Fe_{1-x}Mo_x)_{80}B_{20}$ at temperatures 300K, 77K and 6K are shown in Fig. 4.31(a,b,c). In spite of the different values of T_c due to slight difference in Mo-content, the Mössbauer spectra up to 4% Mo are quite similar. The lines are much broader than in the case of Fe-B and Fe-Ni-B amorphous alloys. The hpyerfine field distributions could be fitted to quasi-symmetrical Gauss profiles (as described before) with a relative width increasing from 25-29%. Some degreee of assymmetry of the lines was observed in the Mo-rich compositions, but not analysed in this work.

The hyperfine field decreases rapidly and a growth of central component with increasing Mo, is apparently observed. It should be mentioned that in the case of Mo-rich alloys (more than 5 at %), although the structureless spectrum reveals hardly any resolvable magnetic hyperfine splitting, it is nevertheless in a weakly magnetic state.

The compositional dependence of the average value of the hyperfine field at 300K, 77K and 6K is shown in Fig. 4.32. By replacing 10 at % Fe by Mo in $Fe_{80}B_{20}$, the values of average hyperfine field at 6K is 40% smaller than that of $Fe_{80}B_{20}$. It is found, that the average hyperfine field decreases linearly as a function of Mo concentration in the range $0 \leq x \leq .125$. A good fit to the $\overline{HF}$(Fe) at 6K in these concentration range can be obtained, based on the following equation:

$$\overline{HF}(Fe) = (29.3-86.7x)\text{Tesla} \qquad (58)$$

The linear behaviour of $\overline{HF}$(Fe) at 6K as a function of Mo concentration is consistent with the dependence of average magnetic moment/TM atom on x.

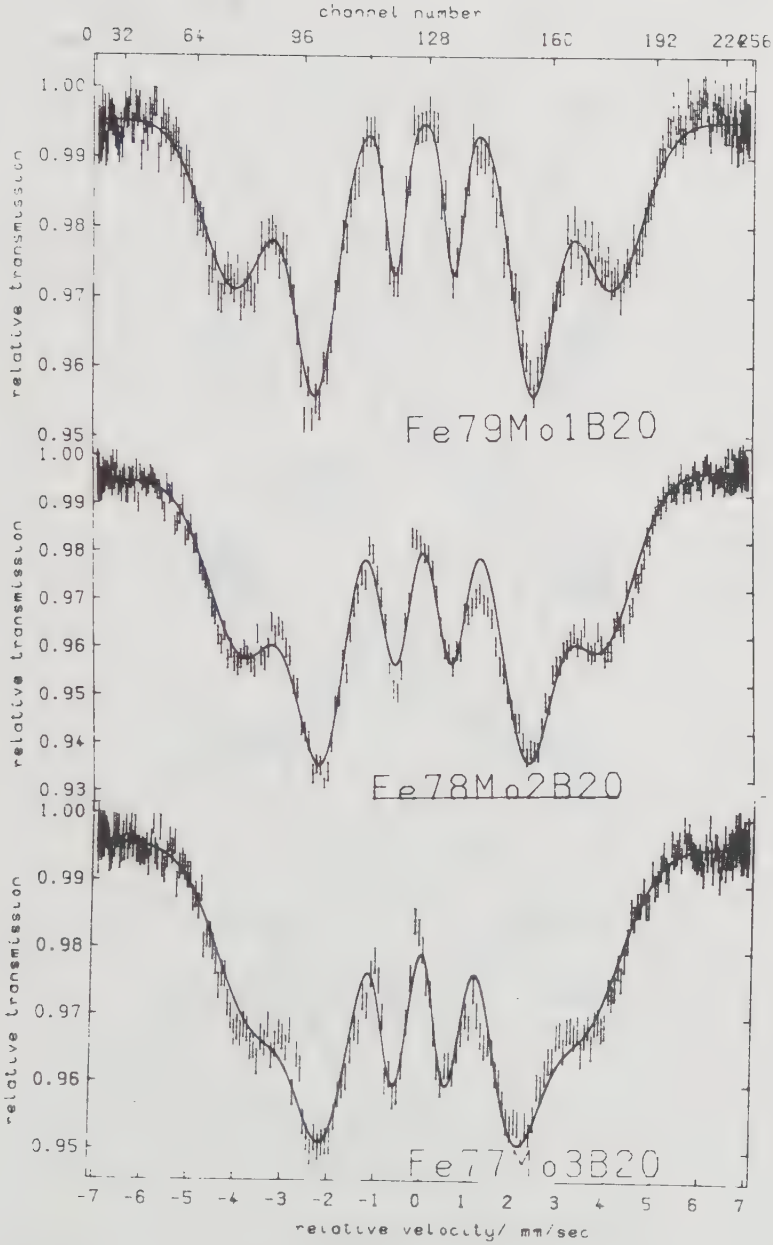

Fig. 4.31(a): MS for $(FeMo)_{80}B_{20}$ at RT

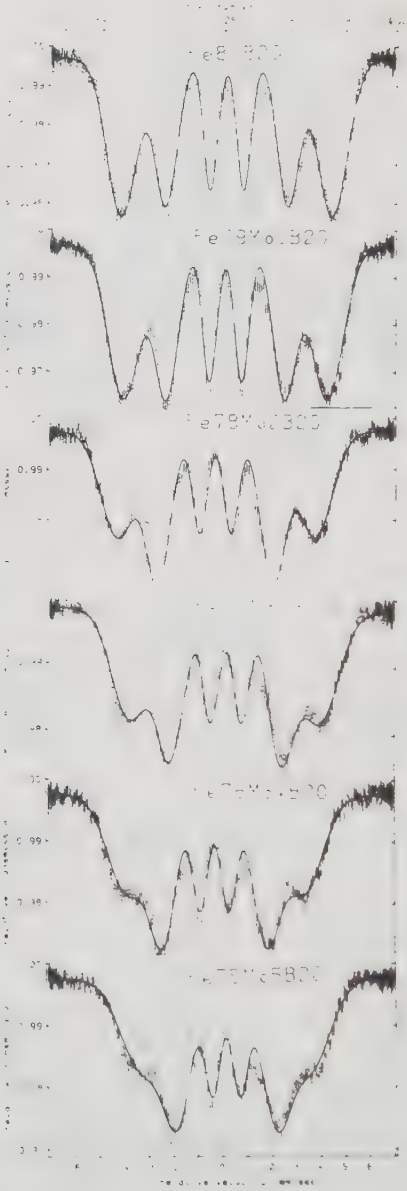

Fig. 4.31(b): MS for $(FeMo)_{80}B_{20}$ at 77K

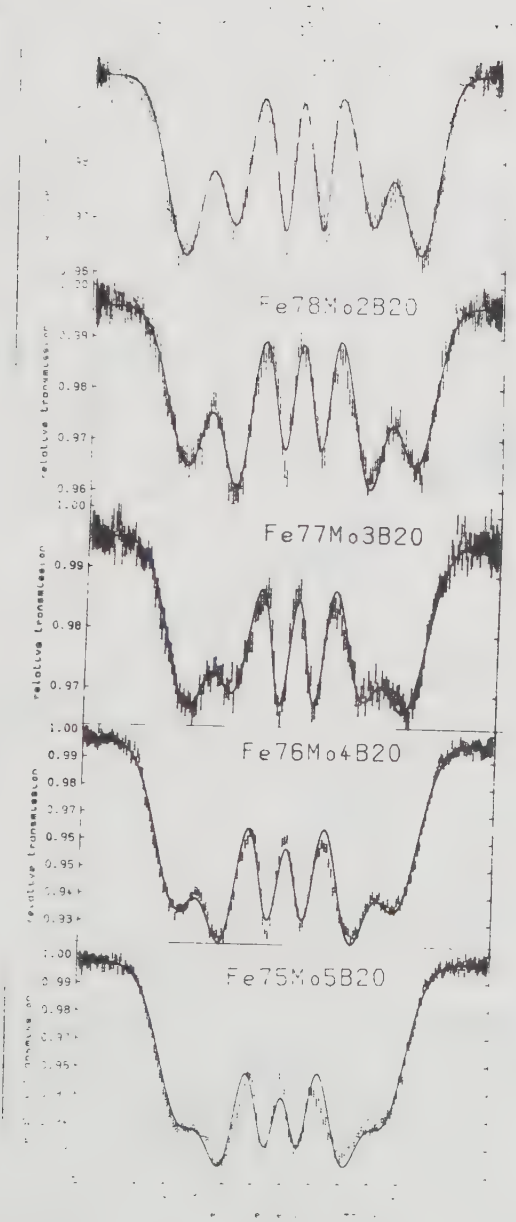

Fig. 4.31(c): MS for $(FeMo)_{80}B_{20}$ at 6K

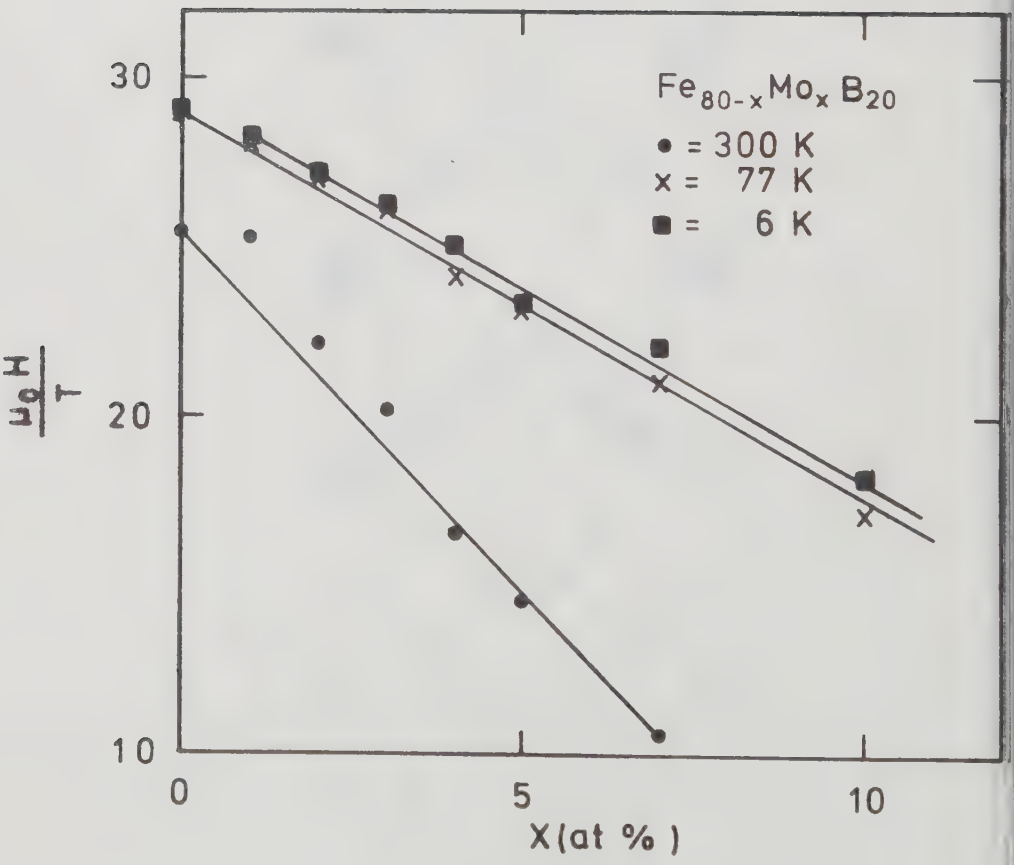

Fig. 4.32: The average hyperfine field at 300K, 77K and 6K of amorphous $Fe_{80-x}Mo_xB_{20}$ as a function of Mo concentration x

Table 4.14: Parameters obtained from analysis of Mössbauer effect data of $Fe_{80-x}Mo_xB_{20}$ at 300, 77 and 6K, respectively

Compound			T	$\mu_o \cdot H^*$	I·S +	Q·S(x10)	$2\Delta H_{\frac{1}{2}}$
Fe	Mo	B	K	T	mm/sec	mm/sec	H
80	-	20	300	25.42	0.043(1)	-0.006(1)	19
			77	28.98	0.059(1)	-0.009(2)	20
			6	29.08	0.059(1)	-0.006(2)	20
79	1	20	300	25.39	0.041(2)	-0.001(1)	20
			77	28.03	0.048(1)	-0.003(1)	20.3
			6	28.17	0.056(1)	-0.001(1)	20.8
78	2	20	300	22.15	0.043(1)	-0.011(3)	24
			77	27.03	0.050(1)	-0.001(1)	23
			6	27.22	0.056(2)	-0.008(3)	22
77	3	20	300	20.21	0.054(2)	-0.003(2)	25.0
			77	26.04	0.050(1)	0.001(1)	26.0
			6	26.25	0.055(1)	-0.005(3)	24.0
76	4	20	300	16.51	0.030(3)	0.001(1)	28
			77	24.19	0.043(2)	0.003(2)	27
			6	25.18	0.070(2)	-0.002(1)	22.0
75	5	20	300	14.64	0.045(1)	0.004(2)	27
			77	23.12	0.048(2)	0.003(1)	25
			6	23.33	0.065(2)	-0.001(1)	23.0
73	7	20	300	10.67	0.051(1)	0.056(1)	-
			77	21.16	0.050(1)	0.012(2)	26
			6	22.00	0.060(1)	-0.001(1)	22.4
70	10	20	300	-	0.051(1)	0.055(1)	-
			77	17.14	0.051(1)	0.012(2)	25
			6	18.29	0.055(1)	-0.003(2)	22.4

+ I.S. values are calculated with respect to α-Fe at room temperature. Figures in the paranthesis indicate the error in third place.

* Error in hyperfine field calculation ±0.20 T.

Table 4.14 shows that the isomer shift of such alloys increases with Mo concentration, which varies in magnitude from +.041±-.002 (for x=0) to +.070±.002 (for x=.125). As discussed previously, quadrupole splitting in these alloys at temperatures $T<T_c$ can not be expected, which is in agreement with the experimental observation. However, at $T>T_c$, for the samples with 7 at% and 10 at % Mo, a quadrupole splitting has been observed.

In Fig.4.33, the hyperfine field at Fe-sites at 6K is plotted against the calculated iron moment μ_{Fe}. The experimental points exhibit roughly a linear dependence with $\bar{\mu}_{Fe}$ which is represented by

$$\overline{HF}(Fe) = A\ _{Fe}, \text{ with } A = 14\ T/\mu_B \qquad (59)$$

A behaviour similar to that mentioned above is also observed in the $Fe_{100-x}B_x$ amorphous alloys /116/.

It has been observed in these alloys, that up to temperatures as high as .5 T_c the magnetization $M_s(T)$ varies according to Bloch's equation. The values for the coefficient B obtained from the experimental curves are listed in Table 4.13. A reasonable agreeement is found with the B values reported for some of the compositions by Chien et al /106/ from $\overline{HF}(Fe)$ versus $T^{3/2}$ dependence. The concentration dependence of sitffness constant (D) for all the amorphous alloys is shown in Fig. 4.34. A decrease of 45% in D in amorphous alloy $Fe_{80}B_{20}$ by the addition of 10 at % Mo is observed.

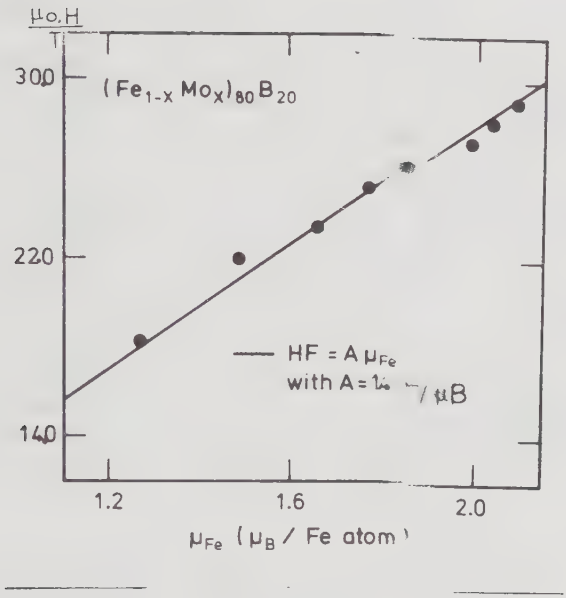

Fig. 4.33: Average hyperfine field (HF) at 6K versus average magnetic moment per atom

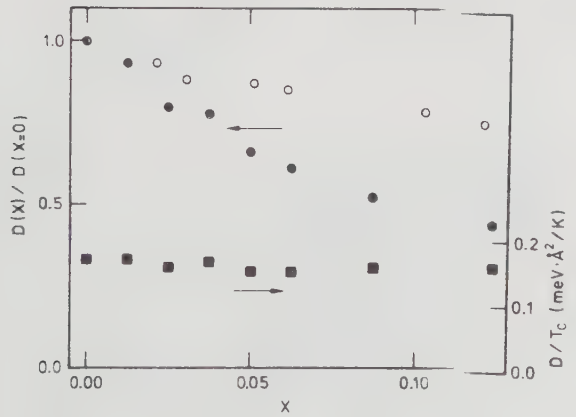

Fig. 4.34: Concentration dependence of the reduced spin-wave stiffness constant D(x)/D(0) (●) and the ratio D/T_c (■) for amorphous $(Fe_{1-x}Mo_x)_{80}B_{20}$ alloys. For comparison values of D(x)/D(0) for b.c.c. $Fe_{1-x}Mo_x$ alloys calculated from /124/ are also shown (o). The circle at x=0 is common.

$Fe_{85-y}Cr_yB_{15}$ $(0 \leq y \leq 20)$ and $Fe_{95-x}Cr_5B_x$ $(15 \leq x \leq 25)$

The temperature dependence of reduced spontaneous magnetization for amorphous alloys $Fe_{85-y}Cr_yB_{15}$ $(0 \leq y \leq 20)$ and $Fe_{95-x}Cr_5B_x$ $(15 \leq x \leq 25)$ is shown in Fig. 4.35. Theoretical predictions based on molecular field theory for S=1 describe reasonably well the temperature dependence of reduced magnetization in crystalline Fe. It becomes immediately obvious that $M_s(T)/M_s(0)$ versus T/T_c curve for these amorphous alloys fall well below that for crystalline Fe. For a fixed Cr concentration the flatness of the measured curves decreases with increasing boron concentration, inconformity with the behaviour observed in $Fe_{100-x}B_x$ /123/ but for fixed boron concentration it increases with the addition of Cr.

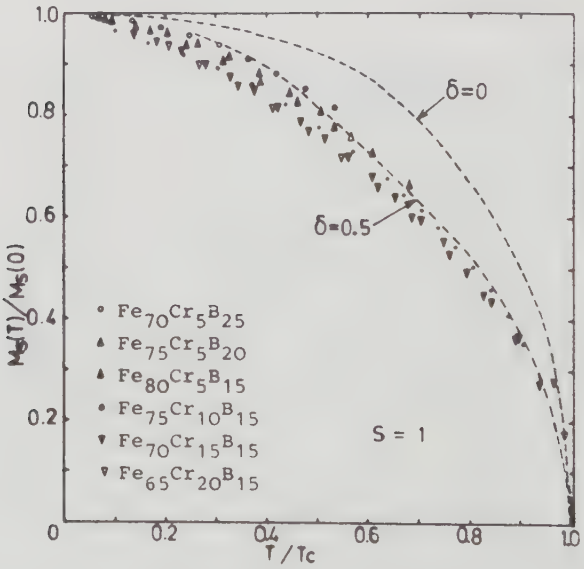

Fig. 4.35: Reduced magnetization M(T)/M(0) versus reduced temperature T/T_c for an applied field of 0.1 Tesla

In Table 4.15, the values of average magnetic moment/TM atom at OK, spin-wave parameters B and D, the ratio (D/T_c) and the Curie temperature (T_c) of the investigated samples are given.

Fig. 4.36 shows $\bar{\mu}$ as a function of Cr concentration. The solid curve in Fig. 4.36, which gives an excellent fit to the observed data, can be obtained using

$$\bar{\mu} = (2.05-9\cdot7y) \qquad (60)$$

The slope $\frac{d\bar{\mu}}{dy}$ for $0 \leq y \leq 20$ is -.9·7 at % Cr, which is in good agreement with the value obtained by Durand /18/ in some amorphous $(FeCr)_{79}P_{13}B_8$ alloys.

Table 4.16 gives the value of average hyperfine field, isomer shift, quadrupole splitting and relative dispersion at temperatures 300K, 77K and 6K for amorphous $Fe_{85-y}Cr_yB_{15}$ and $Fe_{95-x}Cr_5B_x$ alloys.

In Fig. 4.37a Mössbauer spectra of $Fe_{95-x}Cr_5B_x$ $(15 \leq x \leq 25)$ taken at 6K are shown. Fig. 4.37b shows the Mössbauer spectra of $Fe_{75}Cr_{10}B_{15}$ and $Fe_{70}Cr_{15}B_{15}$ at 6K and 300K, 6K, respectively.

A fit to the hyperfine field distributions based on quasi-symmetrical Gauss profiles (as described before) shows that the line width ranges between 20 and 30%. The lines are much broader than in the case of Fe-B and Fe-Co-B amorphous alloys. Some degree of asymmetry in the lines observed for Cr-rich compositions. Alloys containing more than 10 at % Cr could not be fitted at all primarily because the magnetic ordering is not well defined in these alloys.

Table4.15:Spin-wave and magnetization parameters

Compound	T_c(K)	B ($10^{-5}K^{-3/2}$)	D (meVÅ^2)	D/T_c (meVÅ$^2K^{-1}$)	$\bar{\mu}_{exp}$ (μ_B/TM at)	$\bar{\mu}_a$ (μ_B/TM at)	$\bar{\mu}_F$ (μ_B/TM at)
$Fe_{70}Cr_5B_{25}$	522[a]	2.83	92.3	0.177	1.65	1.60	1.46
$Fe_{75}Cr_5B_{20}$	491[a]	3.97	71.2	0.145	1.66	1.62	1.50
$Fe_{80}Cr_5B_{15}$	410[a]	6.26	52.2	0.127	1.65	1.65	1.65
$Fe_{75}Cr_{10}B_{15}$	298[a]	12.00	43.0	0.144	1.15	1.29	1.18
$Fe_{70}Cr_{15}B_{15}$	213[b]	20.00	39.8	0.187	0.78	0.94	0.71
$Fe_{65}Cr_{20}B_{15}$	145[b]	32.60	36.5	0.252	0.54	0.59	0.24
$Fe_{85}B_{15}$	577[c]	3.4[c]	65.5[c]	0.114	2.12[c]	-	-

a - Ref.83 b - present work, c - Ref. 107

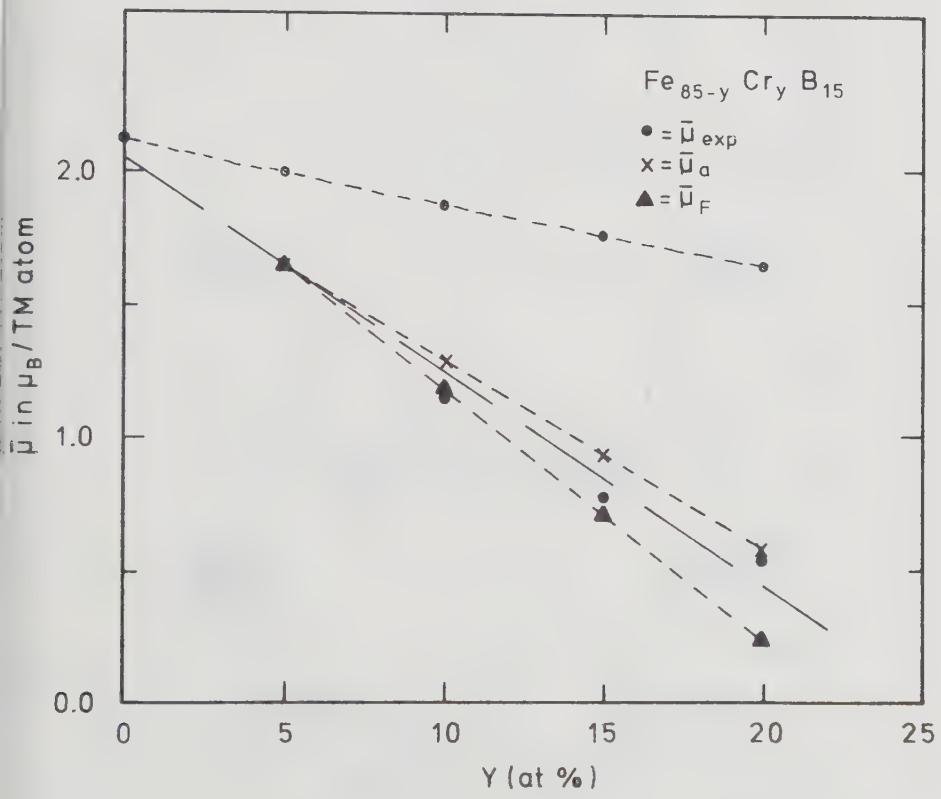

Fig. 4.36: Average magnetic moment versus Cr-concentration O-according to rigid-band model. Other symbols are explained in the text

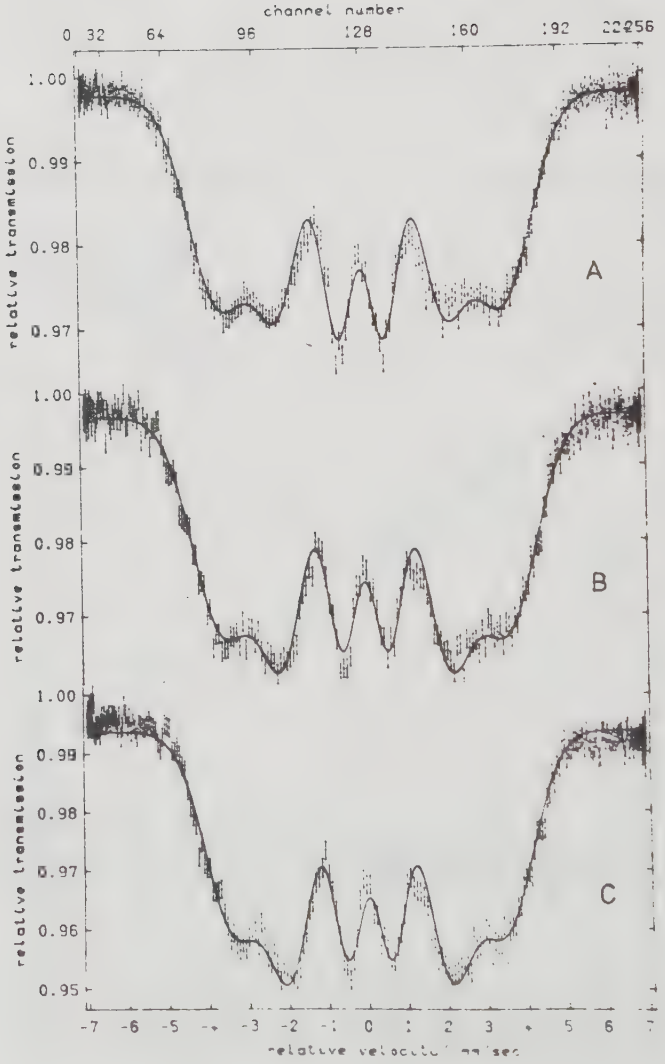

Fig. 4.37(a): Mössbauer spectra of $Fe_{95-x}Cr_5B_x$
A) x=15, B) x=20 and C) x=25 at 6K

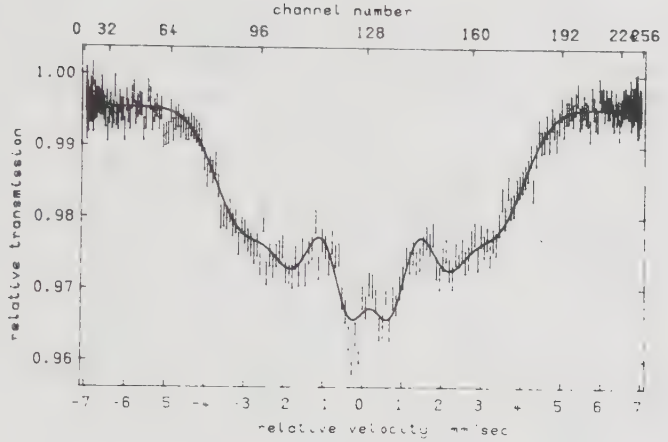

Fig. 4.37(b): Mössbauer spectrum for amorphous $Fe_{75}Cr_{10}B_{15}$ alloy at 6K

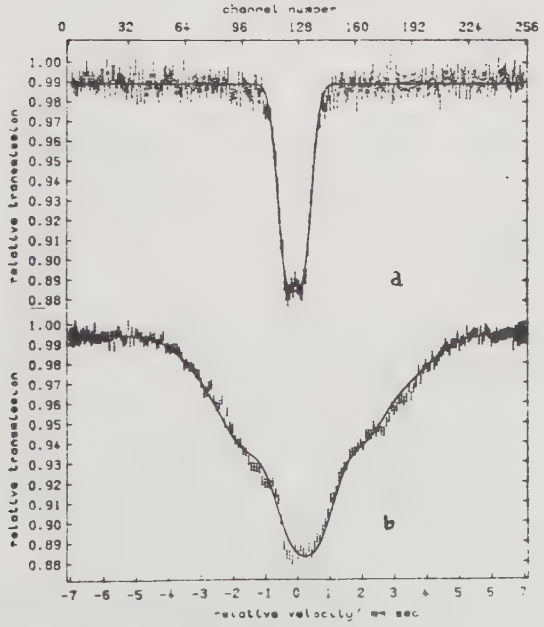

Fig. 4.37(c): Mössbauer spectra for amorphous $Fe_{75}Cr_{15}B_{15}$ alloy at a) 300K and b) 6K

Fig. 4.38 shows the compositional dependence of the average values of the hyperfine field, $\overline{HF}$(Fe) at 77K and 6K, respectively. A small decrease of $\overline{HF}$(Fe) with the increasing boron concentration has been observed whereas the average hyperfine field value decreases faster with the addition of few percent of chromium. For $0 \leq y \leq 10$, the average hyperfine field decreases linearly and suddenly drops to a lower value at 15 at % Cr. Further addition of Cr, e.g., 20 at % Cr did not significantly change the average hyperfine field value at 6K from that found in 15 at % Cr alloy. The behaviour of $\overline{HF}$(Fe) as a function of y in the linear region can be fitted well using the following equation:

$$\overline{HF}(Fe) = (29.4 - .7y)\,\text{Tesla} \qquad (61)$$

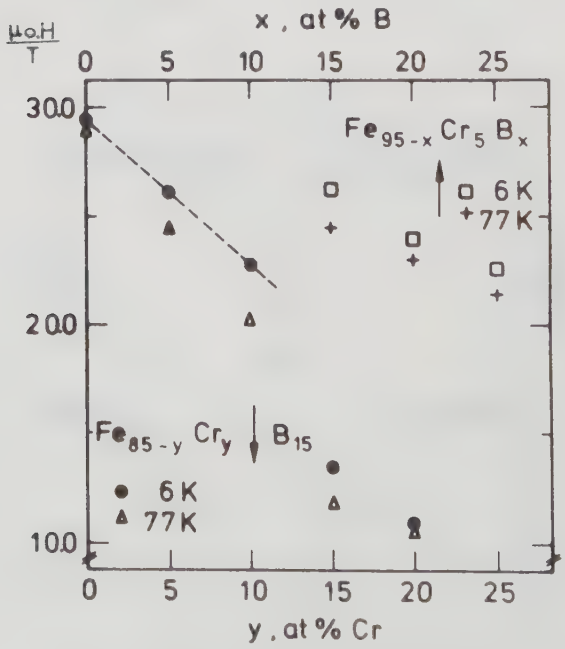

Fig. 4.38: Concentration dependence of the average hyperfine field at 6K and 77K

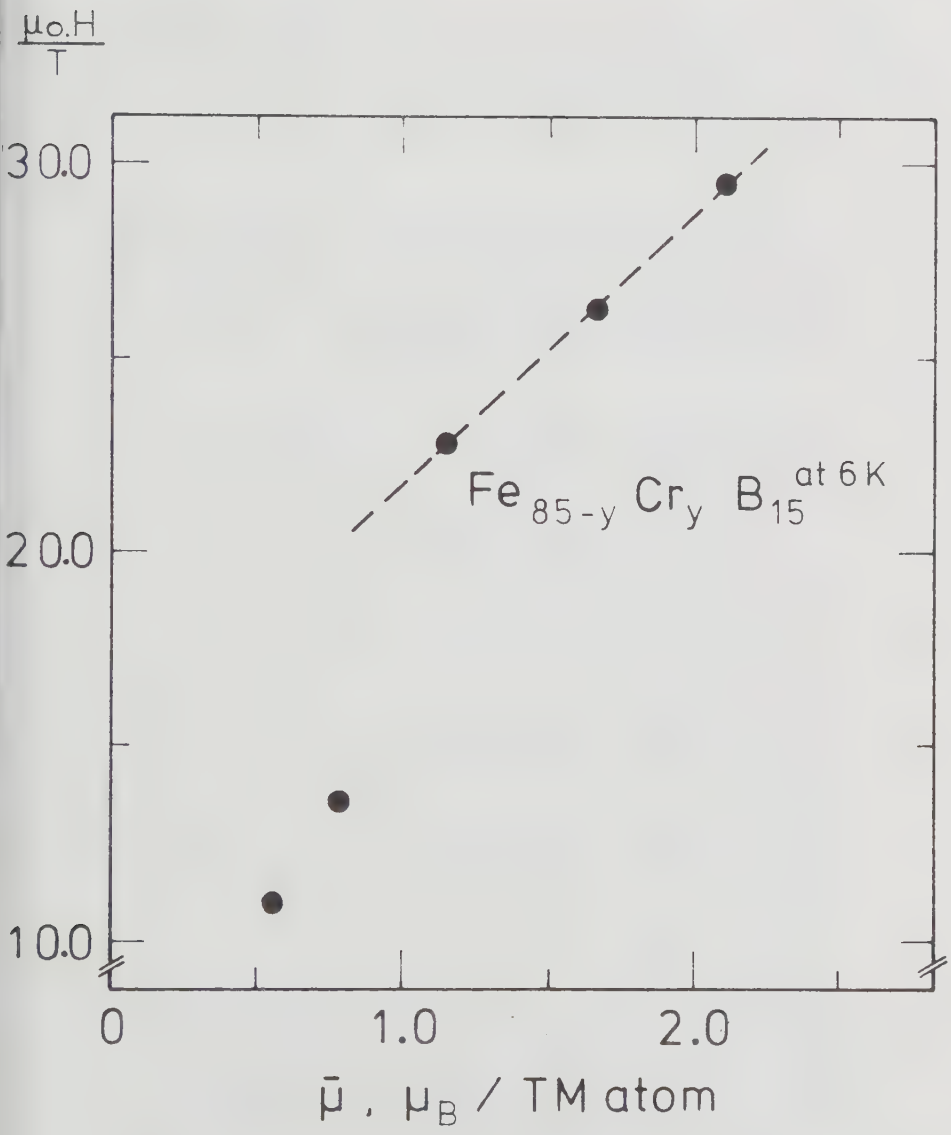

Fig. 4.39: Average hyperfine field as a function of $\bar{\mu}$ for amorphous $Fe_{85-y}Cr_yB_{15}$ alloys

In Fig. 4.39 $\overline{HF}$(Fe) as a function of average magnetic moment $\bar{\mu}$/TM atom is shown. The relation between $\overline{HF}$(Fe) and average magnetic moment/TM atom can be described in the linear region by the phenomenological equation (1).

The isomer shift for these alloys (see table 4.16) increases with the addition of boron and chromium. The quadrupole splitting in the magnetically ordered state has been observed to be insignificant. However, at $T>T_c$, a pure quadrupole interaction can be clearly seen, Fig. 4.40.

At low temperatures the magnetization can be described by Bloch's $T^{3/2}$ law as seen in Fig. 4.41 for the amorphous alloys containing Cr. Similar to other amorphous ferromagnets, this low temperature behaviour persists up to .3-.7 T_c, i.e., up to much higher temperatures than for crystalline systems. The experimental values of the coefficient B, are listed in table 4.15 together with the values of the spin-wave sitffness constant (D). For $Fe_{95-x}Cr_5B_x$ alloys, D and D/T_c increase with x consistent with similar behaviour observed in $Fe_{100-x}B_x$ alloys /107/. In case as the Curie temperature decreases more rapidly with y than D does, the ratio D/T_c increases. Fig. 4.42 shows the variation of D and D/T_c of amorphous alloys due to the addition of Cr, also included in this figure are the values of D as a function of y for $Fe_{1-y}Cr_y$ crystalline alloy for comparison.

Mössbauer spectra for amorphous $Fe_{80}Cr_5B_{15}$ alloy taken at various temperature are shown in Fig. 4.43. In Fig. 4.44, the temperature dependence of $\overline{HF}$(Fe) normalized to its value at T=0 is plotted against $T^{3/2}$ for $Fe_{80}Cr_5B_{15}$ and $Fe_{70}Cr_{15}B_{15}$. The observed values of the coefficient B of $6.5 \cdot 10^{-5}$ $K^{-3/2}$ and $24 \cdot 10^{-5}$ $K^{-3/2}$ respectively agree reasonably well with the values of B obtained from magnetization meausrements, table 4.17.

Table 4.16: Parameters obtained from analysis of Mössbauer effect data of $Fe_{85-y}Cr_yB_{15}$ and $Fe_{95-x}Cr_5B_x$ at 300, 77 and 6K, respectively.

Fe	Cr	B	T / K	$\mu_o \cdot H^*$ / T	I.S $^+$ / mm/sec	Q.S(x10) / mm/sec	$2\Delta H_{\%}$ / H
85	-	15	300	26.01	0.032(1)	-0.001	20.0
			77	29.20	0.030(1)	-0.003	20.0
			6	29.50	0.032(1)	-0.001	20.5
75	10	15	300	-	0.035(2)	0.053	25.0
			77	20.30	0.037(1)	-0.001	28.0
			6	22.82	0.038(1)	-0.001	27.8
70	15	15	300	-	0.062(1)	0.054	28.0
			77	11.87	0.064(2)	-0.001	28.9
			6	13.65	0.062(1)	-0.003	29.0
65	20	15	300	-	0.036(1)	0.053	29.0
			77	10.75	0.035(1)	-0.003	28.0
			6	11.50	0.057(1)	-0.007	30.2
80	5	15	300	17.00	0.019(1)	-0.003	28.0
			77	24.40	0.024(2)	-0.003	28.0
			6	26.25	0.020(1)	0.000	29.5
75	5	20	300	15.03	0.035(1)	-0.001	28.5
			77	23.03	0.040(2)	-0.001	28.5
			6	24.16	0.039(1)	-0.007	28.9
70	5	25	300	14.85	0.041(1)	-0.001	29.8
			77	21.53	0.045(1)	-0.003	29.8
			6	22.60	0.045(1)	-0.003	29.5

$^+$ I.S. values are calculated with respect to α-Fe at room temperature. Figures in the paranthesis indicate the error in third place.

* Error in hyperfine field calculation ±0.35 T

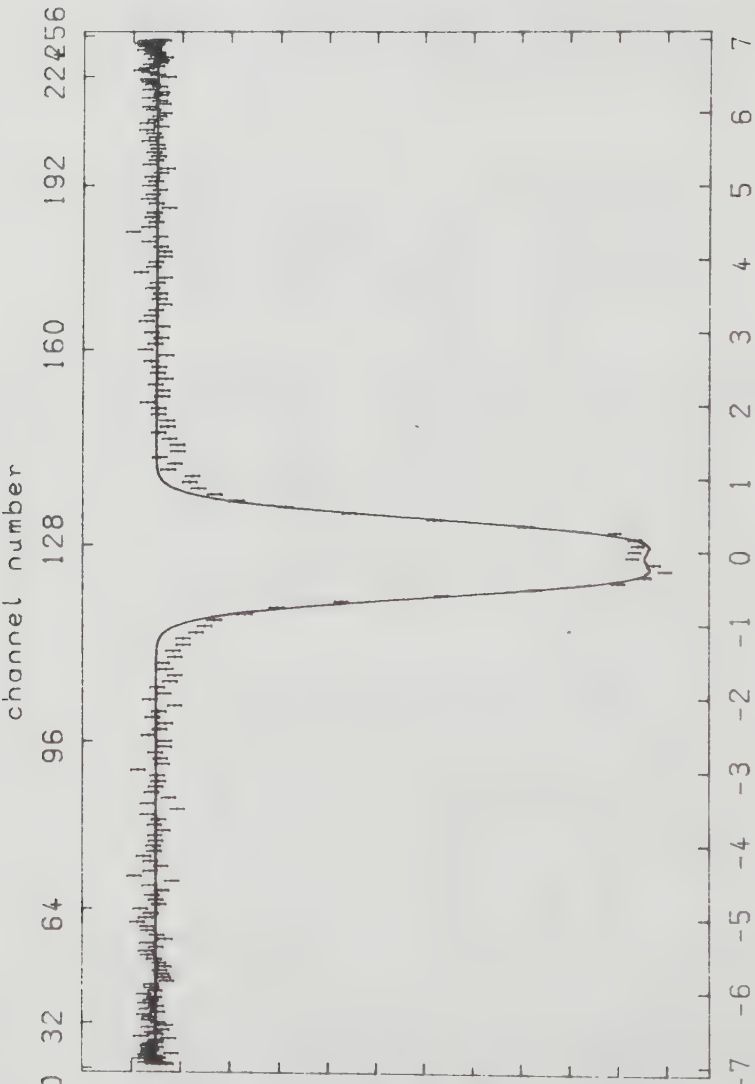

Fig. 4.40: Mössbauer spectrum of $Fe_{65}Cr_{20}B_{15}$ at room temperature (i.e. at $T<T_c$)

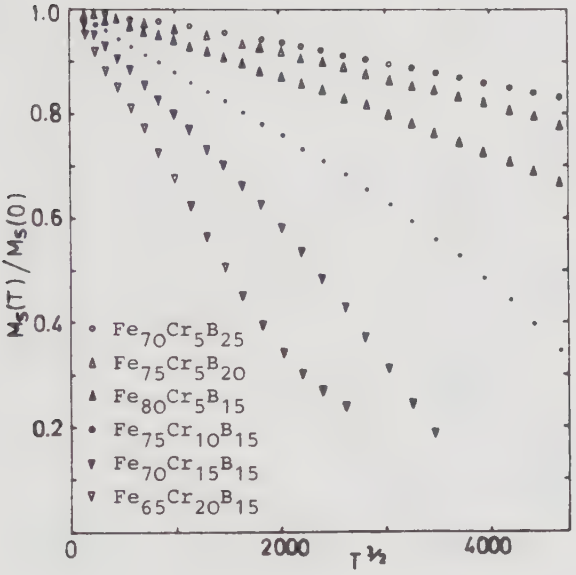

Fig. 4.41: Reduced magnetization M(T)/M(O) versus $T^{3/2}$. Applied field -0.52 Tesla

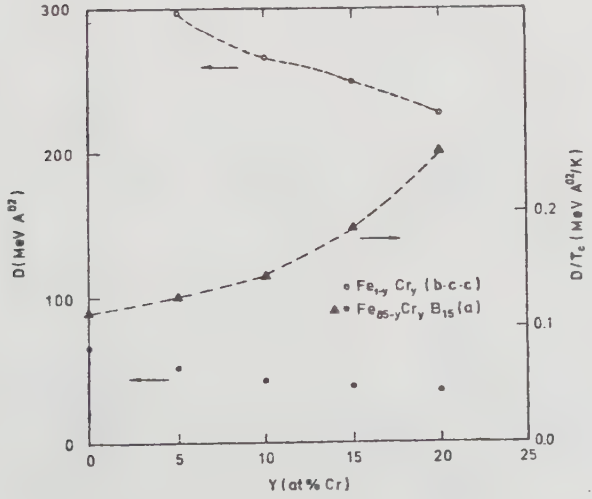

Fig. 4.42: Composition dependence of stiffness constant (D) and the ratio (D/T_c) for crystalline and amorphous Fe-Cr alloys

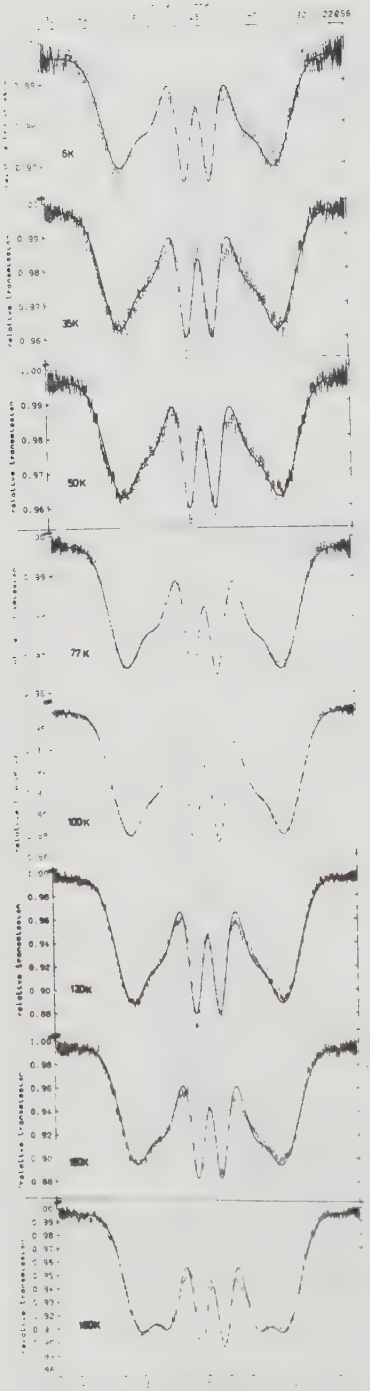

Fig. 4.43:
Mössbauer spectra of amorphous $Fe_{80}Cr_5B_{15}$ alloys of various temperatures

Table 4.17: Values of coefficient 'B' from Mössbauer spectroscopy

Sample	B (10^{-5} $K^{-3/2}$)
$Fe_{80}Cr_5B_{15}$	6.5
$Fe_{70}Cr_{15}B_{15}$	24.0

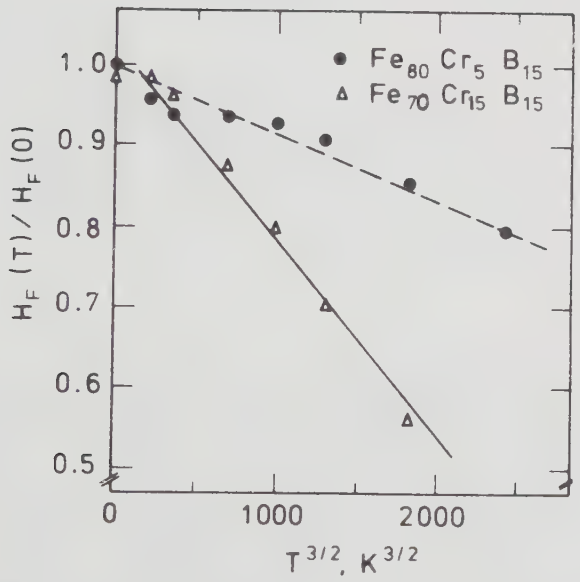

Fig. 4.44: Reduced hyperfine field versus $T^{3/2}$ for $Fe_{80}Cr_5B_{15}$ and $Fe_{70}Cr_{15}B_{15}$

Discussion

Average magnetic moment as a function of Mo and Cr concentration

It can be seen from the results, table 4.13 and 4.15 and Fig. 4.30, 4,36 that the decrease of average magnetic ($\bar{\mu}$) for amorphous $(Fe_{1-x}Mo_x)_{80}B_{20}$ ($0 \leq x \leq .125$) and $Fe_{75-y}Cr_yB_{15}$ ($0 \leq y \leq 20$) with increasing Mo and Cr concentration is much steeper than their crystalline counterparts. The case of crystalline b.c.c. $Fe_{1-x}Mo_x$ and $Fe_{1-y}Cr_y$ alloys, the initial slope (as the chromium or molybdenum concentration tends to zero) is found to be -2.1 μ_B/atom, which is close to that expected on the basis of a simple rigid-band model, -2.0 μ_B/atom /124/. The average magnetic moment/TM atom, determined from the spontaneous magnetization at OK for these crystalline alloys for high concentration of Mo and Cr, as a function of outer electron configuration exhibit large deviations from the Slater-Pauling curve.

The variation of $\bar{\mu}$ as a function of Mo and Cr concentration for amorphous $(Fe_{1-x}Mo_x)_{80}B_{20}$ and $Fe_{85-y}Cr_yB_{15}$ is shown by the solid lines and the corresponding slopes are found to be -8.1 μ_B ($0 \leq x \leq .125$) and -9.7 μ_B ($0 \leq y \leq 20$), respectively. These slope values for high concentrations of Mo and Cr being greater than that expected from a rigid-band model and hence these alloys like their crystalline counterparts, show considerable deviations from the Slater-Pauling curve. The rigid-band approximation should be applicable only for small concentrations of impurities that weakly perturb the periodic potential of the matrix. The rigid-band approximation should fail for $|Z| \geq 2$, e.g., in the case for Mo, Cr in Fe as is evident from Fig. 4.30 and 4.36 and table 4.13 and 4.15.

Two other approaches have been taken to calculate the average magnetic moment/TM atom for amorphous $Fe_{85-y}Cr_yB_{15}$ alloys. In the first approach, $\bar{\mu}$ is calculated from the weighted average per formula unit ($\bar{\mu}_a$), attributing $2\mu_B$, $-4\ \mu_B$ and $0\ \mu_B$ to the Fe, Cr and B atoms, respectively. In the second, Friedel's formula /17/ is used to calculate $\bar{\mu}$. It is obvious from the table 4.15 and Fig. 4.36 that the values of $\bar{\mu}_F$ (average magnetic moment/TM atom from Friedel's formula) are closer to experimental values than $\bar{\mu}_a$. The behaviour of $\bar{\mu}$ as a function of Mo and Cr can be physically understood on the basis of Friedel's model as described below.

In terms of the Friedel's model (given in detail in sec. 2), the repulsive potentials on the impurities Mo and Cr are large enough to repell the majority spin virtual bound state above the Fermi-level. Analysis of the tabel 4.18 shows that the virtual bound state is practically empty for Mo and Cr in amorphous $Fe_{80}B_{20}$ and $Fe_{85}B_{15}$, respectively. The paramter $-(\xi+Z)$, which has a value of 10 when the 3d state has been pushed above the Fermi-level (E_F) or 0 when it lies below E_F, has been found to be almost 10 for Mo and Cr in amorphous $Fe_{80}B_{20}$ and $Fe_{85}B_{15}$ alloys, respectively. This implies that 3d↑ impurity virtual bound state for both the systems lies just above the Fermi-level. The 3d↑ virtual bound state being above the Fermi-level, five 3d electrons will be transferred to 3d↓ band of the host and the average magnetic moment will be reduced by $10\ \mu_B$ in addition to the change due to the valence electron difference between the impurity and the host. Therefore, charge transfer from the virtual bound state will result in the enhancement of the impurity moment at the expence of the host moment. The virtual bound state model assumes the 3d↑ and 3d↓ charge displacements to occur over screening lengths which are functions of the densities of states of the two sub-bands and does predict appreciable host moment perturbations consistent with the neutron data for crystalline systems /125/.

In recent works /18,126/, it is reported that in several Fe-based amorphous alloys containing Mo and Cr, the Curie temperature and the average magnetic moment of the alloys decrease with the increasing amount of Mo and Cr. It is concluded from these experimental results that such a behaviour of $\bar{\mu}$ and T_c due to the presence of an antiferromagnetic exchange interaction between Fe and (Mo,Cr), which is likely to be greater than the ferromagnetic Fe-Fe interaction. However, the results of the present work show a much faster decrease with Mo, Cr addition and can be explained satisfactorily only on the basis of virtual bound state model and not in terms of rigid-band model.

Table 4.18: Effect of TM-substitutions for Fe in $Fe_{80}B_{20}$ and $Fe_{85}B_{15}$ amorphous alloys

solute	Z	$\bar{\xi}$	Z↑	Z↓	n=5+Z↑
Mo	-2	-7.6	-4.8	+2.8	0.2
Cr	-2	-7.9	-4.95	+2.95	0.05

Ref. to table 4.18:

Z↑ and Z↓ are the changes in population of the majority and minority spin bands, respectively, and Z = Z↑+Z↓. n is the number of electrons within the corresponding virtual bound states and ξ is the slope of the average moment versus solute content curve.

Average hyperfine field versus average magnetic moment

The hyperfine field at iron site obtained from Mössbauer spectroscopy measurement has been used in combination with the saturation magnetization at OK, to evaluate the separate contribution of Fe and Mo atoms to the average magnetic moment of amorphous $(Fe_{1-x}Mo_x)_{80}B_{20}$ alloys. It

is found that the composition dependence of the ratio d[HF(x)/HF(0)]/dx is -2.8. This implies a decrease of the hyperfine field at iron site with the addition of Mo. A linear variation in the magnetic moment of iron with Mo concentration would produce a similar change in the hyperfine field at the iron site. It is thus interesting to interpret such a variation in hyperfine field as reflecting a change in average iron moment. Assuming that the magnetic moment on the Mo atom does not change with the Mo concentration and is negligibly small as in the crystalline cases /124/, the value of $\bar{\mu}_{Fe}$ have been calculated from $\bar{\mu}$ (table 4.19). The experimental points lie on a straight line represented by equation (59).

Table 4.19: Magnetic moment for amorphous $(Fe\text{-}Mo)_{80}B_{20}$ alloys

Compound	$\bar{\mu}$ (μ_B/TM at)	$\bar{\mu}_{Fe}$ (μ_B/Fe at)
$Fe_{80}B_{20}$	2.09	2.09
$Fe_{79}Mo_1B_{20}$	2.01	2.04
$Fe_{78}Mo_2B_{20}$	1.94	1.99
$Fe_{77}Mo_3B_{20}$	1.78	1.85
$Fe_{76}Mo_4B_{20}$	1.69	1.78
$Fe_{75}Mo_5B_{20}$	1.56	1.66
$Fe_{73}Mo_7B_{20}$	1.36	1.49
$Fe_{70}Mo_{10}B_{20}$	1.12	1.27

In the case of crystalline b.c.c. $Fe_{1-x}Mo_x$, the results obtained from the neutron scattering experiments of Low and Collins /125/ show that there is not only a widespread disturbance about (10 A°) in the moment on all

the iron atoms surrounding an impurity site but also an antiparallel moment (0.1±0.6) associated with the impurity. An observed slight increase of the Fe moment $\bar{\mu}_{Fe}$ is also confirmed by the similar increase of the hyperfine field HF(Fe), i.e., a positive slope d[HF(x)/HF(0)]/dx = +.22 for b.c.c. $Fe_{1-x}Mo_x$ alloys. Campbell /127/ after an analysis of neutron scattering data, showed that the moment on an iron atom varies in an oscillating manner as the distance from an impurity atom increases. Thus, in case of crystalline b.c.c. $Fe_{1-x}Mo_x$, an increase of hyperfine field at iron site with increasing x is observed with a similar increase in average iron moment, whereas a decrease of average iron moment with increasing Mo concentration has been observed in case of amorphous $(Fe_{1-x}Mo_x)_{80}B_{20}$ alloys. The main difference between the amorphous and crystalline alloys comes from the difference in the atomic configurations beyond the first nearest neighbour.

Fig. 4.39 shows the plot of hyperfine field $\overline{HF}$(Fe) versus $\bar{\mu}$ for amorphous $Fe_{85-y}Cr_yB_{15}$ alloys. In the linear region down to $\bar{\mu} \simeq 1\ \mu_B$, $\overline{HF}$(Fe) can be fitted to equation (1). The hyperfine field at Fe-site depends on the change in magnitude of the moment on the surrounding sites because Cr is known to diminish the moment on the Fe-site in crystalline alloys /128/. If the moments on the surrounding sites are antiparallel and increase in magnitude the local moments will decrease. The hyperfine field is proportional to the local site moment rather to any single neighbour site moment, because the coefficient 'a' is greater than the coefficient 'b' in equation (1). It is found that the magnetic moment/Fe atom present remains almost constant at 2.15 μ_B ($\bar{\mu}$ for $Fe_{85}B_{15}$ = 2.14 μ_B) up to a Cr concentration of 10 at % for these amorphous alloys. The composition dependence of the ratio $d[\overline{HF}(y)/\overline{HF}(0)]/dy$ is -0.02, $\overline{HF}(0)$ being the average hyperfine field in $Fe_{85}B_{15}$ at 6K.

This implies a slight decrease of the hyperfine field at iron site with the addition of Cr up to 10 at %, the decrease being faster beyond 10 at % Cr. A faster decrease of Fe moment beyond 10 at % Cr could be due to the increased tendency of Cr atoms clustering around Fe atoms and thereby reducing Fe moment considerably. In the crystalline iron-chromium system, the neutron scattering results show that /129/ the moments on the chromium atoms are antiparallel to those on the iron atoms, at least in the composition range 15-40 at % chromium.

It is observed in this work that the substitution of Cr in these amorphous alloys has a much more dramatical influence on the decrease of $\overline{HF}$(Fe) than in the crystalline alloy when Cr content is more than 10 at %. The stronger decrease of $\overline{HF}$(Fe) with increasing Cr content may be due to a significant change of the band structure, with changes of the magnetic moments of Fe and Cr, rather than a simple antiparallel orientation of the 4 μ_B Cr moments against the 2 μ_B iron moments.

Temperature dependence of spontaneous magnetization

It is obvious from Fig. 4.35 that the reduced magnetization versus reduced temperatures for the amorphous $Fe_{95-x}Cr_5B_x$ and $Fe_{85-y}Cr_yB_{15}$ alloys falls below that for Fe. This seems to be a feature which all the amorphous ferromagnetic alloys studied /130/ so far have in common. Two general, but basically opposite theoretical approaches have been proposed to justify the diminished curvature of the reduced magnetization versus reduced temperature curve in amorphous ferromagnets. In the first approach, a fixed unique value is assigned to the exchange coupling constant between spins on magnetic atoms and the amorphous

nature of the alloy is taken into account by assuming a random distribution of local anisotropy fields /131,132/. In the second approach, the structural fluctuations in the amorphous materials are assumed to manifest themselves in a distribution of exchange integrals /66/. Despite the fact that both the above mentioned approaches demonstrate that the universal magnetization curve for an amorphous ferromagnetic material must characteristically fall below that for the crystalline counterpart, the second approach is usually preferred to the first one for comparison with the experimental results for two reasons. First, contrary to the observed Mössbauer spectra, the theories under the first category predict a flat (structureless) Mössbauer spectrum /104, 106/ for amorphous ferromagnets below the Curie temperature. Second, the prediction based on the theory of Gubernatis et al /132/ that an identical value for the coefficient B of the $T^{3/2}$ term in equation (3) should be observed for both crystalline and amorphous ferromgnets is in direct contradiction with the experimental findings (table 4.13 and 4.15). Of the various theories proposed under the second category, only the molecular field approach of Handrich /66/ provides results in a simple analytical form.

Equation (31) (sec. 2) shows that

i) by setting $\delta=0$, the well known molecular field expression for crystalline ferromagnets is recovered and

ii) a progressive increase in the value of δ results in increased depression of spontaneous magnetization over the entire temperature range for $T \leq T_c$.

The observed temperature dependence of spontaneous magnetization is fitted in terms of the relation (31) by using various values of δ for S=1 with the result that the theoretical curves for $\delta=.5$ and S=1 gives a reasonable overall fit to the experimental data.

Although equation (31) is capable ofyielding a lower universal magnetization curve for glassy ferromagnets, it is still far from giving a quantative agreement with the experimental results. As is obvious from Fig. 4.35, even for the most reasonable values of δ=.5 for S=1, the experimental data lie above the theoretical curve for temperatures close to T_c and below for low enough temperatures. Similar disagreement between the theoretically predicted (δ=0) and experimentally observed variation for spontaneous magnetization with temperature has also been found in the case of crystalline ferromagnets. Such a discrepancy between the theory and experiment arises basically from the inadequacy of the molecular field approximation in the low temperature region, where a spin-wave description is more appropriate, or in close vicinity of the Curie temperature where a Heisenberg model gives better quantitative agreement with the observed temperature dependence of magnetization. Tsuei and Lilienthal /91/ find that the universal magnetization curve for amorphous $Fe_{75}P_{15}C_{10}$ alloy lies well below that for crystalline Fe_3P and the difference between them is quite significant. Contrary to the above observation, Vincze et al /133/ based on their Mössbauer studies on $(Fe_{1-x}Ni_x)_{75}B_{25}$ alloys in both amorphous as well as crystalline state, find no substantial difference between the reduced hyperfine field versus reduced temperature curve of the corresponding amorphous and crystalline alloys and hence conclude that structural disorder has a minor effect on the shape of hyperfine field curve whereas the high metalloid content is responsible for the rather fast decrease of hyperfine field with temperature in these materials. Therefore, the basic mechanism responsible for the faster decrease of spontaneous magnetization with temperature in amorphous ferromagnets compared with that in their crystalline counterparts is still not clear. Inspite of that, a distribution of the exchange interactions, as inferred from Mössbauer studies, remains a useful interpretation so far as the magnetic and electrical properties of amorphous ferromagnets are concerned.

Low temperature magnetization and spin-wave excitation

The following observations have been made for amorphous $(FeMo)_{80}B_{20}$ alloys on the basis of low temperature experimental results:

i) the stiffness constant (D) and Curie temperature (T_c) decrease with increasing Mo concentration. The composition dependence of D normalized to its value at x=0 is shown in Fig. 4.34 for amorphous $(FeMo)_{80}B_{20}$ alloys as compared to that for b.c.c. Fe-Mo crystalline alloys calculated from Aldred's data /124/. It is seen that, the values of D decrease about twice as fast in the amorphous alloys reaching for x=.125 about 45% of its value for x=0. As both D and T_c are proportional to the exchange interaction (J), the above mentioned decrease of D and T_c means a decrease of the average strength of the exchange interaction.

ii) The ratio D/T_c, which is a measure of the range of exchange interaction remains almost independent of Mo concentration, Fig. 4.34. These values are smaller than that of Fe and thereby suggest that at low temperatures the range of exchange interaction in these amorphous alloys is essentially confined to the nearest neighbours only.

For $Fe_{95-x}Cr_5B_x$ amorphous alloys D and D/T_c increase with x in a similar manner as observed in $Fe_{1-x}B_x$ /107/. In the case of $Fe_{85-y}Cr_yB_{15}$ amorphous alloys D is decreasing with increasing y (the rate of decrease being much steeper beyond y=10 at % Cr) indicating a reduction in the strength of the exchange interaction with the Cr substitution. However, as the Curie temperature decreases faster with y than D does the ratio D/T_c increases, which could be taken as an evidence for an increase of the range of exchange interaction with increasing chromium content. In addition to the above observation, table 4.15 and 4.17,

show that the values of the coefficient B obtained from the magnetic and Mössbauer measurements are in close agreement between the B values determined from these two methods suggests that the conventional spin-wave theory completely accounts for the observed low temperature magnetic behaviour.

The above observations are similar to those found in $(FeNi)_{80}B_{20}$, $(FeNi)_{75}B_{25}$ and $(FeCo)_{80}B_{20}$ amorphous alloys and hence the low temperature magnetization for the amorphous alloys containing Mo and Cr can be interpreted in a similar way as given in section 4.3.

Isomer shift

The observed increase of the isomer shift as a function of Mo and Cr concentration (see table 4.14 and 4.16) in these Fe-based alloys can be interpreted in a way similar to that discussed in the case of $(FeNi)_{80}B_{20}$, $(FeNi)_{75}B_{25}$ and $(FeCo)_{80}B_{20}$ in section 4.3.

4.5 ^{57}Fe isomer shifts due to low concentration of transition metals (T=Ni,Co,Cr,Mn,V) in amorphous $Fe_{80}T_3B_{17}$ alloys

When an impurity is put into an iron matrix, then the screening of the impurity excess charge causes a change in the charge and spin density at the neighbourin matrix atoms. In the case of magnetic transition d-element impurities, this charge screening takes place mainly by d-electrons, owing to the large d-electron density of states of the iron. The Mössbauer effect is very suitable for the investigation of the charge and spin density perturbation caused by the impurity at the matrix atoms, because the isomer shift and the hyperfine field are sensitive to changes in both the d and s electron charge and spin density, respectively.

In view of this, the influence of substitution of Fe with Ni,Co,Mn,Cr,V and some of the 4d and 5d element on the isomer shift as well as on the hyperfine field has been studied in the eutectic alloy $Fe_{83}B_{17}$. The Mössbauer spectra of ^{57}Fe measured at 6K for eight iron-based amorphous alloys with soluble magnetic d-impurities are shown in Fig. 4.45. The results of the study of Mössbauer spectra of ^{57}Fe due to various impurities are presented in table 4.20. In Fig. 4.46, the isomer shift and hyperfine field due to various transition metal impurities (about 3 at %) in $Fe_{80}T_3B_{17}$ is plotted as a function of number of outer electrons. The hyperfine field varies systematically with the addition of impurities. The isomer shift increases almost linearly except in the case of Mn.

There was no indication of any quadrupole splitting within the experimental error for all environments.

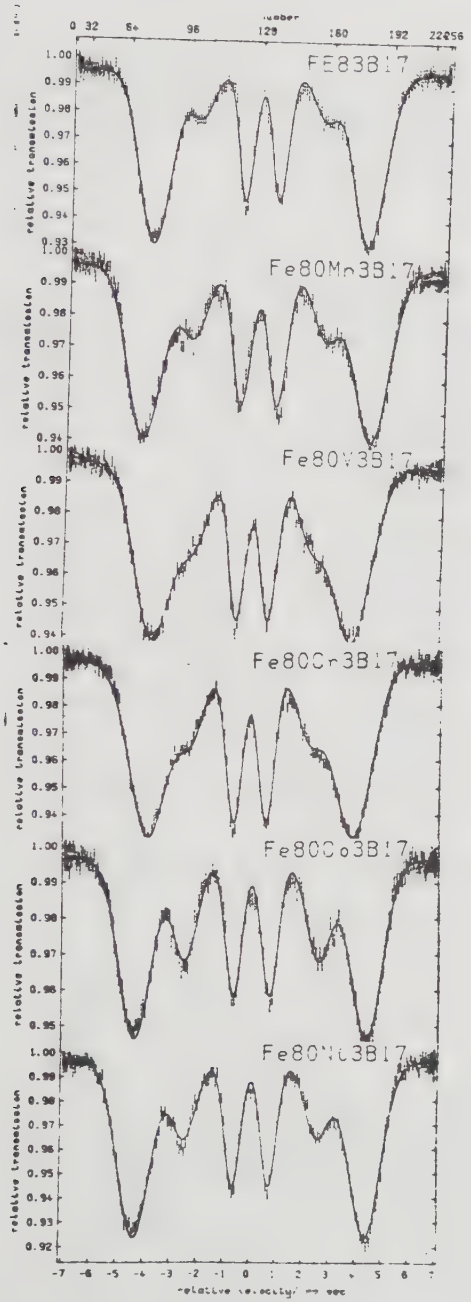

Fig. 4.45: Mössbauer spectra of amorphous $Fe_{83}T_3B_{17}$ alloys at 6K

Table 4.20 : $Fe_{80}T_3B_{17}$ system: Average isomer shift (I.S.) at 6 K and average hyperfine field $\overline{HF}(Fe)$; the uncertainties are ΔI.S.=±0.002 mm/sec and $\Delta\overline{HF}(Fe)$=±0.25 T

amorphous alloys	I.S. * (mm/s)	$\overline{HF}(Fe)$(Tesla) (T=6K)
$Fe_{83}B_{17}$	0.072	29.25
$Fe_{80}V_3B_{17}$	0.047	26.35
$Fe_{80}Cr_3B_{17}$	0.052	26.15
$Fe_{80}Mn_3B_{17}$	0.092	29.40
$Fe_{80}Co_3B_{17}$	0.082	29.30
$Fe_{80}Ni_3B_{17}$	0.100	28.91
$Fe_{80}Mo_3B_{17}$	0.045	26.25
$Fe_{80}W_3B_{17}$	0.055	25.98

* values relative to metallic iron at room temperature

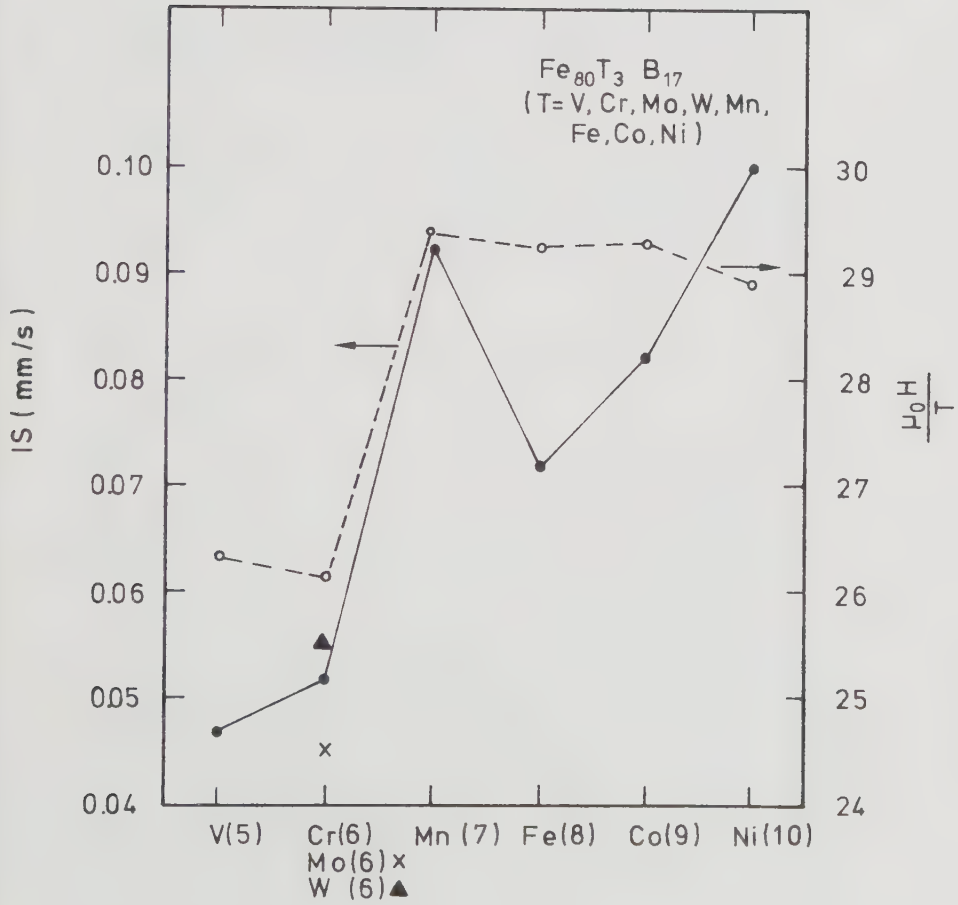

Fig. 4.46: Average hyperfine field and isomer shift (IS) are plotted against outer-electron concentration

As yet it is not possible to propose a full interpretation of present data because detailed band structures of the various TM-M amorphous alloys are not known. Nevertheless, it is evident that the variations in the shifts are associated with the filling up of the d-bands of the transition metals. The observed increase of the isomer shift as a number of outer electrons indicates that either the s-electron density at the nucleus decreases or there is an increase in the d-electron density. One might, thus, expect that in these amorphous alloys part of the conduction electrons of the impurity will tend to move towards the d-band of the host, if one then considers the antishielding effect of the d-electrons on the s-electrons /136/, then the s-electron charge density decreases at the iron nucleus.

4.6 Crystallization of TM-M glasses

Since amorphous alloys are thermodynamically unstable, transformation to stable crystalline phases should occur during heating and hence the crystallization process is an important problem in the study of amorphous alloys. It has been found that distinct changes in some properties related to the stucture are induced by heating, even at temperatures appreciably lower than the crystallization temperature.

For the understanding of crystallization in amorphous TM-M alloys it is very important to characterize the metastable crystalline phases which appear during crystallization. The most intensively studied glasses are the binary ones, $Fe_{1-x}B_x$ ($0.15 \leq x \leq 0.26$), especially $Fe_{80}B_{20}$, because they have the simplest possible forms. In the case of annealed $Fe_{80}B_{20}$ up to 500°C for 2 hours, only α-Fe and tetragonal metastable Fe_3B seem to be present /137/. The Mössbauer lines of this phase are still present after heat treatments of 2 hours at 600 and 700°C, where very intensive lines of Fe_2B are also present according to the decomposition of Fe_3B in α-Fe and Fe_2B as shown in Fig. 4.47. Only after two hours heat treatment at 900°C, $Fe_{80}B_{20}$ is completely decomposed in the two stable phases α-Fe and Fe_2B in the right intensity ratio 1:1. Thus, in the Fe-B system, it is found that the Fe environments in the glassy phase are similar to those of the tetragonal Fe_3B (isostructural to Fe_3P) intermetallic compound which is formed during the crystallization. As the structure of Ni_3B and Co_3B (cementit type, or orthorombic) is different from Fe_3B, one would expect changes in the short-range order of Fe-B glasses due to the replacement of Fe by Co or Ni.

In this work the crystallization of $(Fe_{0.5}Co_{0.5})_{1-x}B_x$ (x=15 and 24) glasses is investigated by Mössbauer spectroscopy.

Results and Discussion

The samples of $Fe_{38}Co_{38}B_{24}$ and $Fe_{42.5}Co_{42.5}B_{15}$ were annealed in argon 30 minutes at 450°C and 60 minutes at 430°C, respectively. The Mössbauer spectrum of $Fe_{42.5}Co_{42.5}Co_{15}$ could be fitted to a rather intensive sextet (Lorentzian lines) with HF=34.8 T and a crystalline phase $(FeCo)_3B$ with hyperfine field, 22T<HF<28T, Fig. 4.48b. In the case of the composition with 24% B, only shallow lines with a high value of HF=34.5T appear, Fig. 4.48a.

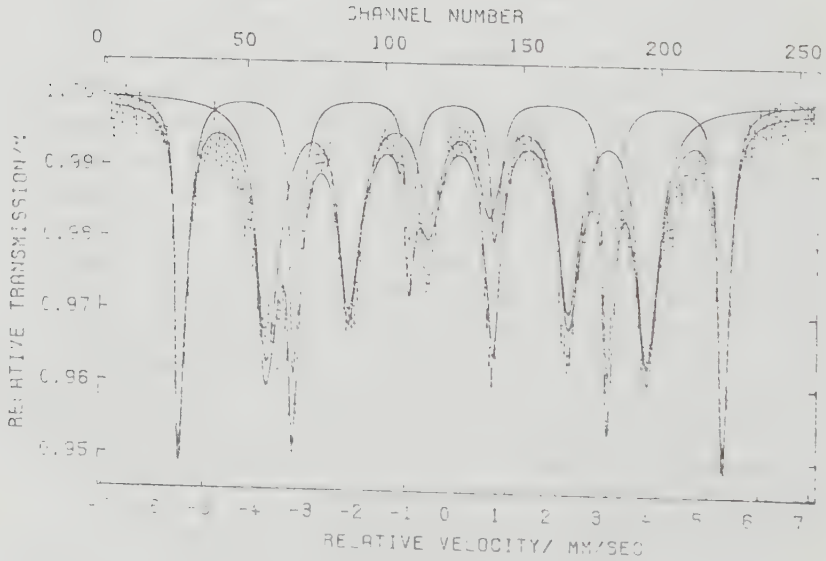

Fig. 4.47: $Fe_{80}B_{20}$, annealed for 2h at 600°C:
$Fe+Fe_3B(+) + Fe_2B + Fe_3B(O)$ /137/

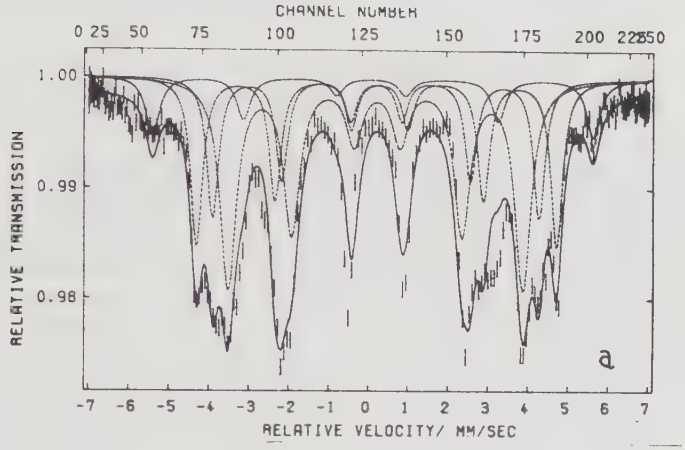

Fig. 4.48(a,b): Mössbauer spectra of a) $Fe_{38}Co_{38}B_{24}$ (annealed in argon 30 minutes at 450°C) and b) $Fe_{42.5}Co_{42.5}B_{15}$ (annealed in argon 30 minutes at 430°C) at RT

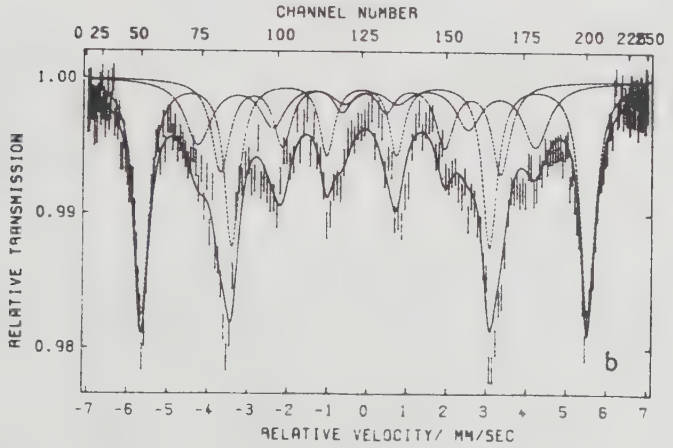

As in the crystallization of amorphous Fe-B and Fe-Ni-B alloys /137,134/, the $(Fe_{0.5}Co_{0.5})_{1-x}B_x$ glasses, in the first phase of the crystallization, decomposes into crystalline, $(Fe_{0.5}Co_{0.5})_3B$ and FeCo alloy according to the relation

$$(Fe_{0.5}Co_{0.5})_{1-x}B_x = x(Fe_{0.5}Co_{0.5})_3B + (1/2-2x)(FeCo)$$

The ratios of the Fe-concentration in the alloy and boride have then to be 0.89 for the composition with 15% B and 0.056 for the one with 24% B in good agreement with the ratios of the corresponding intensities of the Mössbauer lines obtained in this work.

It is thus found that the crystallization processes in the Fe-Co-B and Fe-B system are qualitatively similar, which has also been concluded by Arajs et al /138/, on the basis of their high temperature resistivity results on identical alloys.

5. Determination of the separate contributions of Iron, Nickel and Cobalt to the magnetic moments of the amorphous alloy systems $((Fe_xNi_{1-x})_{80}B_{20}$ and $(Fe_{1-x}Co_x)_{80}B_{20})$

The present section deals with a comparative study of the separate magnetic contribution of Fe, Co and Ni to the average magnetic moment at O K of the amorphous alloys $(Fe_xNi_{1-x})_{80}B_{20}$ and $(Fe_{1-x}Co_x)_{80}B_{20}$. Two complementary approaches have been undertaken. The first approach, i.e., Mössbauer spectroscopy, provides useful information about local magnetic properties (mainly hyperfine field at the iron site). Whereas the second one, i.e., saturation magnetization measurements gives the values of the average magnetic moment per transiton metal atom at O K.

Fig. 5.1 shows the low temperature average magnetic moment per transition metal atom ($\bar{\mu}_{exp}$) at O K in μ_B as a function of composition of $(Fe_xNi_{1-x})_{80}B_{20}$. In this compositional series, nine compositions with x=0.875, 0.75, 0.625, 0.5, 0.375, 0.25, 0.2, 0.1625 have been investigated. It is clear from Figure 5.1, that the average magnetic moment per transition metal atom ($\bar{\mu}$) for the Ni-rich alloys decreases much faster than is expected from a linear extrapolation of the $\bar{\mu}(x)$ dependence starting from the iron rich side. If the trend in the decrease of $\bar{\mu}$ on the Ni-rich side is followed, it seems that Ni in $Ni_{80}B_{20}$ glass should possess a finite but very small moment.

In order to determine the separate contribution of the Fe and Ni atoms to the average magnetic moment per transition metal atom in $(Fe_xNi_{1-x})_{80}B_{20}$ three simple approaches have been taken into consideration.

In the first, a constant value for $\bar{\mu}_{Fe}$ is taken, namely 2.09 μ_B like in $Fe_{80}B_{20}$, and then the corresponding values of $\bar{\mu}_{Ni}$ are calculated according to the following

equation.

$$\bar{\mu} = (1-x)\bar{\mu}_{Ni} + x\bar{\mu}_{Fe} \qquad (5.1)$$

The values of $\bar{\mu}_{Ni}$ obtained in this way are given in table 5.1.

Secondly, in the studies of magnetic alloys, it is reasonable to use for the local hyperfine field $\bar{H}F(Fe)$ at Fe-site in a binary alloy $Fe_{1-x}M_x$ the relation

$$HF = a\mu_{(Fe)} + b\bar{\mu} \qquad (5.2)$$

where the first term gives practically the Fe-core polarisation contribution and second one that of the rest of the alloy. The concentration dependence of the $\bar{H}F(Fe)$ in this alloy series, under the assumption that the values of 'a' and 'b' remain unchanged for different Fe-sites, can be represented by

$$\bar{H}F(Fe) = a\bar{\mu}_{Fe} + b\bar{\mu} \qquad (5.3)$$

In case of $(Fe_xNi_{1-x})_{80}B_{20}$, a≈13 T/$\mu_B$ and b=.68 T/μ_B is found. Thus, it appears that the first term gives a dominant contribution to the hyperfine field. One can, therefore, neglect the second term and use the following equation to determine the value of $\bar{\mu}_{Fe}$ for different 'x':

$$\bar{H}F(Fe) = a\bar{\mu}_{Fe}(x) \qquad (5.4)$$

where 'a' is a hyperfine constant, whose value has been taken to be 13.68 T/μ_B as in $Fe_{80}B_{20}$ and $\bar{\mu}_{Fe}(x)$ has been determined with the aid of equation (5.4). The corresponding values of $\bar{\mu}_{Ni}$ are calculated using equation (5.1) (see table 5.1). Here, $\bar{\mu}_{Fe}(x)$ decreases only 5% in the range $0.3<x<1$, but much faster for $x<0.3$, reaching a value of 1.56 μ_B in $Fe_{10}Ni_{70}B_{19}Si_1$.

Table 5.1

Compound	Method I		Method II		Method III	
	$\bar{\mu}_{Fe}$ in μ_B	$\bar{\mu}_{Ni}$ in μ_B	$\bar{\mu}_{Fe}$ in $\bar{\mu}_B$ HF(Fe/13.6.8)	$\bar{\mu}_{Ni}$ in μ_B	$\bar{\mu}_{Fe}$ in μ_B	$\bar{\mu}_{Ni}$ in μ_B
$Fe_{80}B_{20}$	2.09	-	2.09	-	2.09	-
$Fe_{70}Ni_{10}B_{20}$	2.09	0.73	2.09	0.73	2.09	0.73
$Fe_{60}Ni_{20}B_{20}$	2.09	0.51	2.04	0.66	2.05	0.59
$Fe_{50}Ni_{20}B_{20}$	2.09	0.55	2.02	0.67	2.04	0.63
$Fe_{40}Ni_{40}B_{20}$	2.09	0.52	2.00	0.61	2.04	0.57
$Fe_{30}Ni_{50}B_{20}$	2.09	0.50	1.99	0.56	2.04	0.53
$Fe_{20}Ni_{60}B_{20}$	2.09	0.36	1.93	0.41	2.00	0.40
$Fe_{16}Ni_{64}B_{19}Si_1$	2.09	0.32	1.83	0.38	1.90	0.36
$Fe_{13}Ni_{67}B_{19}Si_1$	2.09	0.30	1.64	0.39	1.71	0.37
$Fe_{10}Ni_{70}B_{19}Si_1$	2.09	0.22	1.56	0.29	1.68	0.27

Method I : Here the average magnetic moment of iron is taken to be constant in the entire range and then $\bar{\mu}_{Ni}$ is calculated.

Method II : μ_{Ni} is calculated on the basis of different $\bar{\mu}_{Fe}$ as a function of 'x'.

Method III: Assuming 'a' and 'b' do not change with 'x' in the non-linear region. Ref. equation (5.5)

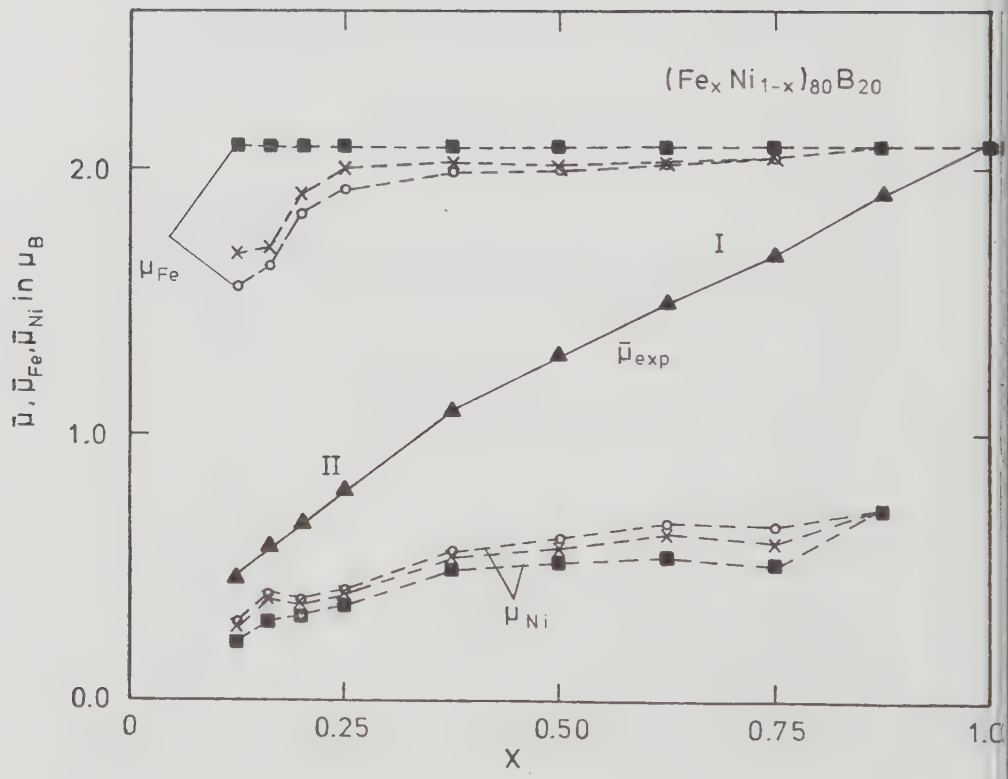

Fig. 5.1: Variation of $\bar{\mu}_{exp}$, $\bar{\mu}_{Fe}$ and $\bar{\mu}_{Ni}$ as a function of x.

In the third approach, 'a' and 'b' have been assumed to be independent of 'x' in the non-linear region and the value of $\bar{\mu}_{Fe}$ is calculated in the following way:

$$\overline{HF}(Fe) = a\bar{\mu}_{Fe} + b\bar{\mu}$$

$$\bar{\mu}_{Fe} = \frac{\overline{HF}(Fe) - b\bar{\mu}}{a}$$

and

$$\bar{\mu}_{Ni} = \bar{\mu} - x\bar{\mu}_{Fe}/1-x \qquad (5.5)$$

where $\bar{\mu}$ = average magnetic moment per transition metal atom.

These calculated values of $\bar{\mu}_{Fe}$ and $\bar{\mu}_{Ni}$ are listed in table 5.1. This shows that $\bar{\mu}_{Fe}$ decreases slowly over the whole region whereas $\bar{\mu}_{Ni}$ decreases faster. This observation shows that the rapid drop of $\bar{\mu}$ at higher Ni concentration is mainly due to a relative strong decrease of $\bar{\mu}_{Ni}$ and that $\bar{\mu}_{Fe}$ does not change too much. The calculated dependences of $\bar{\mu}_{Fe}$ and $\bar{\mu}_{Ni}$ on composition are given in Fig. 5.1. It is seen that in all the three cases $\bar{\mu}_{Ni}$ decreases with 'x' in almost the same way, tending to a finite value (but small) in $Ni_{80}B_{20}$ in case a least square fit made through the experimental points is extrapolated to x=0.

In case of $(Fe_{1-x}Ni_x)_{80}P_{14}B_6$, for x>0.6 the alloy moment $\bar{\mu}_{al}$ decreases far more faster (table 5.2), owing to a decrease of both $\bar{\mu}$(Fe) and $\bar{\mu}$(Ni). But the deviation of the $\overline{HF}$(Fe) from the linear dependence beyond x=0.6 is not large, reaching for instance only 6% at x=0.875, so that one may with enough confidence assume that only a strong decrease of $\bar{\mu}$(Ni) could be responsible for the rapid drop of $\bar{\mu}_{al}$ at higher Ni concentrations. Taking $\bar{\mu}$(Fe)=1.85 for the whole concentration range as seems to be indicated by the dependence of $\overline{HF}$(Fe) on

Table 5.2

Compound	Method I			Method II		
	$\bar{\mu}_{Fe}$ in $\bar{\mu}_B$ HF(Fe)/A	$\bar{\mu}$ * in μ_B	$\bar{\mu}_{Ni}$ in μ_B	$\bar{\mu}_{Fe}$ in μ_B	$\bar{\mu}$ * in μ_B	$\bar{\mu}_{Ni}$ in μ_B
$Fe_{80}P_{14}B_6$	1.85	1.85	-	1.85	1.85	-
$Fe_{70}Ni_{10}P_{14}B_6$	1.84	1.64	0.24	1.85	1.64	0.17
$Fe_{60}Ni_{20}P_{14}B_6$	1.79	1.54	0.79	1.85	1.56	0.61
$Fe_{30}Ni_{40}P_{14}B_6$	1.75	1.23	0.71	1.85	1.23	0.61
$Fe_{30}Ni_{50}P_{14}B_6$	1.71	0.93	0.46	1.85	0.93	0.38
$Fe_{20}Ni_{60}P_{14}B_6$	1.61	0.67	0.36	1.85	0.67	0.28
$Fe_{10}Ni_{70}P_{14}B_6$	1.54	0.24+	0.06	1.85	0.24+	0.05

* values are from /98/

\+ present work

Method I : Same as table (5.1) (Method II)

Method II: Same as table (5.1) (Method I)

the Ni-concentration, one obtains below x=0.5, $.05 < \bar{\mu}(Ni) < 0.5$, for example, $\bar{\mu}(Ni)=0.38$ for x=0.625 and and $\bar{\mu}(Ni)=0.05$ for x=0.875. The value for $\bar{\mu}(Ni)$ obtained for x=0.125 is inconsistent compared to the other values of x. Possibly, this arises due to the fact that both hyperfine field and $\bar{\mu}$ in this case can not be determined to the same accuracy as for other concentrations and a change of only 2% in $\bar{\mu}_{Fe}$ calculated using equation (5.4) causes a 15-25% change in the value of $\bar{\mu}_{Ni}$ from equation (5.1). The values of $\bar{\mu}_{Ni}$ for different concentrations have also been calculated following the second approach (already described in detail in connection with $(FeNi)_{80}B_{20}$ alloys) wherein $\bar{\mu}_{Fe}$ changes with concentration (see table 5.2).

The experimental results can be interpreted qualitatively on the basis of rigid band model. It is observed that for both crystalline and amorphous Fe-metalloid alloys the moment of Fe is nearly unchanged up to quite large metalloid concentration (∿20%) /65/. This was explained by Mott /65/ to be a consequence of metalloid valence electrons going into the s-band of Fe leaving the moment unaltered. Another explanation may be that because the density of states of the spin-up d-band at the Fermi level, $\rho_{d^{\uparrow}}(E_F)$ roughly equals the density of states at the Fermi level of the spin-down d-band $\rho_{d^{\downarrow}}(E_F)$ for Fe and $\rho_{d} >> \rho_{s,p}$, the density of states of the s,p band, the electrons donated by metalloid atoms should initially go to the 3d subbands in equal amounts until $\rho_{d^{\downarrow}} > \rho_{d^{\uparrow}}$ when the moment will start decreasing. It is obvious from table 5.1 that the calculated values of $\bar{\mu}_{Fe}$ and $\bar{\mu}_{Ni}$ show a trend in which the iron moment changes very little throughout the entire range whereas the nickel moment changes drastically. For a constant amount of metalloid, that is 20 at % B, the average magnetic moment per TM atom decreases as a function of nickel concentration. Therefore, adding glassformers to Fe in small amounts increases the number of spin-up and spin-

down electrons about equally and the net moment per Fe atoms does not change. The value of $\bar{\mu}_{Fe}$ in this case has been taken to be 2.09 μ_B as in $Fe_{80}B_{20}$, and the behaviour of the average magnetic moment of the alloy is observed to be influenced due to the presence of various amount of nickel. The Fermi-level for nickel occurs at a position such that the spin-up d-band is almost full, thus the sp electrons from the metalloid go to the unfilled spin-down d-band of nickel. Consequently, there is a decrease in the average magnetic moment of the alloy with the addition of nickel. O'Handley et al /104/, from a rigid band model analysis of magnetic moment data on $(Fe_xNi_{1-x})_{80}B_{20}$ amorphous alloy series, concluded that B metalloid atoms donate ~1.6 electrons per atom to the TM d-band and that Ni should have a finite moment in amorphous $Ni_{80}B_{20}$ alloy.

One thus observes that the introduction of metalloid atoms does not cause moment perturbations on the surrounding Fe atoms whereas they have significant influence on the Ni moments. In addition, Vincze et al /134/ have shown from the analysis of their experimental results on a series of Fe-Ni-B glasses that the distribution of transition metal atoms is not random at high Ni concentrations and the Fe atoms prefer less B neighbors than the Ni-atoms do. Therefore, with more B neighbors for Ni than for Fe, Ni moment decreases much faster than it does in the case of Fe. Furthermore, the calculation of Messmer /135/ shows that Ni-B has stronger tendency towards clustering than Fe-B does.

A very similar explanation of $\bar{\mu}(x)$ dependence has been reported by Durand /111/ for the amorphous $(Fe_xNi_{100-x})_{79}P_{13}B_8$ alloys. In this alloy system, he finds that the moment per Ni-atom increases from zero at x=0 to a roughly constant value of 0.4 μ_B for $x \geq 30$ at %. The variation of $\bar{\mu}_{Ni}$ with x finally achieved by Durand /111/, assuming $\bar{\mu}_{Fe}$ to be constant throughout the entire range, does

not conform to linear variation. Simply, on the basis of bulk magnetic measurements data one can not assume with enough confidence the constancy of $\bar{\mu}_{Fe}$ in the whole compositional range. But a combination of this with the additional local measurement (Mössbauer spectroscopy) at the Fe-site in this work, clearly shows that the $\bar{\mu}_{Fe}$ decreases very slowly in the entire range whereas $\bar{\mu}_{Ni}$ decreases very fast in $(Fe_xNi_{1-x})_{80}B_{20}$ alloy with the decreasing x.

The compositional dependence of average magnetic moment per transition metal atom ($\bar{\mu}_{exp}$) at O K for $(Fe_{1-x}Co_x)_{80}B_{20}$ is shown in Fig. 5.2. The decrease of average magnetic moment of the alloy with the addition of 70 at % cobalt has been found to be 29%. After a slight increase from 1.99 μ_B to 2.0 μ_B in the concentration range $0<x<0.125$, $\bar{\mu}$ decrease practically with 'x' down to 1.27 μ_B in $Co_{80}B_{20}$.

As before, the separate contribution of 'Fe' and 'Co' to the average magnetic moment per TM atom in $(Fe_{1-x}Co_x)_{80}B_{20}$ has been calculated following the above described methods. The calculated values of the individual moments of Fe and Co are given in table 5.3. Fig. 5.2(a,b,c) shows the variation of the individual moments of iron, cobald and average magnetic moment as a function of cobalt concentration in TM. It is seen that the $\bar{\mu}_{Fe}$ remains almost constant throughout the whole compositional range whereas $\bar{\mu}_{Co}$ decreases almost the same way in all three cases. The linear relation between the hyperfine field versus the average magnetic moment per TM atom shows that the contribution of the core polarization term is more effective to the hyperfine field at Fe-sites (see section 4). Thus, we can use equation (5.4) with confidence for the calculation of $\bar{\mu}_{Fe}(x)$. It is obvious that the substitution of Fe with Co does not significantly change the value of $\bar{\mu}_{Fe}(x)$ (see table 5.3), and as such supporting the

Table 5.3

Compound	Method I		Method II		Method III	
	$\bar{\mu}_{Fe}$ in μ_B HF(Fe)/(14.4.2)	$\bar{\mu}_{Co}$ in μ_B	$\bar{\mu}_{Fe}$ in μ_B	$\bar{\mu}_{Co}$ in μ_B	$\bar{\mu}_{Fe}$ in μ_B	$\bar{\mu}_{Co}$ in μ_B
$Fe_{80}B_{20}$	1.99	-	1.99	-	1.99	-
$Fe_{70}Co_{10}B_{20}$	2.01	1.93	1.99	2.07	2.01	1.93
$Fe_{60}Co_{20}B_{20}$	2.00	1.92	1.99	1.95	2.00	1.92
$Fe_{50}Co_{30}B_{20}$	1.99	1.89	1.99	1.89	2.00	1.86
$Fe_{30}Co_{50}B_{20}$	1.97	1.46	1.99	1.45	2.00	1.44
$Fe_{20}Co_{60}B_{20}$	1.96	1.37	1.99	1.35	2.00	1.35

Method I : Same as table (5.1) (Method II)
Method II : Same as table (5.1) (Method I)
Method III: Same as table (5.1)

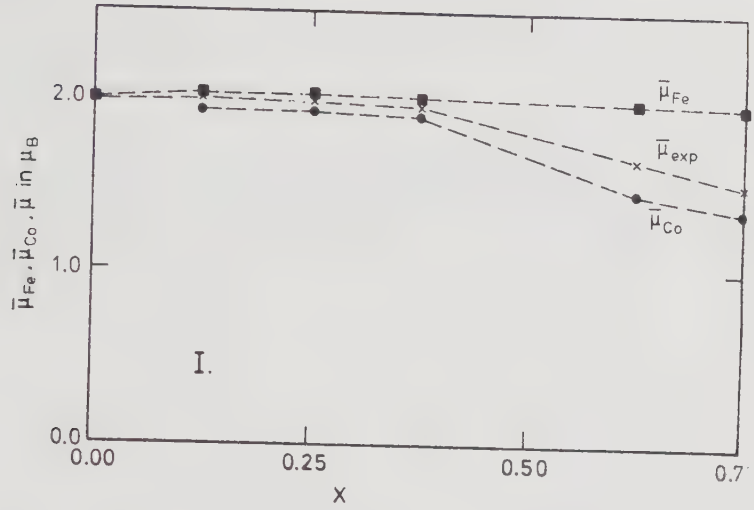

Fig. 5.2(a): Variation of $\bar{\mu}_{exp}$, $\bar{\mu}_{Fe}$ and $\bar{\mu}_{Co}$ as a function of x according to table 5.3

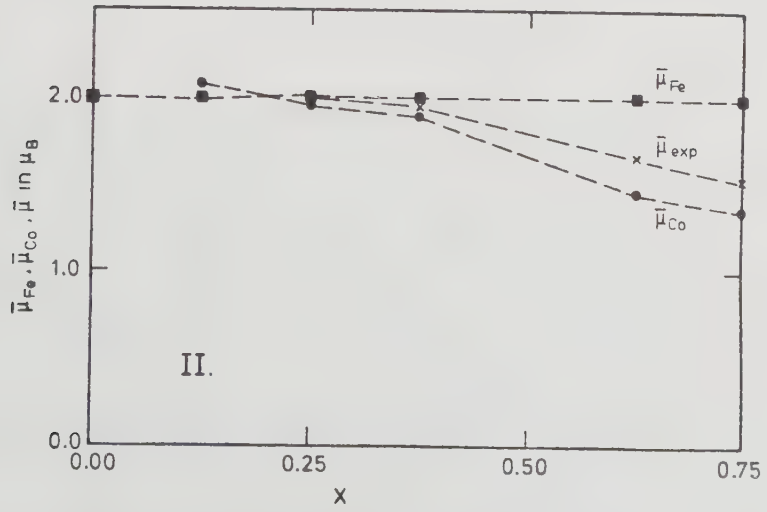

Fig. 5.2(b): Variation of $\bar{\mu}_{exp}$, $\bar{\mu}_{Fe}$ and $\bar{\mu}_{Co}$ as a function of x according to table 5.3

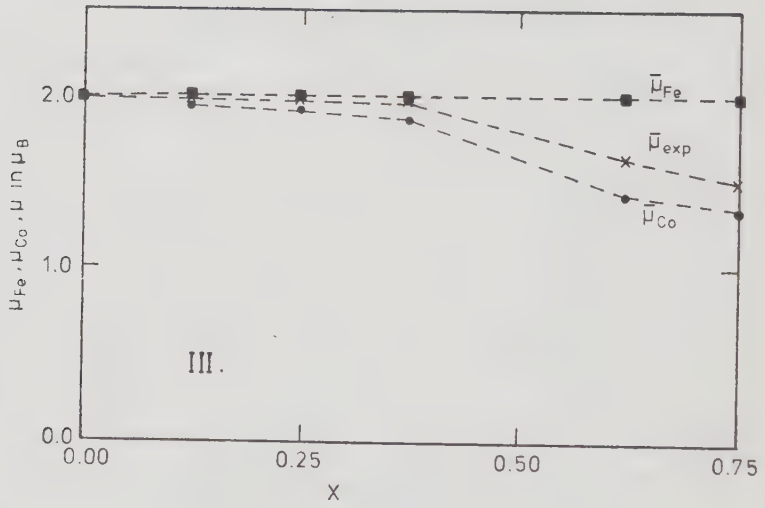

Fig. 5.2(c): Variation of $\bar{\mu}_{exp}$, $\bar{\mu}_{Fe}$ and $\bar{\mu}_{Co}$ as a function of x. Ref. table 5.3

assumption of the constancy of $\bar{\mu}_{Fe}(x)$. The iron-moment $\bar{\mu}_{Fe}$ is taken to be 1.99 μ_B as in $Fe_{80}B_{20}$, which remains constant in the investigated compositional series $(Fe_{1-x}Co_x)_{80}B_{20}$. The analysis of the experimental data can be done qualitatively on the basis of rigid-band model. As crystalline Co has almost a full spin-up d-band and a large density of states for the spin-down d-band, so its alloys are expected to behave in the same way as the Ni-alloys. The calculation, however, shows that there is a vacancy of +0.15 in the Co-spin-up d-band in $(Fe_{1-x}Co_x)_{80}B_{20}$ amorphous alloys. Therefore, initially the spin-up d-band of cobalt atom will get filled up by the transfer of 'sp' electrons from metalloid, and hence the average magnetic moment of the alloy should increase, which is in fact observed experimentally in the range $0<x<0.125$. When the spin-up d-band is completely filled up, the 'sp' electrons from

the metalloid atoms go to spin-down d-band. Consequently, the average magnetic moment per TM atom decreases regularly. This is consistent with the experimental observation.

It is noteworthy that the $(Fe_xNi_{1-x})_{80}B_{20}$ and $(Fe_{1-x}Co_x)_{80}B_{20}$ amorphous alloys show a continuous change in $\bar{\mu}$ as a function of x in the entire compositional range in contrast to their crystalline counterparts.

6. Conclusion

A systematic investigation of the magnetic behaviour of amorphous ferromagnetic alloys having various transition metal-metalloid composition has been carried out. In the first group of alloys, the amount of transition metal is varied whereas in the second group it is kept constant and the amount of metalloid is changed. Hyperfine field distributions, at Fe-sites in Fe-Ni-B, Fe-Co-B, Fe-Cr-B, Fe-Mo-B and Fe-B-M (M=C,Si,Ge) amorphous alloys, have been measured by Mössbauer spectroscopy with good resolution. These results provide detailed information on hyperfine field shifts due to different types of transition metal and metalloid neighbours. The saturation magnetization measurements have been performed as a function of temperature and concentration for the investigation of the bulk magnetic properties. The separate magnetic contributions of Fe,Co,Ni to the average magnetic moment of these alloys have been calculated from the results of these two types of measurements.

i) Average magnetic moment and average hyperfine field

The concentration dependence of $\bar{\mu}$ as a function of 'Ni' in $(Fe_{1-x}Ni_x)_{80}B_{20}$ $(.125 \leq x \leq .875)$ shows that the $\bar{\mu}_{Fe}$ decreases very little in the whole concentration range whereas there is stronger decrease of $\bar{\mu}_{Ni}$ with increasing Ni-concentration. Accordingly, the magnetic moment per Ni atom in amorphous $Ni_{80}B_{20}$ should be much smaller (if any at all) than given by the extrapolation of $\bar{\mu}$ from the iron richer side. The average hyperfine field at Fe-site decreases much faster with the increasing amount of Ni. Experimental results of investigated alloys show that the 3d-electrons are highly localised as strong core po-

larisation contribution, whereas the conduction electron contribution to the hyperfine field (Fe) is very small. However, in case of hyperfine field (Ni), it appears /109/ that in addition to a small core polarisation interaction, the main contribution to hyperfine field (Ni) is due to a strong conduction electron polarisation effect. The ^{61}Ni nuclei experience a broad distribution of magnetic hyperfine fields whose average is proportional to the bulk moment. The average fields, however, are substantially smaller than those in crystalline Fe-Ni alloys of comparable concentration.

In the case of $(Fe_{1-x}Co_x)_{80}B_{20}$, the average magnetic moment of the alloy decreases with the increase of Co concentration and reaches 1.27 μ_B at $Co_{80}B_{20}$. Thus $Co_{80}B_{20}$ is ferromagnetic, whereas $Ni_{80}B_{20}$ shows Pauli-paratype character at 4.2 K. A comparison of the results of the two measurement methods show that there is a linear dependence of $\overline{HF}$(Fe) on the average magnetic moment ($\bar{\mu}$). The calculation of separate moments shows that $\bar{\mu}_{Fe}$ is practically constant over the whole compositional range wheres $\bar{\mu}_{Co}$ decreases with the increasing Co-concentration. The behaviour of average magnetic moment as a function of concentration in $(Fe\text{-}Ni)_{80}B_{20}$ and $(Fe\text{-}Co)_{80}B_{20}$ can be qualitatively understood on the basis of 'charge transfer model'.

The substitution with 'Cr,Mo' in the amorphous Fe-B alloy has a stronger influence on the decrease of average hyperfine field at the Fe-site than on its crystalline counterpart. The stronger decrease of average hyperfine field with the increasing amount of 'Cr,Mo' in Fe-B suggests a significant change of the band structure due to the presence of 'Cr,Mo' with changes of the magnetic moments of both Fe and (Cr,Mo). The average magnetic moment of these alloys with (Cr,Mo) decrease very fast with increasing Cr or Mo content . The composition dependence

of magnetic moment of amorphous alloys containing 'Cr,Mo' can be understood within the virtual bound state model of Friedel /17/. The critical Mo concentration, for which T_c of the corresponding $(FeMo)_{80}B_{20}$ alloy should be zero, is estimated to be about 30 at % Mo.

However, the experimental results of the second group of alloys, in which one metalloid is substituted by another (namely, the substitution of C, Si and Ge in $Fe_{80}B_{20-x}M_x$, (M=C,Si,Ge), can not be understood on the basis of simple charge transfer model. An attempt has been made to interpret the anomaly from the point of view that the size of the metalloids are different, and they fill up the holes either interstitially or substitutionally depending on their size. There is evidence that the inconsistency observed in this group of alloys can be relatively better understood from the consideration of the relation of exchange interaction between Fe-Fe and the co-ordination number 'z' of the atom.

ii) Spin Wave excitation

The Bloch coefficients 'B' obtained from the Mössbauer spectroscopy and magnetization measurements have the same value at least for the glassy alloys under consideration. The decrease of magnetization with increasing temperature at low temperatures is adequately described by the theoretical prediction based on the Heisenberg model, equation (35) (see section 2). However, the range of exchange interaction has a rather pronounced discontinuity between 30 and 40 at % Ni in the amorphous $(Fe_xNi_{1-x})_{80}B_{20}$ alloys, which may be due to some changes in the local arrangement.

The decreasing value of the stiffness constant (D) with increasing 'x' in $Fe_{85-x}Cr_xB_{15}$ alloys indicates the softening of the exchange interaction by Cr-substitution. By alloying with about 10 at % Mo, the Curie temperature and the stiffness constant (D) decrease to less than half their values in amorphous $Fe_{80}B_{20}$. This means a weakening of the average interaction, however not necessarily due to antiferromagnetic Fe-Mo coupling. Thus, the low temperature behaviour of these ferromagnetic alloys can be well explained on the basis of spin-wave theory. The observed ratio D/Tc ($\sim$0.21±.01 MeV $A^{\cdot 2}K^{-1}$) which is a measure of the range of exchange interaction, is always somewhat less in these alloys than that in pure iron, D/Tc=0.27, which implies short-range interaction in the amorphous metals.

iii) Isomer shift

The isomer shift, which is a measure of the s-electron density at the nucleus, exhibits a variety of values for amorphous ferromagnetic alloys. However, a systematic change in the isomer shift with the change of composition observed in this work suggests that there is a possibility of charge transfer from metalloid to the unfilled d-band of the metal and therefore the stronger screening effects of the conduction electrons at the Fe-nucleus. For example, the isomer shift does not change so much by alloying with Ni but it changes drastically when B is substituted by P. The higher the Ni and P concentrations, the stronger the increase in isomer shift suggesting an enhancement of the screening of the s-electrons at the Fe-nucleus. The isomer shift is observed to increase linearly with the increasing amount of Co, Cr and Mo in amorphous Fe-Co-B, Fe-Cr-B and Fe-Mo-B alloys, respectively.

iv) Quadrupole interaction

Due to the hyperfine field distribution, the spectral lines are broad in the magnetically ordered state. The position of the six spectral lines are symmetrical about the isomershift, thus showing no apparent quadrupole interaction. Quadrupole interactions measured in the magnetic state in these alloys are insignificant with respect to the magnetic hyperfine interaction. Because the magnetic hyperfine field direction is different from the axially symmetric principal axis of the EFG's, the effective quadrupole interaction is averaged out. One therefore observes a nearly zero apparent quadrupole interaction in all amorphous ferromagnetic alloys in their magnetically ordered state. However, at $T>T_C$ a pure quadrupole interaction can be seen.

REFERENCES

/1/ Pol Duwez, R.H. Willens and R.C. Crewdson, J. Appl. Phys. 36,2267(1965)

/2/ R.C. Crewdson, Ph.D. thesis, Caltech (1966)

/3/ A.I. Guvanov, Fiz. Tver. Tela 2,502(1960)

/4/ F.E. Luborsky, Amorphous Ferromagnets, North-Holland Publisher, Ed. E.P. Wohlfarth (1979)

/5/ F.E. Luborsky, Amorphous Magnetism II, Ed. by R.A. Levy and R. Hasegawa, Plenum Press, New York and London

/6/ F.E. Luborsky, J.J. Becker, P.G. Frischmann and L.A. Johnson, J. Appl. Phys. 49,1769-74(1978)

/7/ A. Amamou, F. Gautier and B. Loegel, J. Phys. F5, 1342(1975)

/8/ A. Amamou, IEEE Trance. Magnetics 12,948(1976)

/9/ E.J. Lisher, C. Wilkinson, T. Ericsson, L. Häggström, J. Phys. C7,1344(1974)

/10/ R. Wäppling, T. Ericsson, L. Häggström and Y. Anderson, J. Physique 37,C-6,391(1976)

/11/ H.S. Chen, Rep. Progr. Phys. 43,353-432(1980)

/12/ Pol Duwez, Annual Review of Material science, Vol.6,83-117(1976)

/13/ C.C. Tsuei, G. Longworth and S.C.H. Lin, Phys. Rev. Vol.170, No.2,603-606(1968)

/14/ V.V. Bonder, V.A. Povitskiy and Ye F. Makarov, Phys. Met. Metallogr. 30,5,166-169(1970)

/15/ J. Durand and M.F. Lapierre, J. Phys. F. Vol.6, 1185-1192(1976)

/16/ R. Hasegawa, W.A. Hines, L.E. Kabacoff and Pol Duwez, Solid State Communications, Vol.20, 1035-1038(1976)

/17/ J. Friedel, Nuovo Cimento 7, Supp.287-311(1958)

/18/ J. Durand, C. Thompson and A. Amamou, Int. Conf. on Rapidly Quenched Metal III Brighton, Vol.2 (1978)

/19/ T. Kemeny, I. Vincze, B. Fogarassy and S. Arajs, Phys. Rev. B20,476(1976)

/20/ G.S. Cargill III, Solid State Physics 30, Ed. H. Ehrenreich, F. Seitz and D. Turnbull, 227-320 (Academic Press, New York) (1975)

/21/ J. Dixmier and J.F. Sadoc in Metallic Glasses, Ed. J.J. Gilman and H.J. Leamy, 97-113(1978)

/22/ J.L. Finney, Nature 266, 309-314(1977)

/23/ C.N.J. Wagner, Vac. Sci. Tech. 6,650-657(1969) Liquid Metals, Ed. S.Z. Beer, M. Dekker, New York 257-329(1972), J. Non-cryst. Solids 31,1-40(1978).

/24/ B.C. Giessen and C.N.J. Wagner, Liquid Metals, Ed. S.Z. Beer and M. Dekker (New York) 633-695(1972)

/25/ Y. Waseda, H. Okazaki and T. Masumato, J. Matr. Sci.12,1927-1949(1977)

/26/ A. Bienenstock, The Structure of Non-crystalline Materials, Ed. P.H. Gaskell (Taylor and Francis, London) 5-11(1977)

/27/ T.M. Hayes, J. Non-crystalline Solids 31,57-79(1978)

/28/ D. Turnbull, Scripta Met. 11,1131-1136(1977)

/29/ R. Ray, R. Hasegawa, C.P. Chou and L.A. Davies, Scripta Met. 11,973-978(1977)

/30/ M. Takahasi and M. Koshimura, Japan J. Appl. Phys. 16,2269-2270(1977)

/31/ R. Hasegawa and R. Ray, J. Appl. Phys. 49,4174-4179 (1978)

/32/ J. Durand and M. Yung, Amorphous Magnetism II, Ed. R.A. Levy and R. Hasegawa (Plenum Press, New York) 275-288(1977)

/33/ D.E. Polk, Scripta Met. 4,117-122(1970)
D.E. Polk, Acta Met. 20,485-491(1972)

/34/ D. Turnbull, J. Phys. (Paris) Colloque 35,C4-1-C4-10 (1974)

/35/ S.R. Nagel, Scripta Met. 12,43-44(1978)

/36/ R. Yamamoto, T. Mihara and M. Doyama, Phys. Status Solidi(a) 50,165-169(1978)

/37/ U. Gonser, M. Ghafari and H.G. Wagner, J. Magn. and Magn. Matr. 8,175-177(1978)

/38/ T. Kemeny, I. Vincze, B. Fogarassy and S. Arajs, Report KFKI,1978.56(1978)

/39/ J.J. Gilman, Phys. Mag. B37,577-584(1978)

/40/ J.F. Sadoc, J. Dixmier and A. Guinier, J. Non-crystalline Solids 12,46-60(1973)

/41/ D.S. Boudreaux and J.M. Gregor, Rapidly Quenched Metals II, MIT press, Mass., 323-327(1976)
D.S. Boudreaux, J. Appl. Phys. 48,125-128(1977)

/42/ D.S. Boudreaux, Amorphous Magnetism II, Ed. R.A. Levy and R. Hasegawa (New York) 463-648(1977)
D.S. Boudreaux, Phys. Rev. B18,4039-4047(1978)

/43/ I. Vincze, D.S. Boudreaux and M. Tegze, Report KFKI-1979-04, CRIP, Budapest

/44/ C.L. Briant and J.J. Burton, Phys. Status Solidi (b) 85,393-407(1978)

/45/ E.P. Wohlfarth, IEEE Trans. Magn. MAG-14,933-937(1978)

/46/ R. Rhodes and E.P. Wohlfarth, Proc. Roy. Soc. London A273,247-258(1963)

/47/ R.C. O'Handley and D.S. Boudreaux, Phys. Status Solidi(a) 45,607-615(1978)

/48/ K. Yamauchi and T. Mizoguchi, J. Phys. Soc. Japan 39, 541-542(1975)

/49/ P. Oelhafen, E. Hauser, H.J. Güntherodt and K.H. Bennemann, Phys. Rev. Lett. 43,1134(1979)

/50/ P. Oelhafen, unpublished

/51/ H.J. Güntherodt and H.U. Kunzi, Metallic Glasses, Ed. J.J. Gilman and H.J. Leamy (ASM, USA) 304-339 (1978)

/52/ W. Radlik, Diplomarbeit, Ruhr-Universität, West-Germany (1980)

/53/ J.D. Riley et al., Phys. Rev. B20,776(1979)

/54/ S.R. Nagel and J. Tauc, Phys. Rev. Lett. 35,380 (1975)

/55/ P. Oelhafen et al, Solid State Communications 30, 641(1979)

/56/ K. Froböse and J. Jäckle, J. Phys. F7,2331(1977)

/57/ U. Mitzutani et al, Phys. Rev. Lett. 41,661(1978)

/58/ J.K. Krause, T.C. Long, T. Egami and D. Onn, Phys. Rev. B, Vol.21, No.7, 2886-1896(1980)

/59/ J.K. Krause, T.C. Long, D. Onn and F.E. Luborsky, J. Appl. Phys. 50(11),7665-7667(1979)

/60/ L. Berger, AIP conference Proceeding, No.34, 355-357 (1976)

/61/ J. Kübler et al, Phys. Rev. B., Vol. 23 (1981)

/62/ M. Matsuura et al, Solid State Communications, Vol.33, 805-897(1980)

/63/ T. Mizoguchi, AIP conference Proceeding, No.34, 286-291(1976)

/64/ R. Alben, J.I. Budnick and G.S. Cargill III, metallic Glasses, Ed. J.J. Gilman and H.J. Leamy (ASM, USA) 304-339(1978)

/65/ N.F. Mott, Advances in Phys. 13,325-422(1964)

/66/ K. Handrich, Phys. Status Solidi 32,K55-58(1969)

/67/ Y. Koi, A. Tsujimura and T. Hihara, J. Phys. Soc. Japan 19,1493(1964)

/68/ H. Callen, D. Hove and A. Heeger, Phys. Lett. 17, 233(1965)

/69/ T. Wolfram and W. Hall, Phys. Rev. 143,284(1966)

/70/ C.G. Montgomery , J.I. Krugler and R.M. Stubbs, Phys. Rev. Lett. 25,669(1970)

/71/ F. Keffer, Handbuch der Physik, Ed. S. Flügge (Springer-Verlag, Berlin) Vol.18, Part 2,1(1966)

/72/ R.J. Birgeneau et al, Phys. Rev. B, Vol.18, No.5, 2192-2195(1978)

/73/ C.L. Chien et al, Solid State Communications, 28, 645(1978)

/74/ J.S. Kouvel, Magnetism and Metallurgy, Vol.2, 523-575, Ed. A.E. Berkowitz and E. Kneller (Academic Press, New York) (1969)

/75/ E-NiFoo and Der-Hsueh Wu, Phys. Rev. B, Vol.5, 98-101(1972)

/76/ D.A. Shirley, Rev. Mod. Phys. 36,339(1964)

/77/ I. Vincze, Solid State Communications, Vol.25, 689-693(1978)

/78/ A. Abragam and F. Boutron, C.R. Aca. Sci. 252,2402 (1961)
R.B. Watson and A.J. Freeman, Hyperfine Interactions (Academic Press, New York) (1967)

/79/ A. Abragam, L'Effect Mössbauer (Gordon and Breach, New York) (1964)

/80/ M.H. Cohen and D. Turnbull, Nature (London) 189, (1961)

/81/ L. Davies, Proc. of Conference on Metallic Glasses: Sciences and Technology, Budapest, Hungary (1980)

/82/ H.H. Liebermann and C.D. Graham(Jr.), IEEE Trans. Magn. MAG-12,921-923(1976)

/83/ H. Nielsen, Ph.D. thesis, Technical University, Copenhagen (1979)

/84/ H. Fraunfelder, The Mössbauer Effect (Bejamin Press, New York) (1962)

/85/ G.K. Wertheim, Mössbauer Effect, Principles and Applications (Academic Press, New York) (1964)

/86/ R.L. Mössbauer and M.J. Clauser, Hyperfine Interactions, Ed. A.J. Freeman and R.B. Frankel (Academic Press, New York) (1967)

/87/ H. Franke, Ph.D. thesis, Ruhr-Universität, West Germany (1979)

/88/ B. Window et al, Mössbauer effect in rhodium-iron alloys, J. de Physique (Paris) C1,863-864(1971)

/89/ M. Takahasi, C.O. Kim, M. Koshima and T. Suzuki, Japan J. Appl. Phys. 17,741(1978)

/90/ J. Hesse and A. Rübartsch, J. Phys. E, Vol.7, 526-532(1974)

/91/ C.C. Tsuei and H. Lilienthal, Phys. Rev. B, Vol.13, 4899-4905(1976)

/92/ C.L. Chien et al, J. Phys. F, 8,2407(1978)

/93/ R.P. Elliot, Constitution of Binary alloys, First supplement (McGraw Hill, New York) (1965)

/94/ M.H. Cohen and D. Turnbull, Nature (London) 203,(1964)

/95/ U. Herold, U. Köster, Proc. Rapidly Quenched Metals III, Brighton (1978)

/96/ N.N. Greenwood and T.C. Gibb, Mössbauer Spectroscopy (Chapman and Hull, London) (1971)

/97/ H. Bernes, I.A. Campbell and R. Fruchart, J. Phys. Chem. Solids 28,17(1967)

/98/ J.J. Becker, F.E. Luborsky and J.L. Walter, IEEE Trans. Magn. MAG-13,988-991(1977)

/99/ B. Window, J. Phys. E4,401(1971)

/100/ J. Wong, EXAFS Studies of Metallic Glasses in Metallic Glass, Vol.I, Ed. H.J. Guntherödt and H. Beck, Springer-Verlag Publisher (1980)

/101/ J. Doniach et al, J. Vac. Sci. Tech. 12,1123(1975)

/102/ F.E. Luborsky, J. Appl. Phys. 51,5(1980)

/103/ R.C. O'Handley, Solid State Communications, Vol.38, 703-708(1981)

/104/ R.C. O'Handley, R. Hasegawa and C.P. Chou, Appl. Phys. Lett. 29,330-332(1976)

/105/ T.E. Sharon and C.C. Tsuei, Phys. Rev. B5,1047(1972)

/106/ C.L. Chien and R. Hasegawa, J. Appl. Phys. 47,2234 (1976)

/107/ R. Hasegawa and R. Ray, Phys. Rev. B, Vol.20,211-214(1979)

/108/ S.N. Kaul, IEEE Vol. MAG.17, No.2,1208-1215(1981)

/109/ M. Sostarich, S. Dey, P. Deppe, M. Rosenberg, INTERAG, 1981, Grenoble, France

/110/ G. Czjzek et al, Phys. Rev. B1,957(1970)

/111/ J. Durand, Amorphous Magnetism II, 305, Ed. R.A. Levy and R. Hasegawa (1977)

/112/ C.L. Chien and R. Hasegawa, in Magnetism and Magnetic Materials (1975)

/113/ H. Hasegawa and J. Kanamori, J. Phys. Soc. Japan, Vol.31,382-393(1971)

/114/ David G. Onn, J. Appl. Phys. 52(3)(1981)

/115/ R.M. Bozorth, Ferromagnetism, D. Van Nostrand (1951)

/116/ H. Franke et al, J. Mag. Mag. Matr. 15-18,1364(1980)

/117/ H.A. Mook et al, Phys. Rev. Lett. 34,1029(1975)

/118/ D. Axe et al, Phys. Rev. B15,2763(1977)

/119/ C. Herring et al, Phys. Rev. 81,869(1951)

/120/ R.A. Tahirkheli, Phys. Rev. B6,2808(1972)

/121/ T. Kaneyoshi et al, J. Phys. C5,L65(1972)

/122/ E. Vogt, in Magnetism and Metallurgy, Ed. E.A. Berkowitz and E. Kneller, 249(1969)

/123/ S. Hatta et al, J. Appl. Phys. 50,1589(1979)

/124/ A.T. Aldred, J. Phys. C1,244(1968)

/125/ G.G.E. Low et al, J. Appl. Phys. 34,1195(1963)

/126/ M. Sostarich et al, Proc. of Rapidly Quenched Materials 4, Japan (1981), to be published

/127/ I.A. Campbell et al, Proc. Phys. Soc. 86,535(1965)

/128/ A.T. Aldred, Phys. Rev. B14,219(1976)

/129/ M.F. Collins et al, Proc. Phys. Soc. 86, 535(1965)

/130/ R.W. Cochrane et al, Phys. Rev. Lett. 32,576(1974)

/131/ R. Harris et al, Phys. Rev. Lett. 31,160(1973)

/132/ J.E. Gubernatis et al, Phys. Lett. A43,211(1973)

/133/ I. Vincze et al, J. Magn. Mag. Matr. 15-18,1336(1980)

/134/ I. Vincze, T. Kemeny, A.S. Schaafsma, A. Lovas and F. Van Der Woude, KFKI-1980-90, Budapest, Hungary

/135/ R.P. Messmer, Proc. of the Conference on Metallic Glasses: Science and Technology, Budapest, Hungary (1980)

/136/ V. Jaccarino, L.R. Walker and G.K. Wertheim, Phys. Rev. Lett. 13,752(1964)

/137/ H. Franke et al, Proc. Int. Conf. on Rapidly Quenched Material, 3, Brighton (1978)

/138/ S. Arajs et al, Proc. Conference on Metallic Glasses: Science and Technology, Budapest, Vol.2, 189(1980)

ACKNOWLEDGEMENTS

At this point, I would like to acknowledge the assistence, support and friendship of the many of my colleagues who have contributed so many ways to my research and to my time spent in Ruhr-University Bochum in general.

Professor M. Rosenberg directed this research, and I would like to thank him for his guidence and his patience. His physical insight and extensive knowledge were most helpful in clarifying my understanding of many aspects of this work.

My fellow graduate students have been a constant source of help, information and frequently recreation and comic relief over the past three years. I would especially like to mention P. Deppe, G. Böhnke, Uli Jansen, Willi Kettler, Ursula Gores and Marcos d'Aguar with whom I also spent time discussing many topics.

I have benefitted greatly from my association with Drs. M. Sostarich and Y. Khan, who helped me in magnetic measurements and X-ray diffraction analysis. Many helpful and informative discussions were held with Drs. D. Salomon and S.N. Kaul and I wish to thank them for their help and interest. I wish to thank Dr. F.E. Luborsky and Dr. H.V. Nielsen for providing me the amorphous ribbons and for helpful discussions.

The support staff at Institute für Experimentalphysik VI, III and Institute für Werkstoffe der Elektrotechnik will be missed also. Great appreciation for their constant and immediate help in matters of safety and technology are extended to Mr. F. Kleimann and Mr. Rolf Wernhardt.

Many of my friends outside the laboratory, have also offered me encouragement and relief. I am deeply grateful to Miss A. Pfeifer for her infinite skill in typing the manuscript and organizing all related matters.

Finally, I would like to thank my mother, my uncle and my brother for their confidence in me, and their encouragement and support throughout my educational career.

The financial support of the Minister for Science and Research of the Land Nordrhein-Westfalen is greatly acknowledged.

DER DRUCKER - Buscheystraße 138 - 4630 Bochum - Tel. (02 34) 70 41 16